

Electron Reconstruction with the ATLAS Inner Detector

Thomas Martin Atkinson



THE UNIVERSITY OF
MELBOURNE

*Submitted in total fulfilment of the requirements
of the degree of Doctor of Philosophy*

School of Physics
The University of Melbourne

December 2006



Abstract

The LHC will produce proton-proton collisions at a centre-of-mass energy of 14 TeV . ATLAS is a general-purpose detector for the LHC, sensitive to a wide range of physics processes. The total LHC production cross-section is dominated by QCD and so the search for rare physics events requires that ATLAS is able to reconstruct and identify leptons with high efficiency and accuracy. Electrons are measured in two ATLAS sub-detectors: the inner tracker reconstructs the trajectories of all charged particles, providing an estimate of the momentum; while the energies of electrons are measured by the electromagnetic calorimeter.

The baseline track fitter for the inner detector is the Kalman filter (KF). The KF is optimal only when all measurement errors and material interactions can be described by gaussian probability density functions. Electrons lose energy in matter predominantly through bremsstrahlung, which is a strongly non-gaussian process described by the Bethe-Heitler distribution. In this case, a non-linear fitter may provide a better estimate of the trajectory of an electron than the KF.

A non-linear generalisation of the KF, the gaussian-sum filter (GSF), has been developed and validated. The Bethe-Heitler distribution is approximated as a weighted sum of gaussian components. The performance of the GSF has been compared to the KF using both the simulated response of the detector and real data taken at the 2004 ATLAS test-beam.

The performance of the GSF in simulation was first studied using samples of single electron events. The momentum resolution obtained using the GSF is, in general, better than the KF. Several LHC physics processes have also been simulated. Invariant mass distributions, obtained using the GSF, are superior to those from the KF in most cases.

When the GSF was used to reconstruct real data from the test-beam, the momentum resolution was found to be much worse than predicted by simulation. Two factors contribute to the large discrepancy: the residual misalignment of the detector elements; and the material in the upstream beam-line. The impact of upstream material on the momentum resolution has been investigated in detail. The amount of material in the beam-line must be known precisely, both to quantify the performance of the track fitters and for the correct calibration of the electromagnetic calorimeter.

Declaration

This is to certify that:

- i. the thesis comprises only my original work towards the PhD except where indicated,
- ii. due acknowledgement has been made in the text to all other material used,
- iii. the thesis is less than 100,000 words in length, exclusive of tables, bibliographies and appendices.

Call to me and I will answer you and tell you great and
unsearchable things you do not know.

Jeremiah 33:3

For my dad.

For teaching me to think.

Acknowledgements

The following people and inanimate objects have provided me with much help during the course of this work:

- ☆ Thank-you Elisabetta, for your help and a really good thesis topic. Thanks for extricating me from SCT module construction, which despite popular opinion, is unlikely ever to receive a Noble prize.
- ☆ Thank-you Geoff for being my second supervisor. Being second means you get the silver medal.
- ☆ Sorry Geoff for accidentally destroying the SCT module.
- ☆ Thank-you Chris for being an excellent third supervisor. You have shared my pain during failed Ashes campaigns and world-cup upsets.
- ☆ Thanks to the members of the EPP group at the University of Melbourne, many of whom have enjoyed the privilege of proof-reading a work widely considered not to be a literary masterpiece.
- ☆ Thanks to all the people at CERN who have provided so much help: Daniel (for knowing a lot about LHC and nothing about LBW), Richard (for knowing both about LHC and LBW), Alan, Are, Markus, Andi, Wolfgang (A), Wolfgang (L), Ed, Maria, Thomas, Tuan, Igor, Martin and all the other people who, due to the pressure to submit, I have now forgotten.
- ☆ Thanks to everybody at Every Nation Church in Melbourne, in particular Joe, James, John, Jason and Ken. For consistency, a physicist would approximate 'Ken' as 'Jen.'
- ☆ The ATLAS Denmark contingent get their very own bullet point, on account of: their appreciation of Monty Python; their ability to save the world using just napkin origami; their proximity to Legoland; their willingness to submit to an Australian head of state; and their ability to formulate a locally gauge-invariant, relativistic quantum field theory describing the dynamics of beer.

- ☆ Thanks to all the guys in the workshop in the School of Physics, especially to Ash who should learn his own phone number before he learns another language.
- ☆ Thanks to Veronica for the Pavlova with capsicum on the top. Truly visionary!
- ☆ Thanks to my Mac Power Book. I love you very much.
- ☆ Thank you mum and dad for your support. The LHC may yet validate your bizarre interpretation of physics. *“The more physics you have, the less engineering you need.”*
- ☆ Thanks to James, Simon and Will for their continued ignorance and apathy towards Physics. *“All science is either physics or stamp-collecting.”*
- ☆ Thanks to the nasty French border guards who have convinced me that even mean people can get a job.
- ☆ Thanks to Champion in St Genis, for really cheap carrots and very unreasonable opening hours. Thanks to the Sprite vending machine for being there even when Champion wasn't.
- ☆ Thanks to QANTAS for never giving me the emergency exit seat. Bad luck, I own you now.
- ☆ Thanks to that guy in Puerto Rico who gave me a lift to my hotel because I got lost.
- ☆ No thanks to the Australian cricket team. Give me back my urn.

Contents

Abstract	iii
Declaration	v
Acknowledgements	ix
Contents	xi
List of Figures	xvi
List of Tables	xxi
1 Introduction	1
1.1 The Standard Model	1
1.1.1 Constituents of the Standard Model	2
1.2 Inadequacies of the Standard Model	3
1.3 New Directions	4
1.4 The Large Hadron Collider	5
2 The ATLAS Detector	9
2.1 Nomenclature	10
2.2 Detector Design Considerations	11
2.3 The Magnet System	13
2.4 The Inner Detector	13
2.4.1 The Pixel Detector	15
2.4.2 The SCT	17

2.4.3	The TRT	17
2.5	Calorimetry	19
2.5.1	The Electromagnetic Calorimeter (ECAL)	19
2.5.2	The Hadronic Calorimeter (HCAL)	20
2.6	The Muon Spectrometer	21
2.7	Trigger and DAQ	23
2.8	Software	25
3	Track Reconstruction	27
3.1	Passage of Charged Particles through Matter	27
3.1.1	Ionising Energy Loss	27
3.1.2	Radiative Energy Loss	28
3.1.3	Multiple Scattering	29
3.2	Material Budget	30
3.3	Track Reconstruction Procedure	32
3.4	Performance	35
3.4.1	Minimum p_T	35
3.4.2	Maximum p_T	35
3.4.3	Results from Simulation and Test Beam	37
4	Methods of Track Fitting	39
4.1	The Track Model	40
4.1.1	Track Parameters for a Helical Model	42
4.1.2	Track Parameters for a Linearised Helical Model	44
4.1.3	Track Parameters for the ATLAS Tracking Detectors	48
4.2	The Least-Squares Estimator	49
4.2.1	Properties of the LSM	50

4.3	The Kalman Filter (KF)	51
4.3.1	Kalman Filter Operations	52
4.4	Non-gaussian Experimental Noise	54
5	The Gaussian-Sum Filter	55
5.1	Principle	55
5.1.1	Prediction	56
5.1.2	Process Noise	57
5.1.3	Filtering	59
5.1.4	Smoothing	61
5.1.5	Component Reduction	63
5.2	Implementation	64
5.2.1	The Gaussian-Sum approximation to the Bethe-Heitler Model	65
6	GSF Performance	69
6.1	Electron Performance in the Central Barrel	69
6.1.1	Pull Quantities	71
6.1.2	Resolution Quantities	72
6.2	Results using Simplified Simulation	75
6.2.1	Component Reduction Technique	76
6.2.2	Gaussian-Sum approximations to the Bethe-Heiter Model	77
6.3	Performance in the Forward Regions	79
6.4	Reconstruction Using the GSF Mode	79
6.5	Timing Considerations	81
6.6	Kink Finding	82
6.6.1	Identification of a Point of Bremsstrahlung	83
6.7	Summary	89

7	The ATLAS 2004 Test Beam	93
7.1	Overview	93
7.2	The H8 Beam-Line	94
7.2.1	The Filter Target	96
7.2.2	The T48 Target	100
7.2.3	Beam Spread	101
7.2.4	Beam Composition	101
7.3	Layout of the CTB	102
7.3.1	The Inner Detector	102
7.3.2	The Calorimeters	106
7.3.3	The Muon Detectors	106
7.3.4	Beam-line Elements	106
7.3.5	Trigger	107
7.4	Tracking Geometry	107
7.4.1	Validation of the Tracking Geometry	108
7.5	Electron Reconstruction	115
7.5.1	Simulation	115
7.5.2	Real Data	120
7.6	Beam-line Material Study	126
7.6.1	Tail Fraction versus Beam Energy	130
7.6.2	Studies with Extra Inner Detector Material	130
7.6.3	Calorimeter Beam-line Material Study	133
7.7	Pion Veto	138
7.8	Performance with Real Data	142
7.9	Summary	143
8	Physics Case Studies	145

8.1	$J/\psi \rightarrow ee$	145
8.2	$Z \rightarrow e^+e^-$	149
8.3	$H \rightarrow ZZ^* \rightarrow 4e$	151
8.4	Tracker / Calorimeter Performance	156
9	Conclusion	159
9.1	Summary	159
9.1.1	Monte-Carlo Studies	160
9.1.2	Test-beam Studies	161
A	The SCT Outer End-cap Module	163
A.1	Design of the SCT Outer End-cap Module	163
A.1.1	Wafer Positioning and Alignment	163
A.2	Melbourne Assembly Procedure	164
A.2.1	Wafer-Spine Assembly	167
A.3	Representations of the Module Geometry	169
A.3.1	Assembly Station Representation	169
A.3.2	Metrology Coordinates	171
A.3.3	Module Measurement Software	173
A.3.4	Control Software for the CMM	175
A.3.5	Results	176
B	GSF Implementation and EDM	177
B.1	The Common Track Class	177
B.1.1	Extended representations of trajectory	178
B.2	Configuring the GSF	179
B.2.1	Extrapolator	179
B.2.2	Measurement Updator	181

B.2.3	The Fitter	181
B.3	Fitting a Track	182
B.3.1	ITrackFitter Methods	183
C	The CTB Tracking Geometry	185
	Bibliography	187

List of Figures

1.1	LHC experimental areas	7
1.2	LHC event rates	8
2.1	The ATLAS detector	10
2.2	The ATLAS inner detector	16
2.3	Layout of the ATLAS calorimeters	20
2.4	The ATLAS trigger / DAQ	23
2.5	The Gaudi-Athena framework	26
3.1	The Bethe-Heitler distribution	30
3.2	Tracker material budget	31
3.3	Measurements in the tracker sub-detectors	33
3.4	TRT drift-circle left-right ambiguity	34
3.5	Definition of minimum transverse momentum	36
3.6	Definition of the sagitta	37
4.1	Parameters describing a helical trajectory	42
4.2	Particle trajectories in a solenoidal field	43
4.3	Particle trajectory: φ versus ρ	45
4.4	Particle trajectory: φ versus $\cot(\theta)$	46
4.5	Particle trajectory: ρ versus $\cot(\theta)$	47

5.1	KL-mixture approximations to the Bethe-Heitler distribution	67
5.2	CDF-mixture approximations to the Bethe-Heitler distribution	68
6.1	Single electron pdf from the GSF and KF	71
6.2	Track parameter pull distributions	73
6.3	Track parameter resolution distributions	74
6.4	GSF and KF resolution as a function of energy	75
6.5	Probability transform of q/p	76
6.6	GSF resolution using different component reduction techniques	77
6.7	GSF resolution as a function of number of components - fast simulation	78
6.8	Resolution in the forward trackers	80
6.9	q/p distributions using GSF mean and mode	80
6.10	GSF timing profiles	82
6.11	Momentum estimate at different locations in the detector	84
6.12	True positions of bremsstrahlung vertices	85
6.13	Reconstructed position of photon emission	88
6.14	Momentum distributions for tracks identified by the kink finder	90
6.15	Effective momentum resolution versus p_T	92
7.1	Particle production rates at the T4 target	95
7.2	Layout of the H8 beam-line (high energy period)	97
7.3	EM interactions in the filter target	98
7.4	Hadronic interactions in the filter target	99
7.5	Lepton and hadron production rates from the T48 target	100
7.6	Layout of the CTB	103
7.7	Inner detector elements within the CTB	105
7.8	Beam-line elements upstream of the CTB	107

7.9	CTB tracking geometry	109
7.10	Detector pull distributions for simulated 9 GeV/c muons	111
7.11	Detector pull mean values	112
7.12	Detector RMS values without corrections for multiple scattering	113
7.13	Detector RMS values with corrections for multiple scattering	114
7.14	Parameter pull distributions for simulated 9 GeV/c muons	116
7.15	Parameter pull mean values	117
7.16	Parameter σ values without corrections for multiple scattering	118
7.17	Parameter σ values with corrections for multiple scattering	119
7.18	Pull parameter distributions for 9 GeV/c electrons	121
7.19	Resolution parameter distributions for 9 GeV/c electrons	122
7.20	GSF and KF resolution as a function of energy	123
7.21	Track multiplicity in simulation and data	125
7.22	Normalised q/p residuals in simulation and data	125
7.23	GSF momentum resolution in simulation and data	126
7.24	Global track q/p distributions	128
7.25	Global track q/p integrated tail fractions	129
7.26	Silicon track segment q/p distributions	129
7.27	Pixel track segment q/p integrated tail fractions	131
7.28	SCT track segment q/p integrated tail fractions	132
7.29	Integrated tail fraction profiles for different beam momenta	133
7.30	Integrated tail fraction for additional inner detector material	134
7.31	Energy deposited per calorimeter sampling	135
7.32	CTB photon run setup	136
7.33	Total calorimeter energy for the CTB photon run	137
7.34	Photon run tail efficiency	138

7.35	TR hits and HCAL energy for 20 GeV/c positrons	140
7.36	GSF and KF reconstruction performance with extended simulation	142
7.37	GSF performance in extended simulation and data	143
8.1	True momenta of the leptons from the J/ψ decay	147
8.2	Normalised q/p residuals of the leptons from the J/ψ decay	147
8.3	Invariant mass of the J/ψ	148
8.4	True momenta of the leptons from the Z decay	149
8.5	Normalised q/p residuals of the leptons from the Z decay	150
8.6	Invariant mass of the Z boson	150
8.7	True momenta of the leptons from the H decay	152
8.8	Normalised q/p residuals of the leptons from the H decay	153
8.9	Invariant mass of the H boson	154
8.10	Momentum (tracker) and energy (ECAL) distributions	157
8.11	Tracker and ECAL performance as a function of energy	158
A.1	SCT outer end-cap module	164
A.2	SCT module mechanical parameters	165
A.3	SCT outer end-cap module assembly station	168
A.4	Image of the four wafers on the assembly station	169
A.5	Assembly station representation of the module geometry	170
A.6	Metrology jig	172
A.7	The SCT module geometry catalogue	173
A.8	Commands to run the module measurement software	174
A.9	The Melbourne CMM	175
A.10	Control GUI for the CMM	175
B.1	ComponentParameters UML	179

B.2 MultiComponentStateOnSurface UML	179
C.1 TrackingVolume UML	186
C.2 Layer UML	186

List of Tables

1.1	Constituent fermions of the Standard Model	3
1.2	Comparison of the fundamental forces	3
1.3	LHC machine parameters	6
2.1	Design parameters of the ATLAS detector	9
2.2	Key parameters of the pixel system	15
2.3	Key parameters of the SCT	18
2.4	Key properties of the electromagnetic calorimeter	21
2.5	Key properties of the hadronic calorimeter	22
2.6	Low luminosity trigger menu	24
3.1	Energy loss variables	28
3.2	Evolution of the tracker material budget	31
3.3	Tracker reconstruction performance	38
6.1	Mean and RMS values of pull distributions	72
6.2	Mean and RMS values of resolution distributions	72
6.3	Performance of GSF mean and mode algorithms	81
6.4	Fraction of reconstruction time spent in fitting	82
6.5	Performance of the kink finder using truth constrains	85
6.6	Kink finder performance at 10 GeV/c	87

6.7	Reconstructed resolution quantities at 10 GeV/c	89
6.8	Kink finder performance at 20 GeV/c	91
6.9	Single electron performance in p_T	92
7.1	Material distribution in the CTB tracking geometry	109
7.2	Mean and RMS values of pull distributions	123
7.3	Mean and RMS values of resolution distributions	123
7.4	Reconstructed data sets	124
7.5	Reconstructed data sets for the upstream material study	127
7.6	Reconstructed data sets the study of additional tracker material	133
7.7	Definitions of pion veto variables	139
7.8	Parameters of run 2102413	141
7.9	Parameters of run 2102107	141
8.1	J/ψ reconstruction quantities	146
8.2	$Z \rightarrow e^+e^-$ reconstruction quantities	151
8.3	Reconstruction quantities of the leptons from the H decay	155
8.4	Invariant mass resolution quantities of the $4e$ from the H decay	155
A.1	SCT outer end-cap module mechanical specifications	166
A.2	Assembly station representation of the module geometry	170
A.3	Metrology representation of the module XY geometry	171
A.4	Metrology representation of the module Z profile	173
A.5	Specifications of the QV-Pro 606 CMM	176

Chapter 1

Introduction

The last four decades have seen remarkable theoretical and experimental advances which have lead to the identification of what are widely regarded to be the elementary constituents of matter and the fundamental forces which act between them. These discoveries comprise what is now known as the *Standard Model* [1–4]. The development of the Standard Model (SM) emphasises the major goal of physics - simplification and unification of seemingly diverse, often apparently unrelated, natural phenomena. The SM successfully accounts for all atomic, nuclear and sub-nuclear processes requiring only a dozen matter particles (*fermions*), a dozen force carriers (*gauge-bosons*) and the as yet unobserved Higgs boson.

The SM is a relativistic quantum-mechanical description of nature; mediating packets (quanta) of energy facilitate interactions between matter particles. Of the four known fundamental forces, quantum field theories of the strong, weak and electromagnetic interactions have been developed and incorporated into the SM. The SM also provides the mechanism for the unification of the weak and electromagnetic forces in the electroweak sector. Gravity, the dominant force acting on large scale structures in the universe, is not described by a quantum field theory. At the start of the 21st century, the foundation of physics is two robust, yet currently irreconcilable theories: gravity, incorporated into the classical framework of general relativity, and the SM, based on quantum mechanics.

1.1 The Standard Model

The SM is the best representation of the microscopic universe currently available. It incorporates the strong force, described by quantum chromo-dynamics (QCD), and the electroweak force, which itself is a unification of the weak and electromagnetic interactions. A brief and largely qualitative overview of the SM is presented in this section.

Despite its success, the SM possesses a number of limitations and inadequacies (section 1.2). It appears likely that extensions to the SM (section 1.3) are necessary in order to construct a more complete description of nature. Many of these extensions are constrained to manifest at or below an interaction energy of $\sim 1 \text{ TeV}$. Previous particle physics experiments were not capable of producing such energetic interactions. The Large Hadron Collider (LHC - section 1.4) is currently nearing completion at the European Laboratory for Particle Physics (CERN) and will be the first experiment to probe the TeV scale, providing unambiguous conclusions regarding the validity of the SM at such energies.

1.1.1 Constituents of the Standard Model

The particles of the SM can be classified into three types. The matter particles, shown in table 1.1, are fermions (spin- $\frac{1}{2}$). They are further classified depending on whether or not they experience the strong force. Those that do are called quarks, of which there are six *flavours* - $(u, d; c, s; t, b)$, while those that do not are called leptons, $(e, \nu_e; \mu, \nu_\mu; \tau, \nu_\tau)$. All SM fermions experience the weak force while only those carrying an electric charge can undergo electromagnetic interactions. The fermions are grouped into pairs differing by one unit of electric charge, giving rise to three generations of doublets in both the quark and lepton sectors. The fermion masses increase with each generation. All ‘normal’ matter consists of first-generation fermions - up and down quarks, electrons and electron neutrinos. The underlying reason for the repeating pattern of the three fermion generations is not at all understood.

Particles with integer spin are bosons. The 12 force mediating *gauge bosons*, arising from the local symmetries of the SM, are shown in table 1.2. The gauge bosons of the SM all have spin-1.

In addition to the gauge bosons and fermions, the SM postulates the existence of one spin-0 (scalar) particle, the Higgs boson (H^0). The SM does not predict the mass of the H^0 , however certain scattering processes violate unitarity if $m_H \gtrsim 1 \text{ TeV}/c^2$ [5]. For the SM to remain valid at all energies up to the Planck scale (10^{19} GeV) without the introduction of new physics, then the requirements on the Higgs mass are appreciably more stringent: $130 \lesssim m_H \lesssim 190 \text{ GeV}/c^2$ [6]. Experimental searches provide a lower bound on the Higgs mass of $m_H > 114.4 \text{ GeV}/c^2$ at 95% confidence level [7].

In the region $m_H \lesssim 120 \text{ GeV}/c^2$ the Higgs may be identified through its decay to two photons. For higher values of m_H ($130 \lesssim m_H \lesssim 1000 \text{ GeV}/c^2$), a search for the ‘golden decay mode’ of the Higgs into four charged leptons is considered the best approach.

Fermions of the Standard Model				
Generation	Quarks		Leptons	
First	u	d	ν_e	e
Mass	1.5 - 3.0 MeV/c^2	3 - 7 MeV/c^2	$< 2 eV/c^2$	0.511 MeV/c^2
Second	c	s	ν_μ	μ
Mass	1.25 GeV/c^2	95 MeV/c^2	$< 0.19 MeV/c^2$	106 MeV/c^2
Third	t	b	ν_τ	τ
Mass	174 GeV/c^2	5 GeV/c^2	$< 18.2 MeV/c^2$	1.78 GeV/c^2
Charge	$+2e/3$	$-e/3$	0	$-e$

Table 1.1: Constituent fermions of the Standard Model [8]. Each fermion has an associated antiparticle. Quarks and leptons are arranged in three generations of doublets. Each quark can take one of three colour charges, red, green or blue. The leptons are not sensitive to the strong force and are therefore colourless. All quarks and leptons are sensitive to the weak force and those which are electrically charged undergo electromagnetic interactions. The quark masses are estimates only. Since free quarks have never been observed, their masses are highly model dependant.

Fundamental Forces					
Force	Range	Strength	Boson	Mass(GeV/c^2)	Spin
Weak	$< 10^{-18} m$	10^{-5}	W^\pm, Z^0	80, 91	1
E.M.	∞	10^{-2}	photon	0	1
Strong	$< 10^{-15} m$	1	8 gluons	0	1

Table 1.2: A comparison of the range, relative strength and other important properties of the SM forces and their associated gauge bosons [8,9]. The relative strengths of the forces and the masses of the W^\pm and Z^0 bosons are approximate. The other mediators are necessarily massless to preserve the gauge invariance of the theory.

1.2 Inadequacies of the Standard Model

The SM can account for all QCD and electroweak phenomena. To date, no experimental result has been produced which disagrees with the predictions of the SM. Notwithstanding the remarkable agreement between theory and experiment, there remain within the SM a number of deficiencies and features lacking explanation.

The most serious problem with the SM is that the Higgs boson, responsible for the spontaneous symmetry breaking of the electroweak sector, remains unobserved. There is no other mechanism known which is able to produce massive vector bosons in a local gauge model, or massive fermions in a theory which incorporates parity violation (weak interactions are observed to violate parity). Additionally, the mass of the SM Higgs boson is highly sensitive to radiative corrections which, unless there is an incredible fine-tuning, would cause it ultimately to obtain a mass comparable with the Planck scale.

The SM claims to be able to describe all matter in terms of leptons and quarks. Surveys of the cosmos suggest that only $\sim 10\%$ of the matter in the universe is made of SM fermions, the so-called dark matter comprising the remainder. If a new type of fundamental particle is associated with dark matter, then it must be massive but only weakly interacting (a weakly interacting massive particle - WIMP). Such particles would be invisible through normal electromagnetic observations.

The strong and electroweak interactions are the result of distinct fields arising from independent local gauge symmetries, each with a different coupling strength. Extensions to the SM could perhaps unify the strong, electroweak and gravitational interactions as representations of a higher symmetry.

It is difficult to regard the SM as a fundamental model since, even if the neutrinos are assumed to be massless, it contains 19 free parameters. These parameters are not specified by the theory and must be determined experimentally: three coupling constants of the gauge theory $SU(3) \times SU(2) \times U(1)$; three lepton masses; six quark masses; the mass of the Z^0 boson, which sets the scale for weak interactions; four parameters of the CKM matrix; a parameter describing the magnitude of CP-violation in strong interactions; and the mass of the Higgs boson. Additionally, for example, the SM provides no explanation for the origin of the fermions, or the reason for parity violation in weak interactions.

The SM is unable to account for the size of the matter-anti-matter asymmetry in the universe. While the SM exhibits some preference for matter over anti-matter, due to CP-violation through the CKM matrix, this is insufficient to explain the observed discrepancy.

Neutrino flavour oscillations have now been observed. This phenomenon is not incorporated into the SM which assumes neutrinos are massless and therefore prohibits oscillations.

1.3 New Directions

In the quest to overcome the limitations of the SM, many extensions have been proposed. *Grand unified theories* [3, 4] attempt to incorporate the $U(1)$, $SU(2)$ and $SU(3)$ groups of the SM into a higher symmetry. While such theories share many of the problems of the SM - for example, large numbers of free parameters and no gravitational interaction - all SM forces are treated as aspects of the same interaction, represented by a single gauge group (e.g. $SU(5)$ or $SO(10)$) with one coupling constant. Such models are able to explain why the quarks carry fractional charge while the electron-type leptons have $Q = -1$ and why electric charge is quantised. However, such models also manifest proton decay, which has never been observed.

In section 1.2 the apparent fine-tuning of the Higgs mass was discussed. *Supersymmetry* [10,

[11] provides an explanation for the mass of the Higgs without an unnatural degree of fine-tuning. In the *minimal supersymmetric model* (MSSM), each fermion has a new partner boson and vice versa. This symmetry must be broken, otherwise the super-particles would have the same masses as their SM counterparts. The radiative corrections introduced by the additional super-particles cancel out the SM corrections to the Higgs mass. Since the super-particles have never been observed they must be very massive. However, in order that they provide the necessary cancellations in the radiative corrections to the Higgs mass, they are constrained to be $\lesssim 1 \text{ TeV}/c^2$ [11].

Supersymmetry also postulates the existence of a stable massive particle which is sensitive only to the weak and gravitational interactions. If this particle is electrically neutral, it is an obvious dark matter candidate. When supersymmetry is incorporated into grand-unified gauge groups such as $SU(5)$, it forces the couplings of the strong, weak and electromagnetic interactions to converge to a single point at $\sim 10^{16} \text{ GeV}$.

More ambitious models, such as string theory, attempt to produce a quantum theory of gravity. Interactions, at energies many orders of magnitude higher than can be produced in current experiments, are required for such models to be tested.

1.4 The Large Hadron Collider

Although continued theoretical research is necessary and may well provide useful perspective on the shortcomings of the SM, it is unlikely that significant advances will be made without experimental input. A comprehensive study of particle interactions at the TeV scale will provide invaluable insight into the mechanism of spontaneous symmetry breaking in the electroweak sector, which requires a Higgs mass $\lesssim 1 \text{ TeV}/c^2$. Additionally, if supersymmetry plays any part in the cancellation of radiative corrections to the Higgs mass, then the masses of the super-particles must also be $\lesssim 1 \text{ TeV}/c^2$. The LHC [12] will be the first collider to produce interactions at the TeV scale.

The LHC is currently nearing completion at CERN [13], located near Geneva, Switzerland. The LHC is 27 km in circumference, occupying the tunnel that was formally used for the Large Electron-Positron Collider (LEP). Two counter-circulating 450 GeV proton beams are injected into the LHC where they are accelerated to 7 TeV . Superconducting dipoles, cooled to 1.9 K , are used to steer the beams. At four points around the ring the two beams collide with a centre-of-mass energy of 14 TeV . In order to achieve a high luminosity ($0.1 - 1 \times 10^{34} \text{ cm}^{-2}\text{s}^{-1}$), pp collisions are preferred to $p\bar{p}$. First collisions will occur before the end of 2007, albeit at reduced luminosity and energy. The most important parameters of the LHC are provided in table 1.3.

The four experimental areas are also currently under construction. Two detectors, ATLAS (chapter 2) and CMS [14], while optimised for the discovery of the Higgs boson, are sensitive to a wide range of physics processes. Dedicated b-physics (LHC-b [15]) and heavy ion (ALICE [16]) experiments are also approaching completion. The layout of the LHC experimental areas is shown in figure 1.1.

Cross-sections for a variety of physics processes are shown in figure 1.2. The production cross-section, for example, of the Higgs boson is several orders of magnitude higher at the LHC than at the Tevatron, which provides $p\bar{p}$ collisions at a centre-of-mass energy of 1.96 TeV . The total cross-section, at both LHC and the Tevatron, is dominated by low transverse momentum (p_T) QCD processes and is many orders of magnitude higher than the Higgs cross-section. Therefore, leptonic or semi-leptonic final states are the only way to identify rare physics processes embedded in an enormous hadronic background.

LHC Machine Parameters	
Ring circumference (km)	26.659
Beam energy (TeV)	7.0
Stored energy per beam (MJ)	334
Luminosity $cm^{-2}s^{-1}$	$0.1 - 1.0 \times 10^{34}$
Luminosity lifetime (hours)	~ 10
Collision particles	pp or $Pb Pb$
Particles per bunch	1.15×10^{11}
Bunch collision frequency (MHz)	40
Bunch separation	7.5 m (25 ns)
Bunches per beam	2808
RMS bunch length (cm)	7.55
RMS bunch radius (μm)	16.6
Crossing angle (μrad)	300
Average number of interactions per crossing	19.02
Number of dipoles	1232
Dipole magnetic field @ 7.0 TeV (T)	8.33
Dipole cryostat temperature (K)	1.9

Table 1.3: LHC machine parameters [8].

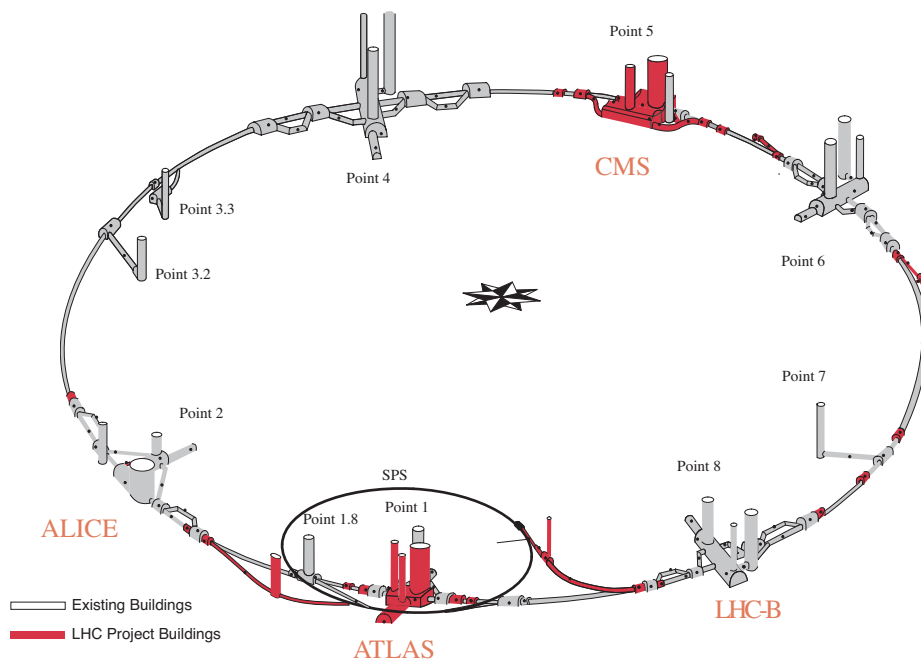


Figure 1.1: LHC experimental areas. The LHC occupies the tunnel formerly containing the LEP experiment. Areas which have been added specifically for the LHC are shown in red.

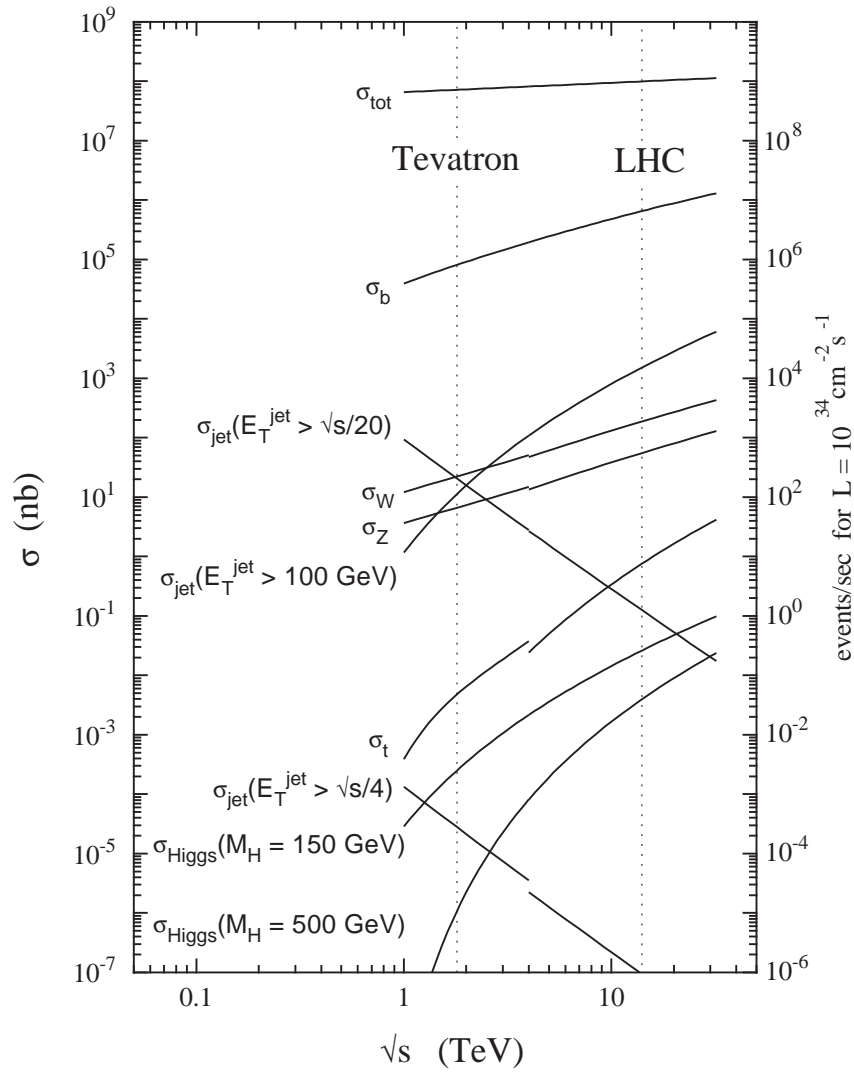


Figure 1.2: Production cross-sections as a function of centre-of-mass energy (\sqrt{s}) for proton-(anti)proton collisions at the LHC and Tevatron [17]. The discontinuity at $\sqrt{s} = 4$ TeV is caused by the transition from $p\bar{p}$ collisions at the Tevatron to pp collisions at the LHC.

Chapter 2

The ATLAS Detector

The two general-purpose detectors for the LHC, ATLAS and CMS, have been designed to exploit the full potential of 7 *TeV* on 7 *TeV* proton-proton collisions at an instantaneous luminosity of $10^{34} \text{ cm}^{-2}\text{s}^{-1}$.

A brief overview of the ATLAS detector is presented in this chapter with the most important design motivations discussed in section 2.2. The detector subsystems are described in sections 2.3 to 2.6. The importance of a robust and efficient trigger is discussed in section 2.7. An overview of the software framework (section 2.8) concludes the chapter.

The ATLAS detector [18–20] is shown in figure 2.1. The most important features of the design are provided in table 2.1.

Parameter	ATLAS
Overall diameter (<i>m</i>)	22
Overall length (<i>m</i>)	46
Total weight (<i>tonnes</i>)	7,000
Solenoidal magnetic field (<i>T</i>)	2
Solid angle coverage for tracking ($\Delta\varphi \times \Delta\eta$)	$2\pi \times 5.0$
Solid angle coverage for calorimetry ($\Delta\varphi \times \Delta\eta$)	$2\pi \times 9.6$
Total cost (<i>MCHF</i>)	550

Table 2.1: Global design parameters of the ATLAS detector [20].

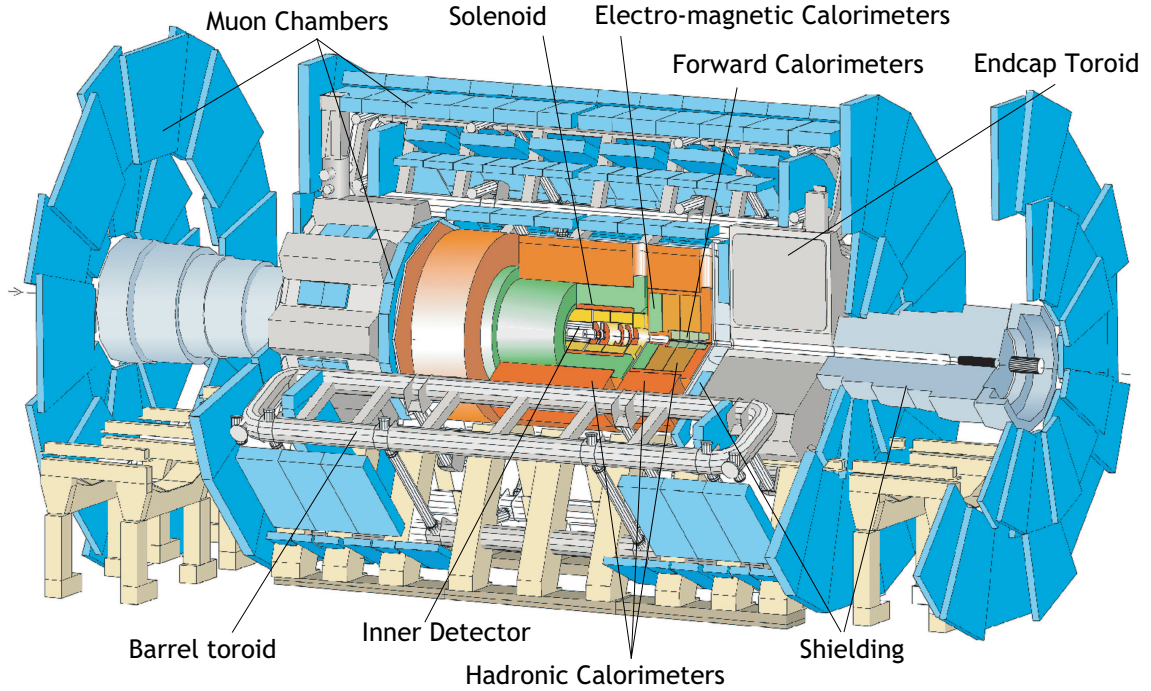


Figure 2.1: The ATLAS detector.

2.1 Nomenclature

ATLAS has a cylindrical super-structure, consisting of a central *barrel* region and two lids (*end-caps*). Given this geometry, the position of a specific detector element within ATLAS is naturally given in cylindrical coordinates, (r, φ, z) . The z -axis is defined by the axis of symmetry of the solenoidal magnetic field, r is the transverse distance of a point from the z -axis and φ is the azimuthal angle¹.

The kinematics of proton-proton collisions are described *inclusively* - the properties of the event are considered as a whole rather than as many separate fragments. The energy and longitudinal momentum (p_z) of any particle produced in a collision can be written as [8]:

$$E = m_T \cosh(y), \quad p_z = m_T \sinh(y), \quad (2.1)$$

where m_T is the *transverse mass*, which can be defined in terms of the rest mass (m_0) and the momentum of the particle in the transverse projections (p_x, p_y):

¹The detector frame is slightly shifted with respect to the so-called *physics frame*, the z -axis of which points along the beam-line; physics analyses proceed necessarily in the coordinate system defined by the direction of the beam, not the symmetries of the detector.

$$m_T^2 = m_0^2 + p_x^2 + p_y^2. \quad (2.2)$$

The *rapidity*, y , is:

$$y = \frac{1}{2} \ln \left\{ \frac{E + p_z}{E - p_z} \right\}. \quad (2.3)$$

In a hadron collider, the distribution of the number of collision products (N) is approximately flat with respect to rapidity ($dN/dy \sim 0$). Furthermore, the difference in rapidity between two particles is independent of any Lorentz boost along the z -axis - a particularly useful feature in a hadron machine given that the momenta of partons within a proton are unknown. In the relativistic limit ($p \gg m$), the *pseudo-rapidity* (η) can be used as an approximation to the true rapidity. Conveniently, it depends solely on the polar angle (θ) through the relation:

$$\eta = -\ln \left\{ \tan \left(\frac{\theta}{2} \right) \right\}. \quad (2.4)$$

In many cases it is useful to characterise the three-momentum of a relativistic particle traversing the ATLAS detector in terms of the transverse component of its momentum (p_T), and its direction in (φ, η) .

2.2 Detector Design Considerations

ATLAS consists of three major subsystems arranged like layers of an onion around the interaction point:

- The **inner tracker** is located closest to the interaction point. It measures the trajectories of all charged particles originating from proton collisions. The entire inner detector is enveloped by a solenoidal magnetic field of approximately $2 T$.
- Electromagnetic (ECAL) and hadronic (HCAL) **calorimeters** are located at intermediate radii and measure the energies of electrons, photons and hadrons.
- The **muon spectrometer** measures the direction and momentum of muons which penetrate the large amounts of material contained within the calorimeters.

The designs of the subsystems are constrained by a number of requirements:

- **Four-Momentum Measurement:** The size of the ATLAS detector reflects both the energy spectrum of particles produced in LHC collisions, and the particular technologies incorporated in the detector design. Proton-proton interactions at 14 TeV produce particles across a wide range of energies (a few hundred MeV to a few TeV). The air core torioids of the muon spectrometer provide a magnetic field $\sim 0.5 T$. Therefore, a long lever arm is required to achieve sufficient bending power for a precise measurement of energetic muons. (CMS achieves a comparable muon momentum resolution using a smaller detector since the field in the muon system is $\sim 2 T$.) Precise estimates of the energies of photons, electrons and hadrons are provided by the calorimeters.
- **Detector Acceptance:** The detector must almost completely enclose the interaction point, ensuring that no particle of interest escapes ATLAS unobserved. When the detector acceptance is large, the presence of particles which do not interact with the detector (neutrinos) can be inferred by an energy-momentum imbalance. To facilitate a wide geometric acceptance, all subsystems have barrel and end-cap components. The calorimeter end-caps have been designed to accept particles as close to the beam-line as $\theta = 1^\circ$ ($\eta = 4.8$).
- **Particle Identification:** In addition to precision measurements of momentum and energy, ATLAS must provide powerful particle identification capabilities; electrons and muons (and to a lesser extent photons and τ -leptons) provide strong evidence for rare physics processes which are embedded in an enormous hadronic background. For example, at a transverse momentum of 40 GeV/c , the electron to jet production ratio is a few 10^{-5} . This is almost two orders of magnitude lower than the ratio obtained at the Tevatron, since the increase in the cross-section for QCD jet production is much greater than for W and Z bosons. ATLAS has therefore been designed to provide powerful lepton identification and jet rejection in the range $|\eta| < 2.5$.
- **Robustness:** The particle flux and radiation levels from LHC collisions are significant. Moreover, ATLAS is expected to take data for in excess of 10 years. Design of sensitive detector elements, in particular at high η , where the particle flux is greatest, presents a significant technical challenge. After a time, material in the high radiation regions will become active, making maintenance extremely arduous, especially since access to many parts of the detector is difficult. ATLAS has therefore been designed to operate for long periods of time with minimal intervention. Furthermore a significant amount of redundancy has been incorporated into ATLAS, allowing independent measurements of important physics processes by different subsystems and therefore protecting against critical failures.

- **Trigger:** At design luminosity, inelastic proton-proton collisions occur at a rate of $\sim 10^9$ Hz . Data can be written out at about 100 Hz based on an average event size of 1-2 MB . The trigger must therefore facilitate a reduction in the event rate of 10^7 . It is not possible, even with the most powerful processors currently available, to achieve a full trigger decision in the 25 ns between adjacent bunch crossings. Therefore, a three-level triggering system is required and data is cached temporarily in pipelines pending a trigger decision. With such an extreme reduction in the event rate, the trigger must be carefully designed so not to introduce bias into a physics analysis.

2.3 The Magnet System

LHC collisions will produce muons up to ~ 1 TeV/c . Design specifications dictate that the momentum resolution on these muons should be \mathcal{O} 10%. A strong magnetic field is required over a large volume to deflect such energetic particles. Superconductor technology is the only practical option for such magnets due to both cost and size constraints.

ATLAS has been designed so that the muon spectrometer is capable of making stand-alone measurements over a large solid angle and energy range. Two independent magnet systems are therefore required.

A solenoidal 2 T field deflects all charged particles within the inner detector. The solenoid is located directly in front of the ECAL and is only 45 mm thick to minimise the inert material before the calorimeter. Even so, the material within the magnet is one of the factors limiting the energy resolution in the region $1.2 < |\eta| < 1.5$.

The magnetic field in the muon spectrometer is provided by superconducting air-core toroids. Both the barrel and end-cap toroids consist of eight flat coils, wound in series with NbTi/Cu cable. Liquid helium is used to cool the magnets to the operating temperature of 4.5 K .

2.4 The Inner Detector

The inner detector [19, 21] reconstructs the trajectories of all charged particles emerging from the interaction region over a range $|\eta| < 2.5$. The design of the inner detector is motivated by a stringent set of criteria:

- **Efficient, robust pattern recognition:** The inner detector consists of layers of sensitive elements which record the position of a particle at many points along its trajectory. Pattern recognition is the process by which measurements (or *hits*) from the detector

elements are assigned to a particular track candidate. An individual detector element is required to have a high detection efficiency with a small probability of registering a false positive. The detector elements have a high granularity so that the occupancy is low, minimising the number of ambiguities arising during pattern recognition. To protect against critical failures, no individual measurement dominates the momentum estimate. The detector incorporates a degree of redundancy in all sensitive elements and read-out electronics to ensure continued functionality over the lifetime of the experiment.

- **Durable:** Because it is located closest to the beam-line, the radiation levels within the inner detector are extreme. The detector elements have been designed to withstand a high particle flux over many years.
- **Particle identification:** The inner detector identifies a particle's sign of charge from the helicity of the track. Additionally, the tracker is capable of performing stand-alone electron identification by measuring transition radiation in the TRT (section 2.4.3). Together with the ECAL or muon spectrometer, combined electron or muon identification is possible.
- **Secondary vertexing:** The inner detector provides precise measurements of secondary vertices from particles which decay away from the interaction point (b -jets and τ -leptons in particular).
- **Triggering:** Information from the inner detector is used by trigger algorithms to identify electron, muon, τ -lepton and b -jet candidates.

The inner detector is cylindrical in design, consisting of a barrel region and two end-caps. It has an outer radius of 1.1 m and is 5.6 m in length - extending slightly beyond the solenoid. The field in the parts of the inner detector not enclosed by the solenoid is appreciably inhomogeneous, resulting in a degradation in momentum resolution at high η . The layout of one quadrant of the inner detector is shown in figure 2.2.

Three detector subsystems comprise the inner detector:

- **The pixel detector:** High granularity silicon pixel detectors are located closest to the interaction point.
- **The semi-conductor tracker (SCT):** Precision silicon micro-strip detectors are located at intermediate radii.
- **The transition radiation tracker (TRT):** A straw tube tracker is located farthest from the interaction point. By also collecting transition radiation it is capable of performing electron identification.

Track reconstruction algorithms are used to determine the trajectories of charged particles from the response of the detector subsystems. The material in the tracker causes a deterioration in reconstruction performance. These issues are addressed in chapter 3.

2.4.1 The Pixel Detector

Three pixel barrel layers and three discs in each end-cap provide precise measurements of the position of charged particles close to the interaction point. Because of its proximity to the beam-pipe, the pixel detector dominates measurements of track impact parameters and provides vertex reconstruction capabilities. Table 2.2 summarises the main features of the pixel subsystem. Each pixel module is required to have a high granularity to maintain a low occupancy. The pixel size is significantly smaller in the $R\varphi$ (bending) plane to provide an accurate p_T measurement. The two dimensional pixel array is bump-bonded to 16 front-end read-out chips, where the electrical signal is amplified and compared to a threshold to give a binary readout. While there are 47,268 pixels per module, there are only 46,080 readout channels. So that all pixels are connected, it is sometimes necessary to couple (*gang*) two (non-adjacent but near-by) pixels to the same output. A hit in a ganged pixel produces a two-fold ambiguity which must be resolved offline.

Parameter	ATLAS
Barrel layer radii (cm)	5.1, 8.9, 12.3
End-cap disc z -position (cm)	49.5, 58.0, 65.0
Total number of barrel (end-cap) modules	1456 (288)
Barrel module tilt in $R\varphi$	20°
Module active area (mm^2)	16.4×60.8
Number of pixels per module	47,268
Pixel size ($R\varphi \times R/z$) (μm)	50×400
Total active area of silicon (m^2)	1.7
Total channels	80×10^6
Average number of hits per track	3
Resolution in $R\varphi$ (μm)	~ 10
Resolution in R/z (μm)	~ 100

Table 2.2: Key parameters of the pixel system [20].

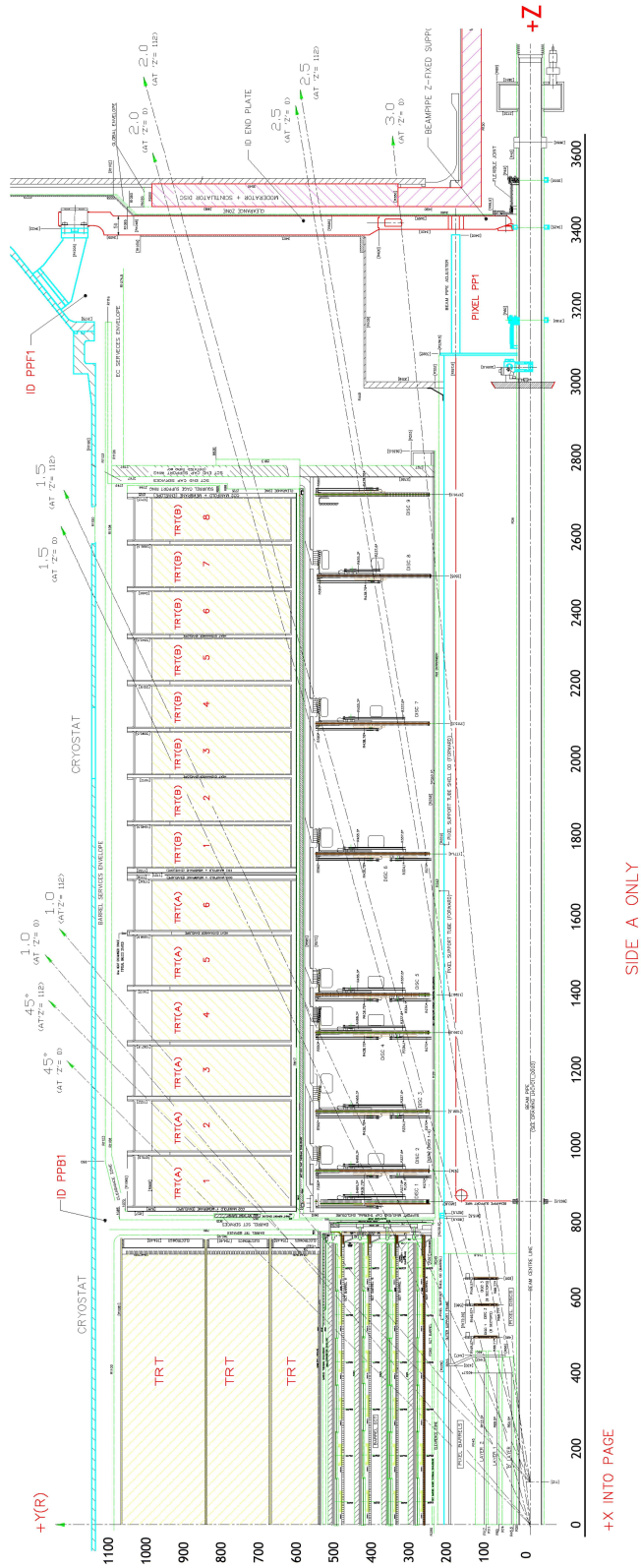


Figure 2.2: The layout of the ATLAS inner detector.

2.4.2 The SCT

The SCT provides precision spatial measurements of the $R\varphi$ coordinate at intermediate radii ($30 \rightarrow 56$ cm). The most important features of the SCT are presented in table 2.3. The SCT has four barrel layers, each 1.53 m long, covering the pseudo-rapidity range $|\eta| < 1.4$. The two SCT end-caps each have nine discs increasing the acceptance to $|\eta| < 2.5$. The SCT is populated with modules of silicon micro-strip detectors. Each module has two active silicon planes, back-to-back, one offset at 40 mrad with respect to the other. The combination of a front and back side measurement forms a two-dimensional *space-point*.

SCT barrel modules are rectangular in design, with two silicon wafers mounted on either side. Each strip has a 80 μm pitch, giving an intrinsic resolution of 23 μm . Four different designs (inner, middle, short-middle and outer) of end-cap module are required to ensure adequate η coverage. End-cap modules have a trapezoidal shape with strips on one side projecting to the z -axis. The end-cap strip pitch varies from 50 to 90 μm . Outer and middle modules use two silicon wafers per side, for a total strip length of 12 cm, while for the inner and short-middle modules, one wafer per side gives a strip length of 6 cm.

High track multiplicities from LHC collisions limit the level to which corrections for detector misalignment can be made during reconstruction. It is foreseen that such corrections will be performed down to the module level, but not for each individual sensor. This places stringent requirements on the assembly procedure for SCT modules. Each silicon wafer must be placed with an accuracy of ~ 5 μm with respect to all other sensors on the module. The development of an assembly method for outer end-cap modules is discussed in appendix A.

The 768 micro-strips per silicon plane are wire-bonded to six on-detector, front-end chips. After amplification, the signal is passed through a single-strip discriminator which produces a binary output based on a comparison with an externally configurable charge threshold. Read-out to off-detector electronics is through an optical link that is free from electrical interference.

2.4.3 The TRT

The TRT comprises the bulk of the volume of the inner detector, extending in radius from $56 \rightarrow 107$ cm. As with the pixels and SCT, it consists of a barrel section and two end-caps. Due to financial constraints, the TRT coverage is limited to $|\eta| < 2.0$.

The TRT consists of 250,000 straw tube detectors. In the barrel region, the straws are orientated parallel to the z -axis while in the end-caps they are distributed radially, projecting towards the beam-line. The inside of each tube is layered with a thin aluminium foil which

Parameter	ATLAS
Inner radius (<i>cm</i>)	30
Outer radius (<i>cm</i>)	56
Number of barrel layers	4
Number of discs per end-cap	9
Total number of barrel (end-cap) modules	2112 (1976)
Barrel module tilt in $R\varphi$	11°
Number of strips per module	1536
Total active area of silicon (m^2)	60
Total channels	6.2×10^6
Average number of hits per track	8
Intrinsic $R\varphi$ resolution (μm)	23
Space-point resolution in $R\varphi$ (μm)	17
Space-point resolution in R/z (μm)	500

Table 2.3: Key parameters of the SCT [20].

acts has a high-voltage cathode. A gold-plated tungsten anode wire of diameter $30 \mu m$ is positioned in the middle of the straw. Each tube is filled with a $Xe - CO_2 - O_2$ (70/27/3%) gas mixture. A charged particle traversing the TRT ionises the gas, liberating charge carriers which drift in the electric field. Charge collected on the anode is read out at the end of the straw.

The purpose of the TRT is two-fold: firstly it contributes, on average, 35 measurements of $R\varphi$ per reconstructed track, with a spatial resolution of $\sim 170 \mu m$. Secondly, the TRT provides electron identification through its sensitivity to transition radiation photons. These are soft X-rays, produced when highly relativistic charged particles traverse a boundary between materials with different dielectric constants. Since the probability of emitting a TR photon at any given boundary is small, the TRT uses polypropylene foils and fibres, embedded between the straws, to ensure many transitions.

The TRT is read-out by double-threshold binary electronics. The low threshold ($\sim 200 eV$) records the passage of a minimum ionising particle. A higher level threshold ($\sim 5 keV$) detects the presence of transition radiation.

2.5 Calorimetry

The calorimeters measure the energies and positions of electrons, photons and jets. In doing so they stop these particles penetrating into the muon spectrometer.

When a relativistic photon or electron is incident on a thick absorber, it initiates an electromagnetic cascade, generating secondary photons by bremsstrahlung ($e \rightarrow e\gamma$) and electrons by pair production ($\gamma \rightarrow e^+e^-$). The longitudinal development of the shower is dependant on the particle energy and the radiation length of the material (x_0). A narrow transverse profile is characteristic of an electromagnetic cascade.

Hadrons passing through matter also initiate cascades through inelastic hadron-nuclei interactions. The shower produces secondary hadrons and leptons and has a comparatively wide transverse profile.

The nuclear interaction length is about an order of magnitude greater than x_0 . Therefore, like most general purpose experiments, ATLAS uses two different calorimetry systems to measure electrons and photons (the ECAL) and hadrons (the HCAL). The layout of the calorimetry systems is shown in figure 2.3.

2.5.1 The Electromagnetic Calorimeter (ECAL)

The ECAL [19, 22] is a high granularity lead / liquid argon (LAr) sampling calorimeter with a barrel and two end-caps. Its accordion geometry of interlaced absorbers and electrodes ensures complete azimuthal coverage with minimum density variation. Showers initiated in the lead produce secondary particles which ionise the liquid argon. The charge is collected on copper electrodes and read out. The thickness of the barrel (end-cap) is ~ 24 (~ 35) x_0 , ensuring that electrons and photons are contained within the ECAL.

Since the solenoid and cryostat contribute $\sim 2x_0$ directly in front of the calorimeter, a pre-sampler corrects for energy losses in the upstream material in the region $|\eta| < 1.8$. The high granularity of the calorimeter, particularly in the first sampling, provides powerful π^0 / γ separation and good electron identification capabilities. Additionally, multiple samplings of the shower are used to resolve its pointing vector. The important properties of the four ECAL samplings are provided in table 2.4.

The uncertainty on an energy estimate from the ECAL, $\sigma(E)$, is given by:

$$\frac{\sigma(E)}{E} = \frac{a}{\sqrt{E}} \oplus b. \quad (2.5)$$

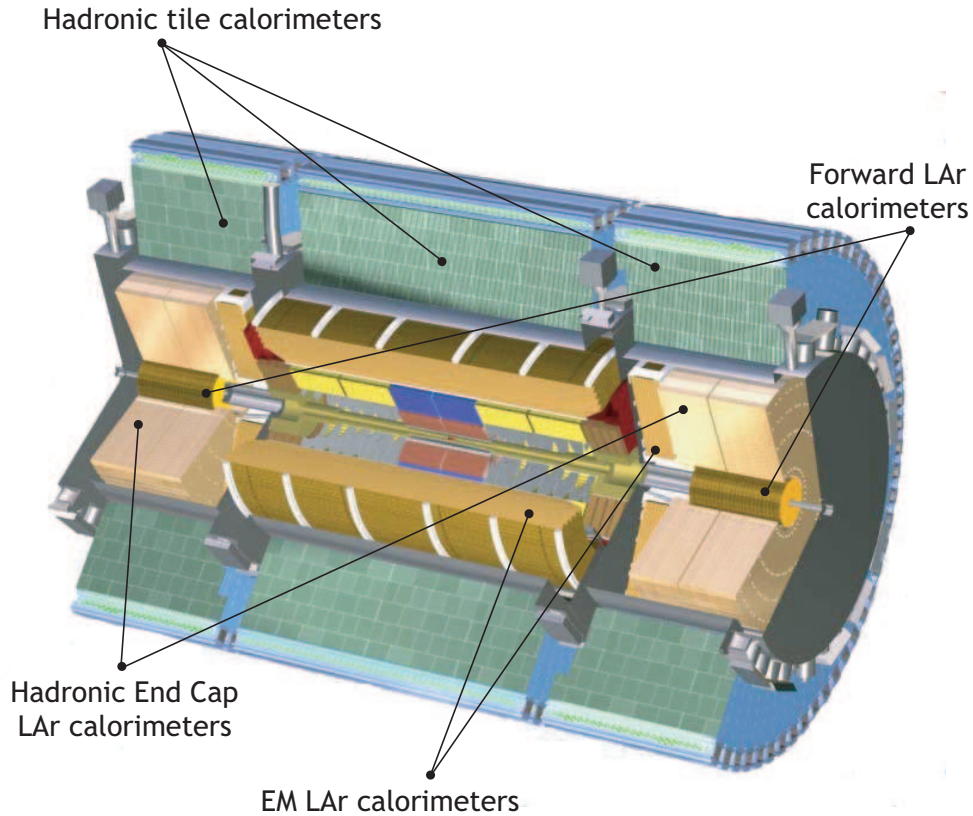


Figure 2.3: Layout of the ATLAS calorimeters.

Typical values for a and b , derived from stand-alone test-beam measurements of individual ECAL modules, are presented in table 2.4.

2.5.2 The Hadronic Calorimeter (HCAL)

The HCAL [19, 22] is a sampling calorimeter, measuring the energies and positions of jets. A summary of the most important aspects of the HCAL is provided in table 2.5.

The HCAL barrel uses 14 mm thick iron absorbers (which also form the return yoke for the tracker solenoid) to initiate hadronic cascades and 3 mm plastic scintillator tiles as the active material. The barrel HCAL provides coverage over $|\eta| < 1.6$.

The high level of radiation in the forward regions would cause severe damage to plastic scintillators. In the end-caps, which span $1.6 < |\eta| < 3.2$, parallel copper plates are submerged in liquid argon, which is preferred as the active medium because of its inherent radiation hardness.

	Barrel	End-cap
Granularity ($\Delta\eta \times \Delta\varphi$)		
Pre-sampler	0.025×0.1	0.025×0.1
Sampling 1	0.003×0.1	$0.003 \times 0.1 \rightarrow 0.006 \times 0.1$
Sampling 2	0.025×0.025	0.025×0.025
Sampling 3	0.050×0.025	0.050×0.025
Channels		
	110,208	63,744
Intrinsic Resolution		
Stochastic sampling term (<i>a</i>)	10%	10 \rightarrow 12%
Constant term (<i>b</i>)	0.2%	0.35%

Table 2.4: Key properties of the electromagnetic calorimeter [20].

A high density forward calorimeter (FCAL) extends the solid angle coverage between $3.2 < |\eta| < 4.8$. The primary motivation behind the FCAL is to enclose the interaction point more completely, therefore reducing tails in the measurements of missing transverse energy. The FCAL uses copper and tungsten absorbers and liquid argon as the active medium.

Equation 2.5 describes the uncertainty on an energy estimate from the HCAL. The values of *a* and *b* (shown in table 2.5) have been determined from test-beam studies of barrel and end-cap HCAL modules using a pion beam.

2.6 The Muon Spectrometer

Being relatively heavy and without experiencing the strong force, muons provide a clean, unambiguous signature of many processes ATLAS was designed to search for. Precision muon reconstruction and efficient triggering are therefore features of the detector design. High energy muons penetrate the calorimeters and are deflected by the toroidal magnetic field, which is approximately orthogonal to the particle trajectory, ensuring maximum bending.

The muon spectrometer [19, 23] has a barrel region ($|\eta| < 1.0$), end-caps ($1.4 < |\eta| < 2.7$) and *transition* regions ($1.0 < |\eta| < 1.4$) where the barrel and end-cap fields overlap, creating inhomogeneities in the field and reducing the bending power.

Granularity ($\Delta\eta \times \Delta\varphi$)		
Barrel	$0.1 \times 0.1 \rightarrow 0.2 \times 0.1$	
End-caps	$0.1 \times 0.1 \rightarrow 0.2 \times 0.2$	
Forward	0.2×0.2	
Channels		
Barrel	9852	
End-caps	5632	
Forward	3524	
Samplings		
Barrel	3	
End-caps	4	
Forward	3	
Intrinsic Resolution		
	<i>a</i>	<i>b</i>
Barrel	45%	1.3%
End-caps	75%	2.3%

Table 2.5: Key properties of the hadronic calorimeter [20].

Four different types of position-sensitive detector are used to provide triggering and precision measurements over a large pseudo-rapidity:

- **Monitored drift tubes (MDTs)** give precision ($\sim 80 \mu m$) one-dimensional measurements of the trajectory in the bending plane over $|\eta| < 2.0$.
- **Cathode strip chambers (CSCs)** are preferred to MDTs for precision ($\sim 80 \mu m$) measurements over $2.0 < |\eta| < 2.7$, where the neutron-induced background is higher.
- **Resistive plate chambers (RPCs)** possess a coarser spatial resolution than the MDTs and CSCs. However their fast response and excellent time resolution ($\sim 1 ns$) facilitate the triggering capabilities of the muon spectrometer. RPCs are used in the region $|\eta| < 1.05$ and contribute two-dimensional measurements, determining the track trajectory in the non-bending plane.
- **Thin gap chambers (TGCs)** provide triggering capabilities and the second spatial

coordinate over $1.05 < |\eta| < 2.4$.

2.7 Trigger and DAQ

The high collision frequency and data rate necessitates a versatile and robust trigger and data acquisition (DAQ) system [19]. The ATLAS trigger / DAQ is designed to inspect all bunch crossings and retain a small selection for offline analysis at a maximum rate of $\sim 100 \text{ Hz}$. At $10^{34} \text{ cm}^{-2}\text{s}^{-1}$ the total number of collisions is $\sim 10^9 \text{ sec}^{-1}$. To reduce the event rate by the required factor of 10^7 , the selection process is divided up into three steps, illustrated in figure 2.4.

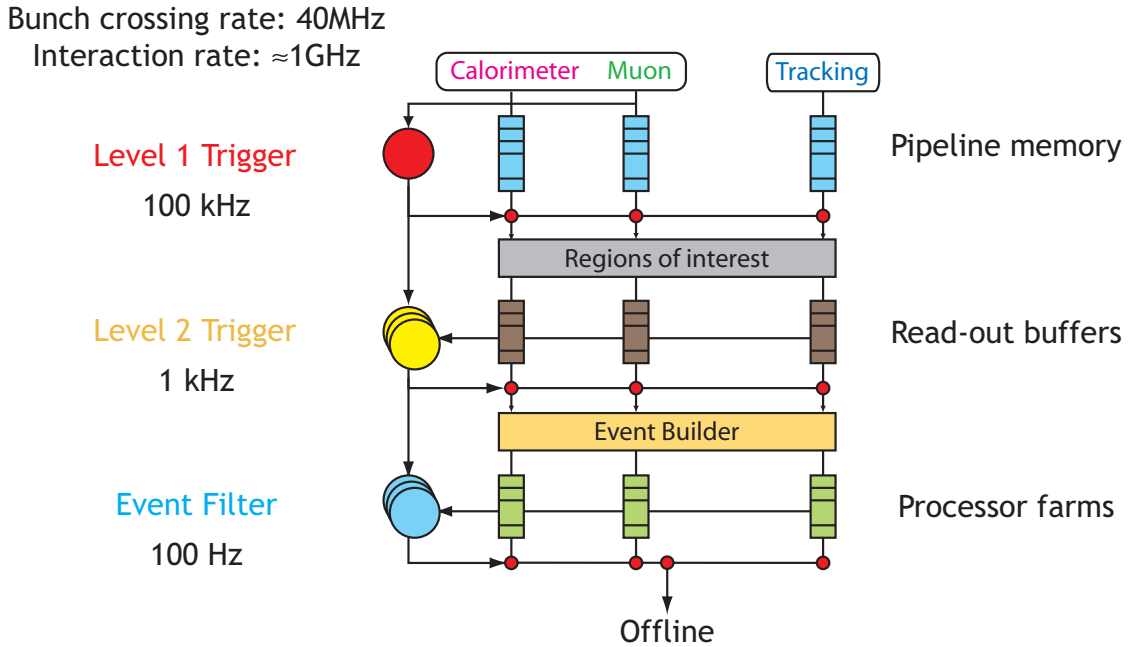


Figure 2.4: Block diagram of the trigger / DAQ system.

The *level-1* trigger [24] is responsible for making a fast, preliminary selection of events containing isolated electromagnetic clusters, muons, high p_T jets or large missing p_T , based on crude estimates of transverse energy from the calorimeters and transverse momentum from the muon spectrometer. It is designed to reduce the event rate to less than 100 kHz (a rejection power of 10^4). Owing to the short time between beam crossings and the geometric expanse of the detector, it is not possible to make a level-1 decision in real time. As a result, the data from each detector element is stored in a *pipeline* - a small amount of memory on every element which holds the data until requested. Information from at most 128 bunch crossings can be retained in each pipeline, allowing the level-1 trigger about $3 \mu\text{s}$ (not including latency of data transfer) to make a decision. Because of the rapid response necessary, the

level-1 trigger is implemented using custom-made hardware.

A level-1 trigger initiates the transfer of data from all pipelines (for the particular bunch-crossing) to off-detector *read-out buffers*. The *level-2* trigger [25] utilises the full precision and granularity of the detector, but reconstruction is limited to a small *region of interest* identified at level-1. This reduces the amount of information that must be processed to only a few percent of the total data set. Additionally, rapid pattern recognition algorithms reconstruct tracks from hits in the inner detector, allowing more refined particle identification. The level-2 trigger has approximately ~ 20 *ms* to provide a decision.

The data from all read-out buffers, for bunch-crossings accepted by level-2, is transferred to processor farms. The *event builder* provides the interconnections between the read-out buffers and the processors. The level-3 trigger (called the *event filter*) [25] performs a preliminary reconstruction of the entire bunch-crossing and makes a final decision whether to retain it for offline analysis. The data volume is small enough to allow the level-2 and level-3 triggers to operate on commercially available architectures.

The trigger criteria reflect the importance of high p_T physics (refer figure 1.2, page 8). A provisional trigger menu for an instantaneous luminosity of $10^{33} \text{ cm}^{-2} \text{ s}^{-1}$ is shown in table 2.6.

Trigger Type	Threshold (GeV)	Rate (kHz)
Isolated electron / photon	25	12.0
Di-electrons / di-photons	15	4.0
Isolated muon	20	0.8
Di-muons	6	0.2
τ -jet * E_T^{miss}	25 * 30	2.0
1-jet, 3-jet, 4-jet	200, 90, 65	0.6
Jet * E_T^{miss}	60 * 60	0.4
Electron * muon	15 * 10	0.1
Others (monitor, calibration, etc.)		5.0
Total		25.1

Table 2.6: A provisional trigger menu for an instantaneous luminosity of $10^{33} \text{ cm}^{-2} \text{ s}^{-1}$ and an assumed initial bandwidth of 25 *kHz* [20].

2.8 Software

The amount of data produced by ATLAS, and the longevity of the experiment requires a flexible and adaptable software framework. The design of the software [26] reflects these challenges, incorporating a modular, distributed analysis paradigm; routine tasks such as simulation, data reconstruction and analysis are too large for a single cluster and so are divided across the computing resources of many institutions.

An object orientated approach is the optimal solution for such a complex problem. C++ [27] was chosen as the programming language for the majority of the software development, both for its versatility in creating class inheritance structures and for its portability across many different architectures.

In order to ensure modularity, a separation is made between algorithms and data structures. The *Gaudi* framework [28], developed by the ATLAS and LHCb collaborations, defines the structure of the data objects and a common interface for algorithms (figure 2.5). The framework itself provides a set of abstract and template base classes, contributing only minimal functionality. *Athena* [29] is the collection of *concrete* implementations of Gaudi structures which comprise the ATLAS software framework.

Athena is linked to a number of external packages: Geant 4 [30] is the simulation engine used predominantly to determine the detector response; physics generators such as Pythia [31] are integrated into Athena to study specific processes arising from proton-proton collisions.

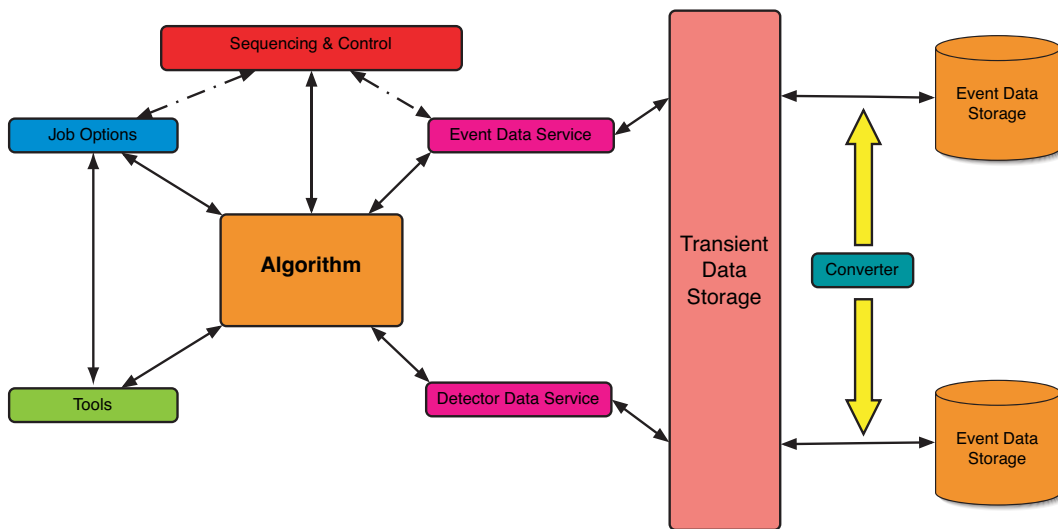


Figure 2.5: The structure of the Gaudi framework [28]. Algorithms are responsible for the manipulation of data objects. Helper tools (called *AlgTools*) perform lightweight tasks for algorithms. Data objects are used to hold both detector specific information and event data. During run-time, data structures are held in transient storage. A sub-set of transient objects can be written to mass storage through the use of a converter. Sequencing and control commands determine the order of algorithm execution. Job options scripts, written in python [32], supply instructions to the sequencing and control block as well as providing algorithms and helper tools with run-time information.

Chapter 3

Track Reconstruction

In this chapter, some important aspects of the inner detector are considered in detail: charged particles moving through the inner detector inconveniently interact with the material, causing energy loss and perturbing the trajectory. The passage of charged particles through matter is explained in section 3.1; the material distribution within the tracker is discussed in section 3.2; section 3.3 provides an introduction to the procedure of track reconstruction; finally, the performance of the tracker is considered in section 3.4.

3.1 Passage of Charged Particles through Matter

3.1.1 Ionising Energy Loss

The predominant energy-loss mechanism for moderately relativistic particles, other than electrons, is ionisation. The process is stochastic, but, since the fluctuation in energy loss is small with respect to the mean, a deterministic approximation is normally made. The mean rate of energy loss is given by the Bethe-Bloch equation [8]:

$$-\frac{dE}{dx} = Kz^2 \frac{Z}{A} \frac{1}{\beta^2} \left[\frac{1}{2} \ln \frac{2m_e c^2 \beta^2 \gamma^2 T_{max}}{I^2} - \beta^2 - \frac{\delta(\beta\gamma)}{2} \right], \quad (3.1)$$

where β and γ are the relativistic kinematic variables, E is in MeV and x is in cm . All constants are defined in table 3.1.

Symbol	Definition	Units / Value
K/A	Constant of proportionality	$0.3071 \text{ MeV } g^{-1} \text{ cm}^2$
M	Mass of incident particle	MeV/c^2
z	Charge of incident particle	
m_e	Electron mass	$0.511 \text{ MeV}/c^2$
Z	Atomic number	
A	Atomic mass	$g \text{ mol}^{-1}$
ρ	density	$g \text{ cm}^{-3}$
I	Mean excitation energy	eV
$\delta(\beta\gamma)$	Density effect correction	
T_{max}	Maximum energy a particle can impart to an electron	MeV

Table 3.1: Summary of variables used in the Bethe-Bloch equation.

T_{max} is given as:

$$T_{max} = \frac{2m_e c^2 \beta^2 \gamma^2}{1 + 2\gamma m_e/M + (m_e/M)^2}. \quad (3.2)$$

A semi-empirical expression for the mean excitation potential is:

$$I = 16(eV) \times Z^{0.9}. \quad (3.3)$$

The density effect correction (when I is in eV) is given by:

$$\delta(\beta\gamma) = 2 \ln \left(28.816 \frac{1}{I} \sqrt{\rho \frac{Z}{A}} \right) + 2 \ln(\beta\gamma) - 1. \quad (3.4)$$

3.1.2 Radiative Energy Loss

A relativistic electron, being much lighter than a muon or pion, loses energy in matter predominantly by bremsstrahlung: in the presence of the electric field of a nucleus, an electron can radiate a photon ($e \rightarrow \gamma e$). Unlike ionisation, the fluctuation in radiative energy loss is significant. Electron bremsstrahlung is therefore modelled stochastically by the Bethe-Heitler

probability density function (pdf) [8, 33]:

$$f(z) = \frac{(-\ln(z))^{c-1}}{\Gamma(c)}, \quad \text{with} \quad c = \frac{t}{\ln(2)}, \quad (3.5)$$

where z is the ratio of the energy of the electron after bremsstrahlung (E_f) to the initial energy (E_i):

$$z = \frac{E_f}{E_i}. \quad (3.6)$$

The amount of material traversed by the particle, t , is characterised as a fraction of the material's *radiation length* (x_0):

$$t = \frac{x}{x_0}, \quad (3.7)$$

where x corresponds to the physical thickness of material traversed. Both x and x_0 are usually quoted in *cm* - for example $x_0(\text{silicon}) = 9.36 \text{ cm}$. The radiation length of a particular material corresponds to the thickness required for a relativistic electron to lose, on average, all but $1/e$ of its initial energy via bremsstrahlung.

The Bethe-Heitler distribution is assumed to be independent of the energy of the incident electron. Figure 3.1 shows the Bethe-Heitler pdf for a number of different material thicknesses.

At energies $\gtrsim 100 \text{ GeV}$, radiative energy losses become significant for muons and pions. In this case, the Bethe-Bloch equation is an inadequate description of energy loss. For muons and pions, the stochastic nature of bremsstrahlung is generally overlooked and, in the limit of $t \ll 1$, it is standard practice simply to add an additional term in equation 3.1 for radiative energy losses:

$$-\left. \frac{dE}{dx} \right|_{rad} = \frac{E_i}{x_0} \left(\frac{m_e}{M} \right)^2, \quad (3.8)$$

where E_i is again the initial energy of the charged particle.

3.1.3 Multiple Scattering

When a charged particle traverses material, it is deflected by multiple Coulomb scattering. It is normally sufficient to characterise the angular distribution of scattered particles as a gaussian, distributed around zero, with a width [34, 35]:

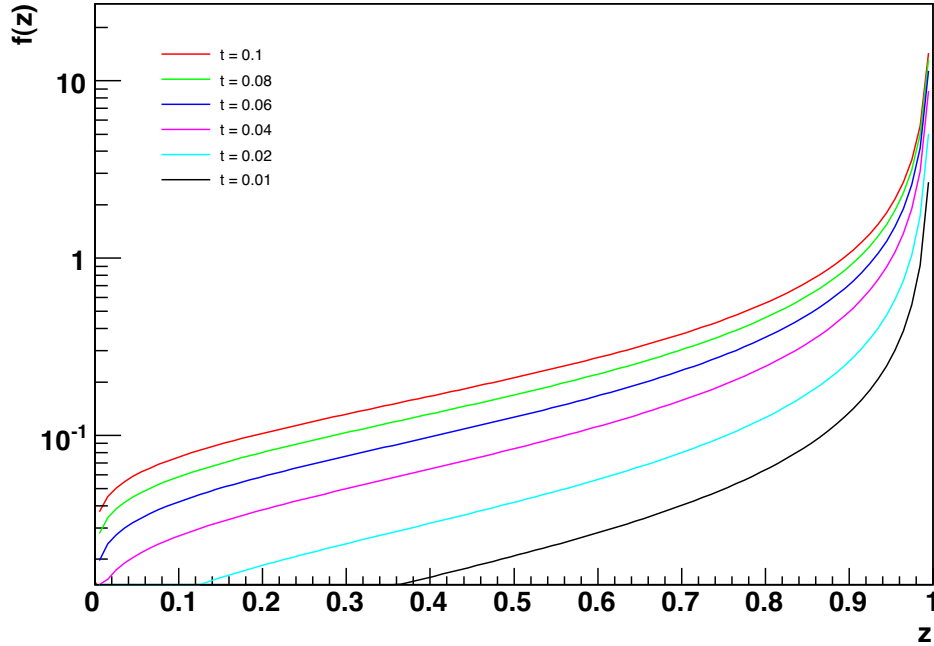


Figure 3.1: The pdf of the Bethe-Heitler distribution as a function of z - the fraction of energy retained by an electron after a bremsstrahlung radiation. The pdf is shown for several thicknesses of material, expressed as fractions of a radiation length (t).

$$\theta = \frac{13.6 \text{ (MeV)}}{\beta c p} z \sqrt{\frac{x}{x_0}} \left[1 + 0.038 \ln \left(\frac{x}{x_0} \right) \right], \quad (3.9)$$

where p is the momentum of the particle.

This approximation covers the central 98% of the angular distribution. Multiple scattering at large angles results in significantly longer tails than produced by a gaussian.

3.2 Material Budget

Modern tracking detectors, based on semiconductor technologies, contain significantly more material than gaseous detectors, due in part to the detector elements themselves but also as a result of the additional material required for on-detector electronics, power distribution, cooling and mechanical support. The inclusion of the auxiliary material creates inefficiencies in pattern recognition, causes a significant degradation in the momentum resolution and affects the intrinsic performance of the ECAL.

The amount of material is lowest in the central barrel region ($|\eta| < 0.8$), rising to a maximum at $|\eta| \sim 1.7$, where the majority of the services are located. Despite a significant effort, the amount of material in the tracker has risen steadily since the initial design. Table 3.2 shows the evolution of the inner detector material budget (in terms of x/x_0). Figure 3.2 shows the material distribution, based on the most up-to-date description of the tracker, as a function of η .

Date	$ \eta \sim 0$	$ \eta \sim 1.7$
1994 (technical proposal)	0.20	0.70
1997 (technical design report)	0.25	1.50
2006 (end of construction)	0.35	1.35

Table 3.2: Evolution of the amount of material (in terms of x/x_0) in the tracker [20]. The material at $|\eta| \sim 1.7$ has decreased between the technical design report and the end of construction. This is due to the rerouting of the pixel services to $|\eta| \sim 3$ (clearly visible in figure 3.2).

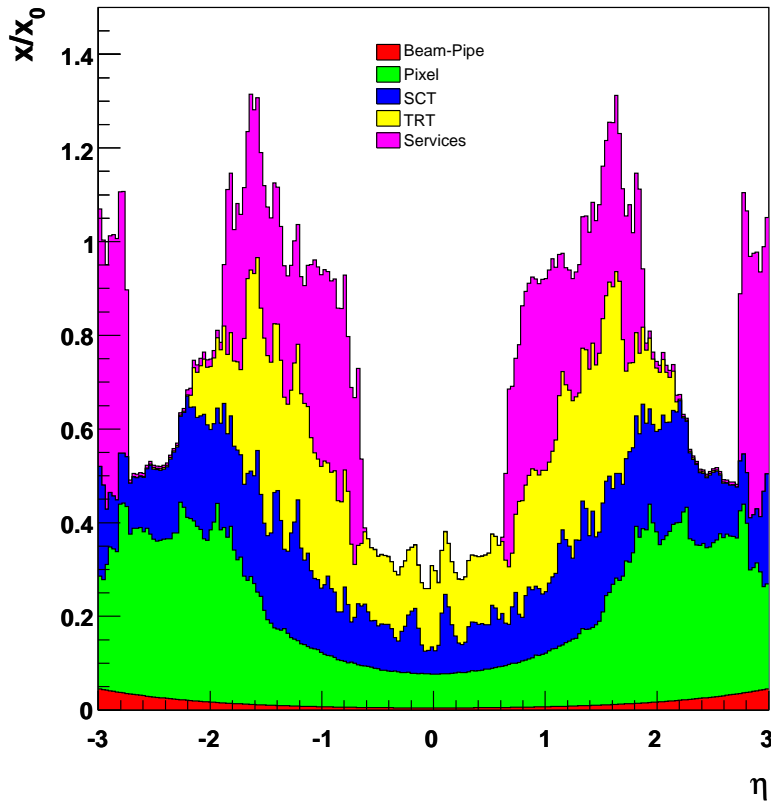


Figure 3.2: Material distribution (in terms of x/x_0) as a function of η in the tracker.

3.3 Track Reconstruction Procedure

Track reconstruction is the process by which the trajectory of a charged particle in a tracking detector is determined from the detector response. Track reconstruction utilises two main components:

- **Pattern recognition:** the association of measurements from individual detector elements to a particular track candidate.
- **Track fitting:** the calculation of the optimal estimate of the track trajectory, along with the appropriate uncertainties and statistical quantities. A track fitter requires a set of measurements provided by the pattern recognition algorithm.

In practice, the reconstruction of tracks in the inner detector requires several cycles of pattern recognition and fitting to ensure a high track finding efficiency and an optimal estimate of the trajectory. Five key steps in the process can be identified [36]:

Data Preparation

During data preparation, the spatial coordinates of hits are determined from the detector response. The position of a hit is provided in the local coordinate frame of the associated detector element. *Clustering* algorithms are used to resolve the centroid of a pixel or SCT measurement and assign the appropriate uncertainty.

The pixel cluster provides a two-dimensional measurement of the position of a particle at the sensor surface. In the local frame of the module, this position is given by the cartesian coordinates $(locX, locY)$, where $locX$ is associated with the high resolution axis of the detector.

Silicon micro-strips provide precision one-dimensional measurements of the particle's position in the $R\phi$ plane. The location of the measurement, in the detector frame, is $locX$ ¹. A second-level of data preparation forms two-dimensional space-points by combining clusters on the front and back sides of a SCT module.

A hit in the TRT is expressed as a one-dimensional *drift-radius* - the distance of closest approach of the particle to a particular TRT anode - given by $locR$ in the local frame of the straw.

¹The end-cap SCT modules require a two-dimensional representation of the measurement. The strips project to the beam-line and therefore the separation between strips increases with distance from the z -axis. Consequentially, the uncertainty on the hit centroid is a function of the position along the strip.

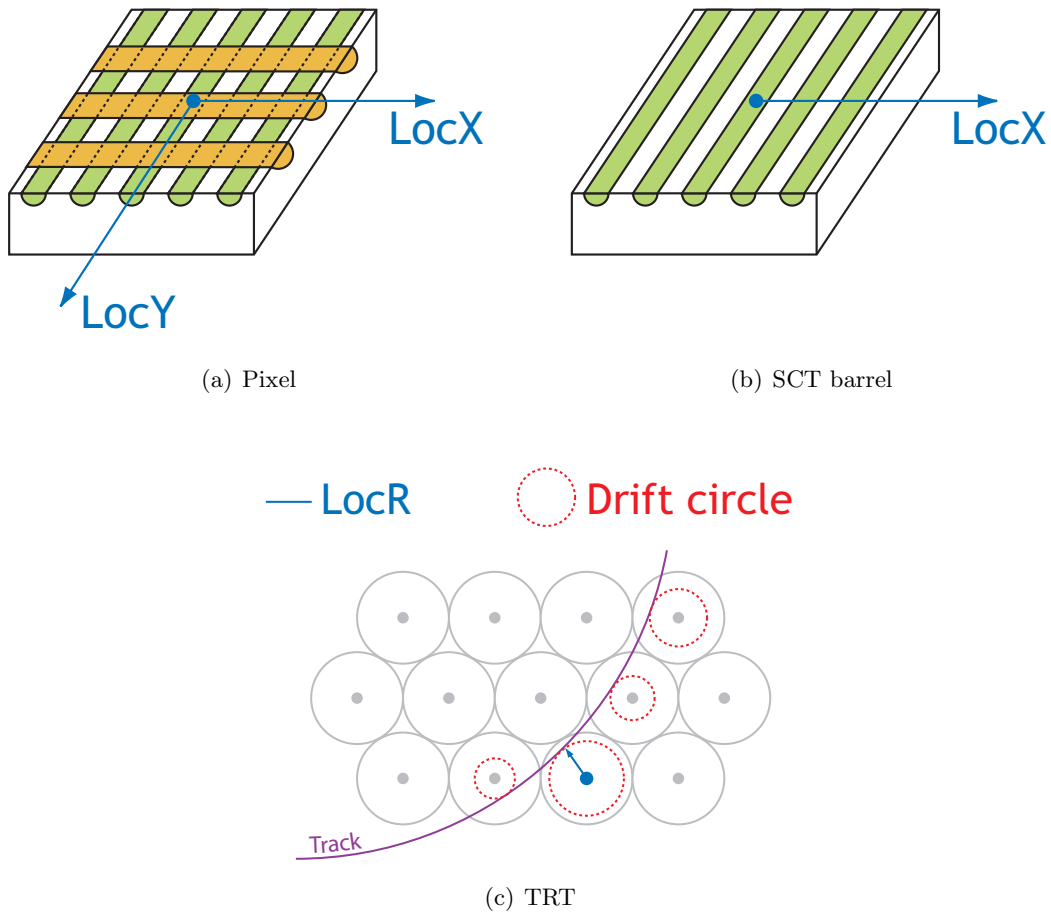


Figure 3.3: Representations of measurements in the tracker sub-detectors. A hit in a pixel module is described by two-dimensional cartesian coordinates. Measurements in a barrel SCT module and a TRT straw are both one-dimensional.

Representations of pixel, barrel SCT and TRT measurements are shown in figure 3.3.

Track Seeding

The first step of pattern matching is to find a track seed - a small number of hits (usually three) all belonging to the same track candidate, from which a crude estimate of the trajectory can be determined. A high speed combinatorial search in the pixels and SCT layers is performed, subject to criteria on maximum curvature and (optional) crude vertex region projectivity.

Silicon Segment Track Reconstruction

All remaining silicon hits belonging to the track are then found. The three measurements provided from the seed are used to establish a narrow “road” through the silicon which defines

the search region for additional hits. A track fit is then applied to produce an estimate of the trajectory. The fitter is generally responsible for the identification and removal of outliers from the track candidate.

At this point it is necessary to resolve a number of possible ambiguities arising from pattern matching: a particle traversing a ganged pixel produces two hits; there may be more than one seed per track; or more than one possible trajectory per seed. As a result, many of the measurements may be shared between several trajectories. An ambiguity processor accepts or rejects tracks based on the quality of the fit and the number of hits shared with other candidates.

TRT Extension

Tracks retained by the ambiguity processor are used to establish a road in the TRT. Drift-circles within this road form a track candidate to which a fit is then applied.

Additional logic may be required to resolve any pattern matching ambiguities arising in the TRT, the most likely of which being the so-called *left-right ambiguity*: with each drift-circle there are two solutions to the distance of closest approach, one on the right, and one on the left of the anode. Most track fitters include the drift-circles sequentially and an incorrect left-right decision for an early drift-circle will result in a poor track fit. This situation occurs predominantly when the drift-radius of the first TRT hit is small, as illustrated in figure 3.4.

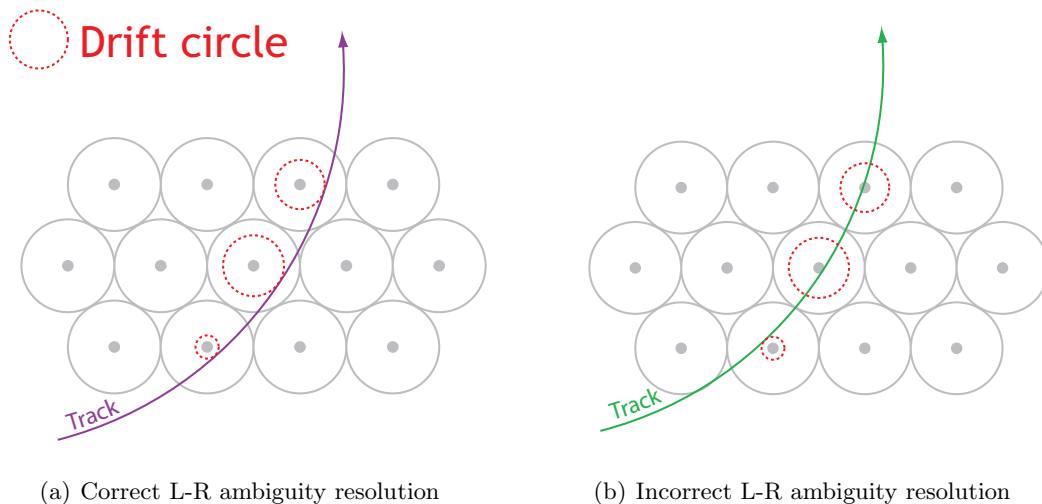


Figure 3.4: An illustration of the consequences of correct and incorrect left-right ambiguity resolution in the first fitted TRT drift-circle. When the incorrect option is chosen, the resulting track fit is poor.

Final Track Fit

A combined fit is applied, incorporating measurements from both the silicon and TRT. If the track quality improves with the inclusion of the TRT then the new track is retained. If the combined fit degrades the track quality then the silicon segment is preferred.

3.4 Performance

Five parameters are required to characterise the trajectory of a charged particle in the inner detector. The parameters are normally expressed at the point of closest approach of the track to the beam-line (the *perigee*): two coordinates give the transverse and longitudinal position of the perigee (the impact parameters); two parameters provide the direction of the track at this point (φ, θ); and one parameter describes the momentum (or transverse component of momentum, p_T). Since there are five degrees of freedom, a minimum of five one-dimensional measurements are required to constrain the track properly.

3.4.1 Minimum p_T

Particles below a critical p_T will not escape the tracker. In the case of an ideal solenoidal field orientated parallel to the z -axis, the trajectory of a charged particle is circular in the transverse plane, characterised by the radius of curvature, R_c . When R_c is equal to half the radius of the inner detector (figure 3.5) the particle is on the verge of curling in the field.

The relationship between p_T and R_c is:

$$p_T = 0.29979 \cdot R_c \cdot B_z, \quad (3.10)$$

where p_T is in GeV/c , R_c is in meters and B_z is the magnetic field ($2 T$). For a particle on the verge of curling, $R_c = 0.55 m$. To escape the tracker, a particle must therefore have $p_T \gtrsim 330 MeV$.

3.4.2 Maximum p_T

As the p_T of a charged particle increases, it is deflected less by the magnetic field. If the deflection is smaller than the intrinsic resolution of the detector elements, it becomes impossible to delineate a finite radius of curvature from a straight line. When this occurs the upper limit of measurable p_T has been reached.

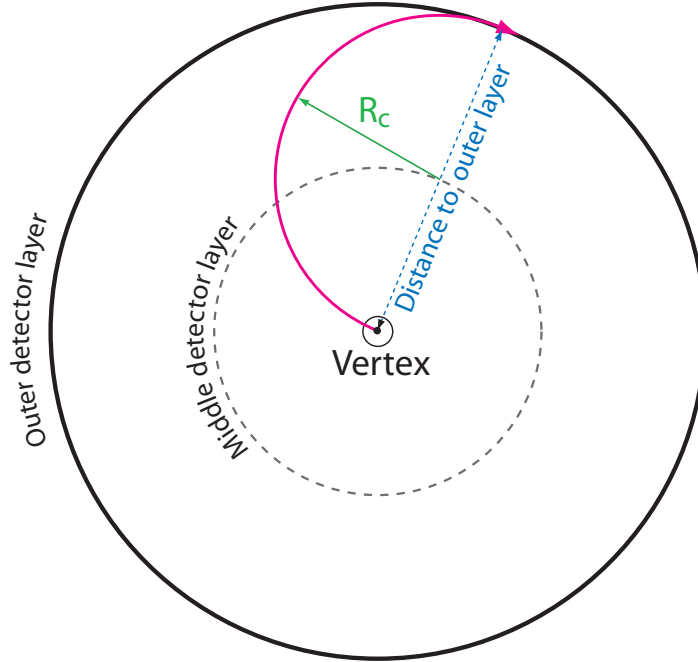


Figure 3.5: The definition of minimum transverse momentum. When the radius of curvature is equal to half the radius of the inner detector, the particle is just contained by the magnetic field. The particle is on the verge of curling in the field when $p_T \sim 330 \text{ MeV}/c$.

The *sagitta*, s , describes the maximal deflection of the track. A chord is constructed in the transverse plane, connecting the vertex point with the track position at the outer radius of the detector. The sagitta is the distance between the midpoint of the chord and the arc of the trajectory (figure 3.6). The relationship between s and R_c is:

$$R_c = \frac{s^2 + (r/2)^2}{2s}. \quad (3.11)$$

With $r \sim 1.1 \text{ m}$ and setting the sagitta equal to the pitch of the detector element at radius $r/2$ ($s = 80 \mu\text{m}$ in the outer SCT layer), the maximum p_T which can be measured is $\sim 1 \text{ TeV}$.

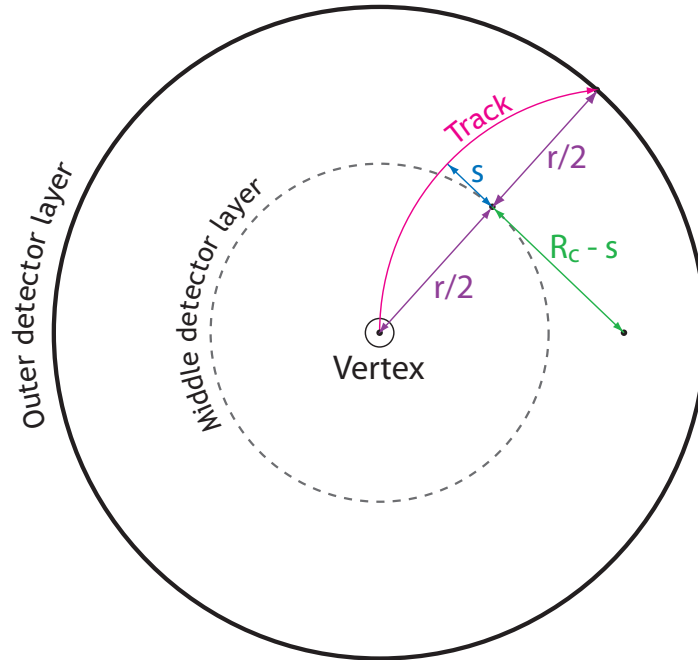


Figure 3.6: The definition of the sagitta, s - the distance between the midpoint of the chord and the arc. As p_T increases, s decreases.

3.4.3 Results from Simulation and Test Beam

A more comprehensive representation of the tracker performance, deduced from extensive simulation and benchmarked using detailed test-beam measurements of detector elements, is given in table 3.3. The reconstruction of electrons and pions is less efficient than muons since they undergo more significant material interactions in the tracker.

Parameter	Value
Reconstruction efficiency for muons with $p_T = 1 \text{ GeV}/c$	96.8%
Reconstruction efficiency for pions with $p_T = 1 \text{ GeV}/c$	84.0%
Reconstruction efficiency for electrons with $p_T = 5 \text{ GeV}/c$	90.0%
Momentum resolution at $p_T = 1 \text{ GeV}/c$ and $\eta \sim 0$	1.3%
Momentum resolution at $p_T = 1 \text{ GeV}/c$ and $\eta \sim 2.5$	2.0%
Momentum resolution at $p_T = 100 \text{ GeV}/c$ and $\eta \sim 0$	3.8%
Momentum resolution at $p_T = 100 \text{ GeV}/c$ and $\eta \sim 2.5$	11%
Transverse impact parameter resolution at $p_T = 1 \text{ GeV}/c$ and $\eta \sim 0$ (μm)	75
Transverse impact parameter resolution at $p_T = 1 \text{ GeV}/c$ and $\eta \sim 2.5$ (μm)	200
Transverse impact parameter resolution at $p_T = 1000 \text{ GeV}/c$ and $\eta \sim 0$ (μm)	11
Transverse impact parameter resolution at $p_T = 1000 \text{ GeV}/c$ and $\eta \sim 2.5$ (μm)	11
Longitudinal impact parameter resolution at $p_T = 1 \text{ GeV}/c$ and $\eta \sim 0$ (μm)	150
Longitudinal impact parameter resolution at $p_T = 1 \text{ GeV}/c$ and $\eta \sim 2.5$ (μm)	900
Longitudinal impact parameter resolution at $p_T = 1000 \text{ GeV}/c$ and $\eta \sim 0$ (μm)	90
Longitudinal impact parameter resolution at $p_T = 1000 \text{ GeV}/c$ and $\eta \sim 2.5$ (μm)	190

Table 3.3: Reconstruction performance of the inner detector [20].

Chapter 4

Methods of Track Fitting

Track reconstruction (section 3.3, page 32) requires two components: a pattern matching algorithm to associate hits to a particular track candidate; and a fitter which determines the track parameters describing the trajectory of the charged particle. This chapter provides an overview of the fitting methods used for the ATLAS tracking detectors.

In order to give the optimal estimate of the track parameters, a fitter requires:

- A set of measurements, provided by the pattern matching algorithm, all associated to the same track candidate.
- An *error model* to assign the correct uncertainties to the track parameters. These errors originate from the intrinsic resolution of the sensors and the interaction of the particle with the detector material.
- A *track model* to describe the form of the trajectory. For example, in the absence of a magnetic field, the track model is linear. For a homogeneous field, the track model is helical. In the more realistic case, where the field is inhomogeneous, the track model is generally not analytical and so a numerical model or approximating function must be used.

In general, the least-squares method (LSM) is the preferred track fitting algorithm, being simple, relatively fast and familiar to experimentalists. A linear LSM is used for track fitting, since for an approximately linear track model and gaussian distributed experimental noise, the uncertainties on the track parameters, determined by the linear LSM, are also gaussian.

The layout of this chapter is as follows: firstly the track model for a charged particle moving in an ideal solenoid is introduced (section 4.1). The approximate linearity of the model is

demonstrated and the appropriate set of track parameters is deduced; secondly, the method of least-squares estimation is explained (section 4.2); thirdly, the Kalman filter is introduced as the regressive form of the LSM (section 4.3); the chapter concludes with a discussion of fitting techniques which incorporate non-gaussian experimental noise (section 4.4).

4.1 The Track Model

The track model describes the trajectory of a particle; it is the solution to the equation of motion. In the case where a charged particle is moving in a static magnetic field ($\mathbf{B}(\vec{x})$), the force on the particle is [37, 38]:

$$\mathbf{F} = \frac{d}{dt} \left(m \frac{d\vec{x}}{dt} \right) = q\mathbf{v} \times \mathbf{B}(\vec{x}), \quad (4.1)$$

where $\mathbf{v} = d\vec{x}/dt$ is the velocity and q is the (signed) charge of the particle¹.

Equation 4.1 can be rewritten in terms of the path-length, $s(t)$:

$$\frac{d^2\vec{x}}{ds^2} = \frac{q}{mv} \frac{d\vec{x}}{ds} \times \mathbf{B}(\vec{x}(s)), \quad (4.2)$$

where v is the magnitude of velocity:

$$v = |\mathbf{v}| = \frac{ds}{dt}. \quad (4.3)$$

The special case of a homogeneous field is considered. Without loss of generality, the magnetic field can be chosen to be orientated parallel to the z -axis: $\mathbf{B} = B\mathbf{e}_z$, $\mathbf{e}_z = (0, 0, 1)$. In this case, equation 4.2 reduces to:

$$\begin{aligned} \frac{d^2x}{ds^2} &= \frac{q}{mv} \frac{dy}{ds} B \\ \frac{d^2y}{ds^2} &= -\frac{q}{mv} \frac{dx}{ds} B \\ \frac{d^2z}{ds^2} &= 0. \end{aligned} \quad (4.4)$$

¹Note bene! \vec{x} denotes a three-dimensional position vector. \mathbf{x} denotes a vector of track parameters.

The solution of this set of differential equations is a helix:

$$\begin{aligned}x(\varphi) &= x_0 + hR_H (\sin \varphi - \sin \varphi_0) \\y(\varphi) &= y_0 - hR_H (\cos \varphi - \cos \varphi_0) \\z(\varphi) &= z_0 + hR_H \cot \theta (\varphi - \varphi_0),\end{aligned}\tag{4.5}$$

where φ is related to the path-length by:

$$\varphi(s) = \varphi_0 + s \frac{h}{R_H} \sin \theta.\tag{4.6}$$

A reference point on the helix ($s = 0$) is given by the coordinates (x_0, y_0, z_0) . The azimuthal direction of the track at this point is φ_0 ($-\pi \leq \varphi_0 < \pi$) and $\theta = \cos^{-1}(dz/ds)$ is the polar angle ($0 \leq \theta \leq \pi$). The radius of curvature, R_H , is related to p_T by:

$$R_H = \frac{p_T}{|\kappa q B|}.\tag{4.7}$$

If q is a multiple of elementary charge (dimensionless), p_T is in GeV/c , B is in tesla (T) and R_H is in meters, then the constant of proportionality is: $\kappa = 0.3 (GeV/c)T^{-1}m^{-1}$.

The parameter h is the *helicity* of the track, defined as:

$$h = -\text{sign}(qB) = \pm 1.\tag{4.8}$$

Figure 4.1 illustrates the track parameters describing a helical trajectory with $h = +1$.

Solutions to the equation of motion, based on the geometry of the inner detector and assuming an ideal solenoidal field, are illustrated in figure 4.2. Several positively charged particles with different transverse momentum and initial direction are shown.

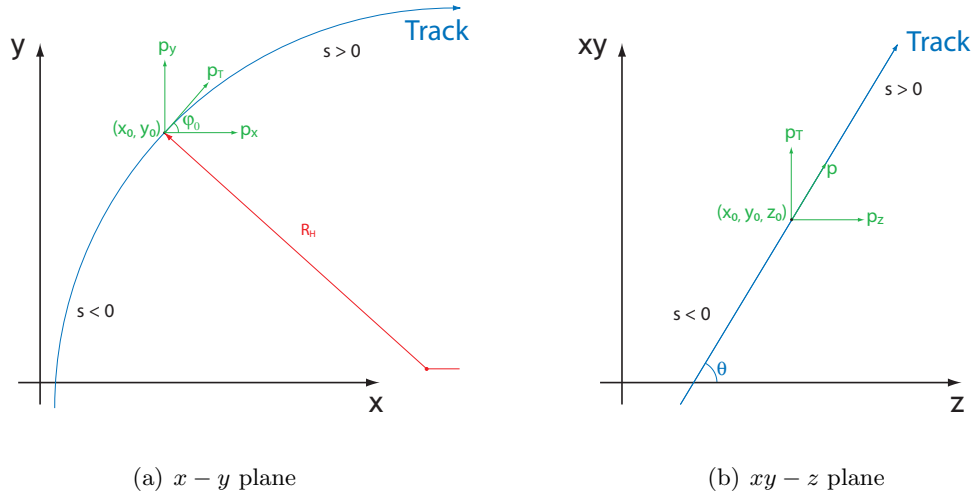


Figure 4.1: Parameters describing the trajectory of a helix with $h = +1$.

4.1.1 Track Parameters for a Helical Model

The solution to equation 4.4 gives six parameters:

$$\mathbf{x} = (x_0, y_0, z_0, \varphi_0, \theta, hR_H). \quad (4.9)$$

It is general practice to express the track parameters at an arbitrary surface within the detector. The surface may correspond to a detector element, inert material or can be an entirely abstract construction. In this approach, $s = 0$ is chosen to be the point at which the track intersects the surface. The parameters (x_0, y_0, z_0) give the position of intersection (the impact coordinates). Using the identity

$$\left(\frac{dx}{ds}\right)^2 + \left(\frac{dy}{ds}\right)^2 + \left(\frac{dz}{ds}\right)^2 = 1, \quad (4.10)$$

and since the geometry of the surface is well defined, one of the three impact coordinates can be derived from the other two, thereby removing one degree of freedom.

The remaining integration constants are a representation of the five free *track parameters*, two coordinates describing the impact position on a given surface, two describing the direction at that point and the (signed) radius of curvature (or alternatively p_T). If the underlying geometry of the detector is cylindrical, then the impact point is given in cylindrical coordinates $(r\varphi, z)$.

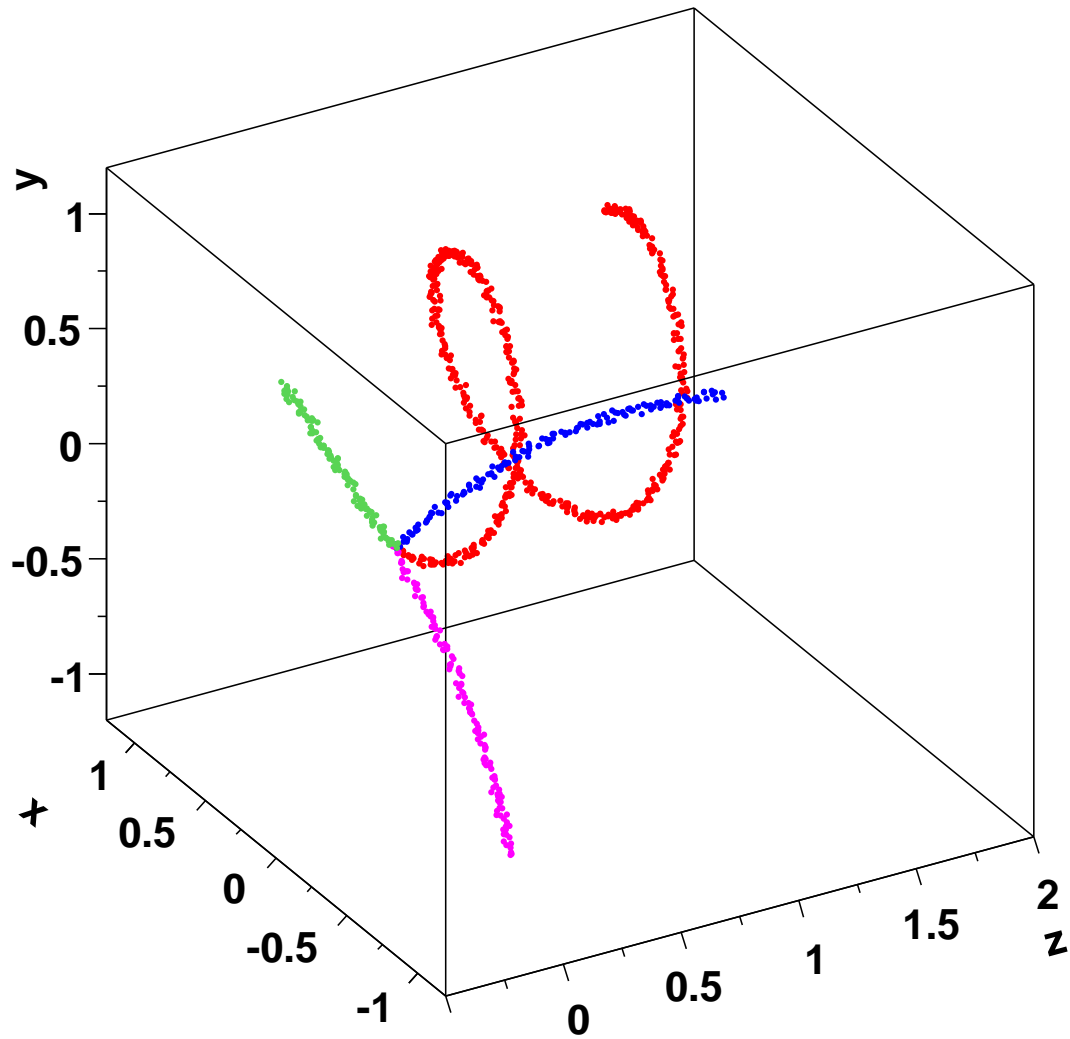


Figure 4.2: Solutions to the equation of motion for a charged particle moving in a homogeneous magnetic field. A 2 T field is orientated parallel to the z -axis. Solutions are shown for positively charged particles with transverse momentum $300\text{ MeV}/c$ (red), $600\text{ MeV}/c$ (blue), $1\text{ GeV}/c$ (purple) and $10\text{ GeV}/c$ (green). The trajectories are shown to a radius of 1.2 m in the $x - y$ plane and up to $z = 2.0\text{ m}$, the approximate dimensions of the inner detector.

The track parameters for a perfect solenoid and assuming a cylindrical detector are:

$$\mathbf{x}_{Helix} = (r\varphi, z, \varphi_0, \theta, hR_H). \quad (4.11)$$

Two factors affect the choice of track parameters: the underlying track model; and the geometry of the detector. In practice, an additional constraint on the parameterisation is that it must allow corrections for material interactions to be incorporated easily.

4.1.2 Track Parameters for a Linearised Helical Model

To use the linear LSM, the track model must be approximately linear. The position of a point on the track can be given in spherical coordinates²:

$$\rho = \sqrt{x^2 + y^2}$$

$$\varphi_t = \tan^{-1} \left(\frac{y}{x} \right) \quad (4.12)$$

$$\theta_t = \cot^{-1} \left(\frac{z}{\rho} \right).$$

If the deflection by the magnetic field ($\Delta\varphi$) is small (the charged particles have high momentum) and all tracks begin near the origin of the coordinate system then:

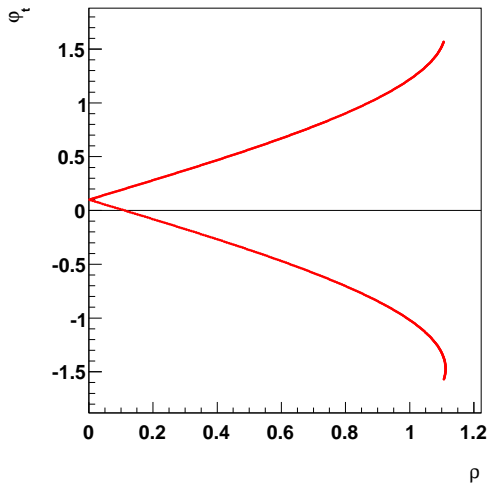
$$\varphi_t = \varphi_0 + \Delta\varphi, \quad (4.13)$$

and since there is no deflection in the longitudinal plane:

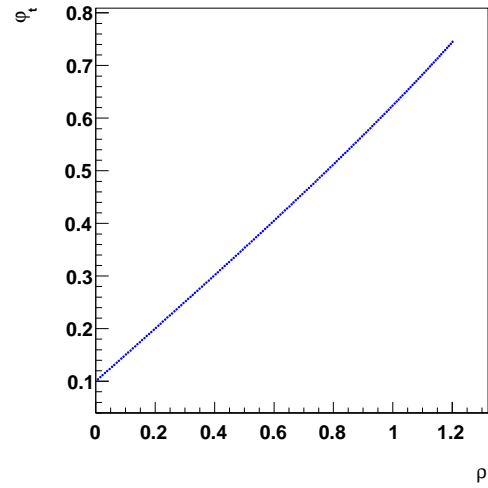
$$\theta_t = \theta. \quad (4.14)$$

Figure 4.3 shows the relationship between φ_t and ρ for positively charged particles. Plots of φ_t versus $\cot(\theta_t)$ (ρ versus $\cot(\theta_t)$) are shown in figure 4.4 (4.5). All helices begin at the origin with initial direction $(\varphi_0, \theta) = (0.1, 0.8)$.

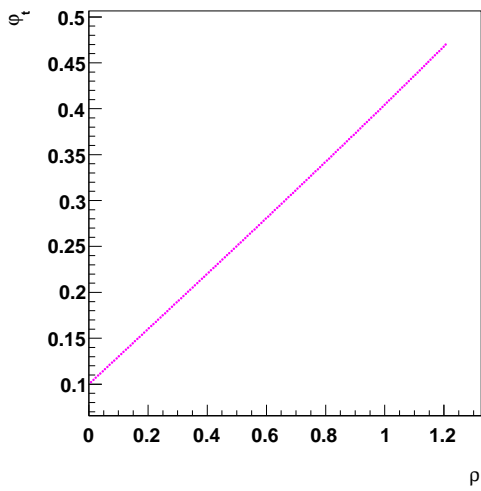
²Note the convention: (φ, θ) describe the direction, (φ_t, θ_t) give the position.



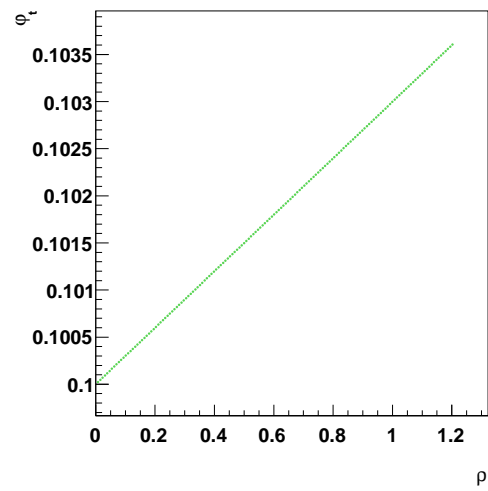
(a) 300 MeV/c



(b) 600 MeV/c

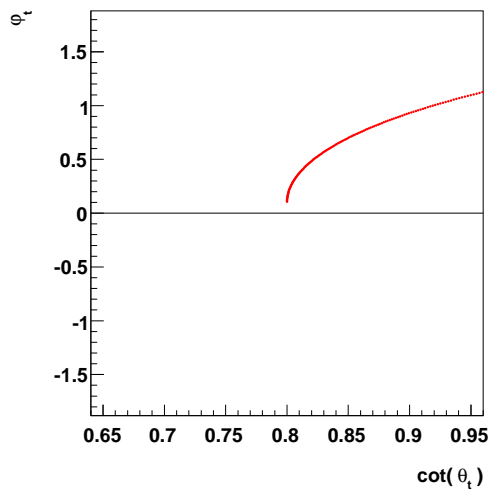


(c) 1 GeV/c

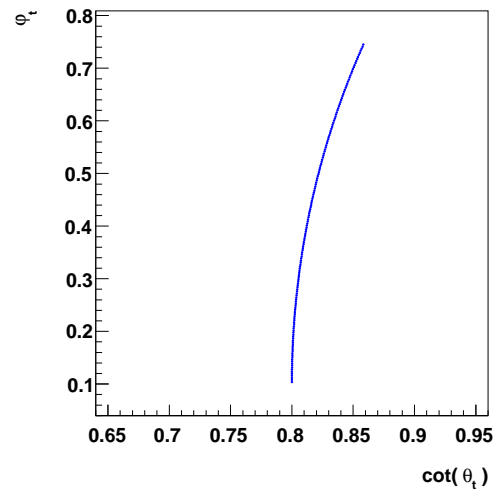


(d) 10 GeV/c

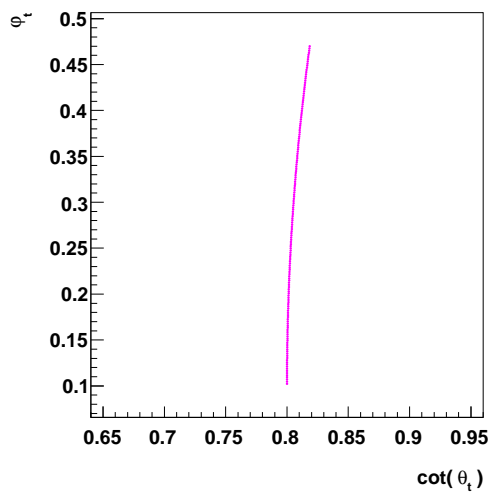
Figure 4.3: Trajectories of positively charged particles: φ_t versus ρ .



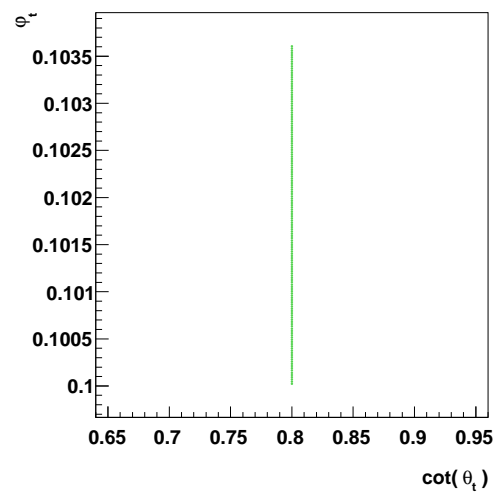
(a) 300 MeV/c



(b) 600 MeV/c

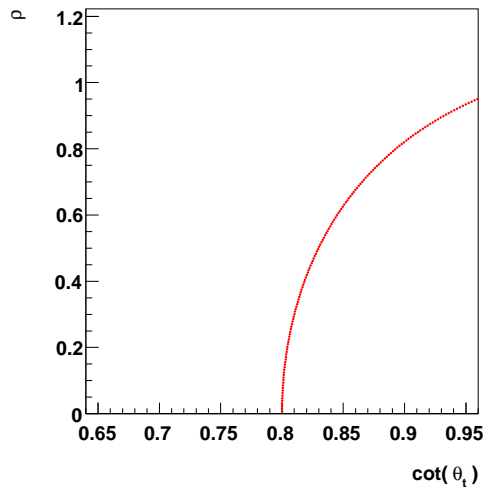


(c) 1 GeV/c

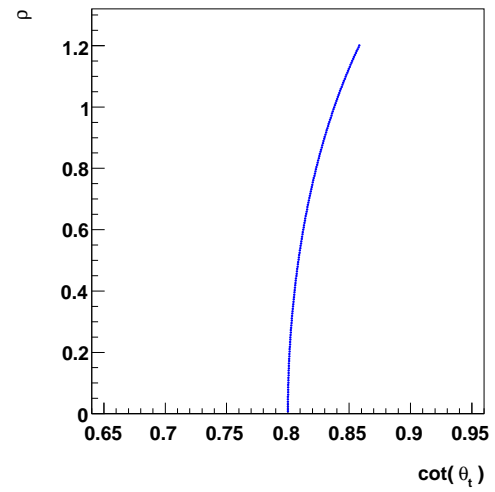


(d) 10 GeV/c

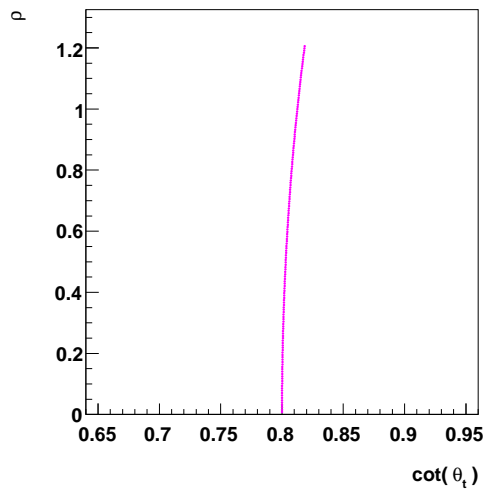
Figure 4.4: Trajectories of positively charged particles: φ_t versus $\cot(\theta_t)$.



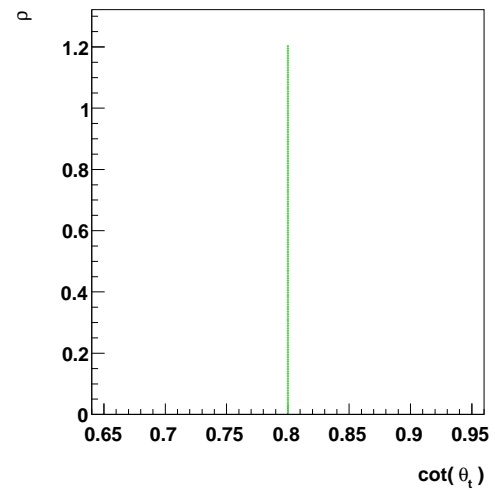
(a) 300 MeV/c



(b) 600 MeV/c



(c) 1 GeV/c



(d) 10 GeV/c

Figure 4.5: Trajectories of positively charged particles: ρ versus $\cot(\theta_t)$.

When $\Delta\varphi$ is small:

$$\varphi_t(\rho) - \varphi_0 \propto \frac{q}{p_T} \rho, \quad (4.15)$$

$$\cot(\theta_t) = \cot(\theta) = \text{constant}.$$

Any particle with a transverse momentum $\gtrsim 330 \text{ MeV}/c$ does not escape the field (section 3.4, page 35). In this case, the track model is approximately linear in the parameters $(\varphi_0, \cot(\theta), q/p_T)$. The track parameters based on a linearised helical model with a cylindrical detector geometry are therefore:

$$\mathbf{x}_{LinearisedHelix} = (r\varphi, z, \varphi_0, \cot(\theta), q/p_T). \quad (4.16)$$

The radius of curvature can be used instead of p_T if desired.

4.1.3 Track Parameters for the ATLAS Tracking Detectors

The ATLAS tracking systems are considerably more complex than the simple case of an ideal solenoid with a cylindrical detector geometry:

- The magnetic field is not homogeneous and in the muon system it is not orientated parallel to the z -axis. Consequently, p_T and $\cot(\theta)$ are not constants of the motion.
- The geometry of individual sensors is not cylindrical. Track finding is most efficient using the local coordinate system of a detector element. Detectors such as the pixels and SCT, which are planar in design, use local two-dimensional cartesian coordinates, while a TRT wire is treated as a one-dimensional object.
- Interactions with material must be accounted for. Corrections for energy loss are applied to p , not to p_T . The helical choice of track parameters invokes an additional degree of complexity, requiring off-diagonal elements of the covariance matrix to be computed for stochastic energy loss models. Multiple scattering is most naturally incorporated using (φ, θ) , not $(\varphi, \cot(\theta))$.

The track parameters of the linearised helical model are therefore not appropriate for the ATLAS tracking systems. The chosen parameter set reflects the complexity of the ATLAS spectrometers while ensuring that the requirement of linearity is approximately satisfied [39]:

$$\mathbf{x}_{ATLAS} = (loc1, loc2, \varphi, \theta, q/p). \quad (4.17)$$

The impact point of the track with a surface is given, in local coordinates, by $(loc1, loc2)$.

4.2 The Least-Squares Estimator

The state vector, \mathbf{x} , describes the trajectory of a particle. In general it cannot be measured directly. A measurement, \mathbf{m} , is however a function of the true state vector, corrupted by experimental noise. This noise is described by a vector of random variables, $\boldsymbol{\epsilon}$. The relationship between the true state vector (\mathbf{x}_{true}) and a real measurement is:

$$\mathbf{m} = \mathbf{f}(\mathbf{x}_{true}) + \boldsymbol{\epsilon}, \quad (4.18)$$

$$\langle \boldsymbol{\epsilon} \rangle = 0,$$

where $\mathbf{f}(\mathbf{x})$ is the track model.

The covariance matrix \mathbf{V} of the experimental noise is:

$$cov(\boldsymbol{\epsilon}) \equiv \mathbf{V}. \quad (4.19)$$

The *weight matrix* \mathbf{W} can be defined as:

$$\mathbf{W} \equiv \mathbf{V}^{-1}. \quad (4.20)$$

The task of track fitting is to find a function, \mathbf{t} , which maps \mathbf{m} on to \mathbf{x} without introducing bias and with the smallest possible uncertainty on the track parameters (*minimum variance*). The fitter produces a state vector of fitted track parameters, denoted $\tilde{\mathbf{x}}$:

$$\tilde{\mathbf{x}} = \mathbf{t}(\mathbf{m}). \quad (4.21)$$

The LSM determines the state vector which minimises the sum of the squares of the weighted *residuals*. A residual is the separation between a measurement and the track: $\mathbf{m} - \mathbf{f}(\mathbf{x})$. Measurements with a large weighting (small uncertainty) contribute more to the fit than

those with a small weighting. The LS estimate of \mathbf{x} is found by minimising the function:

$$M(\mathbf{x}) = (\mathbf{m} - \mathbf{f}(\mathbf{x}))^T \mathbf{W} (\mathbf{m} - \mathbf{f}(\mathbf{x})). \quad (4.22)$$

In the case where the track model can be approximated as linear:

$$\mathbf{f}(\mathbf{x}) = \mathbf{F}\mathbf{x} + \mathbf{c}, \quad (4.23)$$

the LSM estimate is given by [38]:

$$\tilde{\mathbf{x}} = (\mathbf{F}^T \mathbf{W} \mathbf{F})^{-1} \mathbf{F}^T \mathbf{W} \cdot (\mathbf{m} - \mathbf{c}), \quad (4.24)$$

and the covariance matrix (\mathbf{C}) is:

$$\mathbf{C}(\tilde{\mathbf{x}}) = (\mathbf{F}^T \mathbf{W} \mathbf{F})^{-1}. \quad (4.25)$$

4.2.1 Properties of the LSM

Bias

The linear LSM is an *unbiased estimator* under the assumption $\langle \boldsymbol{\epsilon} \rangle = 0$ (equation 4.18). In this case, the measurement $\mathbf{m} = \mathbf{f}(\mathbf{x}_{true}) + \boldsymbol{\epsilon}$ is unbiased and [38]:

$$\langle \tilde{\mathbf{x}} - \mathbf{x}_{true} \rangle = (\mathbf{F}^T \mathbf{W} \mathbf{F})^{-1} \mathbf{F}^T \mathbf{W} \langle \boldsymbol{\epsilon} \rangle = 0. \quad (4.26)$$

The Gauss-Markov Theorem

The linear LSM is the unbiased estimator with minimum variance provided that [38]:

- The measurements are unbiased: $\langle \boldsymbol{\epsilon} \rangle = 0$.
- The model is linear or can be approximated by a linear function.
- All experimental errors are gaussian distributed.

The approximate linearity of the model has already been demonstrated (section 4.1.1), however the requirement of gaussian distributed errors is not always fulfilled. In this case, a

non-linear fitter may provide a better estimate of the track parameters than the linear LSM.

Consistency

As the number of measurements (n) increases, the fitted track parameters ($\tilde{\mathbf{x}}_n$) converge to the true values:

$$\lim_{n \rightarrow \infty} \tilde{\mathbf{x}}_n = \mathbf{x}_{true}. \quad (4.27)$$

4.3 The Kalman Filter (KF)

The estimator described in section 4.2 is a *global fitter*; it requires the construction of a matrix containing all the measurements. In the general case of n measurements with m dimensions, the global LSM computes the inverse of a $nm \times nm$ matrix. The CPU time for this calculation grows $\propto n^3$. A *regressive track fitter* improves the estimate of the track parameters in steps, by incorporating measurements sequentially, thereby avoiding the inversion of large matrices. The optimal track parameters are obtained once all measurements have been included. The regressive least squares estimator is called the Kalman filter [38, 40] (KF).

A filter treats the trajectory as a dynamic system, evolving as a function of the path-length. At a point, s_k , the track intersects a measurement surface. The trajectory between two adjacent measurement surfaces, $k-1$ and k , is given by the *system equation*:

$$\mathbf{x}(s_k) \equiv \mathbf{x}_k = \mathbf{f}_k(\mathbf{x}_{k-1}) + \mathbf{w}_k, \quad (4.28)$$

where the function \mathbf{f}_k is the track model between the two surfaces. A vector of random variables, \mathbf{w}_k , describes the ‘*process noise*’ which arises due to multiple scattering and energy loss mechanisms. Any bias introduced by material interactions can be corrected for, so that without loss of generality:

$$\langle \mathbf{w}_k \rangle = 0, \quad cov(\mathbf{w}_k) \equiv \mathbf{Q}_k. \quad (4.29)$$

In the case of a linear track model, equation 4.28 can be rewritten as:

$$\mathbf{x}_k = \mathbf{F}_k \mathbf{x}_{k-1} + \mathbf{w}_k. \quad (4.30)$$

Since the track state is generally not observed directly, the relationship between the track parameters and the measurement is described by the *measurement equation*:

$$\mathbf{m}_k = \mathbf{h}_k(\mathbf{x}_k) + \boldsymbol{\epsilon}_k, \quad (4.31)$$

where \mathbf{m}_k is the measurement vector at surface k and $\boldsymbol{\epsilon}_k$ is the measurement noise. The distribution of measurement errors can be taken to be unbiased:

$$\langle \boldsymbol{\epsilon}_k \rangle = 0, \quad \text{cov}(\boldsymbol{\epsilon}_k) \equiv \mathbf{V}_k \equiv \mathbf{W}_k^{-1}. \quad (4.32)$$

The function \mathbf{h}_k maps \mathbf{x}_k on to \mathbf{m}_k . For the ATLAS track parameters it is simply:

$$\mathbf{h}_k \rightarrow \mathbf{H}_k = \begin{pmatrix} 1 & 0 & 0 & 0 & 0 \\ 0 & 1 & 0 & 0 & 0 \end{pmatrix}. \quad (4.33)$$

4.3.1 Kalman Filter Operations

The KF invokes three types of operation:

The Prediction

The prediction is the estimate of the state vector at measurement surface k conditional on all previous measurements m_1, \dots, m_{k-1} :

$$\mathbf{x}_{k|k-1} = \mathbf{F}_k \mathbf{x}_{k-1} + \mathbf{w}_k. \quad (4.34)$$

The extrapolation of the covariance matrix from s_{k-1} to s_k is given by linear error propagation:

$$\mathbf{C}_{k|k-1} = \mathbf{F}_k \mathbf{C}_{k-1} \mathbf{F}_k^T + \mathbf{Q}_k. \quad (4.35)$$

Filtering

The predicted state, $\mathbf{x}_{k|k-1}$, is combined with measurement \mathbf{m}_k :

$$\mathbf{x}_{k|k} = \mathbf{x}_{k|k-1} + \mathbf{K}_k (\mathbf{m}_k - \mathbf{H}_k \mathbf{x}_{k|k-1}), \quad (4.36)$$

where \mathbf{K}_k is the *Kalman gain matrix*:

$$\mathbf{K}_k = \mathbf{C}_{k|k-1} \mathbf{H}_k^T (\mathbf{V}_k + \mathbf{H}_k \mathbf{C}_{k|k-1} \mathbf{H}_k^T)^{-1}. \quad (4.37)$$

The filtered covariance matrix is given by:

$$\mathbf{C}_{k|k} = (\mathbf{I} - \mathbf{K}_k \mathbf{H}_k) \mathbf{C}_{k|k-1}, \quad (4.38)$$

where \mathbf{I} is the identity matrix.

Smoothing

Only after the final filtering step are the optimal track parameters determined. These parameters ($\mathbf{x}_{n|n}$) are defined on the surface holding the last measurement to be included (\mathbf{m}_n). It is necessary to calculate the optimal description of the trajectory on all other surfaces ($\mathbf{x}_{k|n}$).

A smoother incorporates information from a second filter running backwards over the set of included measurements (m_n, m_{n-1}, \dots, m_1). The smoothed state at surface k is determined from the forward filtered state ($\mathbf{x}_{k|k}$) and the difference between the next forwards prediction ($\mathbf{x}_{k+1|k}$) and next smoothed state ($\mathbf{x}_{k+1|n}$):

$$\mathbf{x}_{k|n} = \mathbf{x}_{k|k} + \mathbf{S}_k (\mathbf{x}_{k+1|n} - \mathbf{x}_{k+1|k}), \quad (4.39)$$

where \mathbf{S}_k is the *smoother gain matrix*:

$$\mathbf{S}_k = \mathbf{C}_{k|k} \mathbf{F}_{k+1}^T (\mathbf{C}_{k+1|k})^{-1}. \quad (4.40)$$

The covariance matrix of the smoothed state ($\mathbf{C}_{k|n}$) is:

$$\mathbf{C}_{k|n} = \mathbf{C}_{k|k} + \mathbf{S}_k (\mathbf{C}_{k+1|n} - \mathbf{C}_{k+1|k}) \mathbf{S}_k^T. \quad (4.41)$$

4.4 Non-gaussian Experimental Noise

The KF is the optimal filter only if the process noise and measurement errors are gaussian distributed (section 4.2.1). In general, this condition is not fulfilled: measurement errors are not always gaussian - often there is a tail of outlying observations; tails in multiple scattering distributions are not gaussian, particularly if the material is inhomogeneous; for electrons, energy loss is dominated by bremsstrahlung (section 3.1.2, page 28) which is described by a stochastic, highly non-gaussian distribution.

A non-linear generalisation of the KF, called the gaussian-sum filter (GSF), can be used to take such effects into account, if the error distributions can be approximated as gaussian sums. The GSF dismantles the experimental noise into individual gaussian components and uses a separate Kalman filter to process each one. Therefore, the GSF consists of a number of Kalman filters running in parallel.

A GSF has been developed for the reconstruction of electrons in the inner detector. A detailed discussion of the GSF and its implementation is provided in chapter 5.

Chapter 5

The Gaussian-Sum Filter

The linear LSM is the estimator with minimum variance as long as all experimental noise is gaussian distributed (section 4.2.1, page 50). Non-linear fitters may perform better in the case of non-gaussian errors. The gaussian-sum filter [41–43] is a generalisation of the Kalman filter which can account for non-gaussian noise, provided that all distributions can be approximated as weighted sums of gaussian components.

This chapter is divided into two sections: firstly, the general principles of a GSF are introduced (section 5.1); secondly, the application of the GSF to electron tracks is considered (section 5.2). Relativistic electrons loose energy in matter predominantly by bremsstrahlung, which is modelled by the Bethe-Heitler distribution (section 3.1.2, page 28). In order to apply the GSF, the Bethe-Heitler distribution must be approximated by a gaussian sum.

5.1 Principle

The KF has already been discussed in detail (section 4.3, page 51). The linearised system equation (equation 4.30) is:

$$\mathbf{x}_k = \mathbf{F}_k \mathbf{x}_{k-1} + \boldsymbol{\omega}_k, \quad (5.1)$$

$$\langle \boldsymbol{\omega}_k \rangle = 0, \quad cov(\boldsymbol{\omega}_k) = \mathbf{Q}_k, \quad k = 1, \dots, n .$$

As before, \mathbf{x}_k is the state vector of five track parameters at a measurement surface k and \mathbf{F}_k is a linear transform describing the propagation of the state from surface $k - 1$ to k . The

vector of random variables, $\boldsymbol{\omega}_k$, describes the process noise encountered during propagation.

The linearised measurement equation (equation 4.31) is:

$$\mathbf{m}_k = \mathbf{H}_k \mathbf{x}_k + \boldsymbol{\epsilon}_k, \quad (5.2)$$

$$\langle \boldsymbol{\epsilon}_k \rangle = 0, \quad \text{cov}(\boldsymbol{\epsilon}_k) \equiv \mathbf{V}_k \equiv \mathbf{W}_k^{-1}, \quad k = 1, \dots, n.$$

A measurement on surface k is denoted \mathbf{m}_k and \mathbf{H}_k is the linear transform which maps \mathbf{x}_k on to \mathbf{m}_k . Measurement errors are given by the random variable $\boldsymbol{\epsilon}_k$.

5.1.1 Prediction

In the case of a linear filter, the predicted state at a given surface can be characterised by a gaussian distribution $p(\mathbf{x}_k | \mathbf{M}_{k-1})$. The prediction contains information from measurements $\{m_1, \dots, m_{k-1}\}$:

$$p(\mathbf{x}_k | \mathbf{M}_{k-1}) = \varphi(\mathbf{x}_k; \mathbf{x}_{k|k-1}, \mathbf{C}_{k|k-1}), \quad (5.3)$$

$$\mathbf{M}_{k-1} = \{\mathbf{m}_1, \dots, \mathbf{m}_{k-1}\},$$

where $\varphi(\cdot; \boldsymbol{\mu}, \mathbf{G})$ is a multi-variate gaussian pdf with mean $\boldsymbol{\mu}$ and covariance matrix \mathbf{G} . The state vector of the prediction is $\mathbf{x}_{k|k-1}$ and the covariance matrix is $\mathbf{C}_{k|k-1}$.

In the more general case, let process noise and measurement errors be described by weighted sums of gaussian densities. Now the prediction at surface k is a gaussian mixture with an arbitrary number (n_{k-1}) of components:

$$p(\mathbf{x}_k | \mathbf{M}_{k-1}) = \sum_{i=1}^{n_{k-1}} \pi_k^i \varphi(\mathbf{x}_k; \mathbf{x}_{k|k-1}^i, \mathbf{C}_{k|k-1}^i), \quad (5.4)$$

where π_k^i is the weight of component i , subject to the normalisation requirement:

$$\sum_{i=1}^{n_{k-1}} \pi_k^i = 1.$$

5.1.2 Process Noise

Where material exists between surfaces $k - 1$ and k , the prediction ($\mathbf{x}_{k|k-1}$) is computed in several steps. For a KF or GSF, the material is modelled as discrete layers in the detector. When the state under propagation intersects a layer, corrections due to material interactions are introduced.

Multiple Scattering

Multiple scattering produces a random deflection of the particle, changing the direction (φ, θ) of the track. When the material is homogeneous, multiple scattering can be approximated as a gaussian distribution with zero mean and variance given by the Rossi-Greisen formula (section 3.1.3, page 29).

In practice, layers of material are not perfectly homogeneous; they possess an internal structure, creating tails in the multiple scattering distribution. A better approximation of multiple scattering could be achieved using a gaussian mixture, $p(\mathbf{t})$, with N_{ms} components:

$$p(\mathbf{t}) = \sum_{j=1}^{N_{ms}} \alpha_j \varphi(\mathbf{t}; \mathbf{0}, \mathbf{Q}_j), \quad (5.5)$$

$$\sum_{j=1}^{N_{ms}} \alpha_j = 1, \quad \mathbf{t} = (\phi, \theta).$$

Each component has mean zero, a covariance matrix \mathbf{Q}_j and a weight α_j . Corrections are applied to the subset of track parameters perturbed by multiple scattering (\mathbf{t}).

The pdf of the state arriving at the material layer has N components, each with a weight π_i , mean \mathbf{x}_i and covariance matrix \mathbf{C}_i :

$$p(\mathbf{x}) = \sum_{i=1}^N \pi_i \varphi(\mathbf{x}; \mathbf{x}_i, \mathbf{C}_i). \quad (5.6)$$

The incident state vector is *convoluted* with the pdf of the multiple scattering distribution (equation 5.5). Thus the state vector upon leaving the material is:

$$p(\mathbf{x}) = \sum_{i=1}^N \sum_{j=1}^{N_{ms}} \alpha_j \pi_i \varphi(\mathbf{x}; \mathbf{x}_i, \mathbf{C}_i + \mathbf{H}_{ms}^T \mathbf{Q}_j \mathbf{H}_{ms}), \quad (5.7)$$

where \mathbf{H}_{ms} maps \mathbf{Q} on to the covariance matrix of the track state. For the ATLAS track parameters it is simply:

$$\mathbf{H}_{ms} = \begin{pmatrix} 0 & 0 & 1 & 0 & 0 \\ 0 & 0 & 0 & 1 & 0 \end{pmatrix}. \quad (5.8)$$

By approximating the multiple scattering distribution as a gaussian mixture, it is possible to take into account the inhomogeneity without modelling the material distribution to a high degree of accuracy.

Energy Loss

Ionisation is normally approximated as a deterministic process, since the variance is small with respect to the average energy loss. Bremsstrahlung must be treated as a stochastic process since fluctuations are of the same order of magnitude as the mean. Electron bremsstrahlung is modelled by the Bethe-Heitler distribution which is strongly non-gaussian. The model is parameterised in terms of the fraction of energy (z) retained by an electron after bremsstrahlung. The Bethe-Heitler distribution can be approximated as a gaussian mixture, $p(z)$, with N_{el} components:

$$p(z) = \sum_{j=1}^{N_{el}} \delta_j \varphi(z; z_j, Y_j), \quad (5.9)$$

$$\sum_{j=1}^{N_{el}} \delta_j = 1,$$

where δ_j is the weight, z_j is the mean and Y_j is the variance of each component. The mixture must be transformed from a parameterisation in z to q/p so that it can be incorporated into the track state [44]:

$$z_j, Y_j \rightarrow \Delta(q/p)_j, \Delta var(q/p)_j,$$

where $\Delta(q/p)_j$ is the change in q/p of component j and $\Delta var(q/p)_j$ is the change in variance.

The pdf of the state upon entering the material is given in equation 5.6. The convolution of the initial state and the gaussian mixture from equation 5.9 yields:

$$p(\mathbf{x}) = \sum_{i=1}^N \sum_{j=1}^{N_{el}} \delta_j \pi_i \varphi(\mathbf{x}; \mathbf{x}_i + \mathbf{H}_{el} \{\Delta(q/p)_j\}, \mathbf{C}_i + \mathbf{H}_{el}^T \{\Delta var(q/p)_j\} \mathbf{H}_{el}). \quad (5.10)$$

The matrix \mathbf{H}_{el} maps $\Delta(q/p)_j$ on to the state vector and $\Delta var(q/p)_j$ on to the covariance matrix:

$$\mathbf{H}_{el} = \begin{pmatrix} 0 & 0 & 0 & 0 & 1 \end{pmatrix}. \quad (5.11)$$

Once the convolution has been performed, the geometric propagation proceeds to the measurement surface. Without loss of generality, the predicted state, $p(\mathbf{x}_k | \mathbf{M}_{k-1})$, (equation 5.4) can now be assumed to take into account material interactions between surfaces $k-1$ and k .

5.1.3 Filtering

Let the distribution of measurement errors from ϵ_k be modelled as a gaussian mixture, $p(\epsilon_k)$, with e_k unbiased components:

$$p(\epsilon_k) = \sum_{j=1}^{e_k} \lambda_k^j \varphi(\epsilon_k; \mathbf{0}, \mathbf{V}_k^j), \quad (5.12)$$

$$\sum_{j=1}^{e_k} \lambda_k^j = 1,$$

where λ_k^j is the weight and \mathbf{V}_k^j is the covariance matrix of a component.

It therefore follows that the measurement (equation 5.2) can be expressed as a pdf conditional on the state vector \mathbf{x}_k :

$$p(\mathbf{m}_k | \mathbf{x}_k) = \sum_{j=1}^{e_k} \lambda_k^j \varphi(\mathbf{m}_k; \mathbf{H}_k \mathbf{x}_k, \mathbf{V}_k^j). \quad (5.13)$$

The filtered state of \mathbf{x}_k is conditional on measurement \mathbf{m}_k and the set of measurements \mathbf{M}_{k-1} :

$$p(\mathbf{x}_k | \mathbf{M}_k) \equiv p(\mathbf{x}_k | \mathbf{m}_k, \mathbf{M}_{k-1}). \quad (5.14)$$

Application of Bayes' theorem yields:

$$p(\mathbf{x}_k | \mathbf{M}_k) = \frac{p(\mathbf{m}_k | \mathbf{x}_k) p(\mathbf{x}_k | \mathbf{M}_{k-1})}{\int p(\mathbf{m}_k | \mathbf{x}_k) p(\mathbf{x}_k | \mathbf{M}_{k-1}) d\mathbf{x}_k}. \quad (5.15)$$

It can be shown [42] that equation 5.15 can be rewritten as a double summation over the predicted state (with n_{k-1} components) and the mixture of measurement errors (with e_k components):

$$p(\mathbf{x}_k | \mathbf{M}_k) = \sum_{i=1}^{n_{k-1}} \sum_{j=1}^{e_k} q_k^{ij} \varphi(\mathbf{x}_k; \mathbf{x}_{k|k}^{ij}, \mathbf{C}_{k|k}^{ij}), \quad (5.16)$$

where $\mathbf{x}_{k|k}^{ij}$ is the mean and $\mathbf{C}_{k|k}^{ij}$ is the covariance matrix of a single filtered component.

The updated state is then a mixture of $n_k = n_{k-1}e_k$ components. The weights of the filtered state (q_k^{ij}) components are given by:

$$q_k^{ij} \propto \pi_k^i \lambda_k^j \varphi(\mathbf{m}_k; \mathbf{H}_k \mathbf{x}_{k|k-1}^i, \mathbf{V}_k^j + \mathbf{H}_k \mathbf{C}_{k|k-1}^i \mathbf{H}_k^T). \quad (5.17)$$

The constant of proportionality is determined by the requirement that the filtered weights sum to unity.

The state vector and covariance matrix of each component in the filtered mixture are calculated using the KF equations (equations 4.36 and 4.38):

$$\mathbf{x}_{k|k}^{ij} = \mathbf{x}_{k|k-1}^i + \mathbf{C}_{k|k}^{ij} \mathbf{H}_k^T \mathbf{W}_k^j (\mathbf{m}_k - \mathbf{H}_k \mathbf{x}_{k|k-1}^i), \quad (5.18)$$

$$\mathbf{C}_{k|k}^{ij} = \left(\left(\mathbf{C}_{k|k-1}^i \right)^{-1} + \mathbf{H}_k^T \mathbf{W}_k^j \mathbf{H}_k \right)^{-1}. \quad (5.19)$$

The χ^2 of each component in the filtered mixture (χ_F^2) is determined from the weighted residual of the filtered state vector and the measurement:

$$(\chi_F^2)_k^{ij} = \left(\mathbf{m}_k - \mathbf{H}_k \mathbf{x}_{k|k}^{ij} \right)^T \left(\mathbf{V}_k^j - \mathbf{H}_k \mathbf{C}_{k|k}^{ij} \mathbf{H}_k^T \right)^{-1} \left(\mathbf{m}_k - \mathbf{H}_k \mathbf{x}_{k|k}^{ij} \right). \quad (5.20)$$

It is convenient to represent the filtered state in terms of a single index - the total number of components in the updated state (n_k):

$$p(\mathbf{x}_k | \mathbf{M}_k) = \sum_{l=1}^{n_k} q_k^l \varphi(\mathbf{x}_k; \mathbf{x}_{k|k}^l, \mathbf{C}_{k|k}^l). \quad (5.21)$$

Additionally, it is often desirable to represent the filtered state from the GSF as a single state vector and covariance matrix. These are determined so that the first two moments of the pdf are preserved:

$$\mathbf{x}_{k|k} = \sum_{l=1}^{n_k} q_k^l \mathbf{x}_{k|k}^l, \quad (5.22)$$

$$\mathbf{C}_{k|k} = \sum_{l=1}^{n_k} q_k^l \mathbf{C}_{k|k}^l + \sum_{l=1}^{n_k} \sum_{m>l} q_k^l q_k^m (\mathbf{x}_{k|k}^l - \mathbf{x}_{k|k}^m) (\mathbf{x}_{k|k}^l - \mathbf{x}_{k|k}^m)^T. \quad (5.23)$$

The total “ χ^2 ” of the filter step is a weighted sum of the individual values:

$$(\chi_F^2)_k = \sum_{l=1}^{n_k} q_k^l (\chi_F^2)_k^l. \quad (5.24)$$

By summing the χ^2 at each measurement surface, a total track χ^2 is obtained. Since the filter is non-linear, results will not actually be χ^2 distributed.

5.1.4 Smoothing

The GSF smoother requires a second (backward) filter proceeding in the opposite direction to the first (forward) filter. A combination of the forward and backward estimates is then used to obtain the optimal track state at any measurement surface. Since measurements can only be used once, the predicted state from one filter is combined with the filtered state from the other. In this case, the forward prediction is combined with the backward filtered state.

When the states involved are gaussian mixtures, there are a number of ways to combine the forward and backward estimates:

The Weighted-Mean Smoother

The weighted-mean smoother determines the single gaussian representation of the forward and backward mixtures respectively. The weighted average of the two estimates is then computed. This approach is able to describe only the first and second moments of the smoothed state.

The smoothed state vector at surface k is:

$$\mathbf{x}_{k|n} = (\mathbf{C}_{k|n})^{-1} [(\mathbf{C}_{k|k-1})^{-1}\mathbf{x}_{k|k-1} + (\mathbf{C}_{k|k,\dots,n})^{-1}\mathbf{x}_{k|k,\dots,n}], \quad (5.25)$$

where n is the total number of measurements and $\mathbf{x}_{k|k-1}$ and $\mathbf{x}_{k|k,\dots,n}$ ($\mathbf{C}_{k|k-1}$ and $\mathbf{C}_{k|k,\dots,n}$) are the single gaussian representations of the forward and backward state vectors (covariance matrices).

The covariance matrix is given by:

$$(\mathbf{C}_{k|n})^{-1} = (\mathbf{C}_{k|k-1})^{-1} + (\mathbf{C}_{k|k,\dots,n})^{-1}.$$

The Bayesian Smoother

Unlike the weighted-mean technique, the Bayesian smoother is able to determine higher moments of the smoothed state. The prediction of the forward filter at surface k is (equation 5.4):

$$p(\mathbf{x}_k | \mathbf{M}_{k-1}) = \sum_{i=1}^{n_{k-1}} \pi_k^i(\mathbf{x}_k; \mathbf{x}_{k|k-1}^i, \mathbf{C}_{k|k-1}^i). \quad (5.26)$$

Putting $\mathbf{M}^k = \{\mathbf{m}_k, \dots, \mathbf{m}_n\}$, the backward filtered state at surface k is:

$$p(\mathbf{x}_k | \mathbf{M}^k) = \sum_{l=1}^{n'_k} \beta_k^l(\mathbf{x}_k; \mathbf{x}_{k|k,\dots,n}^l, \mathbf{C}_{k|k,\dots,n}^l), \quad (5.27)$$

where n'_k is the number of components in the mixture and β_k^l are the component weights.

The smoothed state, $p(\mathbf{x}_k | \mathbf{M}_n)$, can be computed by applying Bayes' theorem to equations 5.26 and 5.27. This gives:

$$p(\mathbf{x}_k | \mathbf{M}_n) = \sum_{i=1}^{n_{k-1}} \sum_{l=1}^{n'_k} \pi_k^i \beta_k^l \varphi(\mathbf{x}_k; \mathbf{x}_{k|k-1}^i, \mathbf{C}_{k|k-1}^i) \varphi(\mathbf{x}_k; \mathbf{x}_{k|k,\dots,n}^l, \mathbf{C}_{k|k,\dots,n}^l), \quad (5.28)$$

which can be reduced to [42]:

$$p(\mathbf{x}_k | \mathbf{M}_n) = \sum_{i=1}^{n_k-1} \sum_{l=1}^{n'_k} \gamma^{il} \varphi(\mathbf{x}_k; \mathbf{x}_{k|n}^{il}, \mathbf{C}_{k|n}^{il}). \quad (5.29)$$

The smoothed quantities are given by:

$$\begin{aligned} \gamma_k^{il} &\propto \pi_k^i \beta_k^l \varphi(\mathbf{x}_{k|k-1}^i; \mathbf{x}_{k|k,\dots,n}^l, \mathbf{C}_{k|k-1}^i + \mathbf{C}_{k|k,\dots,n}^l), \\ \mathbf{x}_{k|n}^{il} &= (\mathbf{C}_{k|n}^{il})^{-1} \left[(\mathbf{C}_{k|k-1}^i)^{-1} \mathbf{x}_{k|k-1}^i + (\mathbf{C}_{k|k,\dots,n}^l)^{-1} \mathbf{x}_{k|k,\dots,n}^l \right], \end{aligned} \quad (5.30)$$

$$(\mathbf{C}_{k|n}^{il})^{-1} = (\mathbf{C}_{k|k-1}^i)^{-1} + (\mathbf{C}_{k|k,\dots,n}^l)^{-1},$$

where, for a smoothed component, γ_k^{il} is the weight, $\mathbf{x}_{k|n}^{il}$ is the mean and $\mathbf{C}_{k|n}^{il}$ is the covariance matrix. The constant of proportionality is again determined by the requirement that the total weight of the smoothed state is one.

5.1.5 Component Reduction

The processes of filtering and convolution with material effects increase the number of components in the state multiplicatively. For example, if the predicted state has n_{k-1} components and the measurement is a gaussian mixture with e_k components, then the filtered state has $n_{k-1} \times e_k$ components. Repetition of these processes in track fitting quickly produces a state which is too big to remain computationally manageable. The number of components in the state is therefore artificially restricted to a fixed maximum, N . Increasing the number of components improves the quality of the reduced state, but at a cost of increased overhead.

Two methods of component reduction are considered:

Component Reduction by Largest Weights

The simplest approach is to retain the N components with the largest weights. Computationally, this algorithm is relatively efficient, however it does not preserve the mean and variance of the original distribution, since components are removed from the mixture.

An enhanced approach, while still retaining the components with the largest weights, adds the single gaussian equivalent of the remaining components to the reduced mixture. Using this technique, the first two moments of the original mixture are preserved.

Component Reduction by Close Components

Component reduction is also possible through the identification and merging of similar components. Such components can be identified on the basis of their *Kullback-Leibler* (KL) distance. Two arbitrary probability density functions, p_1 and p_2 , have a KL distance:

$$D_{KL}(p_1, p_2) = 2(d(p_1, p_2) + d(p_2, p_1)) = 2 \left(\int \log \frac{p_1}{p_2} p_1 dx + \int \log \frac{p_2}{p_1} p_2 dx \right). \quad (5.31)$$

If p_i is a gaussian pdf with mean $\boldsymbol{\mu}_i$ and covariance matrix $\mathbf{V}_i \equiv \mathbf{W}_i^{-1}$, the KL distance is:

$$D_{KL}(p_1, p_2) = \text{tr}[(\mathbf{V}_1 - \mathbf{V}_2)(\mathbf{W}_2 - \mathbf{W}_1)] + (\boldsymbol{\mu}_1 - \boldsymbol{\mu}_2)^T (\mathbf{W}_1 + \mathbf{W}_2) (\boldsymbol{\mu}_1 - \boldsymbol{\mu}_2). \quad (5.32)$$

The two components (l and m) of the mixture which have the smallest KL distance are collapsed into their single gaussian equivalent, $\varphi(\mathbf{x}; \boldsymbol{\mu}, \mathbf{V})$:

$$\boldsymbol{\mu} = \frac{1}{q_k^l + q_k^m} \left(q_k^l \mathbf{x}_{k|k}^l + q_k^m \mathbf{x}_{k|k}^m \right), \quad (5.33)$$

$$\mathbf{V} = \frac{1}{q_k^l + q_k^m} \left(q_k^l \mathbf{C}_{k|k}^l + q_k^m \mathbf{C}_{k|k}^m \right) + \frac{q_k^l q_k^m}{(q_k^l + q_k^m)^2} \left(\mathbf{x}_{k|k}^l - \mathbf{x}_{k|k}^m \right) \left(\mathbf{x}_{k|k}^l - \mathbf{x}_{k|k}^m \right)^T. \quad (5.34)$$

The method proceeds recursively; the pair with smallest distance is found and merged into a single component. The distances between all components in the modified mixture are then recalculated and the merging is repeated until the size of the mixture is reduced to N .

5.2 Implementation

Three possible applications of the GSF have been identified:

- Tails in measurement error distributions.
- Tails in multiple scattering distributions.
- Electron bremsstrahlung, which is described by the Bethe-Heitler distribution.

Some gain in performance can be expected by modelling multiple scattering and measurement error distributions as gaussian mixtures. However, it is for the strongly non-gaussian process of radiative energy loss that the most significant improvement is predicted. A version of

the GSF has been developed which incorporates a gaussian-sum approximation of the Bethe-Heitler distribution. The filter has been implemented in the *Athena* (section 2.8, page 25) software framework. An overview of the implementation of the GSF is provided in appendix B.

5.2.1 The Gaussian-Sum approximation to the Bethe-Heitler Model

Radiative corrections are incorporated into the KF by approximating the Bethe-Heitler model as a gaussian distribution. The mean and variance of the approximation are equal to the first and second moment of the Bethe-Heitler pdf:

$$\langle z \rangle \equiv \left\langle \frac{E_f}{E_i} \right\rangle = e^{-t}, \quad (5.35)$$

$$\text{var}(z) = e^{-t \ln 3 / \ln 2} - e^{-2t},$$

where E_i is the initial energy and E_f is the final energy of an electron undergoing bremsstrahlung. The thickness of material traversed, t , is expressed as a fraction of the radiation length ($t = x/x_0$).

In the case of the GSF, the Bethe-Heitler distribution, $f(z)$, is approximated as a gaussian mixture $p(z)$ (equation 5.9):

$$f(z) \approx p(z) = \sum_{j=1}^{N_{el}} \delta_j \varphi(z; z_j, Y_j). \quad (5.36)$$

For a given number of components, $N_{el} \in \{2, 3, 4, 5, 6\}$, the weights (δ_j), means (z_j) and variances (Y_j) must be determined [45]. When $N_{el} > 1$ there are $3N_{el} - 1$ free parameters: N_{el} mean values, N_{el} variances and $N_{el} - 1$ weights. The requirement that the weights sum to unity removes one degree of freedom.

The mixture parameters are also a function of the thickness of material (t). The typical amount of material traversed by a particle, in a single layer and at normal incidence, is $t : [0.02, 0.20]$. Therefore, δ_j , z_j and Y_j have been determined for discrete values of t within this interval [45]. At smaller thicknesses, the Bethe-Heitler distribution tends toward a δ -function, making it increasingly difficult to approximate as a gaussian-sum.

The parameters are found by minimising one of two distance functions: either the KL distance (equation 5.31) - mixtures obtained by minimising the KL distance are hereafter referred to

as *KL-mixtures*; or the *CDF* (cumulative distribution function) distance:

$$D_{CDF} = \int_{-\infty}^{\infty} |F(z) - P(z)| dz, \quad (5.37)$$

where $F(z)$ is the cumulative Bethe-Heitler distribution and $P(z)$ is the cumulative distribution of the gaussian-sum approximation. Mixtures obtained by minimising the CDF distance are referred to as *CDF-mixtures*.

The process by which the mixture parameters are determined does not exactly reproduce the moments of the Bethe-Heitler distribution. However, a small correction can be applied so that the mean and variance of the mixture are identical to those of the Bethe-Heitler distribution (equation 5.35).

The distance minimisation procedure was performed at discrete values of t . However, during reconstruction the trajectory intersects an arbitrary amount of material. Therefore δ_j , z_j and Y_j are parameterised as fifth order polynomials in t .

Figure 5.1 shows a comparison between the Bethe-Heitler distribution and the KL-mixtures. The comparison is made at $t = 0.02$, where the gaussian mixture approximation is least precise. The corresponding CDF-mixtures are shown in figure 5.2.

The KL-mixtures exhibit a curious property; they possess only one “wide” component. The other components have small variances and mean values approximately equal to one. In addition, a mixture pdf is only valid in the interval $z : [0, 1)$. Whilst the probability of obtaining $z < 0$ is negligible in all cases, the KL-mixtures have large extensions into the region $z \geq 1$. The CDF mixtures are shown to do better in constraining the bulk of the pdf to the physical region.

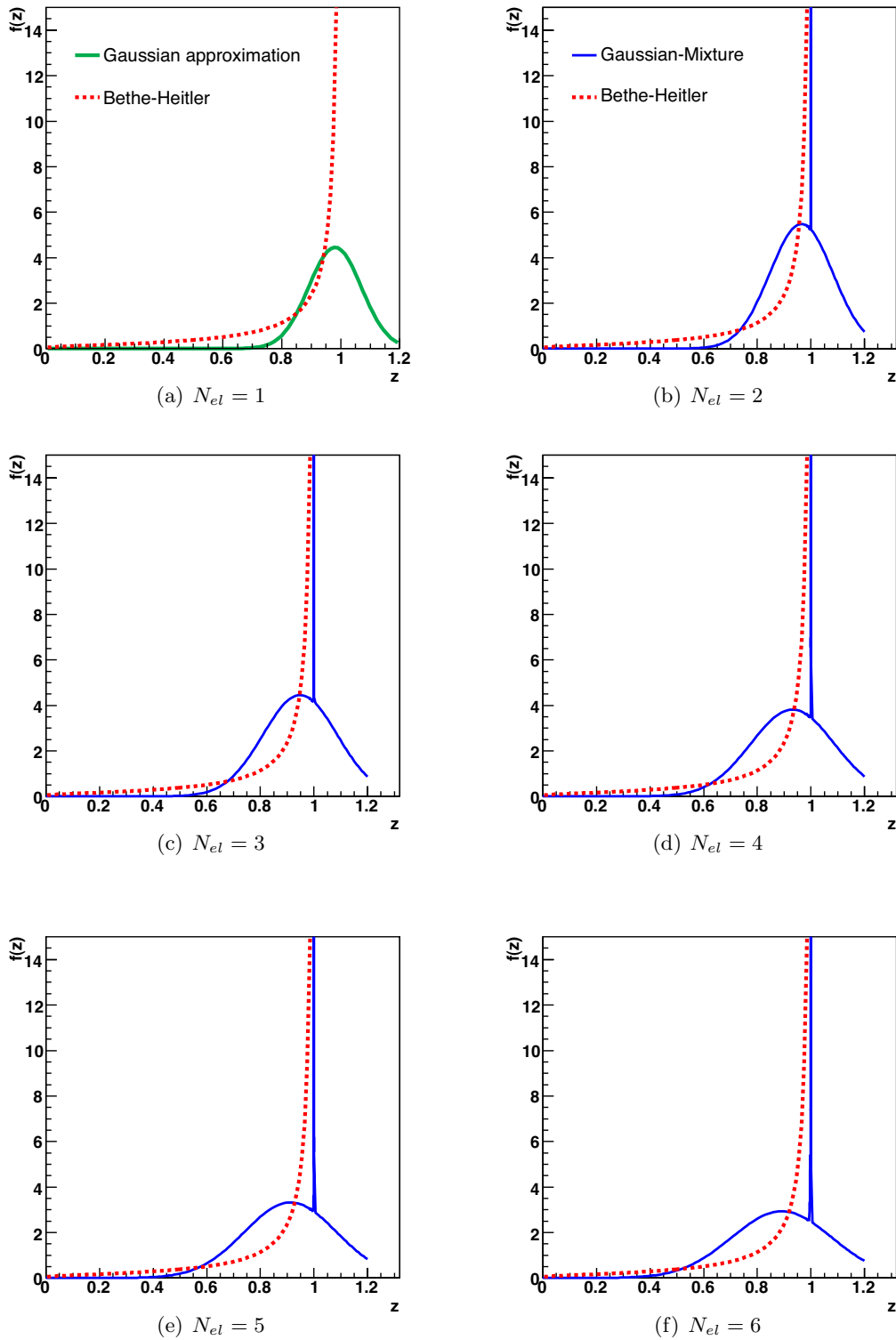


Figure 5.1: Probability density functions of the gaussian mixtures (blue-solid) obtained by minimising the Kullback-Keibler distance. They are compared to a gaussian distribution with mean and variance equal to those of the Bethe-Heitler distribution (green-solid). The Bethe-Heitler pdf is shown in red (dashed). The thickness of material traversed is $x/x_0 = 0.02$.

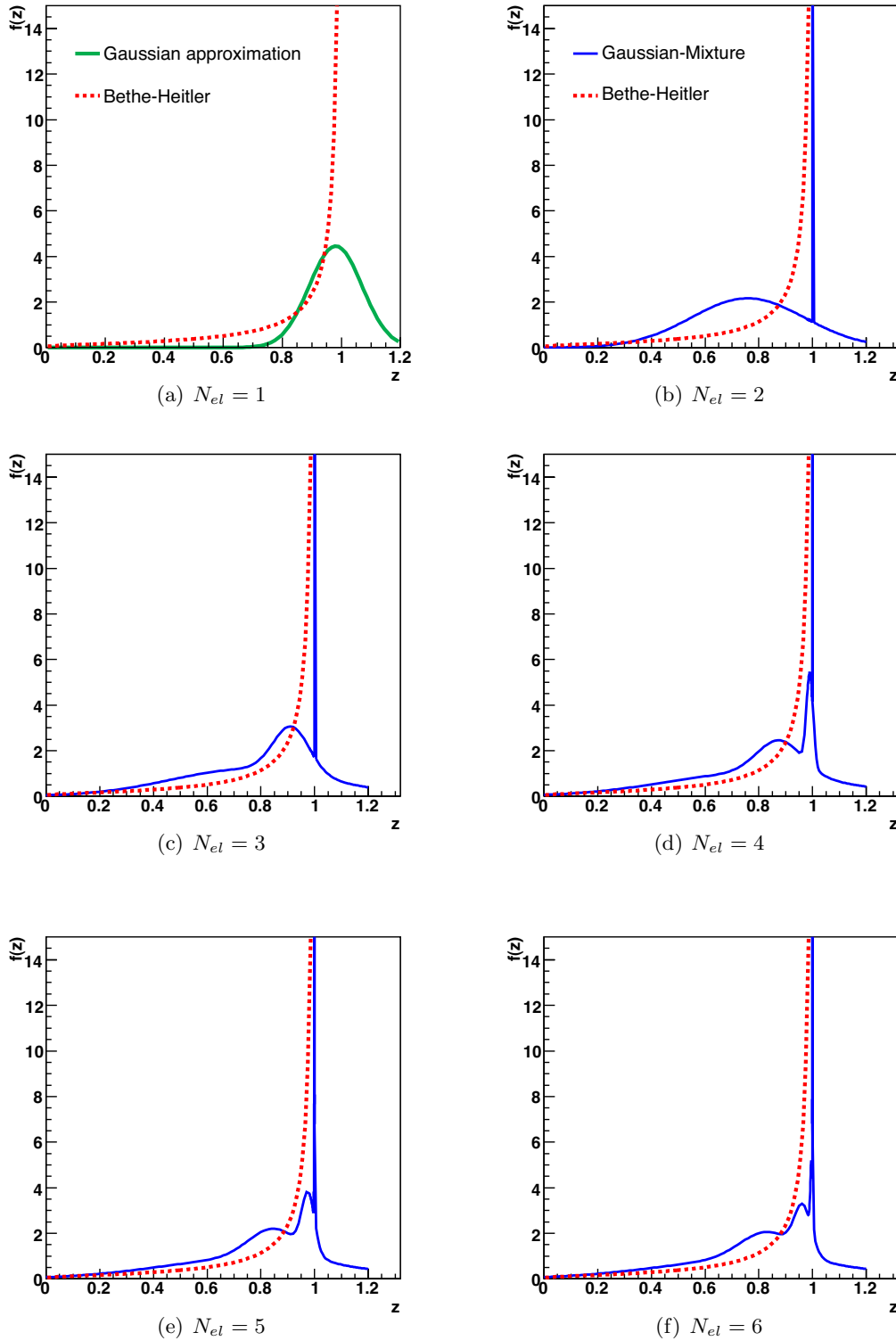


Figure 5.2: Probability density functions of the gaussian mixtures (blue-solid) obtained by minimising the CDF distance. They are compared to a single gaussian distribution with mean and variance equal to those of the Bethe-Heitler distribution (green-solid). The Bethe-Heitler pdf is shown in red (dashed). The thickness of material traversed is $x/x_0 = 0.02$.

Chapter 6

GSF Performance

In this chapter, the performance of the gaussian-sum filter is assessed using samples of single electrons and a simulated response of the ATLAS inner detector. The GSF has also been tested under somewhat more realistic conditions, using data from the 2004 test-beam. The results of that study are presented in chapter 7.

A number of factors are expected to affect the performance of the GSF:

- The momentum of the electron.
- The amount of material traversed along the track trajectory.
- The number of components used in the gaussian-mixture approximating the Bethe-Heitler distribution.
- The minimisation strategy used to determine the gaussian-mixture approximation.
- The number of components remaining after component reduction.
- The strategy used for component reduction.

The impact of these considerations on the performance of the GSF is examined in this chapter.

6.1 Electron Performance in the Central Barrel

An initial study of the GSF performance used samples of single electron events at constant momenta, $p = \{2, 10, 20, 50, 100\} \text{ GeV}/c$. Samples produced at constant p (as opposed to constant p_T) enable a more natural study of energy loss processes which scale with momentum

and not p_T . (The performance of the GSF in p_T is discussed in section 6.7.) Each sample contained 15,000 events, generated using flat distributions across $|\eta| < 0.8$ and $-\pi \leq \varphi < \pi$.

The reconstructed tracks from the GSF and the Kalman filter were compared. The KF incorporates corrections for bremsstrahlung using a single gaussian with the same mean and variance as the Bethe-Heitler distribution (section 5.2.1, page 65). For the purposes of comparison, the same hits were provided to each track fitter, ensuring that neither fit benefited from additional information. Hits were found using the *iPatRec* [46, 47] pattern matching package. The six component CDF-minimised mixture (CDF_6) was used by the GSF as the approximation to the Bethe-Heitler model. 12 components were retained after each component reduction step. A close-component reduction strategy was used, grouping similar components according to their Kullback-Leibler distance.

The results from the two fitting techniques were compared at the perigee - the point of closest approach of the track to the beam-line. The perigee state from the KF is described by a single set of track parameters $(d_0, z_0, \varphi_0, \theta, q/p)$ and an associated covariance matrix: the impact parameters, (d_0, z_0) , are the transverse and longitudinal coordinates of the point of closest approach; the parameters (φ_0, θ) describe the direction of the track at that point; and q/p is the ratio of particle charge to momentum. The parameters (d_0, φ_0) are correlated exclusively with the bending plane while (z_0, θ) are sensitive only to information in the non-bending plane. The q/p parameter is determined from measurements in both the transverse and longitudinal planes. The perigee state from the GSF is a weighted sum of many sets of track parameters, each with its own covariance matrix.

For a single reconstructed track, any one of the perigee parameters can be expressed as a probability density function. In the case of the KF, the pdf is gaussian, while the perigee state from the GSF is a weighted sum of individual components, yielding a distribution which, in general, is non-gaussian. Figure 6.1 shows the difference between the q/p estimates from the KF and GSF for two individual events. The first electron underwent minimal energy loss, while the second experienced a hard bremsstrahlung radiation.

In order to make a useful comparison between the performance of the GSF and the KF, it is necessary to ‘collapse’ the perigee state from the GSF to a single set of track parameters with an associated covariance matrix. It is normal practice to calculate these parameters so that the mean and variance of the gaussian-mixture are preserved.

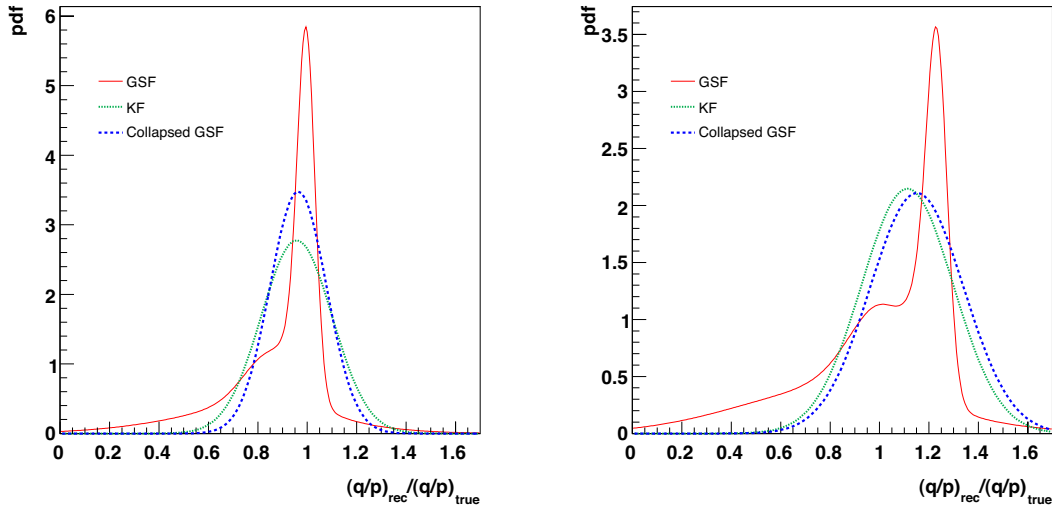


Figure 6.1: The pdf of the (normalised) estimate of q/p for two different electrons, each generated with momentum $10 \text{ GeV}/c$. The electron on the left (right) lost 6% (30%) of its energy due to bremsstrahlung in the inner detector. The perigee state produced by the GSF (red-solid) is compared to the KF (green). The state from the GSF is a weighted sum of 12 gaussian components. The gaussian-sum pdf can be collapsed to an equivalent gaussian distribution with identical mean and variance. This distribution is shown in blue.

6.1.1 Pull Quantities

Pull distributions are used to verify the proper functionality of track reconstruction algorithms and to ensure that the track and error models are correct. For a particular track parameter x_i , with a corresponding covariance \mathbf{C}_{ii} , the pull quantity (P_i) is defined as:

$$P_i = \frac{x_i - x_{i,true}}{\sqrt{\mathbf{C}_{ii}}}, \quad (6.1)$$

where $x_{i,true}$ is the true value of the track parameter.

If all measurement errors and process noise are gaussian, then the pull quantities should be normally distributed with $\mu = 0$ and $\sigma = 1$. When errors are non-gaussian, as in the case of electron tracks, the pull distribution should have $\mu = 0$ and $\text{RMS} = 1$. Figure 6.2 shows the pull distributions for the five track parameters. Table 6.1 provides the corresponding mean and RMS values. The parameters associated with the non-bending plane (z_0, θ) are not sensitive to energy losses and the results from the two fitters are identical. The mean values of these parameters are all consistent with zero. However, parameters sensitive to energy loss ($d_0, \varphi_0, q/p$) exhibit a bias. The mean and RMS values of these parameters are dominated by the events in the tails of the distributions. The tails are highly sensitive to inaccuracies in the modelled material distribution and the inefficiency in pattern matching that is correlated with electrons which undergo catastrophic bremsstrahlung. (Pattern matching algorithms

Parameter	GSF		KF	
	Mean	RMS	Mean	RMS
d_0	0.07 ± 0.01	1.06 ± 0.01	0.11 ± 0.01	1.13 ± 0.01
z_0	0.00 ± 0.01	1.00 ± 0.01	0.00 ± 0.01	1.01 ± 0.01
φ_0	-0.02 ± 0.01	1.03 ± 0.01	-0.07 ± 0.01	1.11 ± 0.01
θ	0.00 ± 0.01	0.92 ± 0.01	0.00 ± 0.01	0.94 ± 0.01
q/p	0.01 ± 0.01	0.98 ± 0.01	-0.06 ± 0.01	1.09 ± 0.01

Table 6.1: Mean and RMS values of the track parameter pull distributions for a sample of 15,000 electrons with $p = 10 \text{ GeV}/c$.

often fail to find hits when the electron has lost a significant amount of energy.)

6.1.2 Resolution Quantities

Figure 6.3 shows distributions of resolution quantities for the reconstructed perigee parameters. The mean and RMS values of these distributions are shown in table 6.2. The performance of the GSF and KF are identical for the parameters fitted in the non-bending plane. The mean values for these distributions are again consistent with zero whereas those for the parameters sensitive to energy loss are all somewhat biased.

Parameter	GSF		KF	
	Mean	RMS	Mean	RMS
	$\times 10^{-3}$		$\times 10^{-3}$	
$d_0 \text{ (mm)}$	4.13 ± 0.41	49.69 ± 0.29	4.54 ± 0.042	51.40 ± 0.30
$z_0 \text{ (mm)}$	0.38 ± 0.85	103.9 ± 0.60	-0.01 ± 0.86	105.3 ± 0.61
φ_0	-0.01 ± 0.01	$0.82 \pm 0.00(4)$	-0.02 ± 0.01	$0.87 \pm 0.00(4)$
θ	$0.00 \pm 0.00(4)$	$0.57 \pm 0.00(3)$	$0.00 \pm 0.00(4)$	$0.58 \pm 0.00(3)$
q/p	-4.81 ± 1.30	158.80 ± 0.92	-2.35 ± 1.32	162.20 ± 0.94

Table 6.2: Mean and RMS values of the track parameter resolution distributions for a sample of 15,000 electrons with $p = 10 \text{ GeV}/c$.

The mean and RMS values of the d_0 , φ_0 and q/p resolution distributions are dominated by large tails, known to be correlated with photon radiation in the innermost layers of the tracker. Since the KF and GSF have similar tail profiles, both methods produce near identical values of mean and RMS. The d_0 distributions from the two fitters appear virtually indistinguishable, while the peak of the φ_0 distribution from the GSF contains a small fraction more events than that of the KF. Visually however, the GSF appears to perform significantly better than the KF around the peak of the q/p distribution.

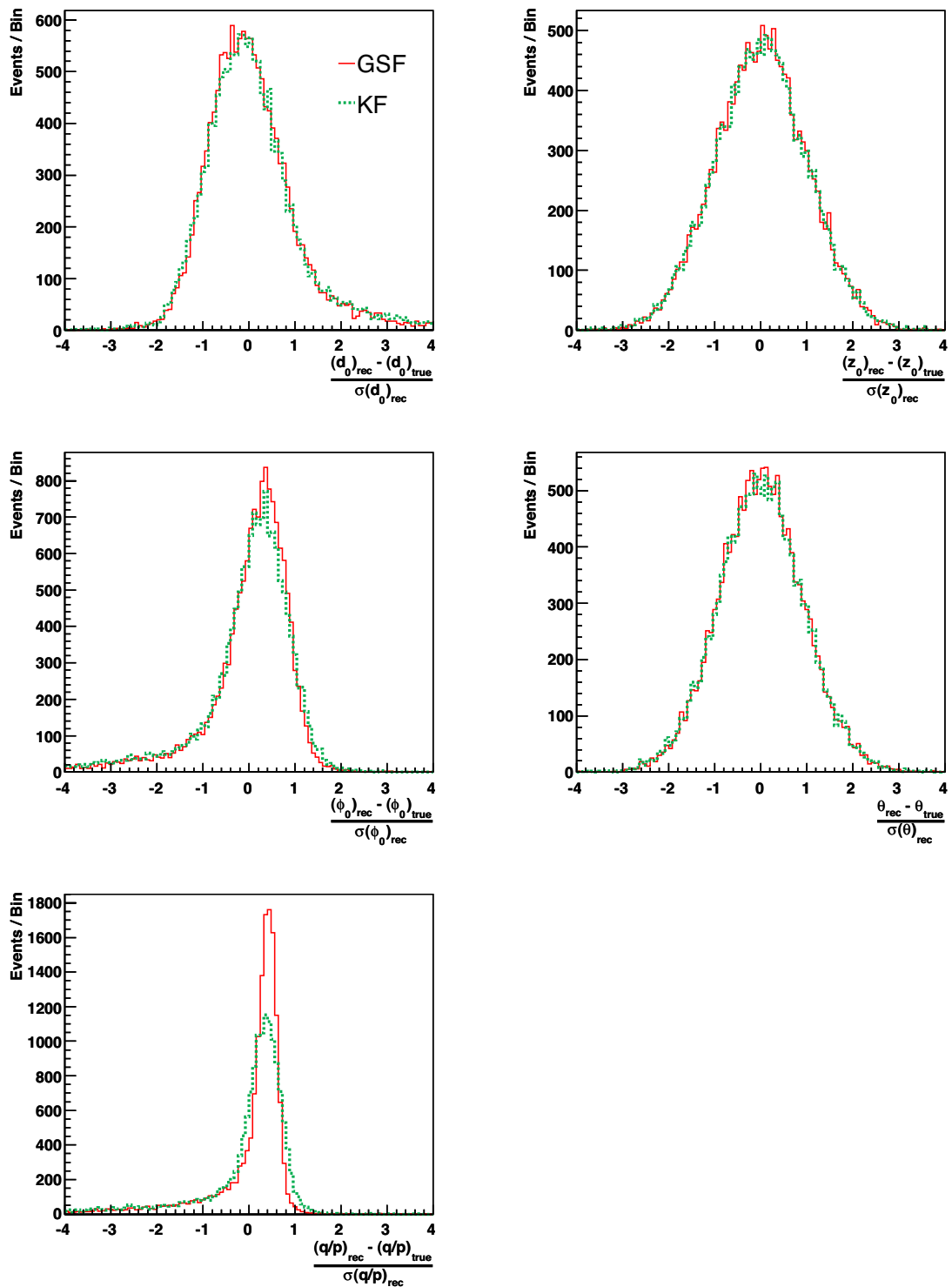


Figure 6.2: Pull distributions for the perigee parameters from 15,000 single electron events with $p = 10 \text{ GeV}/c$. Comparison is made between the GSF (red-solid) and the KF (green-broken).

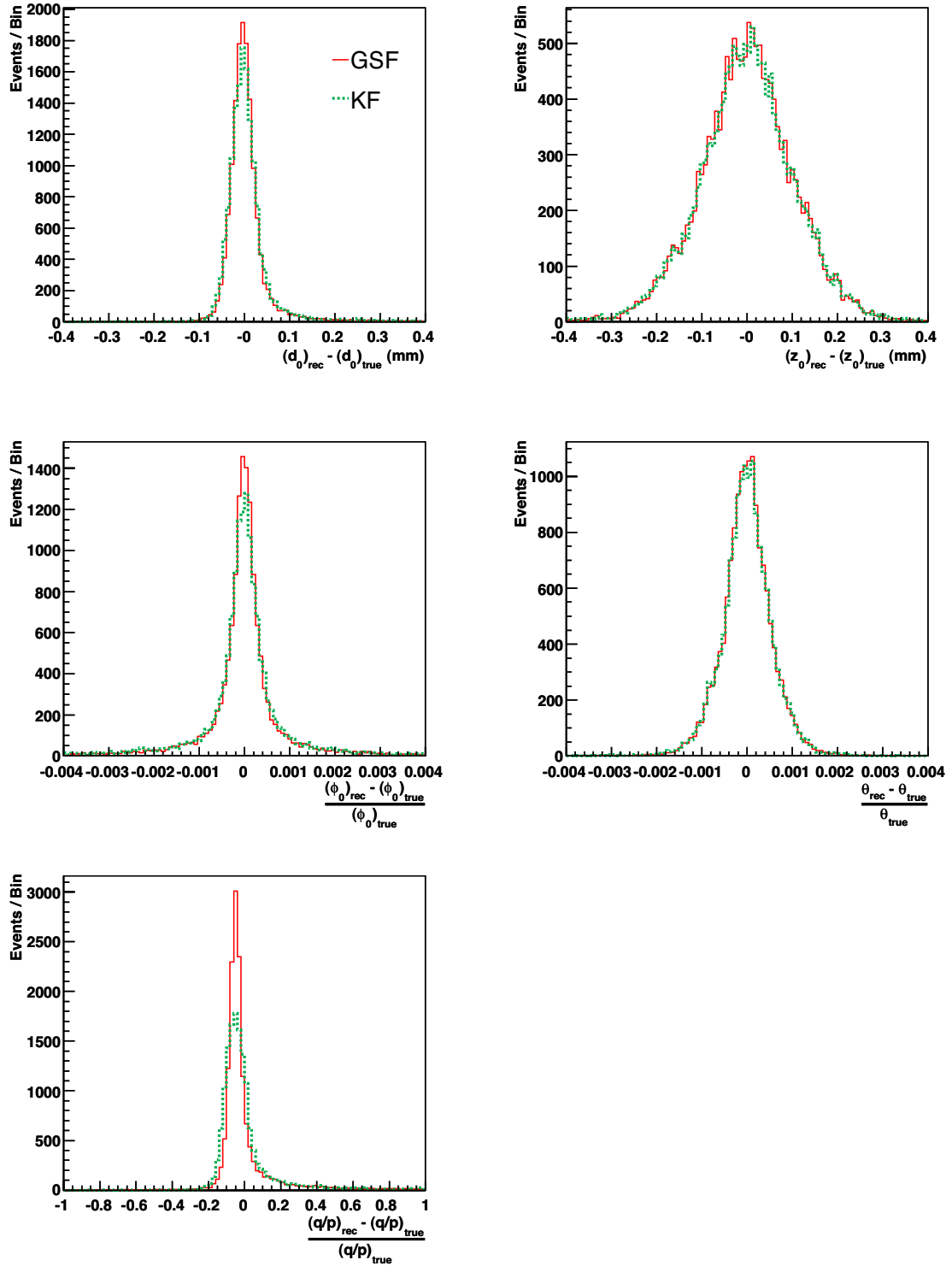


Figure 6.3: Resolution distributions for the perigee parameters from 15,000 single electron events with $p = 10 \text{ GeV}/c$. Comparison is made between the GSF (red-solid) and the KF (green-broken).

To delineate the effect of the tail in the q/p distribution, an *effective resolution* has been defined in terms of a value, $Q(x)$, the symmetric half-width enclosing a fraction, x , of all events. The symmetric half-width was determined around the origin of the distribution (as opposed to the peak), introducing a sensitivity to the true value of q/p in the effective resolution. Values of $Q(68\%)$ and $Q(95\%)$ have been determined, corresponding to $\pm 1\sigma$ and $\pm 2\sigma$ coverage. The value of $Q(68\%)$ quantifies the width of the core of the distribution, while the $Q(95\%)$ interval is determined by the size of the bremsstrahlung tail. Figure 6.4 shows $Q(x)$ as a function of momentum. At all momenta, the core of the GSF distribution is narrower than the KF.

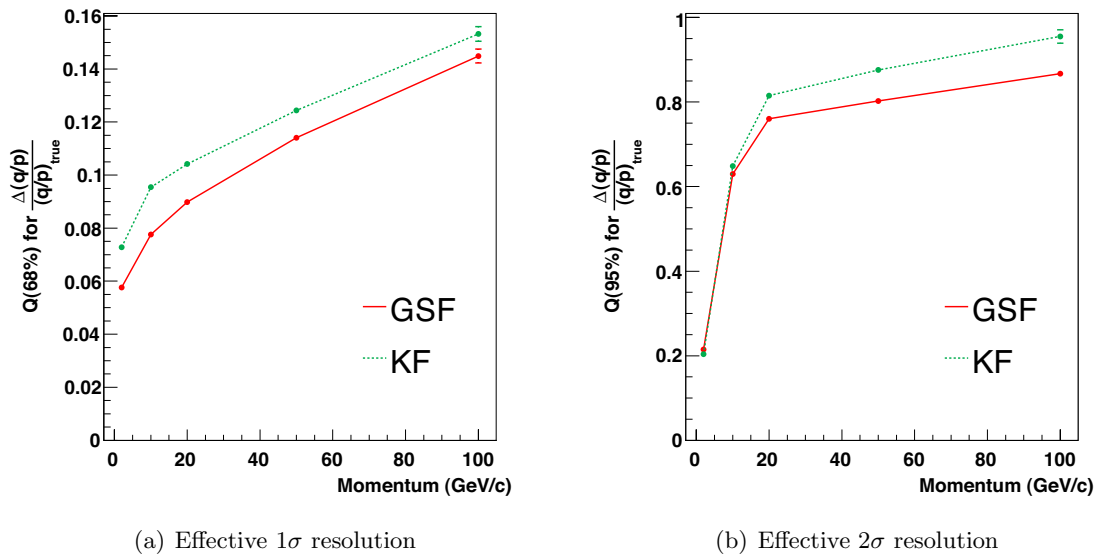


Figure 6.4: Effective 1σ and 2σ momentum resolution as a function of particle momentum. The GSF (red-solid) is compared to the KF (green-broken).

Another comparison between the GSF and the KF was made by integrating the q/p pdf up to the true value (the probability transform of q/p). If the reconstructed pdf accurately represents the true energy losses, then the distribution of probability transforms for q/p should be flat. The GSF and KF probability transforms are shown in figure 6.5. The distribution from the GSF is not perfectly flat, an indication that the gaussian-sum approximation to the Bethe-Heitler distribution is itself imperfect. However, it does give a significant improvement over the KF.

6.2 Results using Simplified Simulation

The intrinsic performance of the GSF was examined in more detail using a fast track simulation framework, *FATRAS* [48]. During simulation, each measurement was smeared with

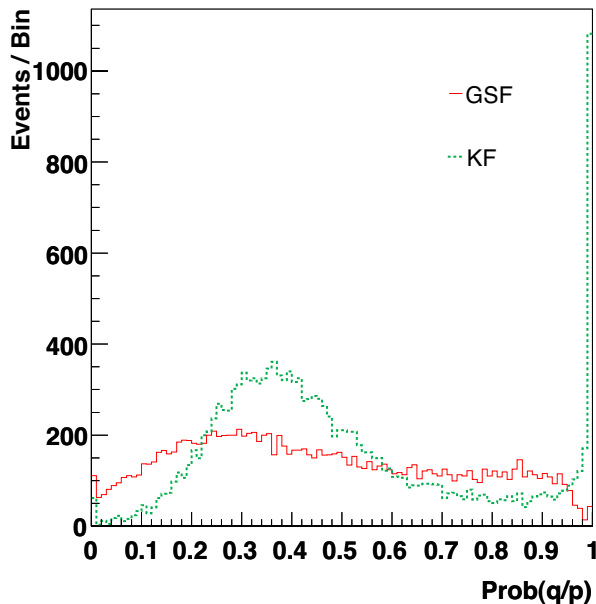


Figure 6.5: Probability transform of the q/p parameter. The GSF (red-solid) is compared to the KF (green-broken).

gaussian errors reflecting the resolution of the corresponding detector element. Energy loss through bremsstrahlung was implemented using a random number generator based on the Bethe-Heitler distribution. No other material effects were applied during the simulation or considered during reconstruction. All results were derived from a sample of 15,000 single electron events with momentum $10 \text{ GeV}/c$ in the central barrel region.

6.2.1 Component Reduction Technique

A component reduction algorithm is a vital part of the GSF, ensuring that the size of the track state remains computationally manageable. Any component reduction algorithm necessarily destroys some of the information in the mixture. It is therefore important to determine the reduction procedure which has least impact on the moments of the track state.

Two component reduction algorithms have been implemented (section 5.1.5, page 63): reduction through removal of components with smallest weights and reduction through grouping of close components (similar components are identified on the basis of their Kullback-Leibler distance).

Figure 6.6 shows the momentum resolution, using the two techniques, as a function of the mixture size after component reduction. The resolution is shown for two component (CDF_2) and six component (CDF_6) gaussian-sum approximations to the Bethe-Heitler model. The

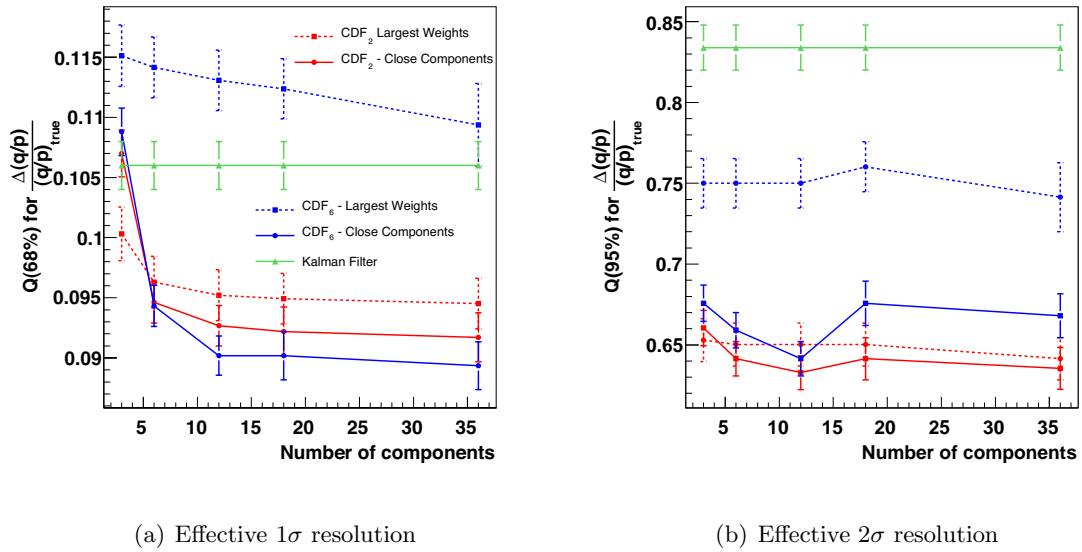


Figure 6.6: Effective resolution as a function of the number of components. Results were produced using the fast track simulation framework. The performance of the component reduction algorithm based on largest weights (broken lines) is compared with the algorithm based on the grouping of similar components (solid lines). Results obtained using the CDF_2 (red) and CDF_6 (blue) mixtures are shown. For reference, the resolution from the KF is indicated by the green line.

1σ momentum resolution from the GSF is better than the KF in all cases except when the largest-weights method is used with the CDF_6 mixture. The cores of the distributions are narrower when the close-components technique is used. The results from the largest-weights approach display a curious feature - the performance of the CDF_2 mixture is better than the CDF_6 mixture.

6.2.2 Gaussian-Sum approximations to the Bethe-Heiter Model

The fast simulation framework was also used to assess the performance of different gaussian-sum approximations to the Bethe-Heitler distribution. Electrons were reconstructed using both the CDF-minimised and KL-minimised mixtures (section 5.2.1, page 65). In this study, the close-component reduction algorithm was used.

The momentum resolution, obtained using different mixtures, is shown in figure 6.7. In the majority of cases, the resolution from the GSF is better than the KF. The mixtures obtained by minimising the CDF distance yield systematically better results than those obtained by minimising the KL distance. No significant improvement in resolution can be achieved by increasing the number of remaining components beyond 12.

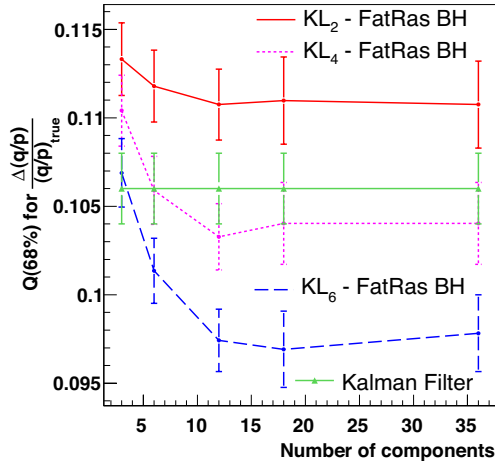
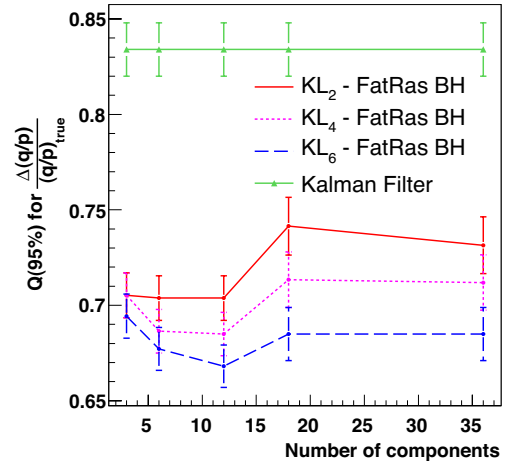
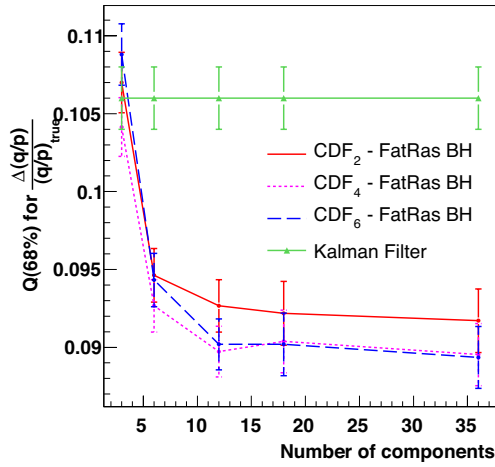
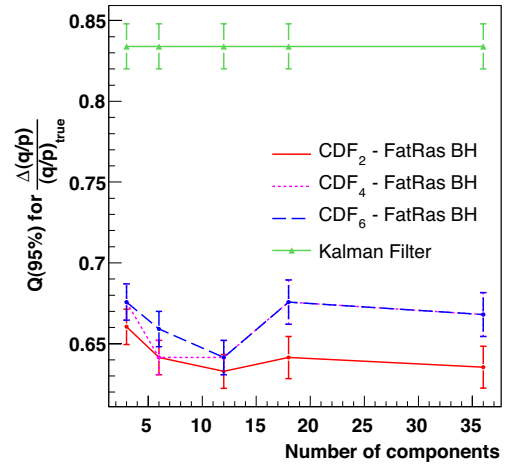
(a) Effective 1σ resolution - KL mixtures(b) Effective 2σ resolution - KL mixtures(c) Effective 1σ resolution - CDF mixtures(d) Effective 2σ resolution - CDF mixtures

Figure 6.7: Effective 1σ and 2σ resolution for $10\text{ GeV}/c$ electrons as a function of the mixture size after component reduction. Results were produced using the fast track simulation framework. The gaussian-sum mixtures obtained by minimising the KL distance are compared with those obtained by minimising the CDF distance. For reference, the resolution from the KF is indicated by the green line.

Henceforth, unless otherwise stated, the GSF uses: the CDF_6 mixture approximating the Bethe-Heitler distribution; the close-components reduction technique; and a maximum of 12 components in the track state.

6.3 Performance in the Forward Regions

The amount of material at $|\eta| > 0.8$ is significantly greater than within the central barrel region, reaching a maximum at $|\eta| \sim 1.7$ (figure 3.2, page 31). A particle in this part of the detector traverses $\sim 130\%$ x/x_0 .

High statistics samples of 5000 single electron events at $10 \text{ GeV}/c$ were generated in localised regions of η , using the full detector simulation. In all, 13 samples were produced covering ($|\eta| \leq 2.6$). The samples were reconstructed with the GSF, KF and the global least-squares estimator in the iPatRec package. The iPatRec fitter does not incorporate corrections for radiative energy loss.

Resolution as a function of $|\eta|$ is shown in figure 6.8. In regions of low material (small $|\eta|$), energy losses due to bremsstrahlung are minimal and so the width of the core is determined by the intrinsic detector resolution and multiple scattering. In this case, the iPatRec fitter gives the best results. However, in regions with a lot of material, both the GSF and KF perform better than iPatRec. The $Q(95\%)$ interval contains a significant fraction of the bremsstrahlung tail, which is not accounted for in the iPatRec fitter. The 2σ effective resolution is always worst for iPatRec; the results from the GSF and KF are similar.

6.4 Reconstruction Using the GSF Mode

The estimate of q/p from the GSF can be expressed as the pdf of a weighted gaussian sum (figure 6.1). It is normal practice to take the mean value of the pdf to compare with the result from the KF. An alternative approach is to use the most probable value of the mixture (the mode). A Newton-Raphson method [49] has been implemented to determine the value of q/p at which the pdf obtains its absolute maximum [50].

A sample of 15,000 single electron events at $p = 10 \text{ GeV}/c$ was reconstructed using both the mean and mode of the q/p estimate from the GSF.

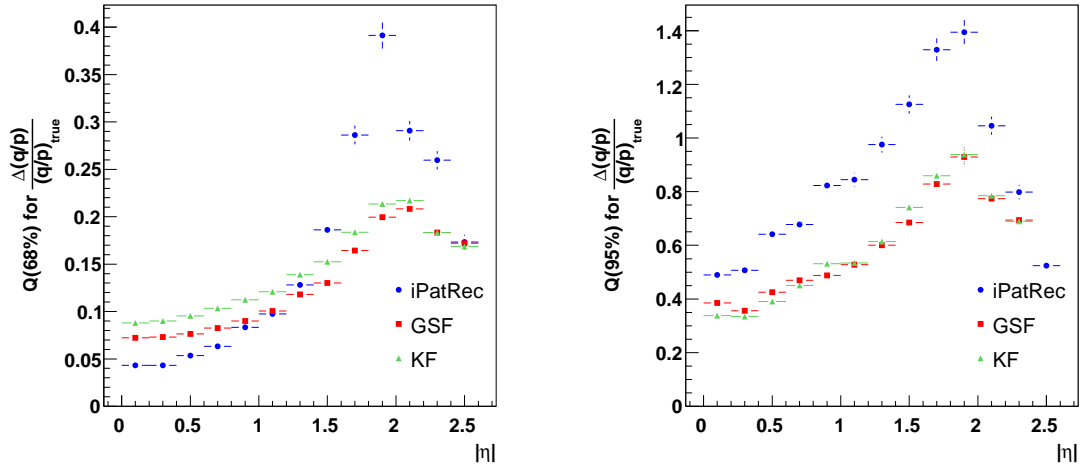
(a) Effective 1σ resolution(b) Effective 2σ resolution

Figure 6.8: Effective 1σ and 2σ resolution for 10 GeV/c electrons as a function of $|\eta|$. The GSF (red-square) is compared to the KF (green-triangle) and the global LSM fitter in the iPatRec package (blue-circle). The results obtained using the iPatRec fitter have no corrections for radiative energy loss.

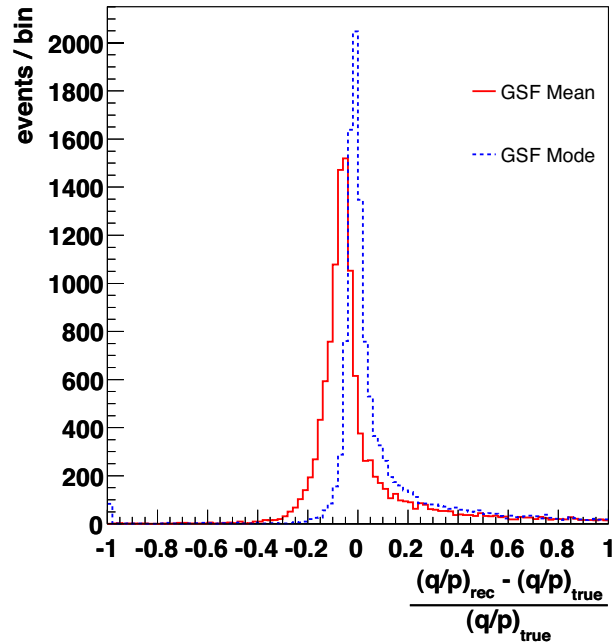


Figure 6.9: Distributions of the mean (red-solid) and mode (blue-broken) of the q/p estimate from the GSF.

	GSF Mean	GSF Mode
Mean	$(2.60 \pm 1.73) \times 10^{-3}$	$(70.7 \pm 1.82) \times 10^{-3}$
RMS	0.213 ± 0.001	0.224 ± 0.001
1σ	0.143 ± 0.003	0.113 ± 0.002
2σ	1.88 ± 0.03	2.06 ± 0.04

Table 6.3: Mean, RMS and effective resolution of q/p distributions produced using the mean and mode of the perigee pdf from the GSF.

The q/p resolution distributions are shown in figure 6.9. A comparison of the key parameters of the two distributions is provided in table 6.3. The mode distribution has a narrower core but a longer tail than the mean distribution. The peak of the mode distribution is centred on zero whereas the peak of the mean distribution is displaced. The mean distribution is approximately unbiased.

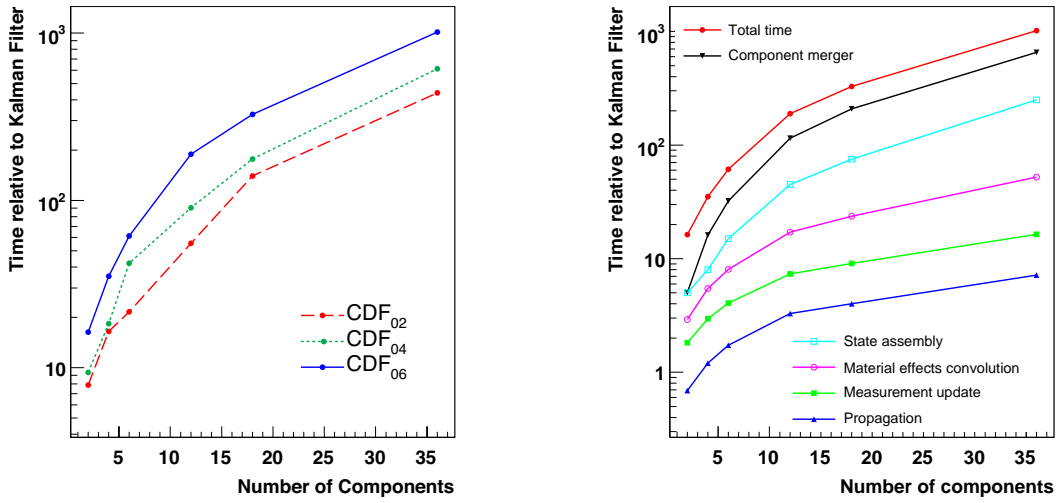
6.5 Timing Considerations

The reconstruction of the full simulation has been used to benchmark the execution time of the GSF. Since the GSF runs a (user-limited) number of Kalman filters in parallel, the improvement in resolution is at the cost of greater CPU time.

For the purposes of comparison, the GSF execution time was normalised to that of the KF. The timing study was based on the reconstruction of 15,000 single electron events with $p = 10$ GeV/c. The close-component reduction algorithm was used in this study.

Figure 6.10(a) shows the relative execution time of the GSF as a function of the mixture size after component reduction. Three different mixtures approximating the Bethe-Heitler distribution are shown. The execution time is strongly dependant on the size of the track state. Figure 6.10(b) shows the time taken in the various components of the GSF. The CDF_6 mixture was used for this study. The process of component reduction dominates the total execution time.

Table 6.4 shows the fraction of the total reconstruction time used by the GSF and KF. In addition to track fitting, the total reconstruction time incorporates the data preparation and pattern recognition steps. Results are based on samples of 15,000 single electron events. The GSF used the CDF_6 mixture and 12 components in the reduced state. Unlike the KF, the GSF dominates the total reconstruction time.



(a) The execution time of the GSF (normalised to the KF execution time), versus the mixture size after component reduction. The execution time is shown for three CDF-minimised mixtures.

(b) The execution time of the GSF (normalised to the KF execution time), versus the mixture size after component reduction. The time taken in the major components of the GSF is shown.

Figure 6.10: The average time taken to fit a single 10 GeV/c electron track using the GSF.

Momentum (GeV/c)	GSF	KF
10	93.2%	9.2%
20	94.3%	9.6%
100	94.2%	10.0%

Table 6.4: The fraction of the total reconstruction time spent in track fitting.

6.6 Kink Finding

The track state is defined not just at the perigee but at any arbitrary surface within the detector. Optimal values of the track parameters at a surface are found through the combination of the forward and backward filters. This process is called smoothing (section 5.1.4, page 61). The gaussian-sum smoother can be used to determine, to a reasonable accuracy, the point at which a bremsstrahlung radiation occurred. The emission of a photon creates a kink in the track trajectory, producing observable changes in all parameters associated with the bending plane.

At each measurement surface, the value of q/p associated with the component with the largest (leading) weight was identified.

Figure 6.11 shows plots of leading q/p versus the position of the track in the transverse

plane. A number of different single electron events are shown, corresponding to different bremsstrahlung radiation scenarios.

6.6.1 Identification of a Point of Bremsstrahlung

By identifying changes in q/p between nearby surfaces, the position of the bremsstrahlung vertex can be estimated. Two searches are employed, one using the silicon and one in the TRT, providing a maximum of two reconstructed bremsstrahlung vertices per track.

If the change in momentum between two adjacent silicon measurements is greater than $1 \text{ GeV}/c$, then a *brem-point* is constructed. The *brem-point* is defined as the position of the track at the nearest material layer.

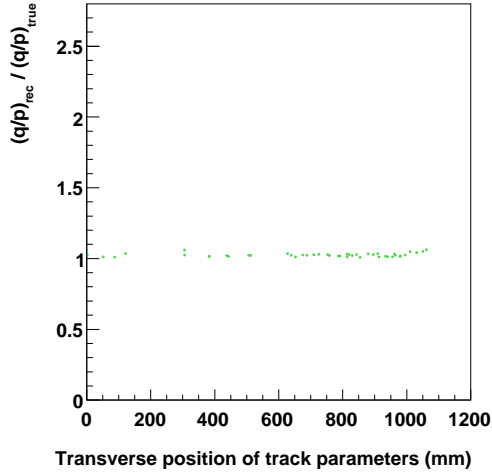
A *brem-point* in the TRT is also flagged if the change in momentum between adjacent measurements is greater than $1 \text{ GeV}/c$. The position of the *brem-point* is defined as the mid-point of the two measurements. When more than one large change in momentum is found, the bremsstrahlung vertex is derived from the measurements associated with the largest momentum change.

If the energy loss in a single bremsstrahlung radiation is $\geq 300 \text{ MeV}$, the true position of the vertex is stored in the Monte-Carlo truth information. Figure 6.12 shows the true positions of the bremsstrahlung vertices in the inner detector for a sample of 15,000 single electron events with initial momentum $50 \text{ GeV}/c$.

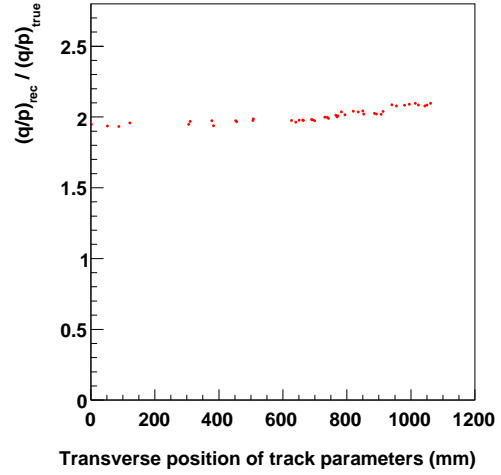
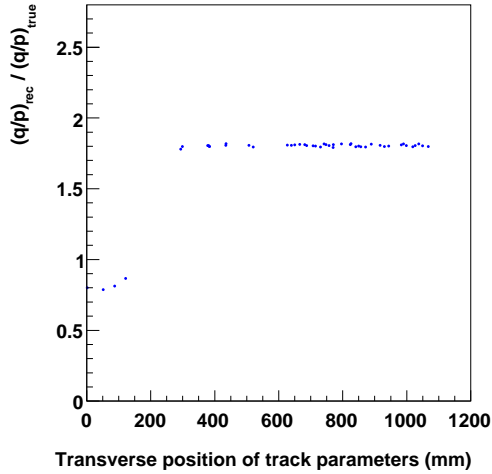
The positions of the reconstructed *brem-points* and true vertices are compared. If the position of the *brem-point* is within 15 cm of the true position in the transverse plane, then the *brem-point* is associated to the true vertex. It is then possible to define an efficiency of association ϵ_{assoc} - the ratio of the number of *brem-points* correctly associated with truth, to the total number of *brem-points* found.

The kink finder algorithm has been validated using a sample of 15,000 single electron events with initial momentum $10 \text{ GeV}/c$. Initially tracks were selected from Monte-Carlo truth information, based on the requirement of exactly one bremsstrahlung vertex on the track. Additionally, the energy loss at the vertex was required to be $> 20\%$ of the electron's initial energy. Given that the electron had lost a significant fraction of its energy, a kink in the trajectory of the track was certain to exist. In this case, it was possible to define an efficiency of identification ϵ_{id} - the number of tracks with a reconstructed kink divided by the total number of tracks satisfying the truth criteria.

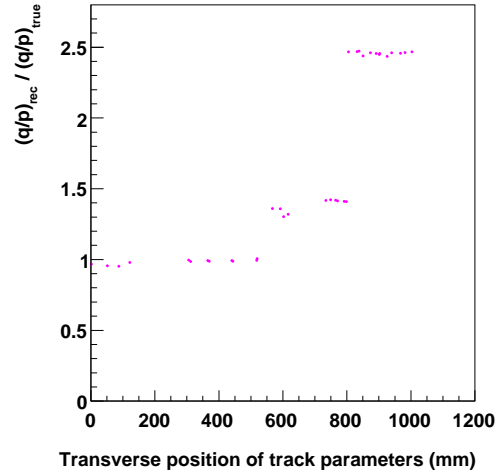
Table 6.5 provides the values of ϵ_{id} and ϵ_{assoc} obtained from the kink finding algorithm.



(a) No bremsstrahlung radiation

(b) Early (irrecoverable) bremsstrahlung: 50% of the electron's energy was lost before the second pixel layer, making an accurate measurement of q/p impossible.

(c) Hard bremsstrahlung radiation in the first SCT layer - 40% of the electron's energy was lost.



(d) Hard bremsstrahlung in the TRT - 45% of the electron's energy was lost at a radius of 626 mm.

Figure 6.11: Normalised q/p versus the transverse position of the track state. Four separate single electron events are shown, each having an initial momentum of $p = 10 \text{ GeV}/c$.

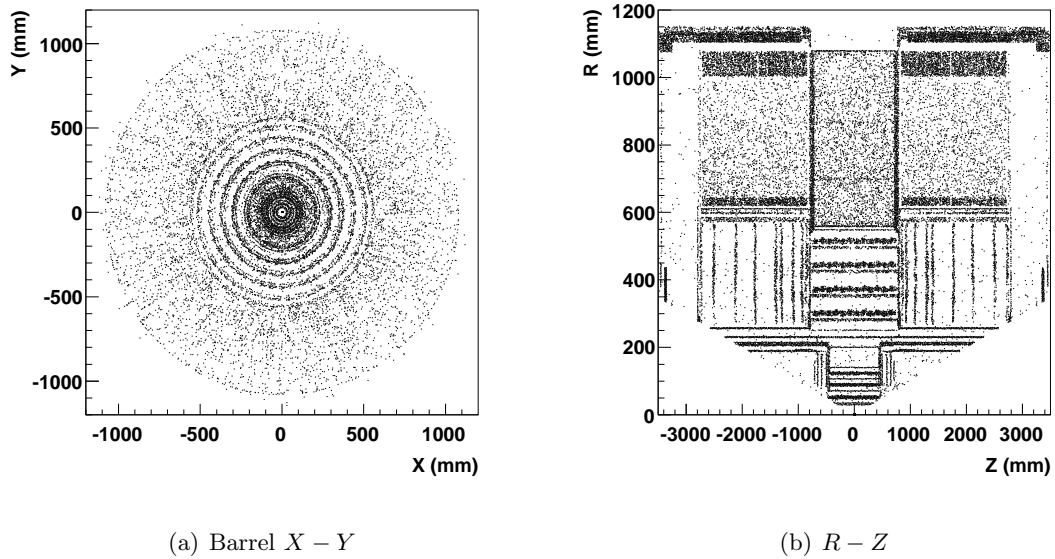


Figure 6.12: The true positions of bremsstrahlung vertices in the inner detector. The plots were generated using a sample of 15,000 single electron events with initial momentum 50 GeV/c .

Single Hard Bremsstrahlung ($> 20\%$ energy loss)	
Tracks reconstructed	1186
Tracks with ≥ 1 kink found	625
ϵ_{id}	0.53
Total number of kinks found	681
Kinks matched to truth	515
ϵ_{assoc}	0.76

Table 6.5: Performance of the kink finder algorithm when events involving a single hard bremsstrahlung radiation ($> 20\%$ energy loss) are selected from truth. The selection is derived from a population of 15,000 single electron events with $p = 10 GeV/c$.

The identification efficiency is poor. There are two main reasons for the inefficiency:

- Photon emission occurs very early or very late in the detector.
- Photon emission causes a change in the electron's trajectory so that measurements after the bremsstrahlung vertex are not found by the pattern recognition algorithm.

These effects were studied using the electrons which underwent a single bremsstrahlung radiation with energy loss $> 20\%$. In this case, 561 of the tracks which satisfied the truth selection criteria had no reconstructed brem-point.

The true position of the bremsstrahlung vertex in the transverse plane is denoted R . Electrons with $R < 90 \text{ mm}$ (the radius of the second pixel barrel) or $R > 850 \text{ mm}$ were labelled as having bremsstrahlung vertices *difficult* to identify, since the photon emission occurs either too early or too late in the detector for the tracker to observe the change. The number of the 561 remaining electrons which also undergo early or late bremsstrahlung is:

A. Number of tracks with no identified kink	561
B. Number of A with $R < 90 \text{ mm}$ or $R > 850 \text{ mm}$	322

There remain 239 electrons, each of which has no reconstructed kink, irrespective of losing a significant amount of energy at intermediate radius. From these events, tracks with < 3 measurements after the true vertex were identified:

C = A - B	239
Number of C with < 3 measurements after the true vertex	142

83% of all tracks, for which no kink was found, either undergo bremsstrahlung early/late in the detector, or are truncated as a result of inefficient pattern recognition. This study illustrates the limitations of the kink finding algorithm: early or late bremsstrahlung vertices are generally not detected and a sufficiently large number of measurements must exist around the photon emission vertex.

In an extension to the initial evaluation of the kink finder performance, values for ϵ_{id} and ϵ_{assoc} have been determined for electron tracks that have been selected based on an expanded set of truth criteria:

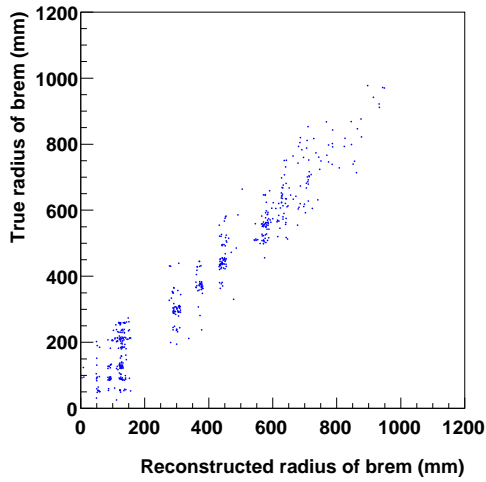
Truth criteria	Tracks Reconstructed	Tracks with Kink	ϵ_{id}	Kinks Found	Kinks matched to Truth	ϵ_{assoc}
Single brems $> 20\%$	1186	625	0.53	681	515	0.76
All brems $> 20\%$	7416	4747	0.64	5611	4784	0.85
All brems $> 10\%$	9234	5455	0.59	6355	5424	0.85
No brems	1296	54	0.04	57	N/A	N/A
All events	12094	5738	(0.47)	6653	5581	0.84

Table 6.6: Results from the kink finder algorithm for a sample of 15,000 single electrons with momentum $10 \text{ GeV}/c$. ϵ_{id} is the ratio of the number of tracks where a reconstructed brems-point has been found, to the total number of tracks. ϵ_{assoc} is the ratio of the number of reconstructed brems-points correctly associated to a true vertex, to the total number of brems-points found.

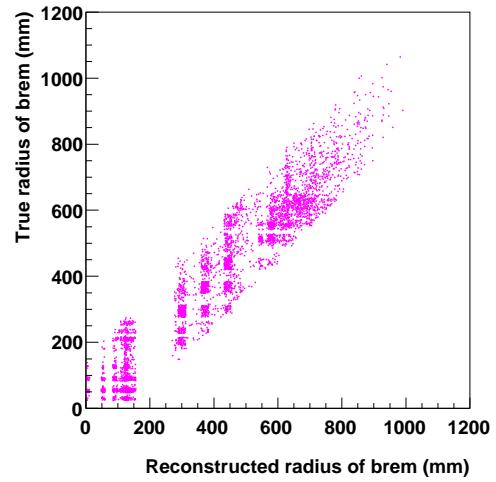
1. Tracks from electrons with only one bremsstrahlung vertex and $> 20\%$ energy loss (considered above).
2. Tracks from electrons with any number of bremsstrahlung vertices, provided that at one vertex $> 20\%$ of the electron's initial energy was lost.
3. Tracks from electrons with any number of bremsstrahlung vertices, provided that at one vertex $> 10\%$ of the electron's initial energy was lost.
4. Tracks from electrons with no bremsstrahlung vertices. This allows an estimation of the fake rate. In this case ϵ_{assoc} cannot be determined.
5. Tracks from electrons with no constraints from truth. In this case, ϵ_{id} should not be considered meaningful as not every reconstructed electron underwent sufficient energy loss to expect a kink.

Figure 6.13 shows the correlation between the true position of photon emission and the reconstructed brems-point for the different truth selection criteria. Table 6.6 provides the corresponding values of ϵ_{id} and ϵ_{assoc} .

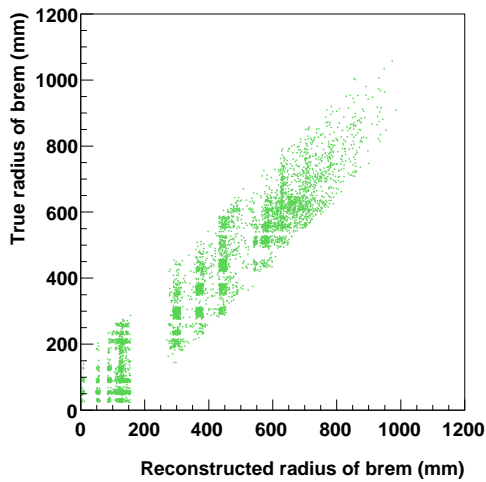
For tracks with brems-points correctly associated with truth, a comparison was made between the momentum estimates from different fitters. The resolution from the GSF has been compared with the least-squares estimator from the *xKalman* [47, 51] track reconstruction package. The xKalman fit does not incorporate corrections for radiative energy losses.



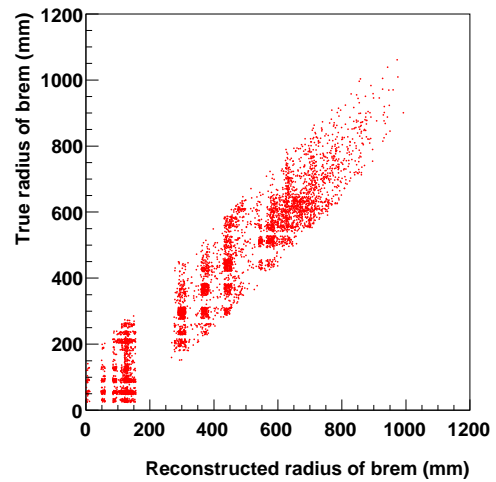
(a) Brem-points from tracks with a single bremsstrahlung photon carrying away $> 20\%$ of the electron's initial energy.



(b) Brem-points from tracks with any number of bremsstrahlung vertices, provided that at one vertex $> 20\%$ of the electron's initial energy is lost.



(c) Brem-points from tracks with any number of bremsstrahlung vertices, provided that at one vertex $> 10\%$ of the electron's initial energy is lost.



(d) All events.

Figure 6.13: Reconstructed position versus true position of the point of bremsstrahlung in the transverse plane.

The distributions are shown in figure 6.14 and the corresponding effective 1σ momentum resolution quantities are provided in table 6.7. The GSF provides a superior estimate of the resolution in all cases except when tracks without bremsstrahlung losses are selected from truth. In this case, the error model provided by the GSF overestimates the uncertainty, since it applies unnecessary corrections for radiative energy losses.

Truth criteria	GSF	xKalman
Single brem > 20%	0.128 ± 0.003	0.432 ± 0.009
All brem > 20%	0.170 ± 0.001	0.616 ± 0.005
All brem > 10%	0.162 ± 0.001	0.487 ± 0.004
No brem	0.085 ± 0.002	$0.018 \pm 0.000(4)$

Table 6.7: Effective 1σ resolution values obtained using the GSF and xKalman. Events were initially chosen from a sample of 15,000 single electrons based on truth selection criteria.

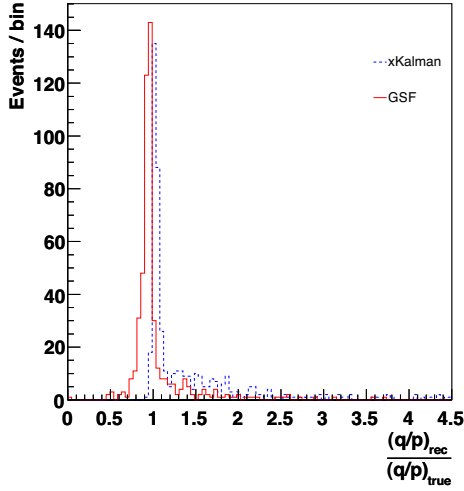
The performance of the kink finding algorithm deteriorates with increasing electron momentum, where changes in an electron's trajectory become harder to detect. The results obtained from a sample of 15,000 single electrons at $p = 20 \text{ GeV}/c$ are shown in table 6.8.

6.7 Summary

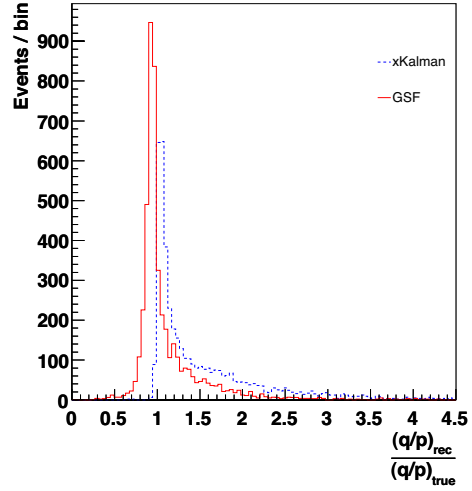
The GSF has been successfully validated using both the detailed simulation of the tracker (sections 6.1 and 6.3) and a fast simulation framework (FATRAS, section 6.2). It has been shown to provide a better estimate of the 1σ effective momentum resolution than the KF. An additional improvement can be achieved if the mode of the gaussian-sum mixture is used instead of the mean (section 6.4). The GSF is considerably more computationally expensive than the KF (section 6.5), necessitating selective use of the GSF in a physics analysis.

The GSF was also incorporated into a kink finding algorithm (section 6.6) used to locate bremsstrahlung vertices in the transverse plane. The algorithm was unable to determine the locations of vertices occurring either very early or very late in the tracker, but was able to find the majority of kinks at intermediate radii.

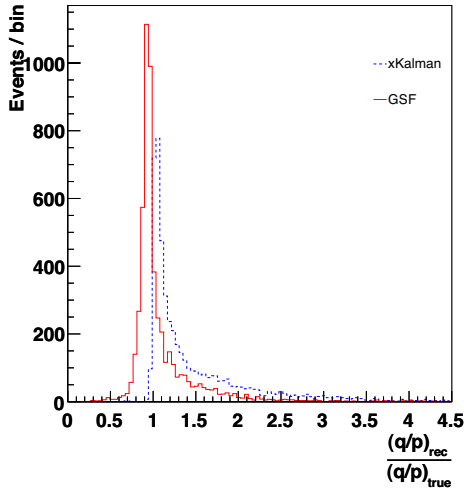
The studies presented in this chapter used samples of single electrons generated at constant momentum. To conclude, a final summary of the single electron performance in p_T is presented. Samples of 15,000 single electrons were generated at $p_T = \{2, 10, 20, 50, 100\} \text{ GeV}/c$, using a flat distribution over $-2.5 \leq \eta \leq 2.5$. Events were reconstructed using the GSF and two versions of the KF: one which includes corrections for bremsstrahlung, KF(BH); and one



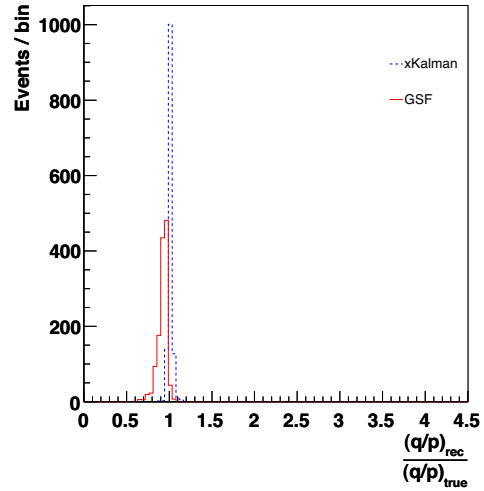
(a) Events with a single true bremsstrahlung radiation carrying away $> 20\%$ of the electron's initial energy.



(b) Events with any number of bremsstrahlung vertices, provided that at one vertex $> 20\%$ of the electron's initial energy is lost.



(c) Events with any number of bremsstrahlung vertices, provided that at one vertex $> 10\%$ of the electron's initial energy is lost.



(d) Events with no bremsstrahlung.

Figure 6.14: Reconstructed momentum distributions for the events identified by the kink finder. In (a), (b) and (c) the track was accepted if an associated reconstructed brem-point was found. In (d) tracks were accepted according to the requirement that there were no true bremsstrahlung vertices on the track. The GSF (red-solid) is compared with xKalman (blue-broken).

Truth criteria	Tracks Reconstructed	Tracks with Kink	ϵ_{id}	Kinks Found	Kinks matched to Truth	ϵ_{assoc}
Single brem > 20%	774	288	0.37	321	231	0.72
All brem > 20%	8010	3670	0.46	4313	3742	0.87
All brem > 10%	9667	3874	0.40	4529	3922	0.87
No brem	835	8	0.01	8	N/A	N/A
All events	12506	3933	(0.31)	4588	3950	0.86

Table 6.8: Results from the brem-point algorithm for a sample of 15,000 single electrons with momentum 20 GeV/c .

which only considers ionising energy losses KF(BB).

Figure 6.15 shows the effective 1σ and 2σ momentum resolution as a function of p_T . The numerical quantities are provided in table 6.9. At 1σ , the mode of the GSF state provides the best estimate of the momentum, while at 2σ , the optimal resolution is obtained using either the mean of the GSF state or the KF(BH). The KF(BB) is consistently the worst performing fitter. The GSF is \mathcal{O} 100 times slower than either KF in all cases.

To develop a more complete understanding of the GSF, it is necessary to test its capabilities under more realistic conditions. The performance of the GSF in the 2004 test-beam is discussed in chapter 7. In parallel, the GSF should be applied in physics analyses where it is likely to provide benefit. Some preliminary studies are presented in chapter 8.

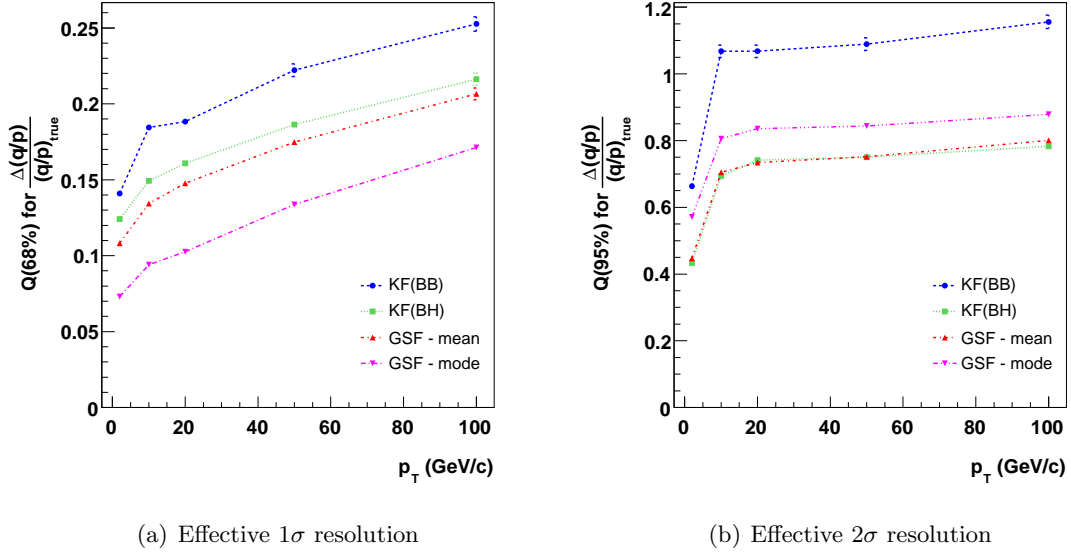


Figure 6.15: The effective momentum resolution as a function of p_T . The mean and mode estimates from the GSF are compared to a KF with corrections for radiative energy loss, KF(BH) and a KF which only considers ionising energy losses, KF(BB).

p_T		GSF mode	GSF mean	KF(BH)	KF(BB)
2 GeV/c	1σ	0.073 ± 0.001	0.108 ± 0.002	0.124 ± 0.002	0.141 ± 0.003
	2σ	0.571 ± 0.010	0.447 ± 0.008	0.433 ± 0.008	0.663 ± 0.011
	$\langle \text{sec/event} \rangle$	0.538	0.538	0.004	0.004
10 GeV/c	1σ	0.094 ± 0.002	0.134 ± 0.003	0.149 ± 0.003	0.184 ± 0.004
	2σ	0.806 ± 0.014	0.705 ± 0.012	0.694 ± 0.011	1.07 ± 0.02
	$\langle \text{sec/event} \rangle$	0.598	0.598	0.007	0.007
20 GeV/c	1σ	0.103 ± 0.002	0.148 ± 0.003	0.161 ± 0.003	0.188 ± 0.004
	2σ	0.836 ± 0.014	0.735 ± 0.012	0.741 ± 0.013	1.07 ± 0.02
	$\langle \text{sec/event} \rangle$	0.601	0.601	0.008	0.008
50 GeV/c	1σ	0.134 ± 0.003	0.175 ± 0.003	0.186 ± 0.003	0.222 ± 0.004
	2σ	0.844 ± 0.015	0.752 ± 0.013	0.750 ± 0.013	1.09 ± 0.02
	$\langle \text{sec/event} \rangle$	0.603	0.603	0.010	0.010
100 GeV/c	1σ	0.171 ± 0.003	0.207 ± 0.004	0.216 ± 0.004	0.253 ± 0.005
	2σ	0.879 ± 0.015	0.801 ± 0.014	0.783 ± 0.013	1.16 ± 0.02
	$\langle \text{sec/event} \rangle$	0.627	0.627	0.011	0.011

Table 6.9: Single electron performance in p_T .

Chapter 7

The ATLAS 2004 Test Beam

7.1 Overview

A monte-carlo based validation of complex algorithms such as the gaussian-sum filter (chapter 6) does not automatically guarantee performance in a real experiment, where misalignment, mis-calibration and uncertainties in the material distribution will all systematically deteriorate the quality of track reconstruction. During the development and construction of ATLAS, a large number of experimental tests of the detector subsystems have been performed. These were used to determine the detector response and to tune the detector simulation.

The response of the detector is best determined in the controlled environment of a *test-beam*. Detector elements are placed into a beam of known momentum and particle composition. All recent ATLAS test-beams have utilised beams extracted from the CERN Super Proton Synchrotron (SPS). The SPS was closed at the end of 2004 in preparation for LHC start-up. The 2004 test-beam was the final attempt, before the commissioning of ATLAS, to determine experimentally the detector response.

The 2004 test-beam used detector elements from all the ATLAS subsystems. They were arranged in a configuration resembling a slice through the ATLAS barrel. For the first time ever, data was recorded simultaneously from all subsystems.

The test-beam data was used to assess the performance of a number of algorithms intended for use in the ATLAS experiment. These included:

- Combined reconstruction of tracks using all the inner detector subsystems.
- Combined electron identification algorithms using data from both the inner detector and calorimeters.

- Combined muon reconstruction using both the inner detector and muon tracker.
- Electron/pion separation studies.
- Alignment algorithms for the inner tracker and muon detector.
- Calibration algorithms for the drift chambers and calorimeters.
- Reconstruction of photon conversions in the inner detector.

The 2004 test-beam is generally referred to as the *Combined Test-Beam* (CTB) since it was the first opportunity to exercise the combined data acquisition, reconstruction and particle identification algorithms listed above.

This chapter begins with a brief description of the beam-line used for the CTB (section 7.2). This is followed by an overview of the CTB layout, with an emphasis on the inner detector (section 7.3). Thirdly, a discussion of the implementation of the CTB tracking geometry is given (section 7.4). The tracking geometry provides a simplified description of the material distribution within the detector, allowing corrections for material interactions to be incorporated during track fitting. The performance of track fitting with and without the tracking geometry is quantified. Electron reconstruction performance using the GSF is then considered in detail and a comparison is made between simulation and real data (section 7.5). The momentum resolution obtained from the real data is much worse than predicted in the simulation. The material in the beam-line, upstream of the active elements, is one of two contributing factors to this discrepancy. The amount of material in the beam-line is deduced through examination of the bremsstrahlung tails in the electron momentum distributions (section 7.6). The impact of the additional beam-line material on the performance of the GSF is then considered and a final comparison is made between improved simulation - containing the appropriate upstream material distribution - and the real data (section 7.8).

7.2 The H8 Beam-Line

The CTB utilised the *H8 beam-line* [52] at the CERN North Experimental Area. Protons with momentum $450 \text{ GeV}/c$ are produced by the Super Proton Synchrotron (SPS). The primary beam is incident on a 30 cm long Beryllium target (known as the T_4 target). The typical beam intensity on the target is a few 10^{12} protons per burst. Protons initiate hadronic showers in the target, producing secondary protons, pions, electrons and their corresponding anti-particles¹. Muons are produced as a decay product of the pions. Figure 7.1 shows the particle production rates per proton on target.

¹For convenience, unless explicitly stated, both electrons and positrons are referred to as electrons.

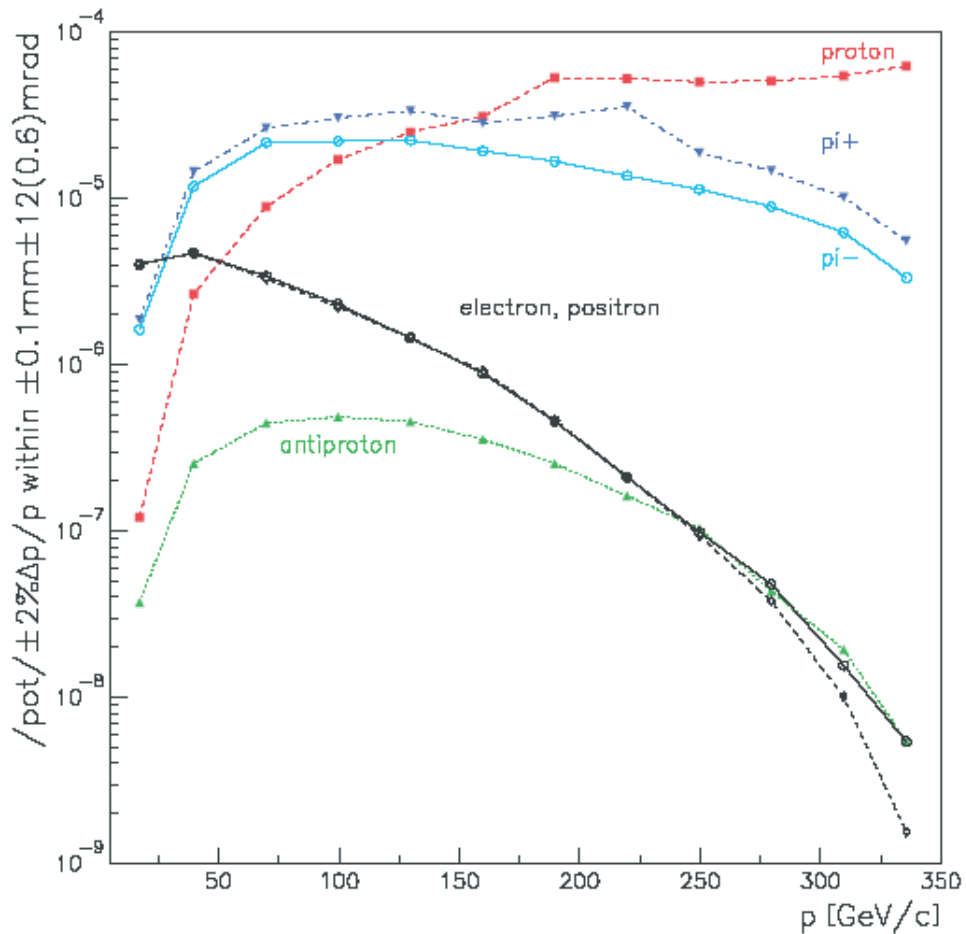


Figure 7.1: Particle production rates, at the T4 target, per incident proton (from Geant 3 simulation). The production rate is calculated inside the required geometric acceptance: the outgoing particles are within ± 1 mm of the incident particle in both the horizontal and vertical directions. Additionally the beam divergence in the *horizontal* (*vertical*) direction is constrained within 12 (0.6) mrad.

H8 is one of three secondary beams extracted from the T4 target. Figure 7.2 shows the layout of the H8 beam-line from the target to the CTB detector elements. With the secondary (T48) target removed, a beam with momentum 10 to 300 GeV/c can be produced. This setup is labelled the *high energy* (HE) configuration. When the T48 target is used, a beam can be produced with momentum 1 to 10 GeV/c; this is the *very low energy* (VLE) configuration. A set of dipole magnets after the T4 target (designated the *lower bend*) deflect charged particles vertically. The polarity of the field determines the polarity of the transported beam. A collimator (C3) is located after the dipole magnets. The vertical position of the collimator defines the momentum of the particles transported to the CTB. The size of the aperture can also be adjusted in the vertical direction, regulating the momentum spread and beam intensity. In the HE configuration, collimators which control the horizontal size of the beam are generally kept open. Closing horizontal collimators simply reduces the particle rate and does not affect

the momentum spectrum of the beam. A second set of dipole magnets (designated the *upper bend*) and another vertical collimator (*C9*) are placed after *C3*. A series of quadrupole magnets, positioned after the dipoles and before the optional T48 target, focus the beam at the experimental area. The dipoles and quadrupoles after the secondary target and the *C12* collimator are used if T48 is in the beam-line, or to select/veto muons. A series of vacuum chambers is located between the main quadrupoles and the beam instrumentation of the CTB.

7.2.1 The Filter Target

The filter target can be optionally inserted into the H8 beam-line between the lower bend dipoles and the *C3* collimator. It is used to provide ‘pure’ electron or hadron beams. One of three targets can be used as the filter:

- 8 *mm* lead: A comparatively short lead target initiates only electromagnetic cascades. As a result, most hadrons pass through the target without energy loss. In contrast, almost all electrons, incident on the lead, produce a cascade. The momentum spectrum of the cascade particles is continuous with a cut-off *at* the momentum of the incident beam. The upper bend and *C9* collimator are configured to select a momentum below that of the incident beam, thus accepting electrons produced in the filter target and collimating the hadrons. Electrons produced by electromagnetic cascades therefore comprise the filtered beam. The 8 *mm* lead target is used when a ‘pure’ electron beam is required.
- 18 *mm* lead: A hadron incident on the longer lead target has a greater chance of producing a hadronic cascade. This cascade has both an electromagnetic and a hadronic component, contributing hadrons and electrons to the filtered beam. Electrons incident upon this target will, as before, produce electromagnetic cascades.
- 1000 *mm* polyethylene: When the polyethylene target is used, the spectrum of electrons from electromagnetic cascades has a cut-off *below* the momentum of the incident beam. While some hadrons shower in the target, most still pass through without interaction. Therefore, the polyethylene target is used to produce a ‘pure’ hadron beam at the incident beam momentum. The upper bend and *C9* collimator are configured to select the same beam momentum as the *C3* collimator. Since all the electrons in the beam are less energetic than the pions, they are collimated.

Figure 7.3 shows the production rate of electrons (within geometric acceptance), from electromagnetic showers in the filter target. Figure 7.4 shows the production of electrons and hadrons for different target types and incident hadrons (pions and protons) of momentum 180 *GeV/c*.

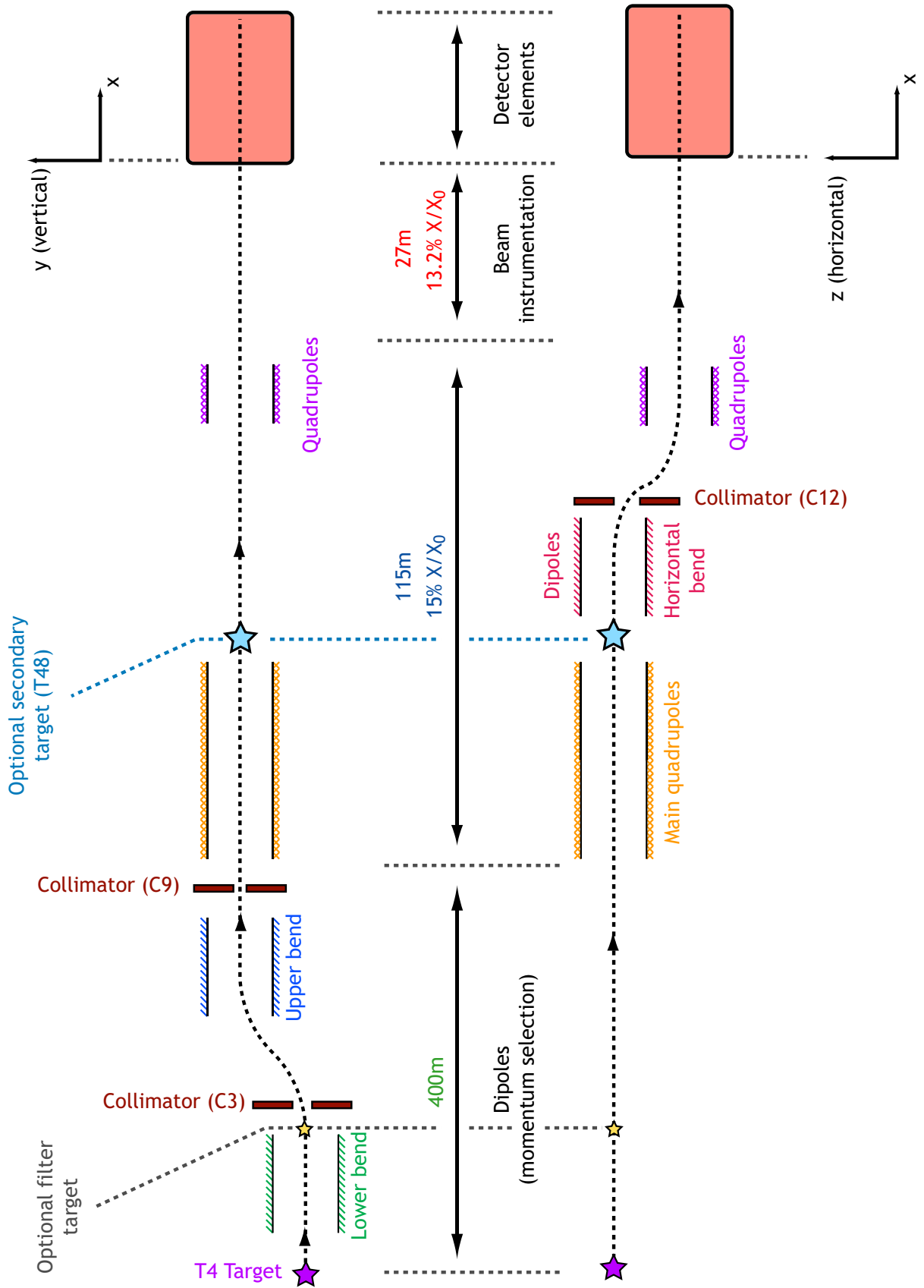


Figure 7.2: Layout of the H8 beam-line (not to scale).

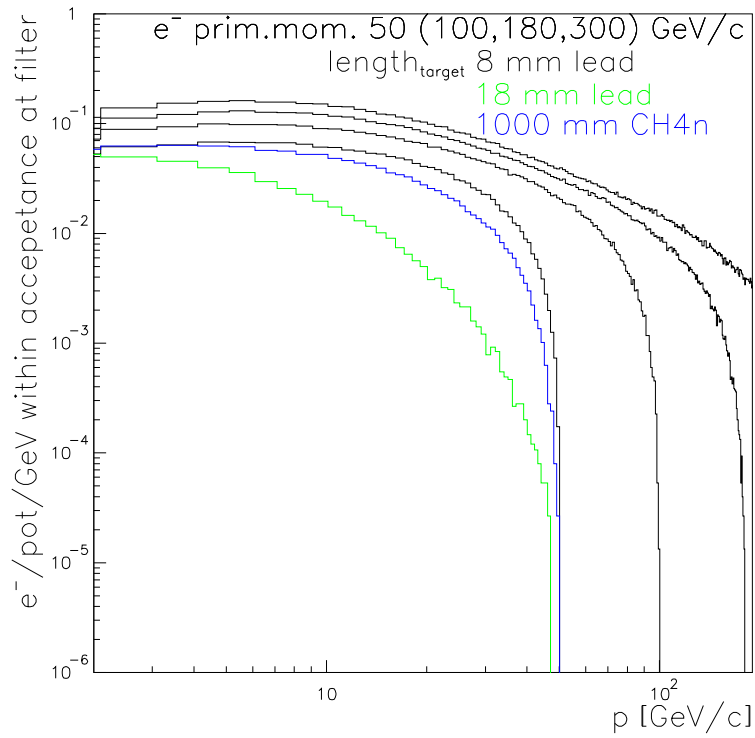


Figure 7.3: Electron production rate (simulation), arising from electromagnetic cascades in the filter target. The yield from an incident beam of 50 GeV/c electrons is shown for the 8 mm lead target (black), 16 mm lead target (blue) and the 1000 mm polyethylene target (green). The momentum distributions of the filtered beam from the lead targets exhibit a cut-off at the incident beam momentum, while the cut-off from the polyethylene target is clearly lower. Similar results are shown for 100 GeV/c, 180 GeV/c and 300 GeV/c secondary electrons incident on the 8 mm lead target.

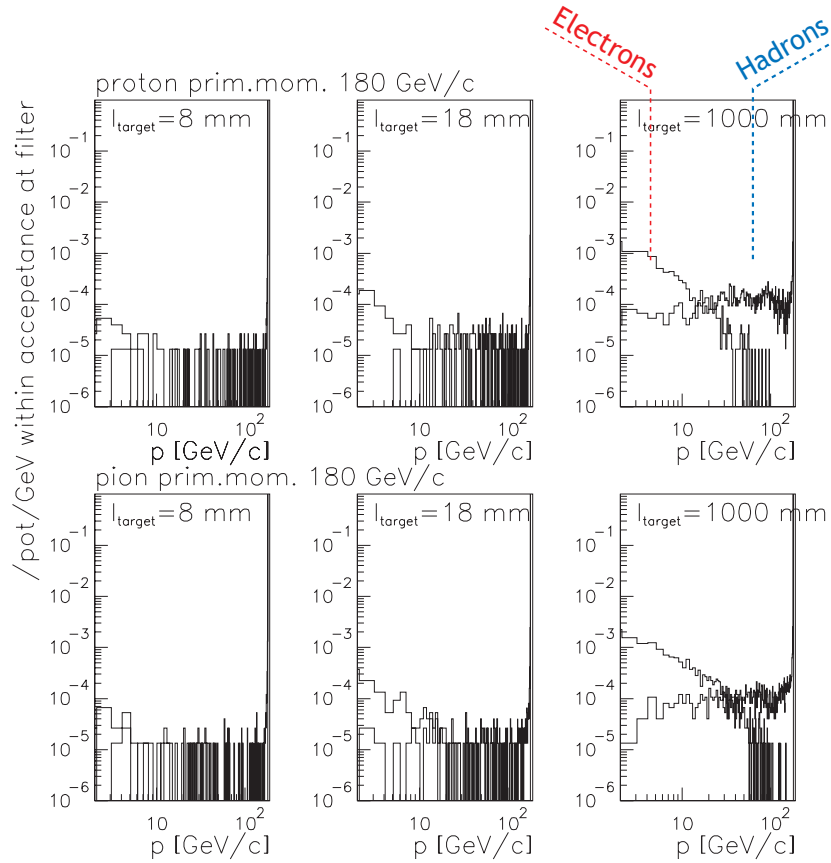


Figure 7.4: Particle flux from the filter target (simulation). Momentum distributions have been obtained for all three filter targets using beams of $180 \text{ GeV}/c$ hadrons. The yield is approximately the same regardless of whether the incident particle is a proton (upper plots) or a pion (lower plots). The yield is about three orders of magnitude less than from electromagnetic cascades. The majority of the hadrons traverse all targets without interaction, hence a large hadronic peak is evident at $180 \text{ GeV}/c$. Those that do shower produce both hadrons and electrons. On average, the cascade hadrons are more energetic than the electrons.

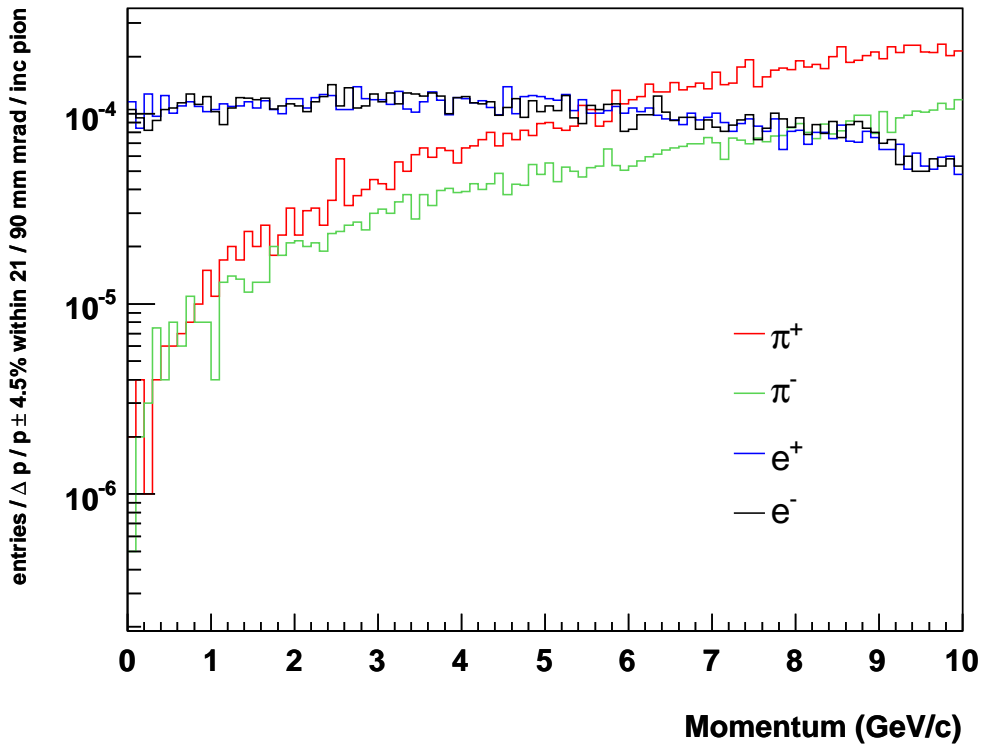


Figure 7.5: Lepton and hadron production rates (simulation), from the T48 target, per incident pion and within geometric acceptance. Pions with momentum $40 \text{ GeV}/c$ are incident on a polyethylene target of thicknesses 100 cm .

7.2.2 The T48 Target

Using the HE configuration, the yield of particles with momenta $< 10 \text{ GeV}/c$ is small. However, the VLE setup can produce beams with momentum down to $1 \text{ GeV}/c$. The VLE configuration requires the insertion of the T48 target into the beam-line. A set of dipoles (designated the *horizontal bend*) deflect the beam from the T48 target in the horizontal direction. The C12 collimator, located approximately 40 m upstream of the CTB detector elements, is used to select the required momentum. A set of quadrupole magnets then focuses the VLE beam at the experimental area.

Typically, a pion beam of momentum 40 to $80 \text{ GeV}/c$ is transported from the T4 target to T48. No filter target is generally used in the VLE beam-line configuration. The comparatively high momentum of the secondary beam helps reduce the muon background, which, due to the kinematics of the pion decay, has a minimum momentum of $\sim 20 \text{ GeV}/c$. The T48 target can be chosen to be either lead, copper or polyethylene. For most of the VLE period, a 1000 mm polyethylene target was used. Figure 7.5 shows the lepton and hadron production rates for $40 \text{ GeV}/c$ pions incident on the polyethylene target at T48.

7.2.3 Beam Spread

The momentum spread for a filtered beam is defined by the opening size of the C3 and C9 collimators. Both collimators have a maximum opening size of 45 *mm*. The fractional uncertainty on the beam momentum is given by:

$$\frac{\Delta p}{p} = \frac{1}{\sqrt{12}} \frac{\sqrt{c_3^2 + c_9^2}}{27} \%, \quad (7.1)$$

where c_3 and c_9 are the **full width** openings of the collimators. The constant, 27 *mm*/%, is the vertical momentum dispersion of the beam at C9 compared to C3. Typical collimator openings for the filtered beam are $c_3 = 45$ *mm*, $c_9 = 15$ *mm*. This gives a momentum spread, $\Delta p/p = 0.51\%$.

In the case of an unfiltered beam, the typical opening size of C3 is $c_3 = 15$ *mm*. Collimator C9 is generally left open. In this case, the beam image is considerably smaller than $c_9 = 45$ *mm* and the rule of thumb is to replace c_9 with 20 *mm*, the approximate size of the beam image. This gives a momentum spread, $\Delta p/p = 0.26\%$.

The opening width of the C12 collimator determines the momentum spread of the VLE beam, which is nominally $\sim 0.32\%$.

The beam spread is further regulated by the quadrupole magnets. The field settings are optimised so that only particles at the specified momentum are focused at the experimental area. Particles with significantly different momenta will not be correctly focused and so may not be accepted by the experimental trigger.

7.2.4 Beam Composition

The composition of the beam can be varied by changing the configuration of the beam-line. The procedure for particle selection is different for the HE and VLE beams.

- **HE electron beam:** Separation of electrons from hadrons is achieved by using a short (8 *mm* lead) filter target. Additional pion rejection is possible by exploiting the synchrotron radiation of the electrons in the upper bend, followed by collimation of the hadrons. For example, suppose collimator C3 is set to select 200 *GeV/c* particles. The magnetic field in the upper bend causes electrons to lose energy due to synchrotron radiation, changing their radius of curvature. For particles with initial momentum 200 *GeV/c*, the mean separation between the electrons and hadrons/muons at the C9 collimator is 16 *mm*. The C9 collimator is set to select a beam momentum below

200 GeV/c . In reality, the HE electron beam contains some hadronic and muonic contamination. The beam profile is characterised by electrons in the central region with a halo of pions and muons.

- **HE hadron beam:** The 1000 mm polyethylene filter target removes electrons while transporting pions at the desired momentum. Furthermore, as with the HE electron beam, synchrotron radiation is used to separate the electrons from the hadrons. The upper bend creates a physical separation between hadrons and electrons and, in this case, the C9 collimator selects the hadrons. Additionally, absorbers (4, 8 and 16 mm of lead) can be placed in the beam-line to remove electrons. Muon contamination of the beam arises from pion decay. This contamination is quite small at high energies. Any muons in the beam can be removed by using the horizontal bend with the C12 collimator and/or by using a veto either in the trigger or offline.
- **HE muon beam:** Muons are derived from a filtered hadron beam through the decay of charged pions. The muon momentum is selected by the horizontal bend and the C12 collimator. Since the muon momentum is always less than that of the hadron beam, C12 collimates the hadrons.
- **VLE beams:** The beam extracted from the T48 target is a mixture of electrons and pions. No further beam purification is performed and so the separation of electrons and pions is possible only as part of an offline analysis.

7.3 Layout of the CTB

A more complete description of the layout of the CTB is provided in [53]. Figure 7.6 illustrates the layout of the ATLAS subsystems within the CTB. Cartesian coordinates are used to describe the positions of the detector elements. For consistency with the ATLAS coordinate system, the x -axis is defined horizontally along the nominal beam-line, while the y -axis points vertically to the sky. The front opening of the magnet which encloses the pixels and SCT defines $x = 0$. Positive x points downstream. A particle in the CTB, moving downstream along the x -axis ($y = 0, z = 0$), has a direction ($\varphi = 0, \eta = 0$) in the ATLAS convention.

7.3.1 The Inner Detector

As with ATLAS, the CTB version of the inner detector comprises pixel, SCT and TRT detector elements. The pixels and SCT were placed inside a 1 m long dipole magnet (the TRT is far too big to fit inside), which provides an approximately constant field of $B_z = 1.4$

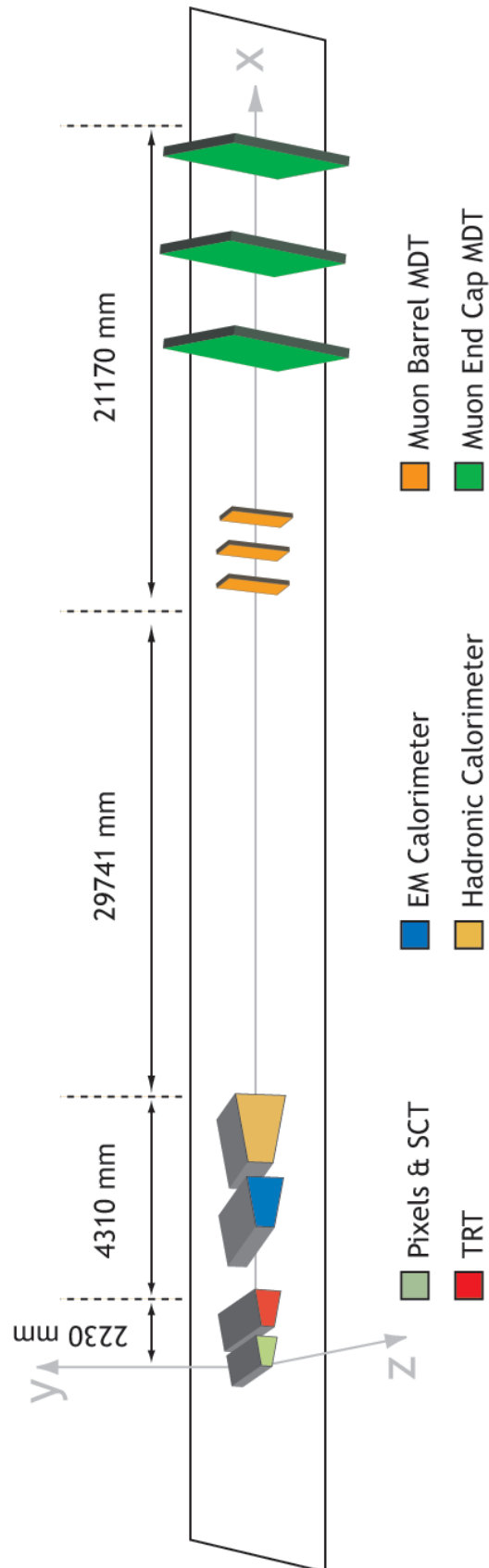


Figure 7.6: Layout of the CTB (not to scale).

T at -850 A. For most of the data taking period, the magnet current was -850 A, although a few runs were taken at other settings. The size of the magnet aperture is $dz = 230$ mm.

Figure 7.7 illustrates the layout of the inner detector elements within the CTB. The configuration of the detector elements changed many times during the CTB. All data considered in this analysis was taken using the same tracker layout. Other configurations are not described.

The Pixel Detector

The pixel detector comprises six modules arranged in three layers. Each pixel module has an active area of $y \times z = 16.4 \times 60.8$ mm². Each module is tilted by an angle of 20° around the z -axis. The pixels are enclosed by an aluminium box with dimensions $dx \times dy \times dz = 175 \times 250 \times 180$ mm³. Mylar windows at the front and back of the box reduce the amount of inert material in the beam-line. The three pixel layers were positioned at $x = \{196.5, 233.3, 268.0\}$ mm.

The SCT

As in the ATLAS barrel, the SCT modules are arrayed in four layers. Two outer end-cap modules are used per layer². Each module is trapezoidal with an active area of $y \times z = 60 \times 120$ mm². The two detectors in the same layer overlap by 4 mm in the y -direction. The four SCT layers are enclosed in an aluminium box, with mylar windows and dimensions $dx \times dy \times dz = 300 \times 300 \times 200$ mm³. During data taking, the front side of the lower silicon module in the third SCT layer was not operational. The layers were positioned along the beam-line at $x = \{381.4, 452.9, 524.9, 595.0\}$ mm.

The TRT

The barrel of the TRT is comprised of 32 wedges. They form a hollow tube with inner radius 558 mm and outer radius 1080 mm. The length of the cylinder is 1425.5 mm. Two TRT wedges were placed behind the SCT in the test-beam setup. The magnet aperture is far too small for the TRT to fit and so the gap between the SCT and TRT was enlarged. In ATLAS there is a 40 mm space between the final SCT plane and the first TRT straws; in the CTB the separation is ~ 1114 mm.

²Production constraints prevented the use of barrel SCT modules in the CTB.

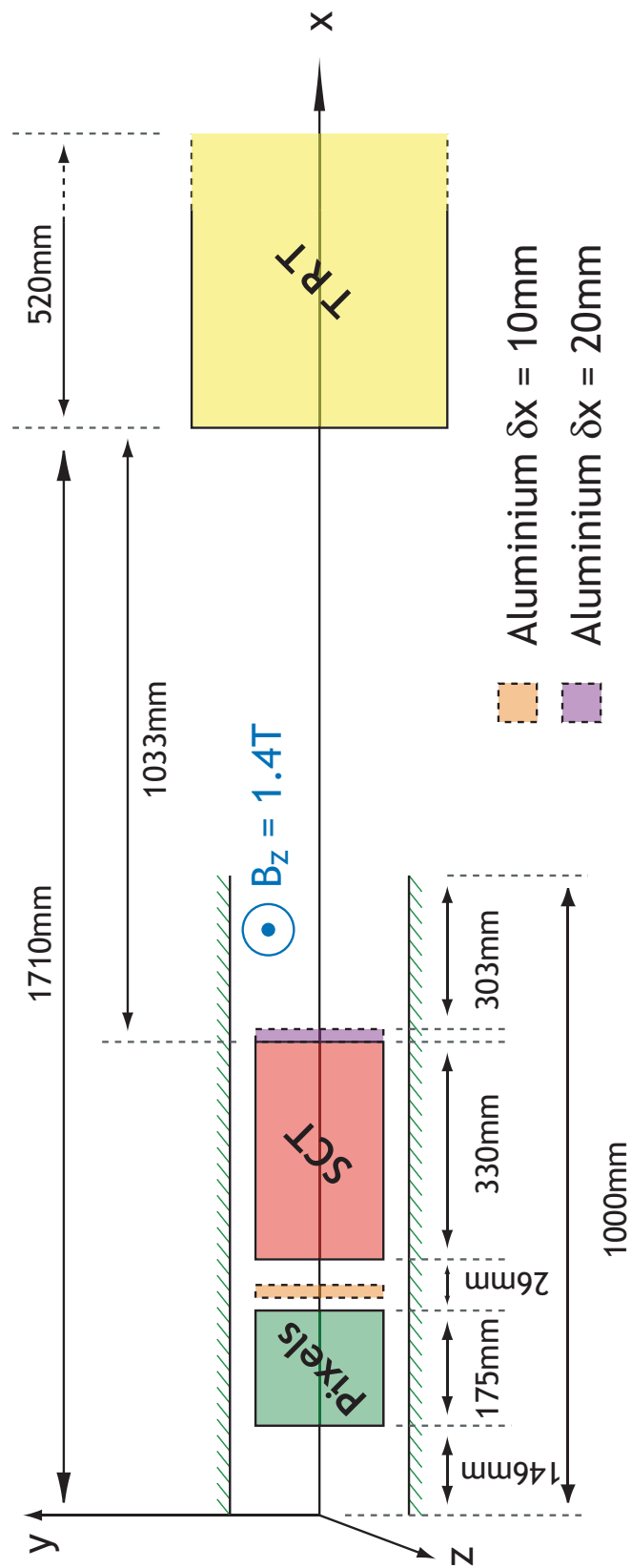


Figure 7.7: Layout of the inner detector elements within the CTB.

Inner Detector Material

The distribution of material within the CTB inner detector was carefully measured and incorporated into the simulation. The total amount of material is roughly equivalent to that of the central barrel region of the ATLAS inner detector. The amount of material in the ATLAS tracker increases significantly at higher values of η (figure 3.2, page 31). To reproduce the maximal amount of material in the full tracker ($1.3 x/x_0$ at $\eta \sim 1.7$), an aluminium block of thickness $dx = 10 \text{ mm}$ ($dx = 20 \text{ mm}$) was placed between the pixel and SCT (SCT and TRT) elements of the CTB for some runs. Each aluminium block has an area $dy \times dz = 200 \times 200 \text{ mm}^2$.

7.3.2 The Calorimeters

A single module of the barrel electromagnetic calorimeter is used, along with three tile calorimeter modules. All detector elements were placed on a common support that could rotate and translate so that a particular η region could be illuminated by the beam. The centre of the support is at $x = 6208 \text{ mm}$. The separation between the back of the TRT and the front of the presampler is $\sim 1800 \text{ mm}$, significantly larger than the separation in ATLAS. The electromagnetic calorimeter is enclosed within a cryostat to cool the liquid argon. The extremities of the cryostat are $x : [3293, 4568] \text{ mm}$. There is a 30 mm gap between the cryostat and the tile calorimeter. The extremities of the tile calorimeter are $x : [4598, 6540] \text{ mm}$.

7.3.3 The Muon Detectors

One outer barrel RPC station (BOS) was placed at $x = 12587 \text{ mm}$. Barrel inner, middle and outer drift chambers (MDTs) were placed at $x = \{34339, 36402, 38685\} \text{ mm}$. These were followed by end-cap inner, middle and outer MDTs at $x = \{40996, 47409, 55509\} \text{ mm}$.

7.3.4 Beam-line Elements

There are a number of beam-line elements, but only those providing a trigger for the CTB or used in offline analysis are discussed. Figure 7.8 shows the position of the important beam-line elements relative to the inner detector magnet.

A 1000 mm long Cerenkov counter was placed at $x : [-18677, -17677] \text{ mm}$. This provides electron/pion separation at low momentum. A scintillator (designated *A*) was placed at $x = -8843 \text{ mm}$. The scintillator has a thickness $dx = 6 \text{ mm}$ and an active area of $dy \times dz =$

$100 \times 100 \text{ mm}^2$. A second scintillator (designated *B*) was placed at $x = -7523 \text{ mm}$. This scintillator has a thickness $dx = 10 \text{ mm}$ and an active area of $dy \times dz = 30 \times 30 \text{ mm}^2$.

The total amount of material (active and inert), downstream of the quadrupoles and before the inner detector, was carefully measured. It amounts to 13.2% of a radiation length.

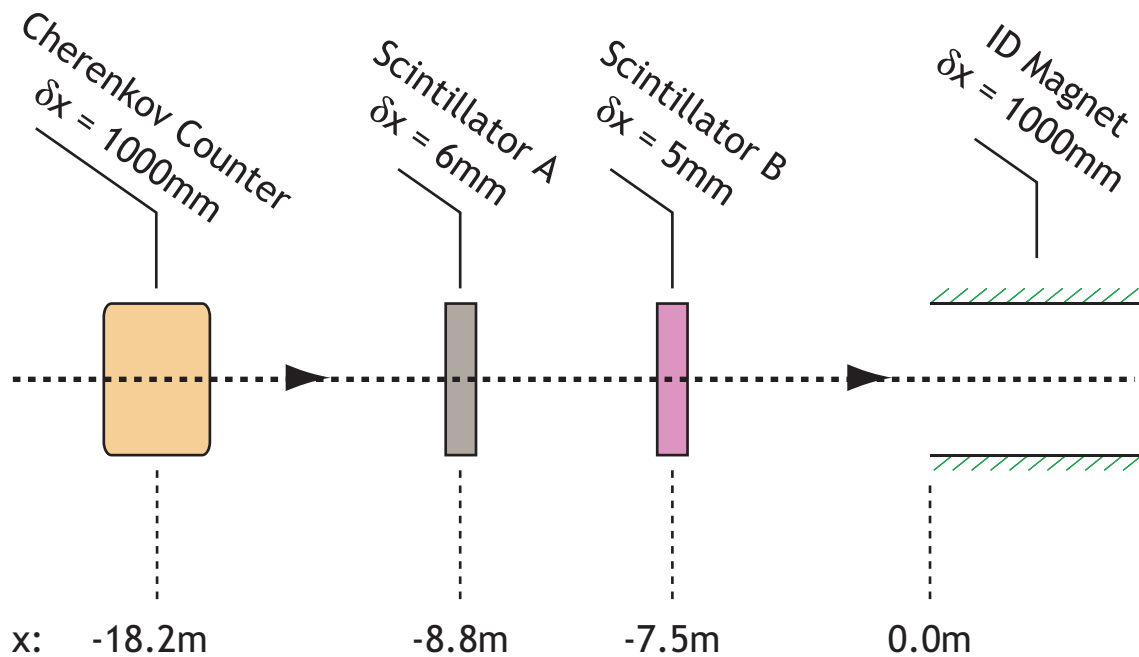


Figure 7.8: Layout of the active elements in the beam-line upstream of the inner detector (not to scale).

7.3.5 Trigger

For the majority of data-taking, the trigger was given by a signal from scintillators A and B in coincidence. For some runs using a VLE beam, scintillator B was physically removed from the beam-line and the trigger was provided by a signal from scintillator A only.

7.4 Tracking Geometry

For a track fitter to incorporate corrections for material interactions, a simplified representation of the material distribution must be provided. A technical discussion of the implementation of the tracking geometry for the CTB inner detector is given in appendix C.

The tracking geometry is a simplification of the material distribution included in the simulation program. In the tracking geometry, the material is distributed on layers, three in the pixels and four in the SCT. The positions of the layers coincide with the locations of

the detector elements. Any inert material is automatically attributed to the nearest layer. The material distribution in the TRT is continuous, however most track fitters include material corrections at discrete points on the track. Therefore, the TRT material distribution is approximated as a series of layers. The number of layers of material in the TRT can be arbitrarily chosen and the algorithm automatically allocates the correct material properties to each layer. The default number of TRT layers is six, and the material properties of all layers are identical. Five numbers characterise the material properties: the layer thickness, x ; the average atomic number, Z ; the average mass number, A ; the density, ρ ; and the radiation length, x_0 . Table 7.1 gives the material properties for each layer of the tracking geometry. A computer-generated image of the material layers is shown in figure 7.9.

7.4.1 Validation of the Tracking Geometry

Simulated single muon events were used to validate the tracking geometry. Samples of 20,000 events have been produced at $p = \{9, 20, 50, 100, 180\} \text{ GeV}/c$. The muons were generated at $x = 0$ with random starting coordinates in the yz plane, reflecting the size of the beam. A flat distribution in $y : [-10, 15] \text{ mm}$ and $z : [-15, 15] \text{ mm}$ was used. No beam divergence was included and importantly, the magnetic field was switched off. In the simulation, a constant field (nominally $B_z = 1.4 \text{ T}$) approximation is used for the inner detector magnet³. The field is applied within the region $x : [0, 1000] \text{ mm}$. The field gradient at $x = 0 \text{ mm}$ and $x = 1000 \text{ mm}$ is therefore not defined. Track fitters use a Runge-Kutta [38] technique for the geometric propagation of the track. The Runge-Kutta propagator requires well defined field derivatives at all points. Therefore, the constant magnetic field approximation introduces an instability during track fitting, resulting in a slight bias in some of the fitted track parameters. Moreover, for muons, the uncertainties on the measured track parameters are dominated by multiple scattering. The effects of multiple scattering are evident in the track parameter distributions, regardless of whether the field is on or off.

Hits, found by an independent pattern recognition algorithm, were fitted using the Kalman filter. The performance of the fitter, with and without corrections for material interactions, has been assessed.

³Field maps of the CTB inner detector magnet are available but had not been successfully integrated into the simulation/reconstruction chain at time of writing.

CTB Material per Layer					
Layer	x (mm)	A	Z	$\rho(g/mm^3)$	$x_0(mm)$
Pixel B	2.34	17.21	8.52	0.0031	91.7
Pixel 1	2.34	16.28	8.10	0.0024	119.4
Pixel 2	2.34	17.97	8.87	0.0031	87.1
SCT 1	1.40	12.92	6.53	0.0033	96.0
SCT 2	1.40	16.56	8.25	0.0026	111.1
SCT 3	1.40	16.56	8.25	0.0026	111.1
SCT 4	1.40	13.28	6.69	0.0041	77.8
TRT (6 layers)	1.00	6.72	3.60	0.0066	59.4

Table 7.1: The material properties of each layer in the CTB tracking geometry. The number of layers used to model the TRT material distribution is, in general, arbitrary. The TRT material properties are given for the default case, in which six layers are used.

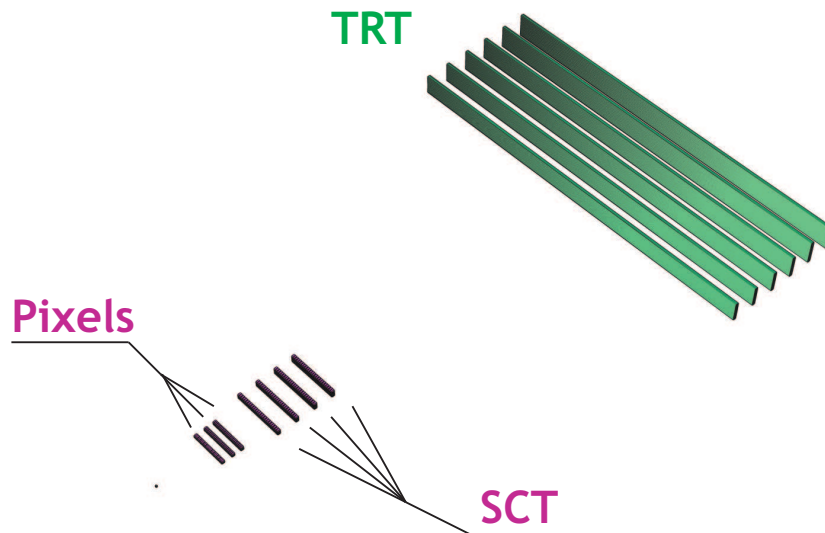


Figure 7.9: A computer generated image of the CTB tracking geometry for the inner detector. There are three pixel and four SCT material layers. The material distribution in the TRT is modelled as six layers.

Detector Pull Quantities

Detector pull distributions are used to validate the tracking geometry independently in each sub-detector. A detector pull quantity is calculated at a measurement surface in the tracker, using the position of a hit and a track. The positions are expressed in the local coordinate frame of the detector element (section 3.3, page 32). A pixel detector provides a two-dimensional measurement ($locX, locY$) while the SCT ($locX$) and TRT ($locR$) measurements are one-dimensional. The detector pull in the $locX$ direction is:

$$pull_{detector}(locX) = \frac{locX_{track} - locX_{measurement}}{\sqrt{\sigma_{track}^2 + \sigma_{measurement}^2}}, \quad (7.2)$$

where σ is the uncertainty on the position. Equivalent expressions exist for $locY$ in the pixels and $locR$ in the TRT. If all measurement and multiple scattering errors are correctly described, then the distribution of detector pulls should be unbiased with RMS = 1.

Figure 7.10 shows the detector pull distributions, both with and without corrections for material interactions, for 9 GeV/c muons. Multiple scattering effects are more pronounced in the $locX$ distributions, since the detector elements have a higher granularity in the $locX$ direction. In the $locY$ direction, the intrinsic detector resolution is the dominant contributor to the uncertainty. Hence, the inclusion of corrections for material interactions is of less benefit. Figure 7.11 shows the mean of the detector pull distributions as a function of beam momentum. All mean values are close to zero. Figures 7.12 and 7.13 show the RMS values as a function of beam momentum. Distributions which include corrections for material interactions have RMS values significantly closer to one. The greatest improvement occurs at low momentum, where multiple scattering has the greatest effect. Even when material interactions are considered, the RMS values of the detector pull distributions are not consistent with one. This is because the material distribution in the tracking geometry is only an approximation of the material distribution in the simulation program.

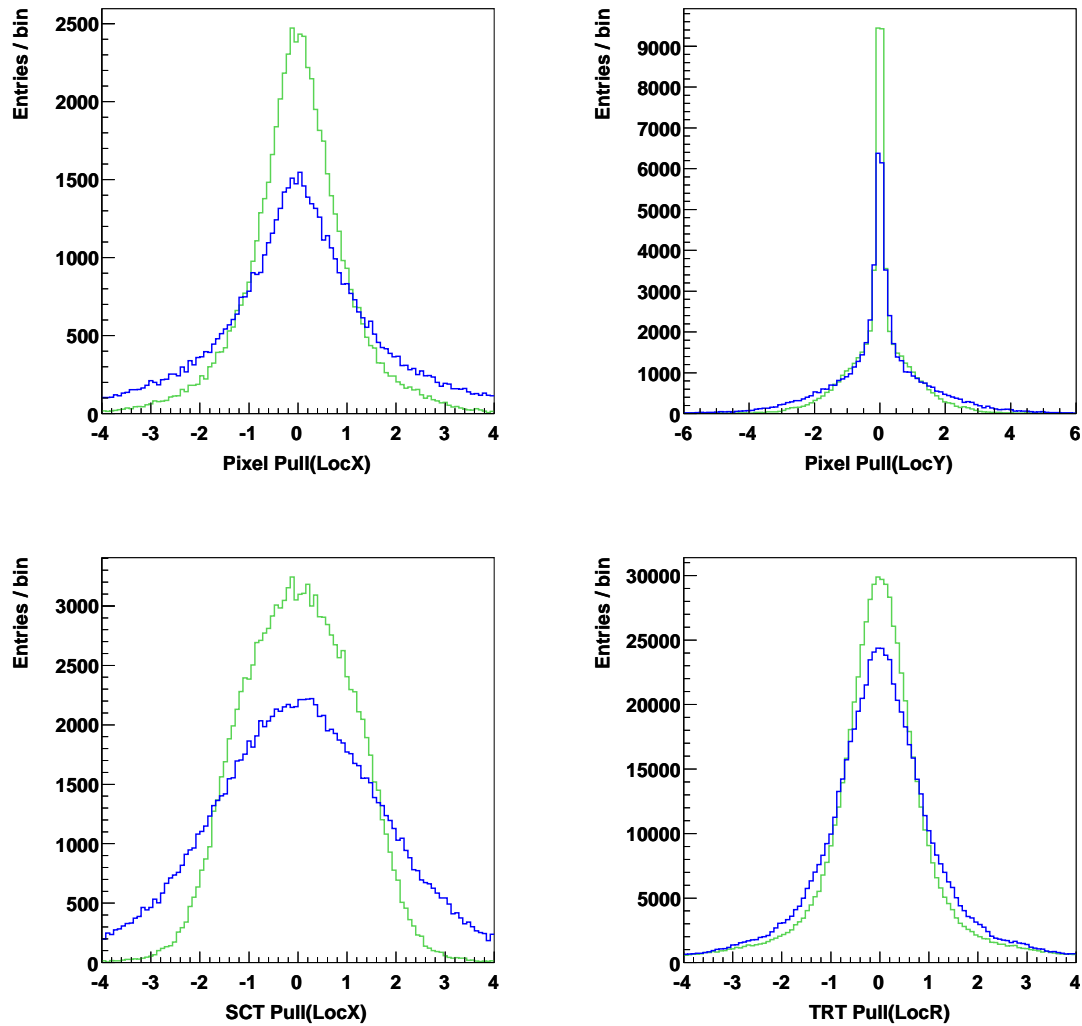
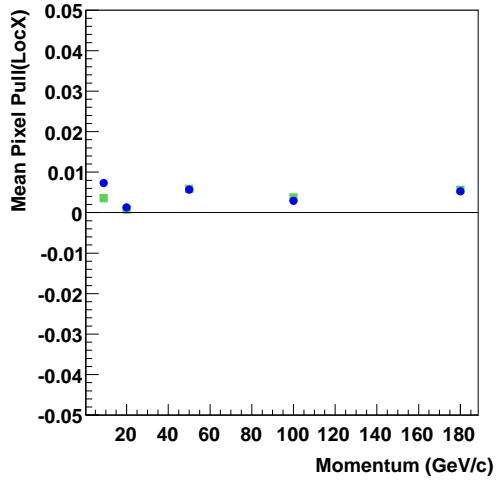
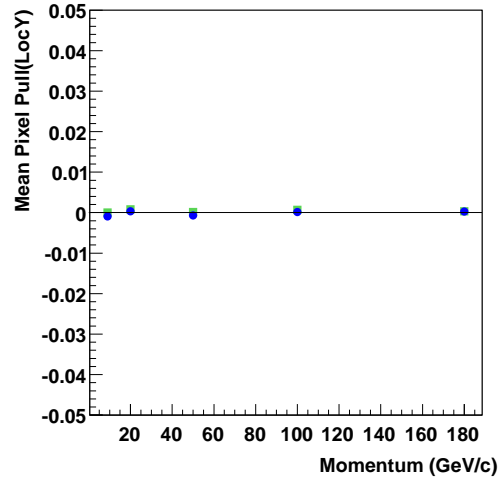


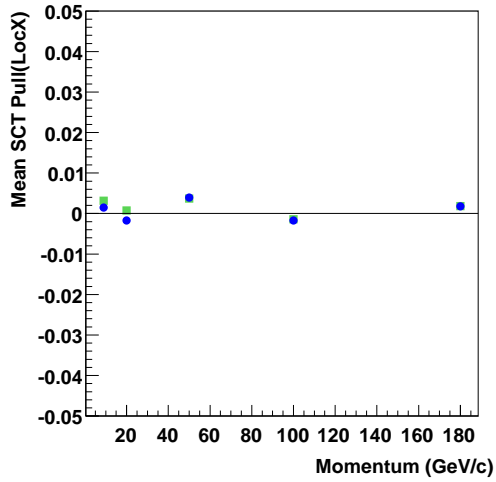
Figure 7.10: Detector pull distributions for reconstructed $9 \text{ GeV}/c$ muons. Results with (without) corrections for multiple scattering are shown in green (blue).



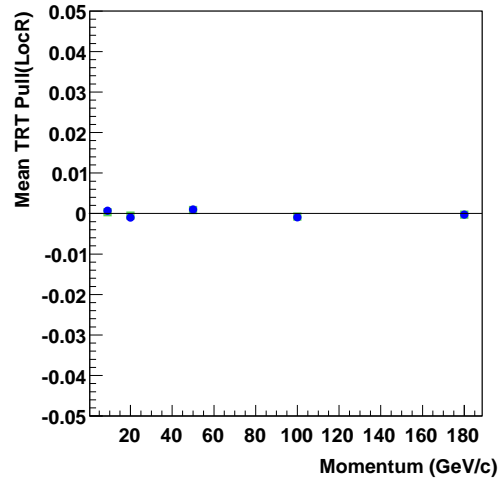
(a) Pixel Pull(LocX) Mean



(b) Pixel Pull(LocY) Mean

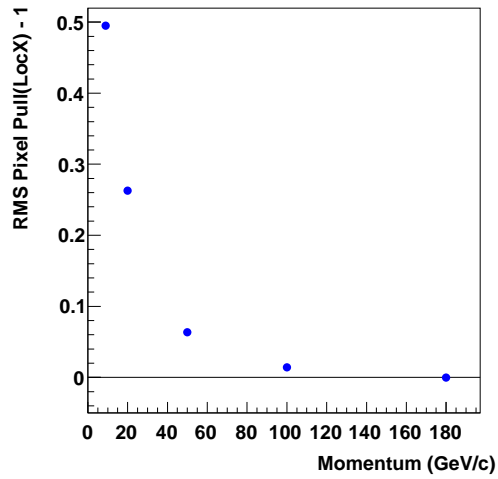


(c) SCT Pull(LocX) Mean

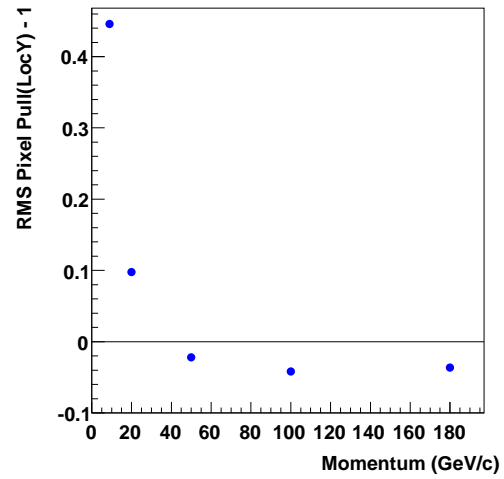


(d) TRT Pull(LocR) Mean

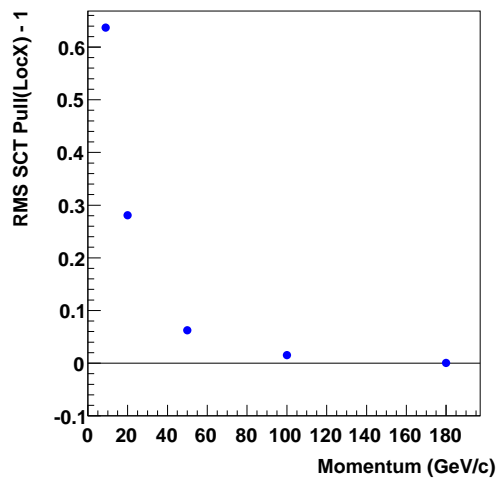
Figure 7.11: The mean values of the detector pull distributions as a function of beam momentum. Results with (without) corrections for multiple scattering are shown as green squares (blue circles). The statistical uncertainty gives error bars which are too small to be seen on this scale.



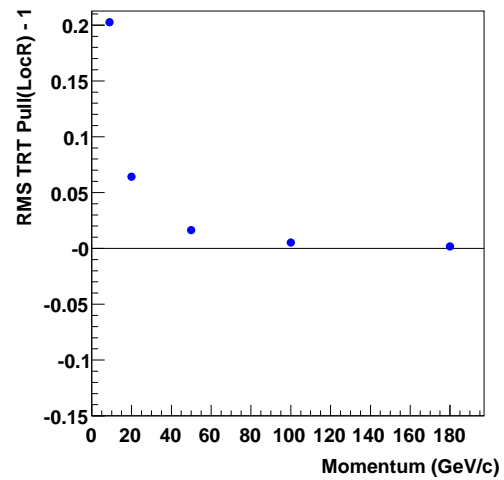
(a) Pixel Pull(LocX) RMS - 1



(b) Pixel Pull(LocY) RMS - 1

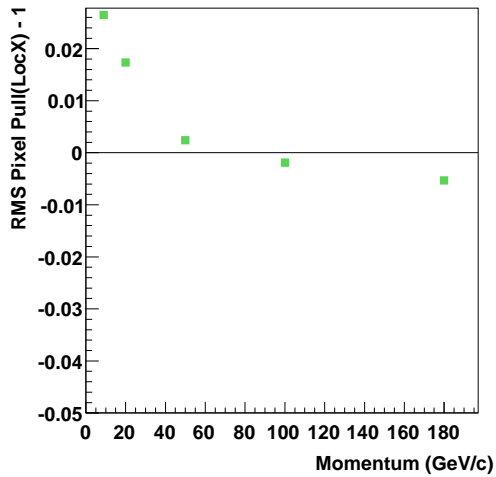


(c) SCT Pull(LocX) RMS - 1

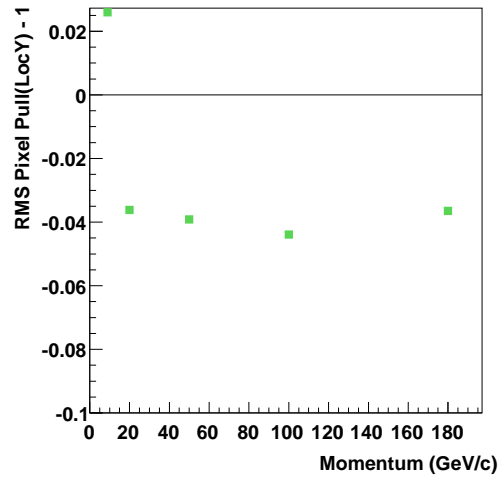


(d) TRT Pull(LocR) RMS - 1

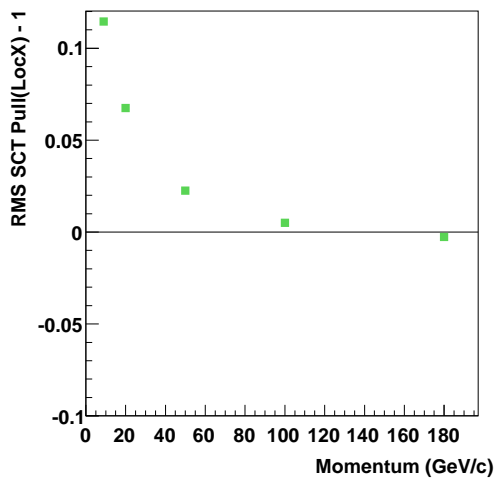
Figure 7.12: The RMS of the detector pull distributions as a function of beam momentum. Results without corrections for multiple scattering are shown in this diagram.



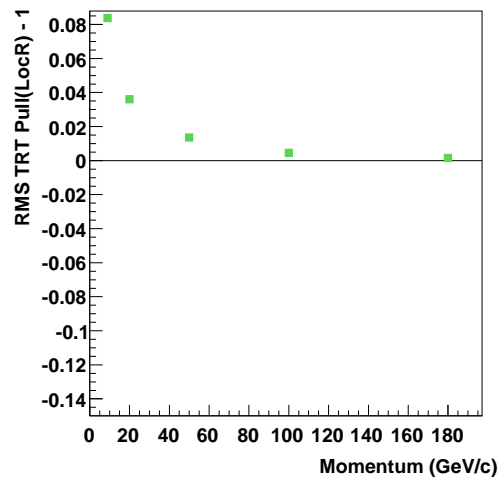
(a) Pixel Pull(LocX) RMS - 1



(b) Pixel Pull(LocY) RMS - 1



(c) SCT Pull(LocX) RMS - 1



(d) TRT Pull(LocR) RMS - 1

Figure 7.13: The RMS of the detector pull distributions as a function of beam momentum. Results including corrections for multiple scattering are shown in this diagram.

Perigee Pull Quantities

When there is no magnetic field, four parameters define the track trajectory, $\mathbf{x} = (d_0, z_0, \varphi_0, \theta)$. The trajectory is expressed at the perigee, the point of closest approach to $(x, y, z) = (0, 0, 0)$. For a measured parameter, x_i , with variance C_{ii} , the pull is (equation 6.1):

$$P_i = \frac{x_i - x_{i,true}}{\sqrt{C_{ii}}}, \quad (7.3)$$

where $x_{i,true}$ is the true value of the parameter.

Figure 7.14 shows the parameter pull distributions, both with and without corrections for material interactions, for 9 GeV/c muons. Multiple scattering has a significant affect on the d_0 and φ_0 distributions. These parameters are correlated with the high resolution axis of the detector elements. Multiple scattering has less impact on the z_0 and θ distributions. These parameters are correlated with the low resolution axis of the detector elements, where the intrinsic detector resolution provides the greatest source of uncertainty. Gaussians have been fitted to all parameter pull distributions. Figure 7.15 shows the mean values of the fits as a function of beam momentum. The mean values of the d_0 and φ_0 distributions are closer to zero when multiple scattering corrections are applied. The proper treatment of multiple scattering does not improve the mean values of the z_0 or θ distributions. Figures 7.16 and 7.17 show the standard deviations of the fits as a function of beam momentum. The standard deviations of the d_0 and φ_0 distributions improve with the inclusion of corrections for multiple scattering, although the results are never exactly consistent with one. A feature of the test-beam reconstruction is the overestimation of errors in the z_0 and θ parameters.

7.5 Electron Reconstruction

The development and validation of the tracking geometry for the CTB inner detector were prerequisites for assessing the performance of dedicated electron fitters such as the GSF. The GSF introduces corrections for radiative energy loss based on the material distribution provided by the tracking geometry.

7.5.1 Simulation

The performance of the GSF was first studied using simulated single electron events. Samples of 20,000 events have been produced at $p = \{2, 9, 20, 50, 100\}$ GeV/c . The electrons were generated at $x = 0$ with flat distributions in $y : [-10, 15]$ mm and $z : [-15, 15]$ mm . A

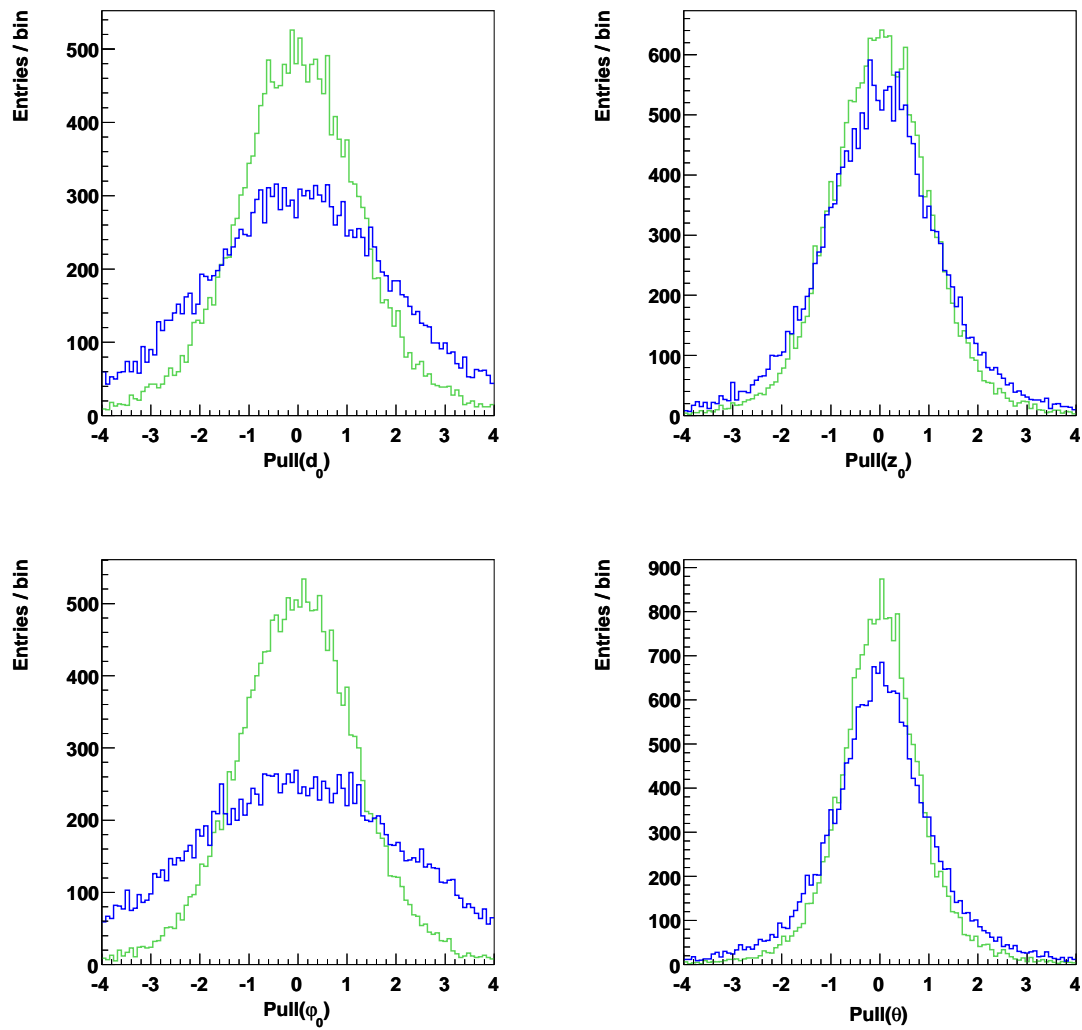


Figure 7.14: Parameter pull distributions for reconstructed 9 GeV/c muons. Results with (without) corrections for multiple scattering are shown in green (blue).

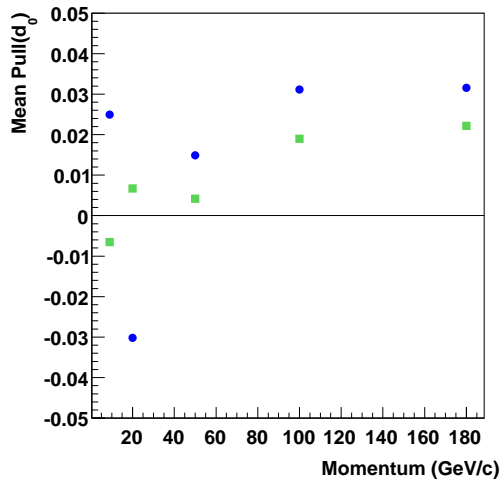
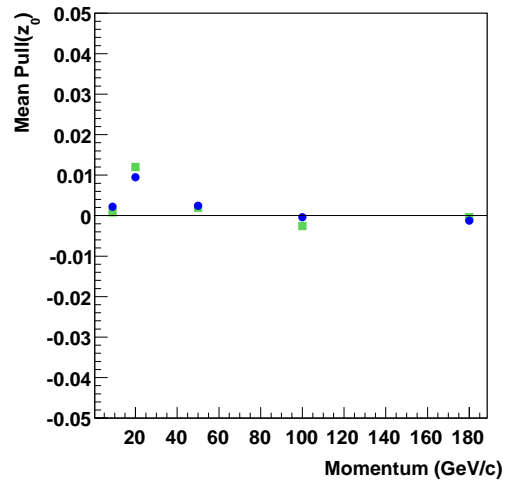
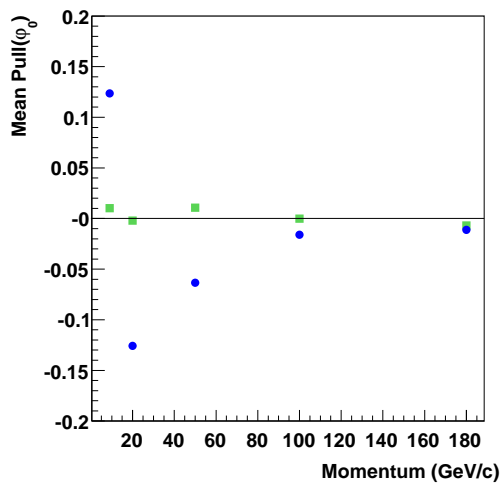
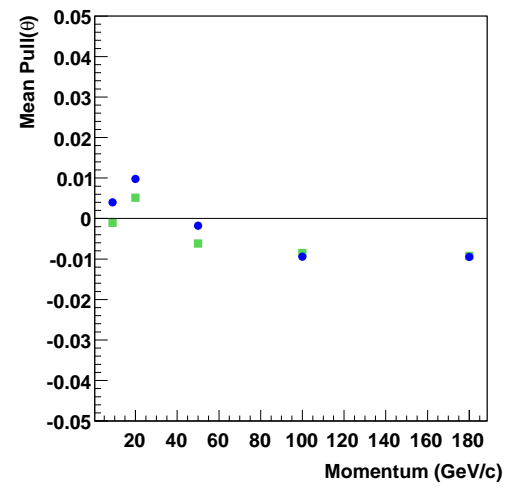
(a) Pull d_0 Mean(b) Pull z_0 Mean(c) Pull φ_0 Mean(d) Pull θ Mean

Figure 7.15: The mean values of the gaussian fits to the parameter pull distributions as a function of beam momentum. Results with (without) corrections for multiple scattering are shown as green squares (blue circles). The statistical uncertainty gives error bars which are too small to be seen on this scale.

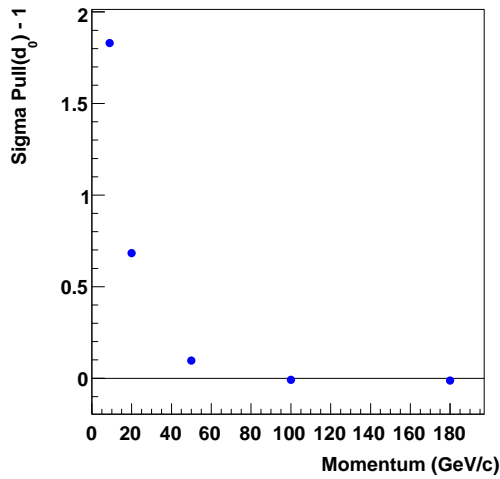
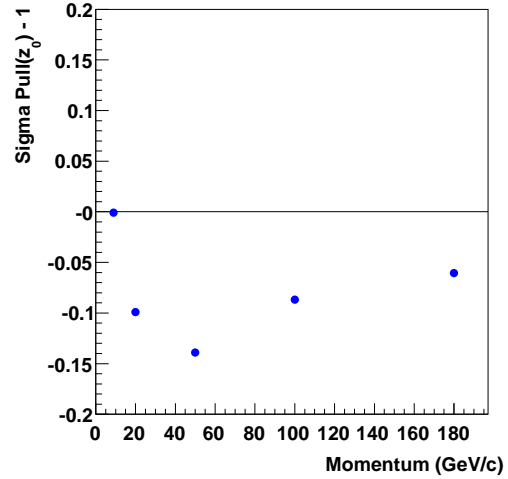
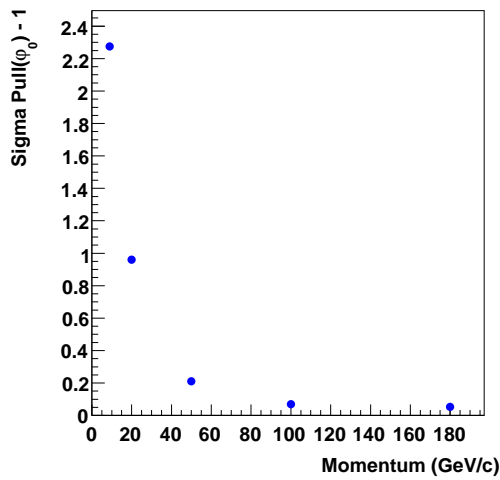
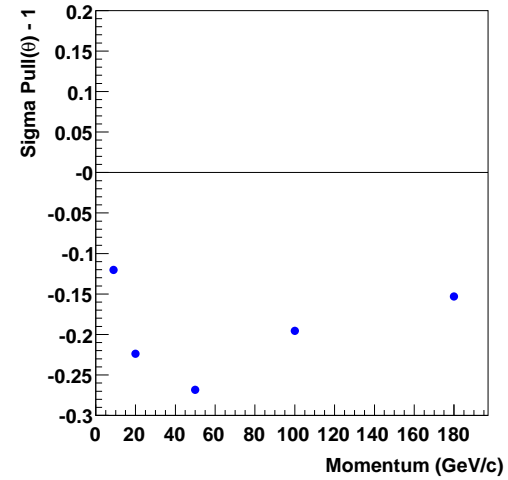
(a) $\sigma(\text{Pull } d_0) - 1$ (b) $\sigma(\text{Pull } z_0) - 1$ (c) $\sigma(\text{Pull } \varphi_0) - 1$ (d) $\sigma(\text{Pull } \theta) - 1$

Figure 7.16: The standard deviations, σ , of the gaussian fits to the parameter pull distributions as a function of beam momentum. Results without corrections for multiple scattering are shown in this diagram.

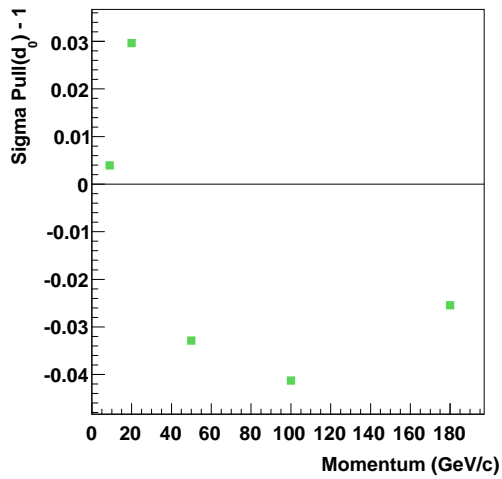
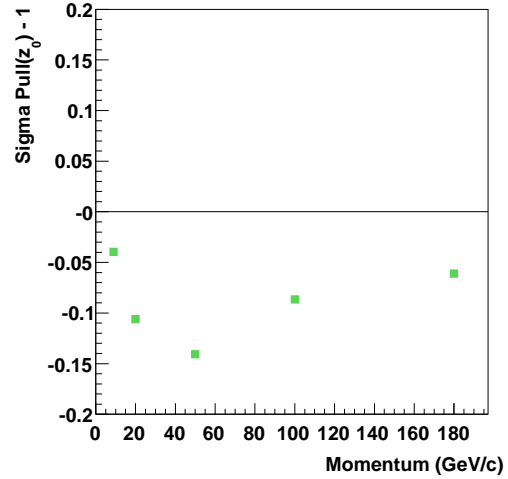
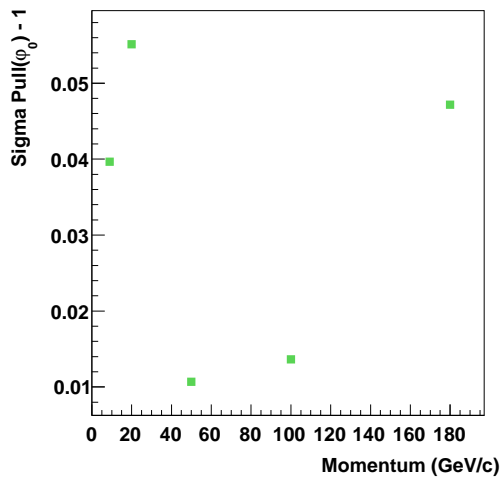
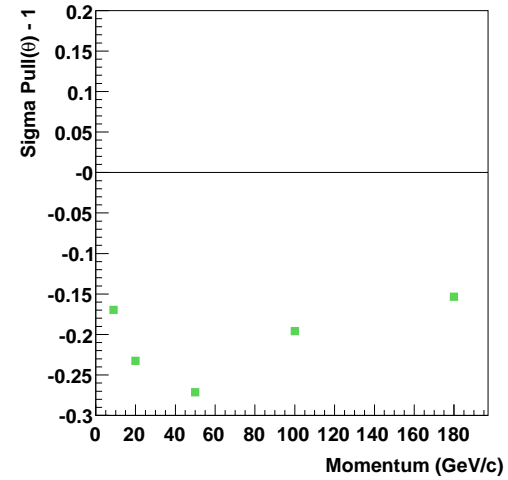
(a) $\sigma(\text{Pull } d_0) - 1$ (b) $\sigma(\text{Pull } z_0) - 1$ (c) $\sigma(\text{Pull } \varphi_0) - 1$ (d) $\sigma(\text{Pull } \theta) - 1$

Figure 7.17: The standard deviations, σ , of the gaussian fits to the parameter pull distributions as a function of beam momentum. Results including corrections for multiple scattering are shown in this diagram.

constant magnetic field of $B_z = 1.4 T$ was applied in the region $x : [0, 1000] mm$. Tracks were reconstructed from hits in the pixels and SCT. At least one pixel hit and four SCT hits were required. In the real data, there is a substantial misalignment between the silicon and TRT. This produces a significant bias on the fitted track parameters if the TRT is included. Therefore, TRT hits are not included in the track fit, either in simulation or real data.

Figure 7.18 shows the pull distributions of the five perigee parameters for $9 GeV/c$ electrons. The mean and RMS values of the distributions are given in table 7.2. In general, these values are close to, but not consistent with, $\mu = 0$ and $RMS = 1$ (c.f. section 6.1.1, page 71). The simplified material distribution in the tracking geometry and the inefficiency in pattern matching when electrons undergo catastrophic bremsstrahlung both contribute to this discrepancy.

The perigee resolution distributions are shown in figure 7.19. The corresponding mean and RMS values are provided in table 7.3. The RMS values of the q/p distributions from the GSF and KF are almost identical, due to the long bremsstrahlung tail (c.f. electron reconstruction in the ATLAS tracker - figure 6.3, page 74). However, in the region of the peak, the performance of the GSF appears to be superior to the KF. In section 6.1.2 (page 72) the *effective resolution*, $Q(x)$, was defined. $Q(x)$ is the symmetric half-width enclosing a fraction, x , of all events in the normalised q/p residual distribution. The value of $Q(68\%)$ (1σ) quantifies the width of the core of the distribution, while the $Q(95\%)$ (2σ) interval is determined by the size of the bremsstrahlung tail. In simulation, the residual, $r(q/p)$, is defined with respect to the generated momentum, $(q/p)_{true}$:

$$r(q/p) = \frac{\Delta(q/p)}{(q/p)_{true}} \equiv \frac{(q/p)_{rec} - (q/p)_{true}}{(q/p)_{true}}, \quad (7.4)$$

where $(q/p)_{rec}$ is the reconstructed value of q/p .

Figure 7.20 shows the $Q(68\%)$ and $Q(95\%)$ values as a function of beam momentum. Below $\sim 50 GeV/c$, the GSF core is narrower than the KF core. At all momenta, the size of the bremsstrahlung tail is identical for the GSF and KF.

7.5.2 Real Data

The momentum resolution obtained from simulation has been compared with real data. The list of reconstructed data sets is provided in table 7.4.

The GSF was used to reconstruct samples of 15,000 events from each data set. The track fit was performed using only pixel and SCT hits. At least one pixel hit and four SCT hits were required. Only events containing a single reconstructed track were considered. Figure 7.21

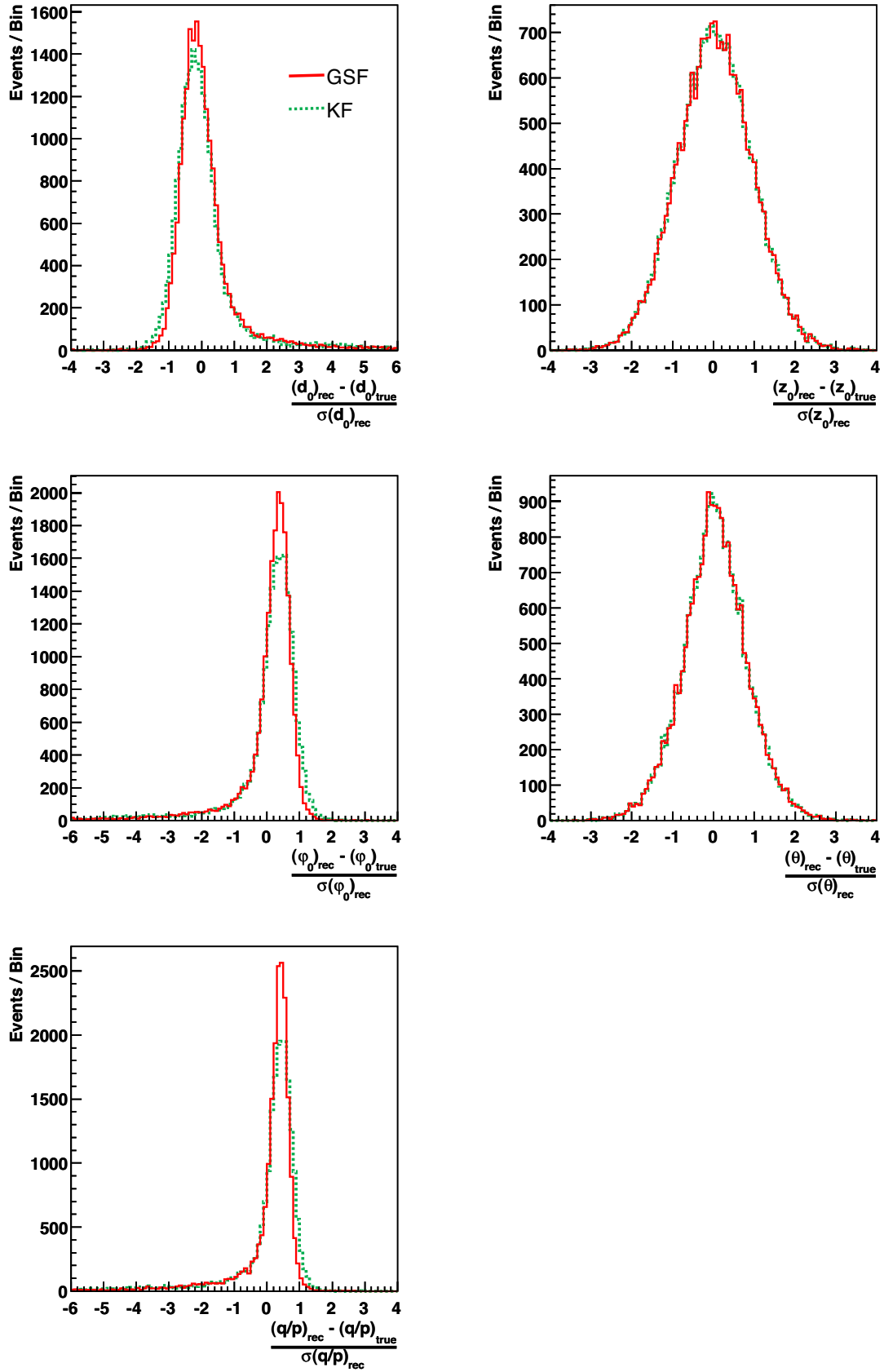


Figure 7.18: Pull distributions for the five fitted perigee parameters from 20,000 simulated 9 GeV/c single electron events. Comparison is made between the GSF (red-solid) and the KF (green-broken)

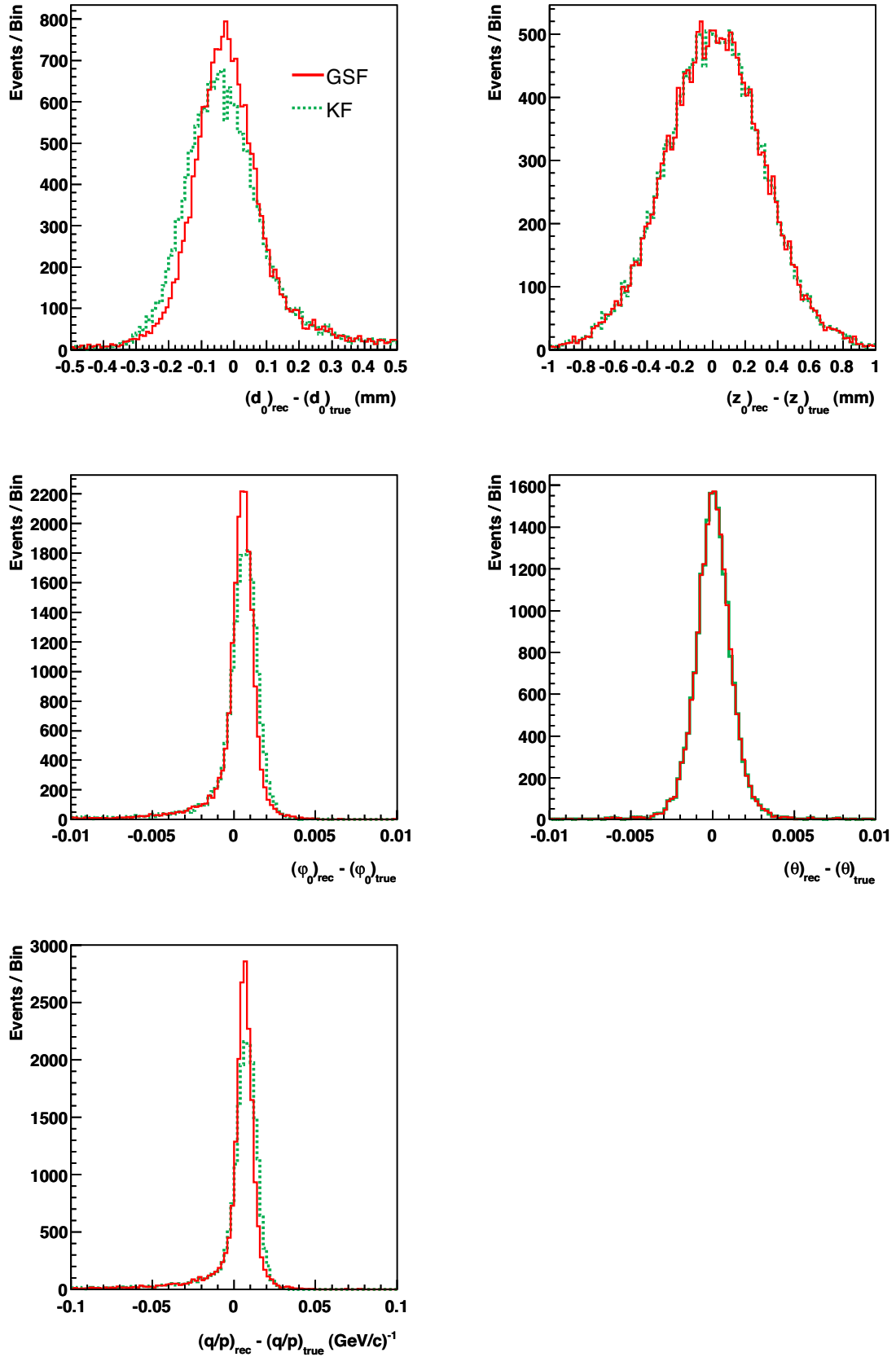


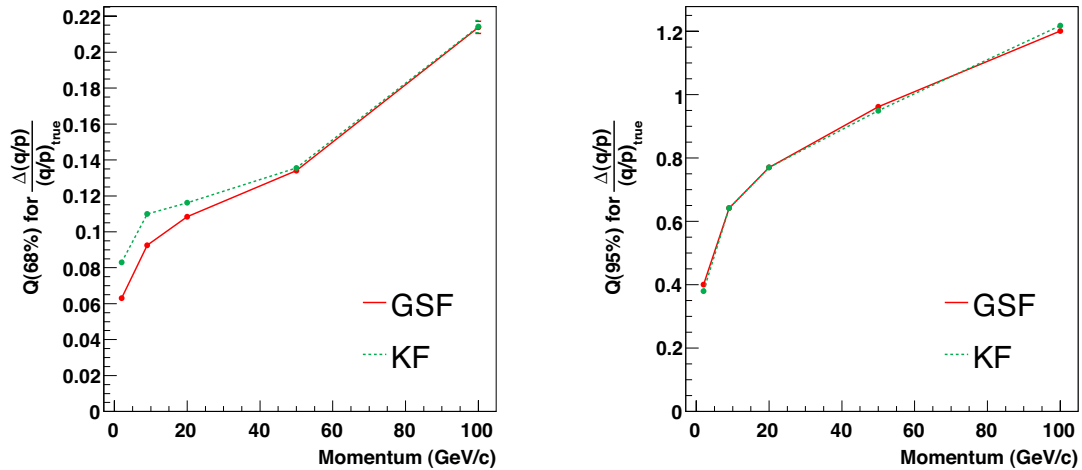
Figure 7.19: Resolution distributions for the five fitted perigee parameters from 20,000 simulated 9 GeV/c single electron events. Comparison is made between the GSF (red-solid) and the KF (green-broken).

Parameter	GSF		KF	
	Mean	RMS	Mean	RMS
\mathbf{d}_0	0.09 ± 0.01	1.03 ± 0.01	0.07 ± 0.01	1.09 ± 0.01
\mathbf{z}_0	0.03 ± 0.01	$0.92 \pm 0.00(4)$	0.03 ± 0.01	$0.92 \pm 0.00(4)$
ϕ_0	0.00 ± 0.01	1.06 ± 0.01	0.04 ± 0.01	1.11 ± 0.01
θ	0.04 ± 0.01	$0.82 \pm 0.00(4)$	0.04 ± 0.01	$0.81 \pm 0.00(4)$
\mathbf{q}/\mathbf{p}	0.03 ± 0.01	1.05 ± 0.01	0.06 ± 0.01	1.09 ± 0.01

Table 7.2: Mean and RMS values of the track parameter pull distributions for simulated 9 GeV/c electrons.

Parameter	GSF		KF	
	Mean	RMS	Mean	RMS
\mathbf{d}_0 (μm)	-12.2 ± 0.9	128 ± 1	-25.6 ± 1.0	134 ± 1
\mathbf{z}_0 (μm)	9.3 ± 2.2	306 ± 2	8.4 ± 2.2	306 ± 2
ϕ_0 ($mrad$)	0.22 ± 0.01	$1.5 \pm 0.0(1)$	0.30 ± 0.01	$1.6 \pm 0.0(1)$
θ ($mrad$)	0.06 ± 0.01	$1.3 \pm 0.0(1)$	0.05 ± 0.01	$1.3 \pm 0.0(1)$
\mathbf{q}/\mathbf{p} ($\times 10^{-3} GeV^{-1}$)	2.88 ± 0.11	15.0 ± 0.1	3.68 ± 0.11	15.5 ± 0.1

Table 7.3: Mean and RMS values of the track parameter resolution distributions for simulated 9 GeV/c electrons.



(a) Effective 1σ resolution

(b) Effective 2σ resolution

Figure 7.20: Effective resolution as a function of beam momentum (simulation). The effective resolution is defined as the half-width of the symmetric interval enclosing 68% (left) and 95% (right) of all events in the normalised q/p residual distribution. The GSF (red-solid) is compared to the KF (green-broken).

Run #	Beam-line	Particle	Momentum	Magnet	Events
2102109	VLE	electron/pion	3 GeV/c	-850 A	15,000
2102105	VLE	electron/pion	5 GeV/c	-850 A	15,000
2102107	VLE	electron/pion	9 GeV/c	-850 A	15,000
2102413	HE	positron	20 GeV/c	-850 A	15,000
2102400	HE	positron	50 GeV/c	-850 A	15,000

Table 7.4: List of the reconstructed data runs.

shows the track multiplicity per event in both simulation and real data. In both cases the average is close to one.

Below 20 GeV/c there is a significant pion contamination of the electron beam. Pions have been vetoed using the Cherenkov counter. A more detailed study of the pion veto is presented in section 7.7.

Figure 7.22 shows the normalised q/p residual for 9 GeV/c electrons and 50 GeV/c positrons in simulation and real data. In real data, the residual is defined with respect to the nominal beam momentum, $(q/p)_{beam}$:

$$r(q/p) = \frac{\Delta(q/p)}{(q/p)_{beam}} \equiv \frac{(q/p)_{rec} - (q/p)_{beam}}{(q/p)_{beam}}. \quad (7.5)$$

Figure 7.23 shows the effective 1σ and 2σ resolution as a function of the nominal beam momentum. The momentum resolution in the real data is significantly worse than the prediction from simulation. Two causes of the discrepancy are identified:

- **Detector misalignment:** Significant detector misalignment still exists in runs taken with magnetic field. The *residual* separation between a measurement and a track is used to determine the level of misalignment. Even the most up-to-date silicon alignment constants produce a bias in the distributions of residuals. In the bending plane, this bias is as large as 20 μm in the pixels and 50 μm in the SCT. The detector misalignment explains why the core of the momentum distribution in the real data is much broader than the simulation.
- **Upstream energy loss:** There is a significant amount of material upstream of the CTB inner detector. Electrons can therefore lose a large fraction of their energy even before they enter the tracker. Catastrophic energy loss, upstream of the CTB, produces a bremsstrahlung tail in the real data which is much larger than the simulation. A detailed study of the upstream material has been undertaken in an attempt to produce better agreement between simulation and real data.

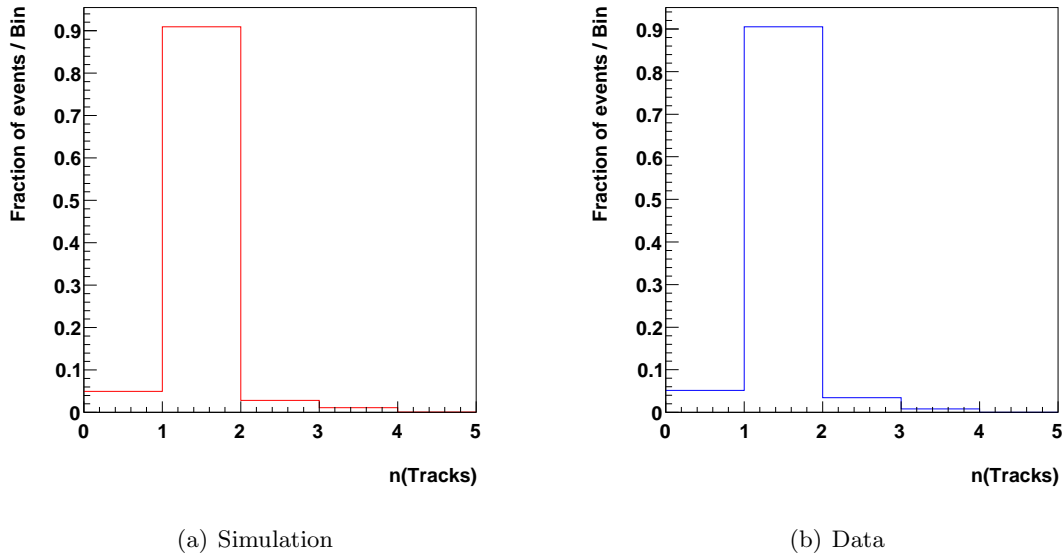


Figure 7.21: The track multiplicity per event in simulation and data.

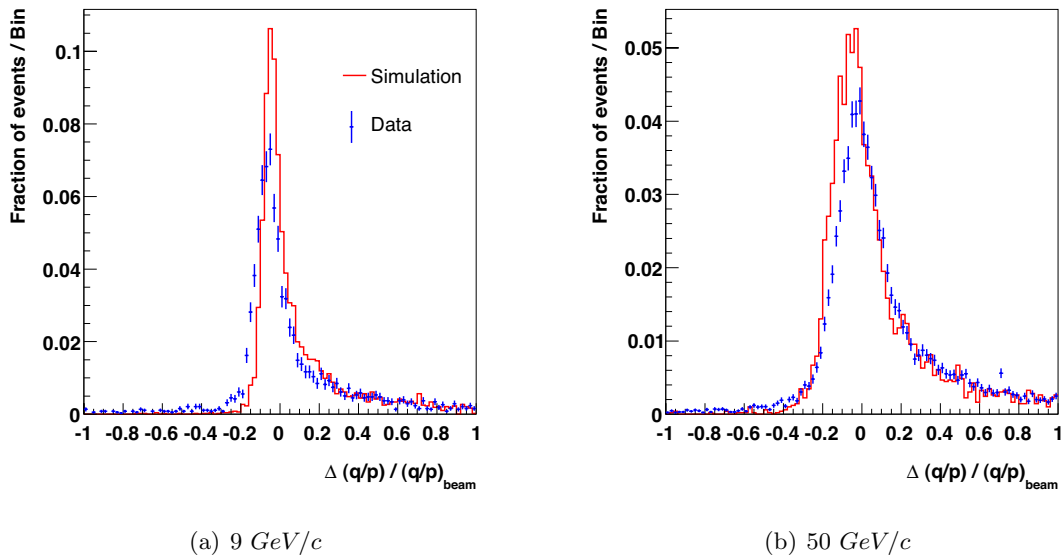


Figure 7.22: The normalised q/p residuals for 9 GeV/c electrons and 50 GeV/c positrons, reconstructed with the GSF from pixel and SCT hits. Simulation (red) is compared with the real data (blue).

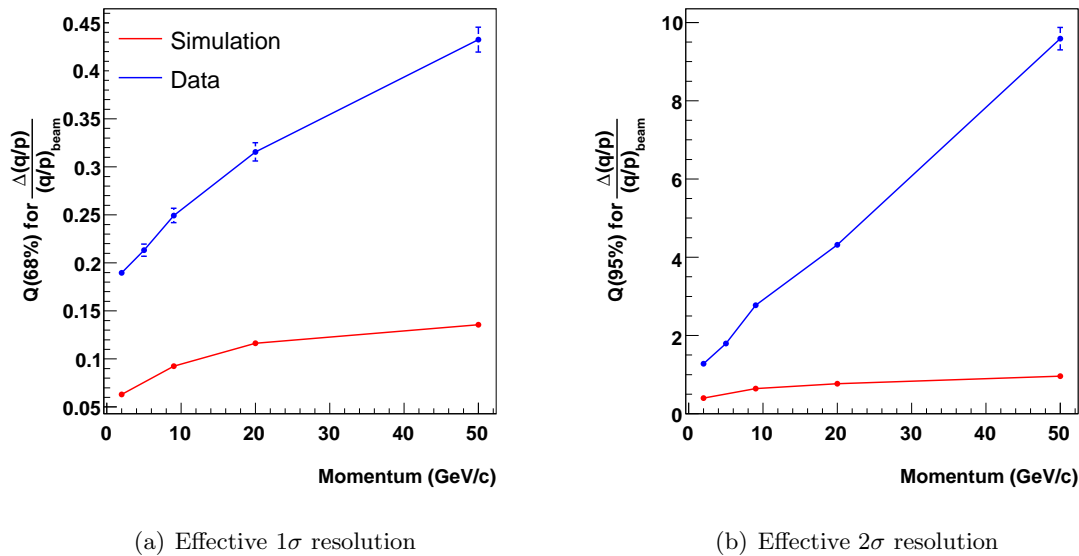


Figure 7.23: The effective momentum resolution from simulation (red) and real data (blue) as a function of the nominal beam momentum.

7.6 Beam-line Material Study

The tail of the momentum distribution in real data is larger than predicted by simulation due to catastrophic energy losses in material upstream of the CTB (section 7.5.2). To obtain better agreement between simulation and real data, the upstream material distribution must be included in the simulation. Figure 7.2 (page 97) shows the H8 beam-line between the T4 target and the inner detector. In the HE runs, the beam momentum at the C9 collimator is known to better than 1% (section 7.2.3). Only the material after this point need be included in the simulation. Two main regions of material between the C9 collimator and the CTB are identified:

- 15% x/x_0 is located inside the magnetic field of the main quadrupoles.
- 13.2% x/x_0 is located in the 27 m immediately upstream of the CTB. Most of this material is contained in the CTB beam-line instrumentation. In this region there is no magnetic field.

For the VLE runs, the momentum of the beam at the C12 collimator is known to better than 1%. Since C12 is downstream of the main quadrupoles, only the 13.2% x/x_0 in the CTB instrumentation should be included in the simulation.

It is difficult to predict the consequences of bremsstrahlung in the main quadrupoles. The fields in the quadrupoles are optimised to transport only particles at the nominal beam momentum to the CTB. Therefore, electrons undergoing significant energy loss in the quadrupoles

may not trigger the detector. The effects of bremsstrahlung in the beam instrumentation are significantly easier to predict. Since there is no magnetic field, the trajectory of the electron is not perturbed by energy loss. Even electrons which lose a large fraction of their energy in the beam instrumentation should be accepted by the trigger.

The CTB sub-detectors are sensitive to upstream energy losses. The size of the tail in the tracker q/p distribution depends on the amount of material in the beam-line. The upstream material distribution can be determined by comparing the size of the tail in the real data with simulation. The upstream material distribution in the simulation is systematically adjusted until a good agreement with the real data is obtained. The data sets used in the beam-line material study are shown in table 7.5.

Run #	Beam-line	Particle	Momentum	Magnet	Events
2102107	VLE	electron/pion	9 GeV/c	-850 A	10,000
2102413	HE	positron	20 GeV/c	-850 A	10,000
2102400	HE	positron	50 GeV/c	-850 A	10,000
2102452	HE	positron	80 GeV/c	-850 A	10,000

Table 7.5: List of the reconstructed data runs used in the upstream material study.

In the initial simulation, described in section 7.5.1, electrons were generated at $x = 0$, without any energy losses upstream of the CTB. The detector description in the simulation has been extended to include the upstream material. The magnetic field of the quadrupoles and the trigger acceptance were not incorporated in the simulation. Samples of 10,000 single electron events have been produced with $p = \{9, 20, 50, 80\} GeV/c$. Three upstream material distributions were considered:

- 13.2% x/x_0 : the electrons were generated at $x = -27 m$ and there was no magnetic field in the upstream region.
- 28.2% x/x_0 : the electrons were produced at $x = -27 m$ and there was no magnetic field in the upstream region. The material in the main quadrupole magnets was represented by a single piece of aluminium, placed at $x = -20 m$, with thickness 13.4 mm.
- 0% x/x_0 : The original simulation, produced at $x = 0$ (section 7.5.2), was also used in this study and compared with the new results.

The simulation and real data were reconstructed using the Kalman filter. Hits in the pixels, SCT and TRT were used in the track fit. At least one pixel hit and four SCT hits were required. Only events containing a single reconstructed track were considered. The Cherenkov counter was used to veto pions. Figure 7.24 shows the normalised q/p distributions for 9 GeV/c electrons and 20 GeV/c positrons. All distributions exhibit large bremsstrahlung tails.

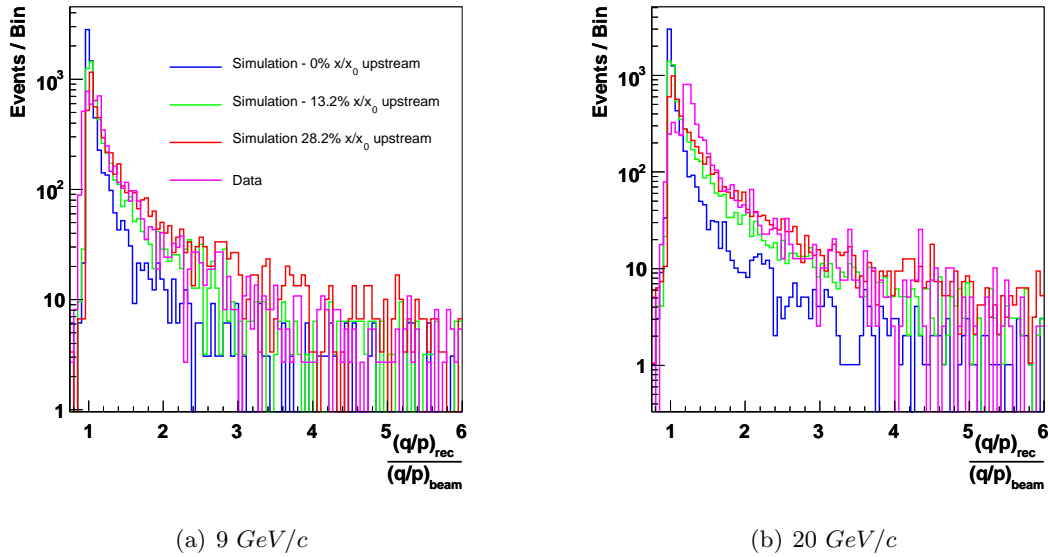


Figure 7.24: Normalised q/p distributions for 9 GeV/c electrons and 20 GeV/c positrons. The track is reconstructed from hits in the pixels, SCT and TRT. The real data is compared to three different versions of the simulation, each using a different upstream material distribution.

Energy losses both before and within the inner detector contribute to this tail. However, the amount of material within the inner detector is the same for all runs, so the differences between the distributions are purely due to the variations in the upstream material distribution.

To make a clear comparison between simulation and real data, the *integrated tail fraction* of the normalised q/p distribution was determined. The tail of the distribution lies to the right hand side of an arbitrarily defined value, f , of normalised q/p . If n_f is the number of tracks with normalised q/p greater than f and the total number of tracks in the histogram is n then:

$$\text{Integrated tail fraction} = \frac{\text{number of events in the tail}}{\text{total number of events}} \equiv \frac{n_f}{n}. \quad (7.6)$$

Figure 7.25 shows the integrated tail fraction, as a function of f , for 9 GeV/c electrons and 20 GeV/c positrons. In the tail of the distribution, the real data is in good agreement with the simulation which includes 13.2% x/x_0 upstream of the CTB. Around the core of the distribution, the real data worse than the simulated predictions due to detector misalignment.

The impact of misalignment can be reduced if the track fitter uses hits from only one tracker subsystem. Momentum estimates were first obtained from the pixel measurements and then from the SCT hits. Figure 7.26 shows the normalised q/p distributions from the pixels and SCT for 9 GeV/c electrons. Integrated tail fraction profiles have been obtained for the pixel (figure 7.27) and SCT (figure 7.28) track segments up to 80 GeV/c. At high momentum, the core of the distribution is very wide since the lever arm of each individual sub-detector

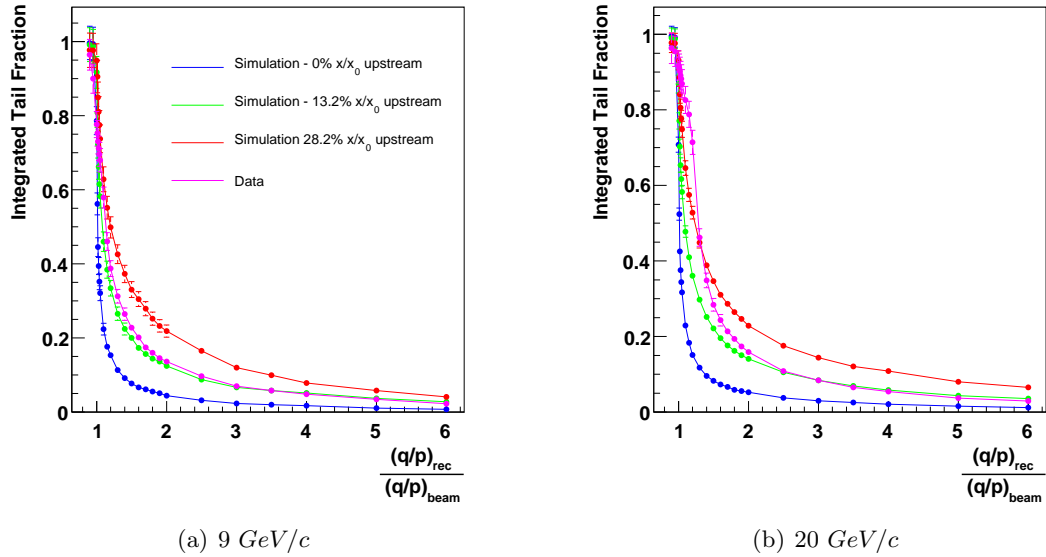


Figure 7.25: The integrated tail fraction profiles for 9 GeV/c electrons and 20 GeV/c positrons. The track is reconstructed from hits in the pixels, SCT and TRT.

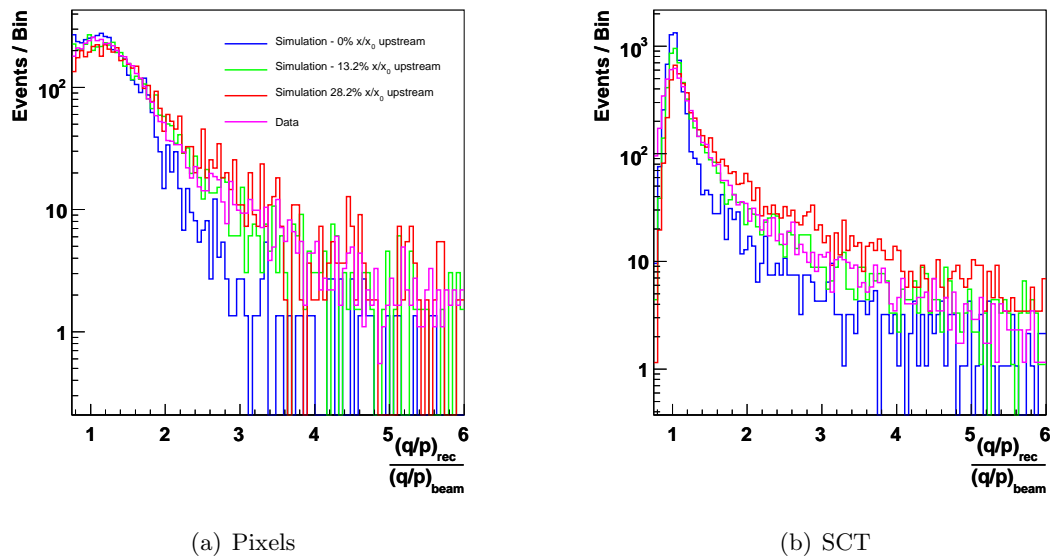


Figure 7.26: Reconstructed q/p distributions for 9 GeV/c electrons. Tracks are reconstructed independently from pixel hits (left) and SCT hits (right).

is small. In the tails of all distributions, there is good agreement between real data and the simulation which includes 13.2% x/x_0 upstream of the CTB. The agreement is not as good in the SCT distributions where the tail in the real data is systematically smaller than the simulation.

The amount of upstream material in the VLE beam-line has been measured to be 13.2% x/x_0 . The tail profile obtained from the real data at 9 GeV/c is in excellent agreement with this measurement.

In the HE beam-line, the material in the main quadrupoles must be considered. The total amount of upstream material has been measured to be 28.2% x/x_0 . The data profiles from the HE runs are inconsistent with this measurement. The likely reason for the discrepancy is that electrons which experience significant bremsstrahlung in the main quadrupoles are not transported to the CTB.

To infer the upstream material distribution, the tracker uses electrons which undergo catastrophic bremsstrahlung in the beam-line. Electrons which lose only a small fraction of their energy cannot be used, since the intrinsic resolution of the tracker is too poor. If the energy loss in the main quadrupoles is small enough, the electron should still be transported to the CTB. Although the tracker is not able to detect soft bremsstrahlung in the quadrupoles, it appears that the calorimeter (section 7.6.3) is sensitive to these energy losses.

7.6.1 Tail Fraction versus Beam Energy

Bremsstrahlung in the magnetic field of the tracker also has an impact on reconstruction performance. If an electron loses enough energy, the deflection by the field will cause it to miss detector elements further downstream. If insufficient detector elements are hit, then track reconstruction fails. At higher beam momenta, it becomes less likely that an electron will lose enough energy to miss downstream detector elements. The detector acceptance should therefore increase with beam momentum. This effect is clearly seen in both simulation and real data. Figure 7.29 shows a slight increase in the size of the tail as a function of beam momentum.

7.6.2 Studies with Extra Inner Detector Material

An additional 10% x/x_0 was inserted between the pixels and SCT to recreate the material distribution in the ATLAS tracker at high η (section 7.3.1). The tail profiles from runs with and without extra material in the tracker have been compared. The two data sets selected for this study are shown in table 7.6. The real data has been compared with simulation which

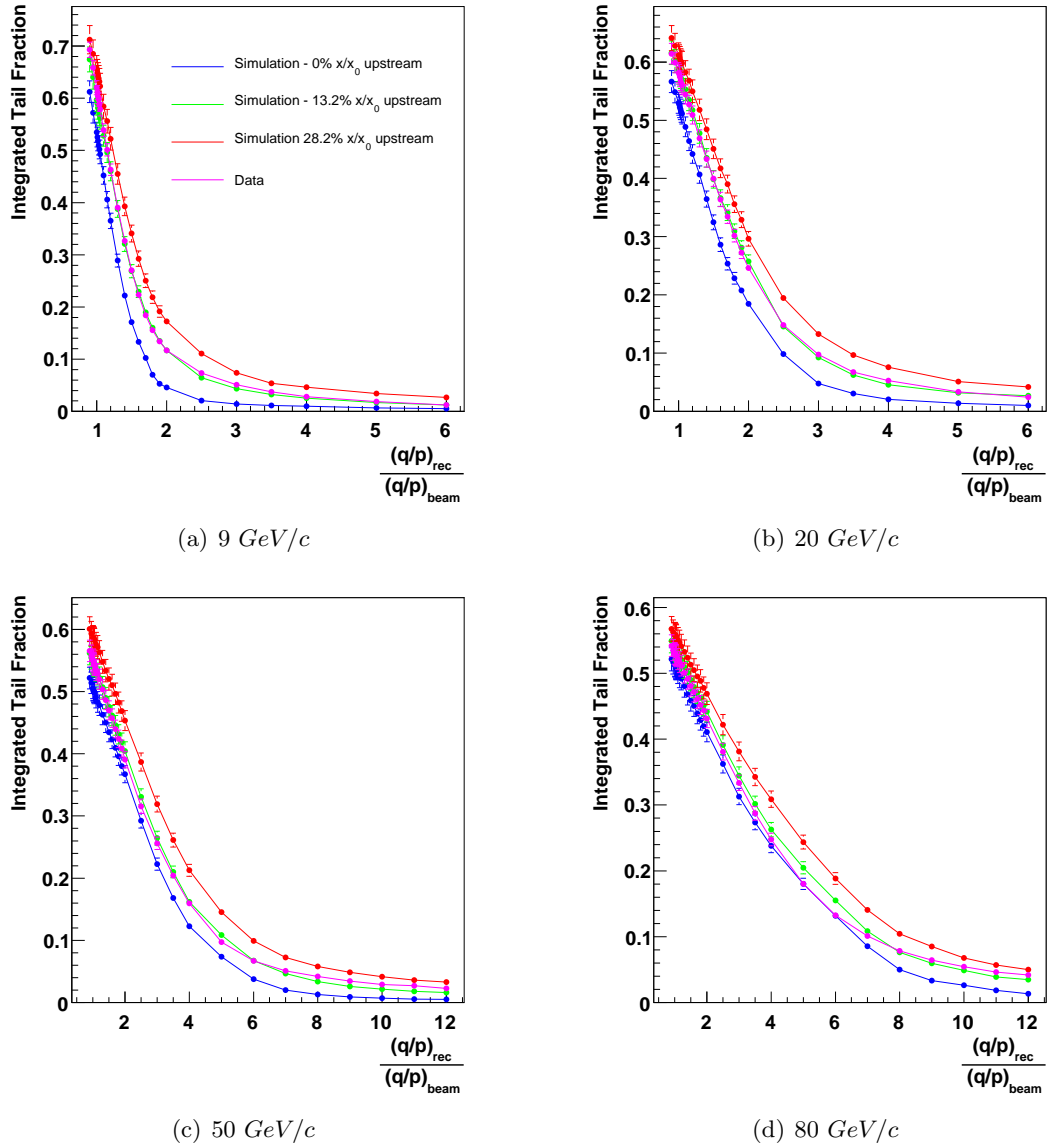


Figure 7.27: Integrated tail fraction profiles for tracks reconstructed from pixel hits.

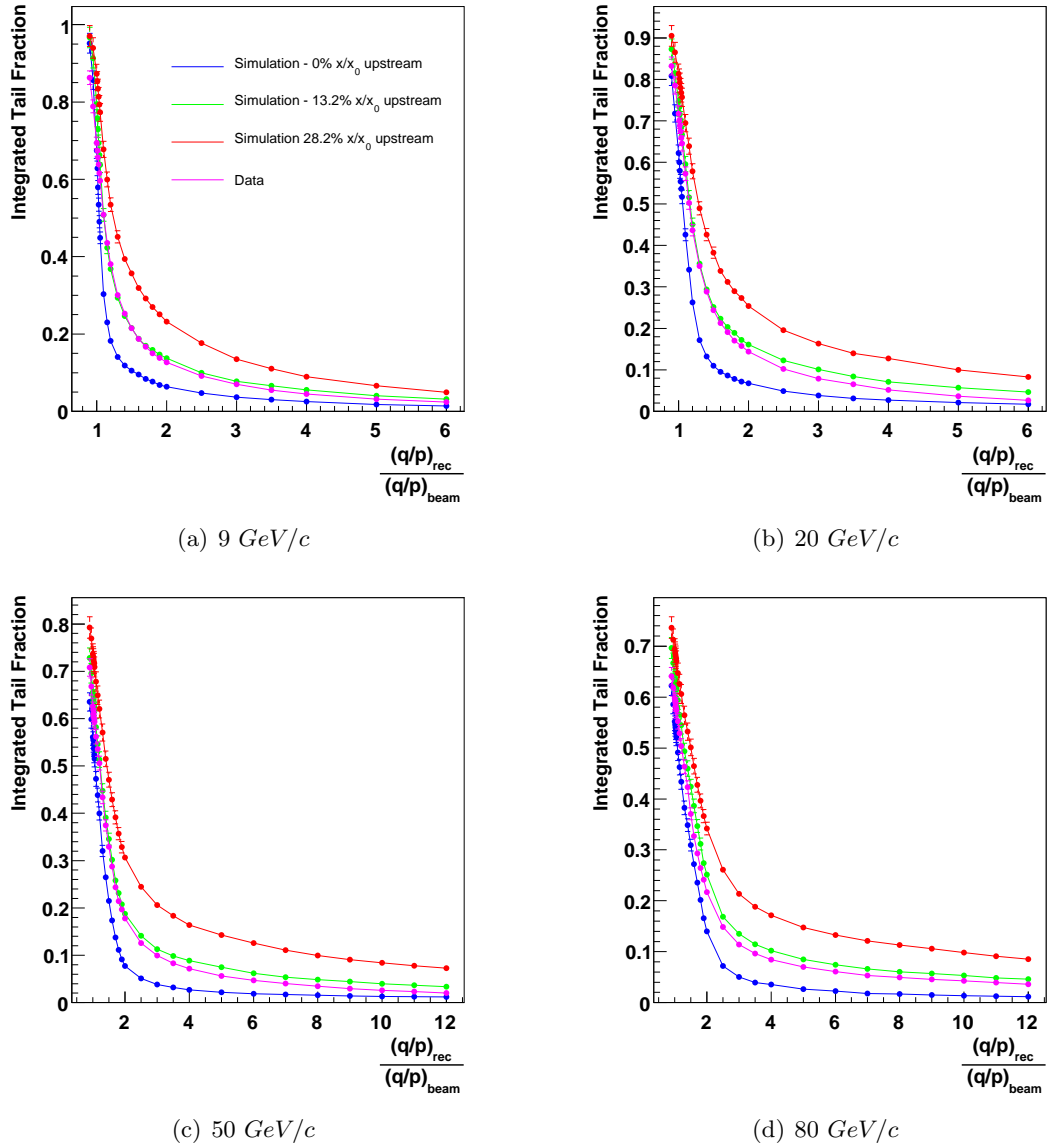


Figure 7.28: Integrated tail fraction profiles for tracks reconstructed from SCT hits.

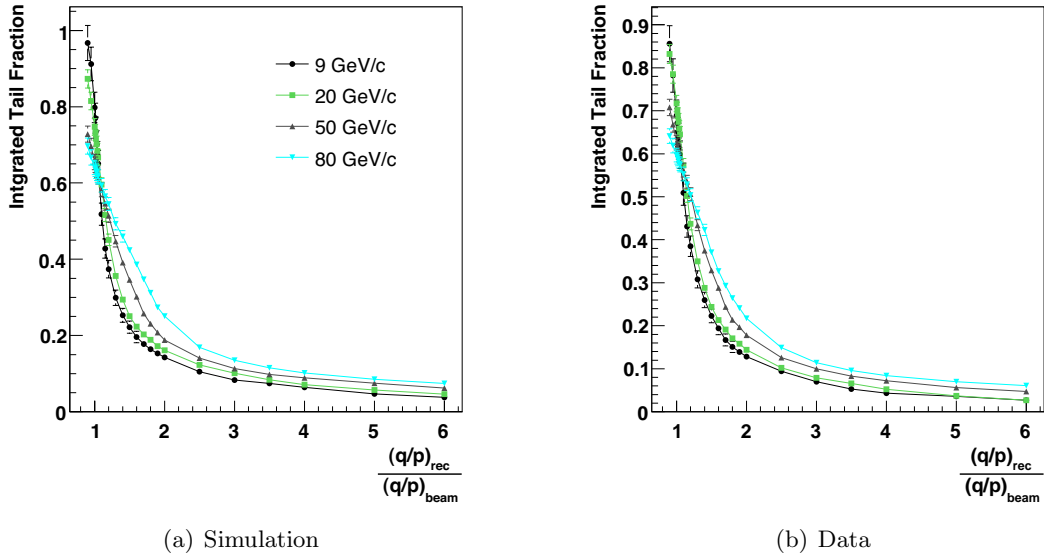


Figure 7.29: The integrated tail fraction profiles, shown for different beam momenta, in simulation and real data. In this case, tracks were reconstructed using hits found in the SCT. In the simulation, the material upstream of the CTB amounted to 13.2% x/x_0 .

includes 13.2% x/x_0 upstream of the CTB.

Figure 7.30 shows the tail fraction profiles, obtained from pixel and SCT track segments. All pixel track segments exhibit similar tail profiles. Since no additional material is included upstream of the pixels, this is expected. However, when additional material is included in the tracker, there is a significant discrepancy between simulation and real data in the SCT profiles. The size of the tail in simulation is much larger than in the real data. Currently there exists no satisfactory explanation for this observation.

Run #	Beam-line	Particle	Momentum	Magnet	Events	Extra ID Material
2102400	HE	positron	50 GeV/c	-850 A	10,000	+0% x/x_0
2102292	HE	positron	50 GeV/c	-850 A	10,000	+10% x/x_0

Table 7.6: List of the reconstructed data sets with and without additional material between the pixels and SCT.

7.6.3 Calorimeter Beam-line Material Study

Electrons which undergo soft bremsstrahlung in the main quadrupoles should be transported to the CTB. While the tracker can only infer the upstream material distribution from catastrophic energy losses in the beam-line, the electromagnetic calorimeter is sensitive to soft bremsstrahlung. The fraction of the total energy deposited per calorimeter sampling is highly dependant on the amount of upstream material. A study of the effect of upstream material on

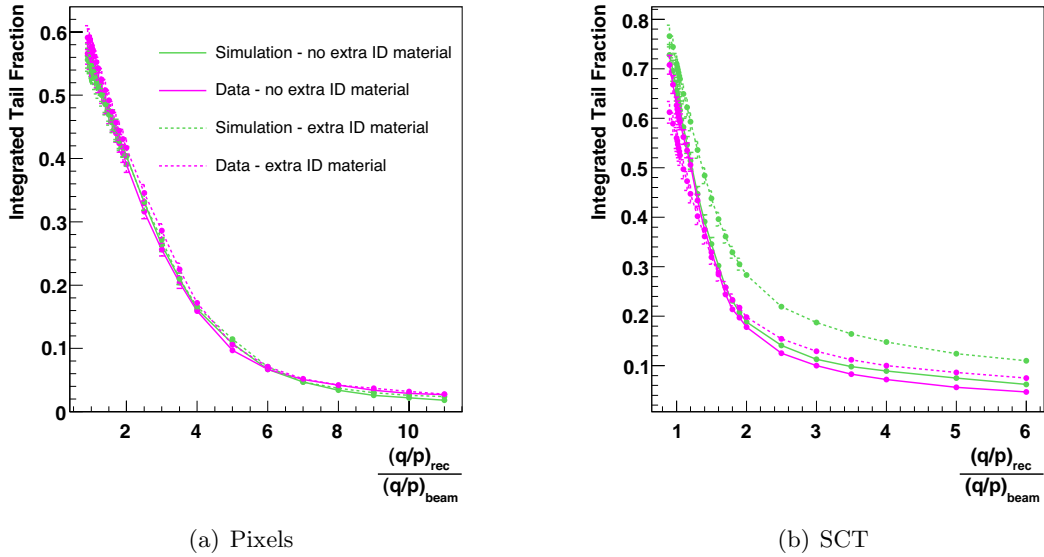


Figure 7.30: A comparison of the integrated tail fraction profiles from data and simulation: produced without any additional material within the inner detector (solid lines); and with an additional 10% x/x_0 between the pixels and SCT (broken lines). Simulation was produced using 13.2% x/x_0 upstream of the CTB. The profiles were obtained using beams of 50 GeV/c positrons.

calorimeter energy distributions has been conducted in parallel with the tracker based investigation [54]. The amount of upstream material in the simulation was adjusted until a good agreement with real data was observed. Figure 7.31 shows the energy collected per ECAL sampling for a 20 GeV positron beam. The real data is compared with simulation which includes 28.2% x/x_0 upstream of the CTB. Simulation and real data are in good agreement when the total amount of upstream material in the simulation is in the range $28.2 \pm 5\%$ x/x_0 .

It appears that the trigger acceptance is a function of the energy loss in the main quadrupoles. Electrons which lose a lot of energy are not transported to the CTB. A preliminary study of the trigger acceptance has been performed using a photon beam [54]. The layout of the CTB detector elements and beam-line instrumentation for the photon runs is shown in figure 7.32. Most of the beam-line instrumentation, used for the HE and VLE runs, has been removed. A converter of thickness 0.05% x/x_0 was inserted 12 m upstream of the CTB tracker. A dipole magnet was located after the converter to separate the electron from radiated photons. A scintillator, displaced relative to the nominal beam line, provided a trigger on electrons which were deflected significantly by the field. In general, both the electron and photon were within the geometric acceptance of the calorimeter.

For this study, a 180 GeV positron beam was incident on the converter. The results from the real data were compared with simulation which incorporated 28.2% x/x_0 upstream of the CTB. Figure 7.33 shows the total energy of the electron and photon in the calorimeter. There

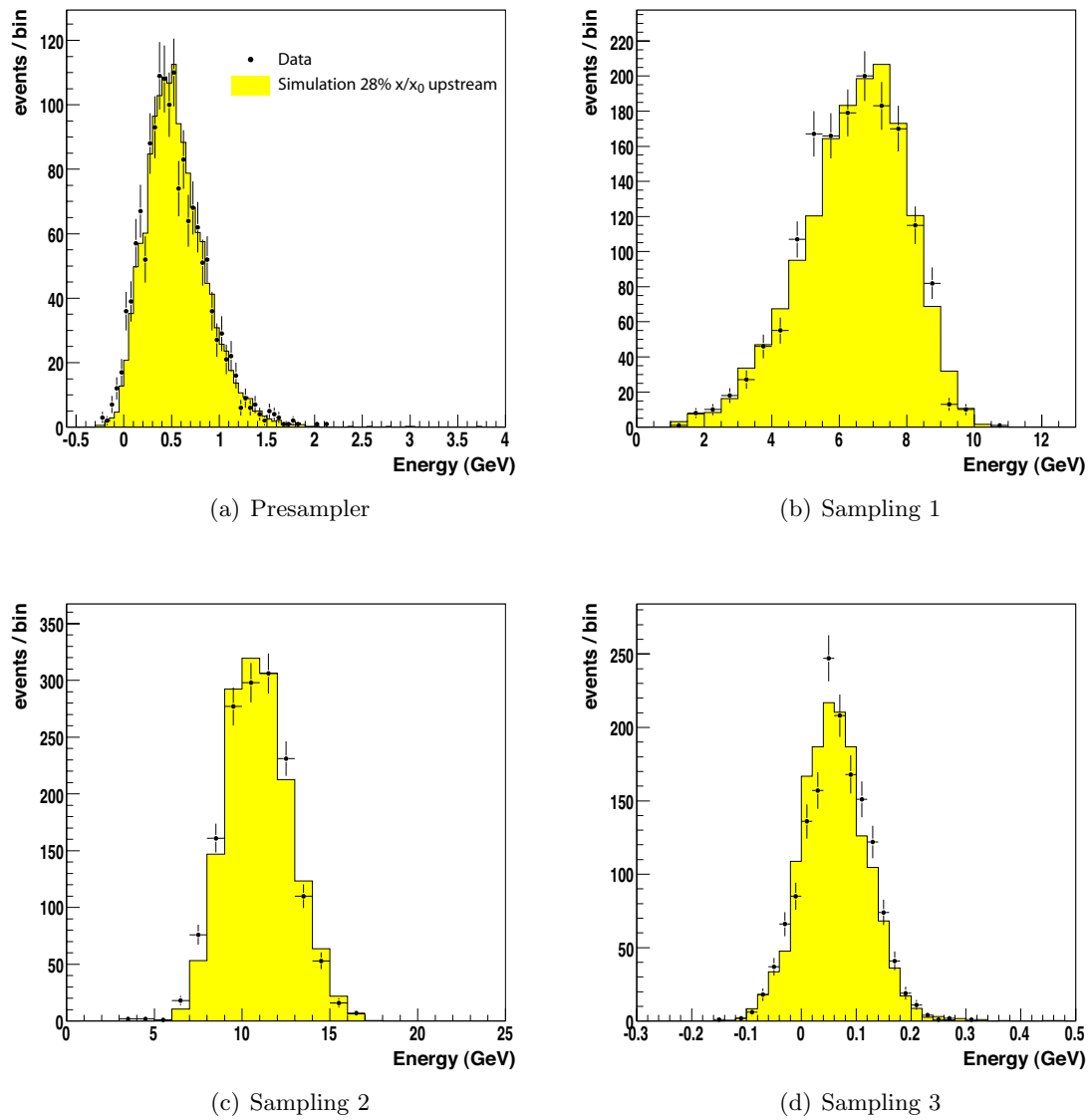


Figure 7.31: Energy deposited per sampling for a 20 GeV positron beam. The simulation includes 28.2% x/x_0 upstream of the CTB [54].

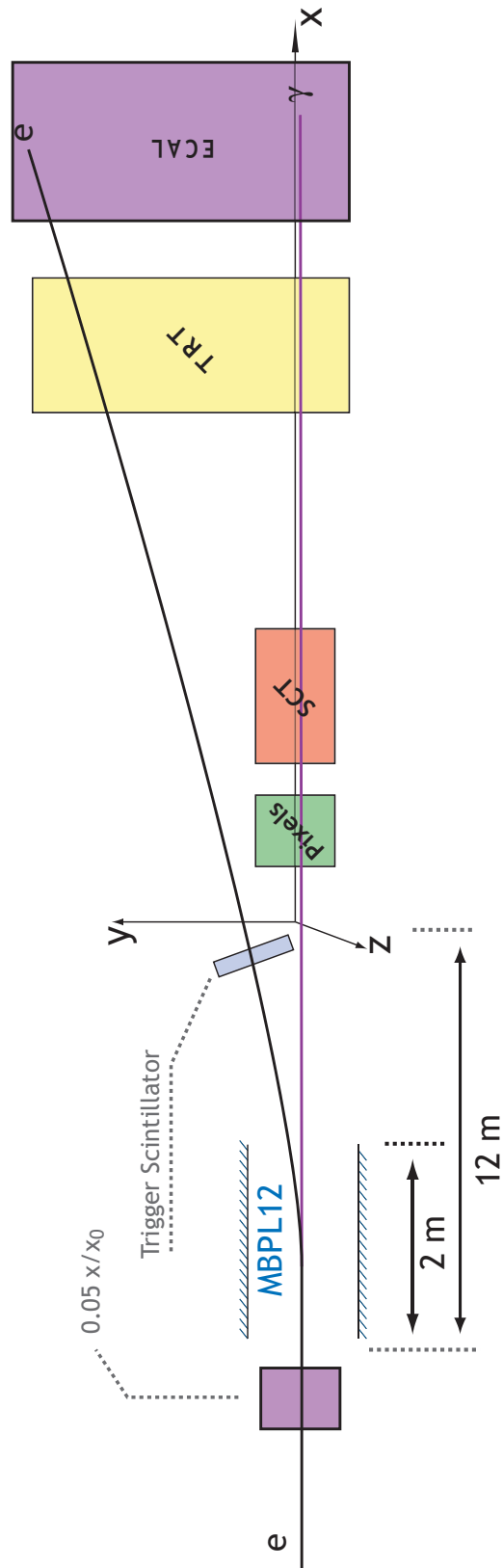


Figure 7.32: Layout of the beam-line and detector elements for the photon runs.

is a low energy tail in both simulation and real data. The fraction of events in the tail of each distribution can be determined, making an arbitrary choice for the energy, E , at which the tail begins. The tail efficiency has been defined as:

$$\text{Tail efficiency} = \frac{\text{Fraction of events in data tail}}{\text{Fraction of events in simulated tail}}. \quad (7.7)$$

Figure 7.34 shows the tail efficiency as a function of E . The efficiency in the core is close to one. If electrons which undergo energy loss in the upstream material are not transported to the CTB, then the efficiency in the tail of the distribution should be less than one. The observed efficiency agrees with this prediction.

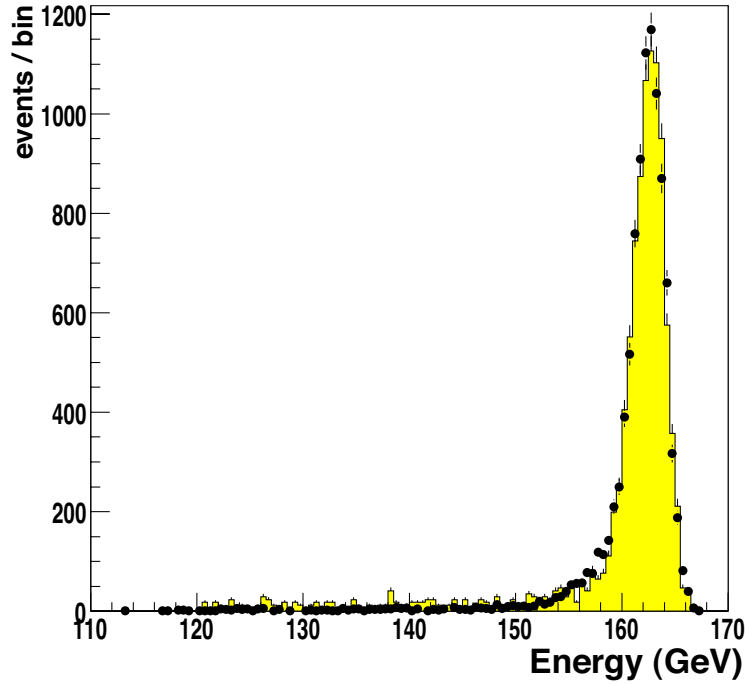


Figure 7.33: Total energy of the electron and photon in the calorimeter [54].

The results from the tracker favour 13.2% x/x_0 upstream of the CTB. The results from the calorimeter support 28.2% x/x_0 . The tracker and calorimeter studies are consistent only if electrons which undergo catastrophic bremsstrahlung in the main quadrupoles are not transported to the CTB. A complete simulation of the beam-line, from the C9 collimator to the CTB, is necessary to provide direct evidence of this hypothesis. The simulation must include an accurate description of the beam-line material distribution and the magnetic field of the quadrupoles.

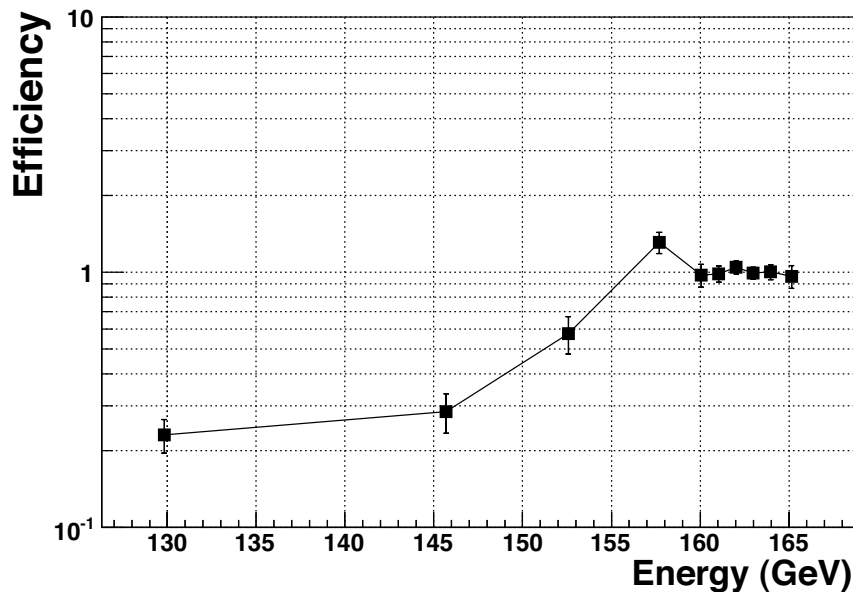


Figure 7.34: Tail efficiency for the photon run [54].

7.7 Pion Veto

Below $20 \text{ GeV}/c$, the electron beam contains a significant pion contamination. The Cherenkov counter has been used to veto pions (sections 7.5.2 and 7.6). The pion rejection power of the Cherenkov counter has been quantified for $20 \text{ GeV}/c$ and $9 \text{ GeV}/c$ beams.

As a starting point, two additional discriminating variables were introduced: the number of transition radiation (TR) hits in the TRT; and the energy collected in the hadronic calorimeter. Cuts on these variables veto events which have:

- Cherenkov counts < 650 .
- Number of TR hits < 3 .
- Hadronic calorimeter energy $> 1.5 \text{ GeV}$.

The cut values were kept constant throughout the study - no optimisation was performed. The number of events remaining after a particular cut depends on the pion rejection and electron efficiency of the cut. Cuts can be applied individually or in combinations. Eight, non-linear simultaneous equations describe the effect of all possible cuts on the number of events:

$$\begin{aligned}
n &= n_e + n_\pi & n_{c,t} &= \epsilon_c \epsilon_t n_e + \frac{n_\pi}{R_c R_t} \\
n_c &= \epsilon_c n_e + \frac{n_\pi}{R_c} & n_{c,h} &= \epsilon_c \epsilon_h n_e + \frac{n_\pi}{R_c R_h} \\
n_t &= \epsilon_t n_e + \frac{n_\pi}{R_t} & n_{t,h} &= \epsilon_t \epsilon_h n_e + \frac{n_\pi}{R_t R_h} \\
n_h &= \epsilon_h n_e + \frac{n_\pi}{R_h} & n_{c,t,h} &= \epsilon_c \epsilon_t \epsilon_h n_e + \frac{n_\pi}{R_c R_t R_h}
\end{aligned} \tag{7.8}$$

The definitions of the variables are provided in table 7.7.

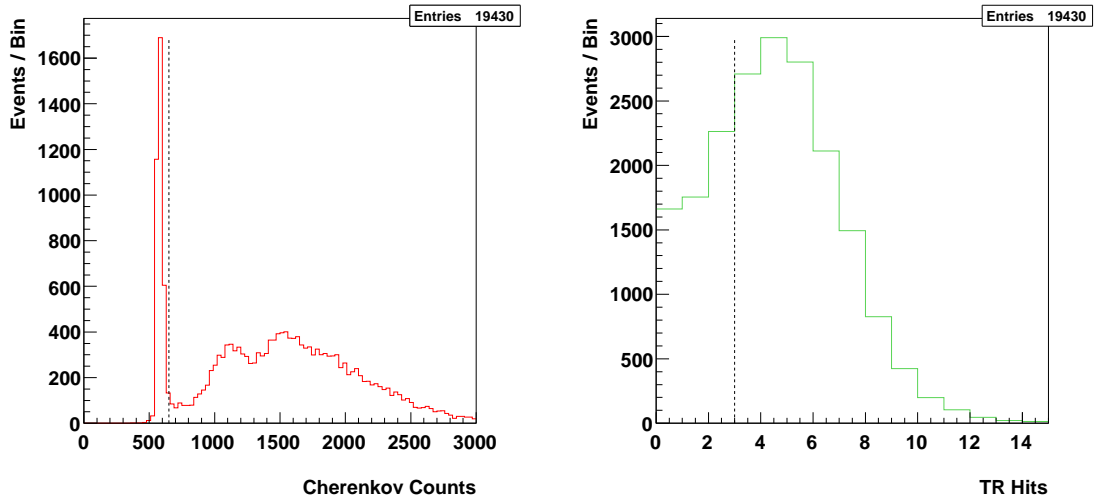
Observables		Unknowns	
n	number of events before cuts	n_e	number of electrons before cuts
n_c	number of events after Cherenkov cut	n_π	number of pions before cuts
n_h	number of events after HCAL cut	R_c	rejection power of Cherenkov cut
n_t	number of events after TR cut	R_h	rejection power of HCAL cut
$n_{c,h}$	number of events after Cherenkov & HCAL cuts	R_t	rejection power of TR cut
$n_{c,t}$	number of events after Cherenkov & TR cuts	ϵ_c	efficiency of Cherenkov cut
$n_{h,t}$	number of events after HCAL & TR cuts	ϵ_h	efficiency of HCAL cut
$n_{c,h,t}$	number of events after all cuts	ϵ_t	efficiency of TR cut

Table 7.7: Definitions of the variables used in equation 7.8. The number of events remaining after the application of a particular cut is dependant on the pion rejection and electron efficiency of the cut. For three cutting variables, there are a total of eight observables and eight unknowns.

In equation 7.8, there are eight observables and eight unknowns. A minimum of three discriminating variables are required to generate enough simultaneous equations for the problem to become well-constrained.

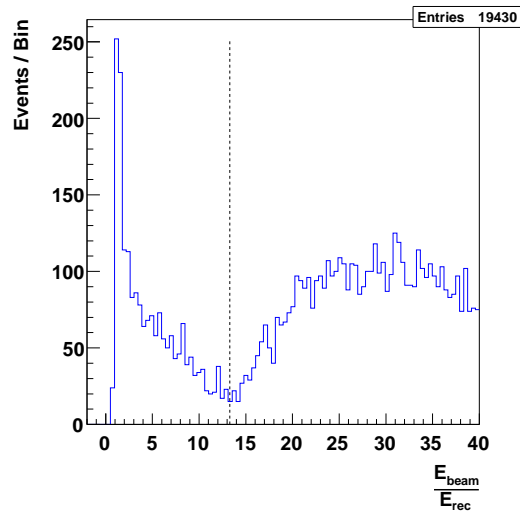
A sample of 20,000 positrons at 20 GeV/c was reconstructed. The distributions of the cutting variables are shown in figure 7.35. All the possible combinations of cuts were then applied to determine the observables of table 7.7. Solutions to the simultaneous equations were then found using *Mathematica* [55]. The results are shown in table 7.8. The Cherenkov cut rejection power is 18.26 for an electron efficiency of 0.928.

Solutions have also been found (table 7.9) for the 9 GeV/c electron run. The pion contamination of the beam is significantly greater at lower momentum, as is the pion rejection power.



(a) Cherenkov counter

(b) TRT



(c) HCAL

Figure 7.35: Distributions of Cherenkov counts, TR hits and normalised HCAL energy for $20 \text{ GeV}/c$ positrons. The cut values for the pion veto are indicated by the vertical lines. The pion enriched region is to the left of the line in all distributions.

Symbol	Meaning	Value
n_e	Number of electrons	16918
n_π	Number of pions	2511
ϵ_c	Cherenkov electron efficiency	0.928
ϵ_t	TR electron efficiency	0.609
ϵ_h	HCal electron efficiency	0.763
R_c	Cherenkov pion rejection	18.26
R_t	TR pion rejection	37.26
R_h	HCal pion rejection	5.07

Table 7.8: Beam composition, electron efficiency and pion rejection factors for run 2102413 - nominally 20 GeV/c positrons.

Symbol	Meaning	Value
n_e	Number of electrons	5420
n_π	Number of pions	13517
ϵ_c	Cherenkov electron efficiency	0.891
ϵ_t	TR electron efficiency	0.669
ϵ_h	HCal electron efficiency	0.728
R_c	Cherenkov pion rejection	164
R_t	TR pion rejection	39.5
R_h	HCal pion rejection	2.19

Table 7.9: Beam composition, electron efficiency and pion rejection factors for run 2102107 - nominally 9 GeV/c electrons.

7.8 Performance with Real Data

In section 7.6, it was shown that the tracker is only sensitive to energy losses in the material just in front of the CTB. It is assumed that electrons which undergo significant energy loss in the main quadrupoles are not accepted by the trigger. The GSF and KF have been used to reconstruct simulation which includes 13.2% x/x_0 upstream of the tracker.

Figure 7.36 shows the effective 1σ and 2σ momentum resolution for the GSF and KF. The resolution is poor in comparison with the simulation which includes no upstream material (figure 7.20, page 123). At low momentum, the resolution from the GSF was expected to be better than the KF. However, due to upstream energy losses, there is no difference in performance between the two fitters. The core of the momentum distribution at 9 GeV/c is narrower than at 2 GeV/c. At very low momentum, multiple scattering in the upstream beam-line has a significant impact on the resolution. At higher momentum, multiple scattering effects become smaller and the intrinsic detector resolution largely determines the size of the core.

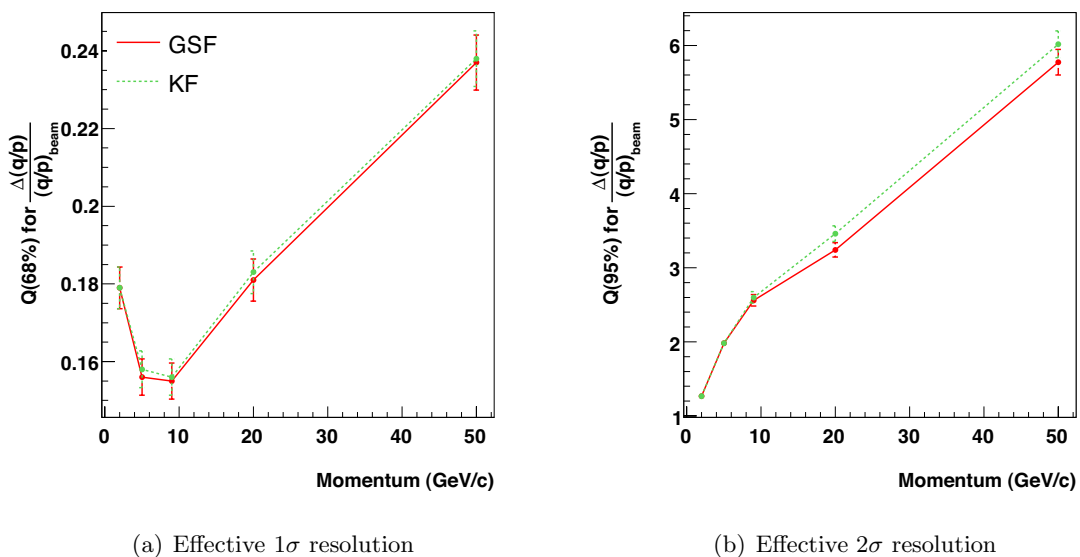


Figure 7.36: Effective 1σ and 2σ momentum resolution as a function of beam momentum for the GSF (red-solid) and the KF (green-broken) using simulation including 13.2% x/x_0 upstream of the pixels.

Figure 7.37 shows the momentum resolution from the GSF in simulation and real data. Both the original simulation, with no upstream material, and the simulation with 13.2% x/x_0 upstream of the CTB, have been considered. The 1σ momentum resolution, from simulation with upstream material, is in good agreement with the real data at 2 GeV/c. This indicates that the multiple scattering in the beam-line is well described by the simulation. At higher momenta, the resolution in real data is consistently worse than simulation due to the

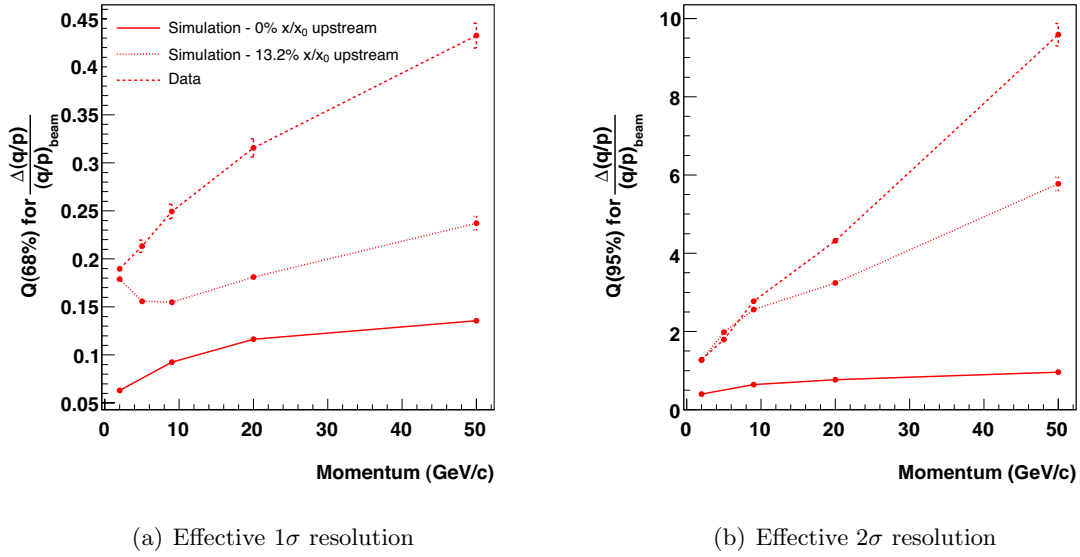


Figure 7.37: Effective 1σ and 2σ momentum resolution from the GSF as a function of beam momentum. The resolution from simulation with and without the additional 13.2% x/x_0 is compared with data.

misalignment of the detector elements. The 2σ momentum resolution, from simulation with upstream material, is in good agreement with data up to $9\text{ GeV}/c$.

7.9 Summary

The performance of the GSF in the CTB was initially tested using simulation (section 7.5.1). The original simulation did not take into account energy losses in the beam-line upstream of the CTB. The results suggested that, at low momentum, the GSF would provide better estimates of the momentum than the KF. However, the momentum resolution in the real data was worse than predicted.

Two factors contributing to the discrepancy were identified: the residual misalignment of the inner detector elements; and energy losses due to bremsstrahlung in material upstream of the CTB.

The amount of material in the upstream beam-line can be deduced by measuring the size of the bremsstrahlung tail in the tracker momentum distribution. The size of the tail in the real data is in excellent agreement with the simulation which incorporates 13.2% x/x_0 upstream of the CTB (section 7.6). The calorimeter can also be used to determine the upstream material distribution. There is only agreement between simulation and real data when a total of 28.2% x/x_0 is included upstream of the CTB.

The results of the upstream material studies using the tracker and calorimeter are consistent only if electrons which undergo significant energy loss in the main quadrupoles are not transported to the CTB. To confirm this hypothesis, a precise simulation of the beam-line is necessary.

The GSF is unlikely to provide any benefit in the CTB, due to the large amount of upstream material and the detector misalignment. In spite of these limitations, the GSF is still expected to improve the momentum estimates of electrons in the complete tracker. In ATLAS, only the beryllium beam-pipe is located before of the first pixel layer. Therefore, the average upstream energy loss is much less than at the CTB. The quality of the alignment is also expected to be much better in the ATLAS tracker than in the CTB.

Chapter 8

Physics Case Studies

In chapter 6, the performance of the gaussian-sum filter was assessed using samples of single electron events. The GSF was shown to produce better estimates of the momentum than the Kalman filter. Therefore, the performance of the GSF should be evaluated in physics analyses where it is likely to provide benefit. A complete analysis of LHC collisions requires the full information of the detector and goes well beyond the scope of this investigation. In this chapter, a preliminary, tracker-based study of several important physics processes is presented. Perfect particle identification has been assumed throughout this study, so that the fitter performance can be determined independently. Electrons and positrons are identified from truth information contained in the Monte-Carlo simulation.

Three physics processes are considered: $J/\psi \rightarrow e^+e^-$ (section 8.1); $Z \rightarrow e^+e^-$ (section 8.2); and $H \rightarrow ZZ^* \rightarrow 4e$ (section 8.3). A Higgs mass of $m_H = 130 \text{ GeV}/c^2$ has been selected for this study. Finally, a brief comparison of the performance of the tracker and ECAL is presented in section 8.4.

8.1 $J/\psi \rightarrow ee$

The J/ψ meson is a bound state of $c\bar{c}$. It has a mass of $3097 (\pm 0.011) \text{ MeV}$ and a width of $93 \pm 2 \text{ keV}$. It has leptonic decay modes, $BR(J/\psi \rightarrow e^+e^-) = BR(J/\psi \rightarrow \mu^+\mu^-) = 5.94 \pm 0.06\%$ [8].

Electrons and positrons from the J/ψ decay will be used to calibrate the ECAL. Some calorimeter calibration algorithms require precise estimates of momentum from the tracker. Additionally, the J/ψ is a possible decay product of a B meson and, because of its relatively high detection efficiency, is invaluable in B-physics analyses.

A sample of 5,000 $J/\psi \rightarrow e^+e^-$ decays has been generated and the tracker response has been determined using the full simulation. Figure 8.1 shows the true momenta of the electron and positron, ordered according to their energy. The leading lepton is more energetic than the secondary lepton.

The electron and positron, identified from Monte-Carlo truth as originating from the J/ψ , were reconstructed using the GSF and KF. Two different Kalman filters were used for track fitting: KF(BH) incorporates corrections for radiative energy loss using a gaussian approximation of the Bethe-Heitler distribution; KF(BB) considered only ionising energy losses according to the Bethe-Bloch formula. The momentum estimate from the GSF was chosen to be the mode of the q/p pdf (section 6.4, page 79).

The reconstructed lepton q/p residuals are shown in figure 8.2. The effective resolution is quantified as the symmetric half-width enclosing 68% (1σ) and 95% (2σ) of all events (cf. section 6.1.2, page 72). The resolution values are given in table 8.1. The momentum resolution is better for secondary leptons, since they are less energetic. The GSF provides the optimal 1σ momentum resolution. The KF(BH) gives the best estimate of the 2σ resolution. The KF(BB) is consistently the worst performing fitter.

The invariant mass distributions of the e^+e^- pair are shown in figure 8.3. The peak of the GSF invariant mass distribution is in good agreement with the accepted mass of the J/ψ . The normalised 1σ and 2σ mass resolution values are provided in table 8.1. The core from the GSF is narrower than either the KF(BH) or KF(BB). However, the tail from the GSF is larger than the KF(BH). The worst estimate of the invariant mass is provided by the KF(BB).

Fitter		Leading lepton	Secondary lepton	Mass
GSF	1σ	0.113 ± 0.004	0.070 ± 0.002	0.092 ± 0.003
	2σ	0.867 ± 0.025	0.451 ± 0.013	0.342 ± 0.010
KF (BH)	1σ	0.169 ± 0.005	0.127 ± 0.004	0.138 ± 0.004
	2σ	0.650 ± 0.018	0.351 ± 0.010	0.330 ± 0.009
KF (BB)	1σ	0.222 ± 0.007	0.122 ± 0.004	0.160 ± 0.005
	2σ	1.16 ± 0.03	0.601 ± 0.018	0.385 ± 0.011

Table 8.1: Effective 1σ and 2σ resolution quantities for: the reconstructed leptons from the J/ψ decay; and the invariant mass of the e^+e^- pair. Values have been obtained using the GSF and two versions of the KF; one using the Bethe-Heitler (BH) model for energy loss and the other using the Bethe-Bloch (BB) formula. The resolution on the invariant mass is normalised to the accepted mass of the J/ψ ($3097 \text{ MeV}/c^2$).

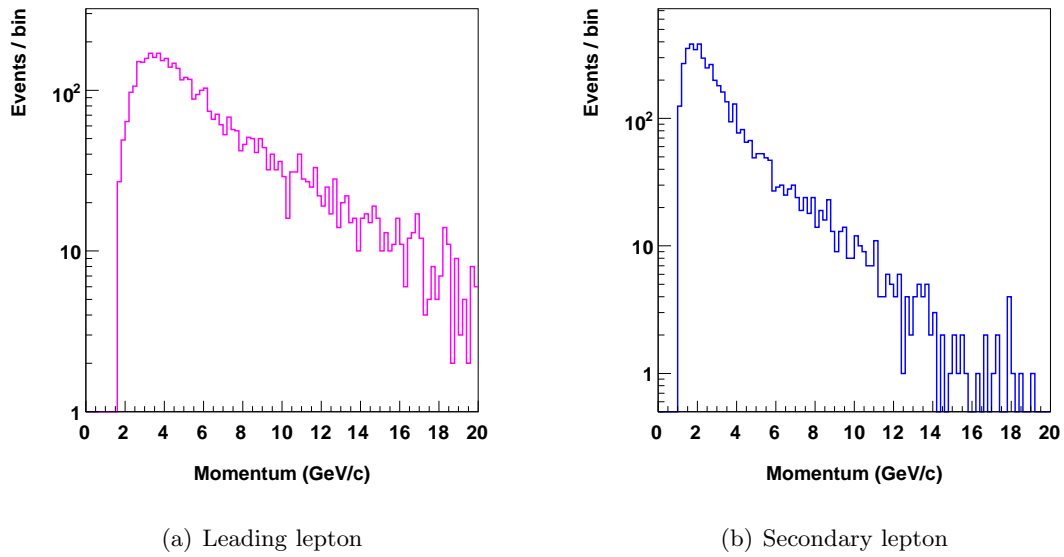


Figure 8.1: Distributions of the true momenta of the electron and positron from the J/ψ decay. The electron and positron are ordered according to their energy. The leading lepton is more energetic than the secondary lepton. Leptons with momenta $< 1 \text{ GeV}/c$ are not retained.

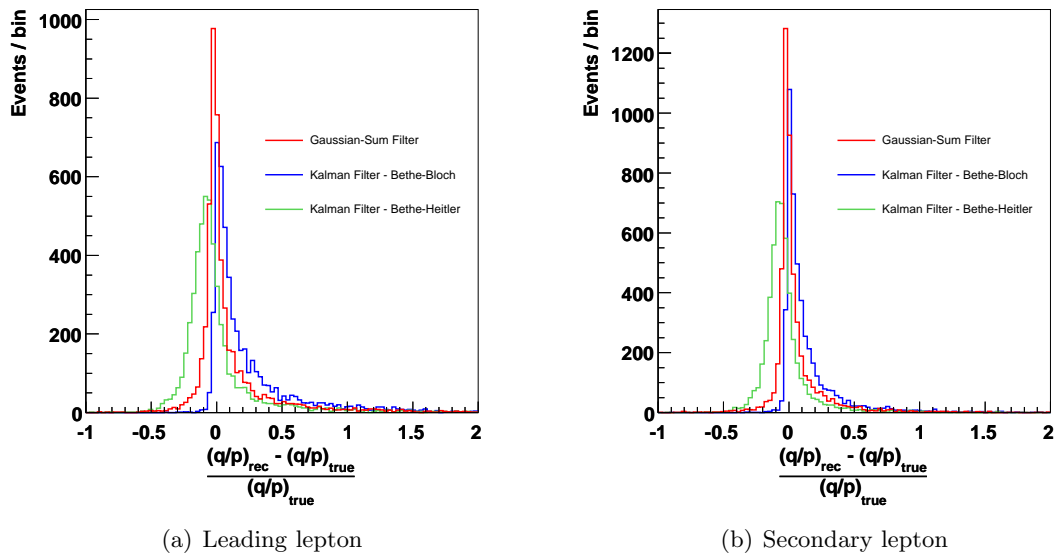


Figure 8.2: Normalised q/p residuals of the two leptons originating from the $J/\psi \rightarrow e^+e^-$ decay. Tracks reconstructed with the GSF (red) are compared with the KF with Bethe-Heitler (green) and Bethe-Bloch (blue) energy loss corrections.

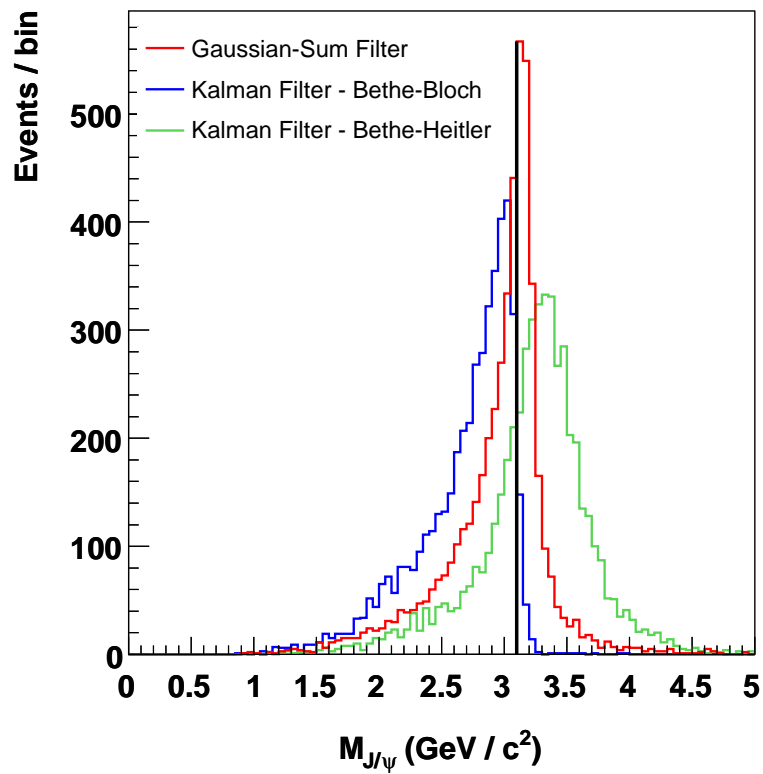


Figure 8.3: The reconstructed invariant mass of the J/ψ meson. Events reconstructed with the GSF (red) are compared with the KF with Bethe-Heitler (green) and Bethe-Bloch (blue) energy loss corrections. The accepted mass of the J/ψ is indicated by the black line.

8.2 $Z \rightarrow e^+e^-$

The Z boson has a mass $91.188 \pm 0.002 \text{ GeV}/c^2$ and a width $\Gamma = 2.495 \pm 0.002 \text{ GeV}/c^2$ [8]. It has an equal probability of decaying into any pair of charged leptons, $BR(Z^0 \rightarrow e^+e^-) = BR(Z^0 \rightarrow \mu^+\mu^-) = BR(Z^0 \rightarrow \tau^+\tau^-) = 1.12\%$. The high rate of Z production at the LHC will contribute to a precise measurement of the W -mass and aid in the calibration of the ECAL.

A sample of 30,000 $Z \rightarrow e^+e^-$ decays has been produced. Figure 8.4 shows the true momenta of the final state leptons. The electron and positron originating from the Z were reconstructed with the GSF and the two versions of the KF discussed in section 8.1.

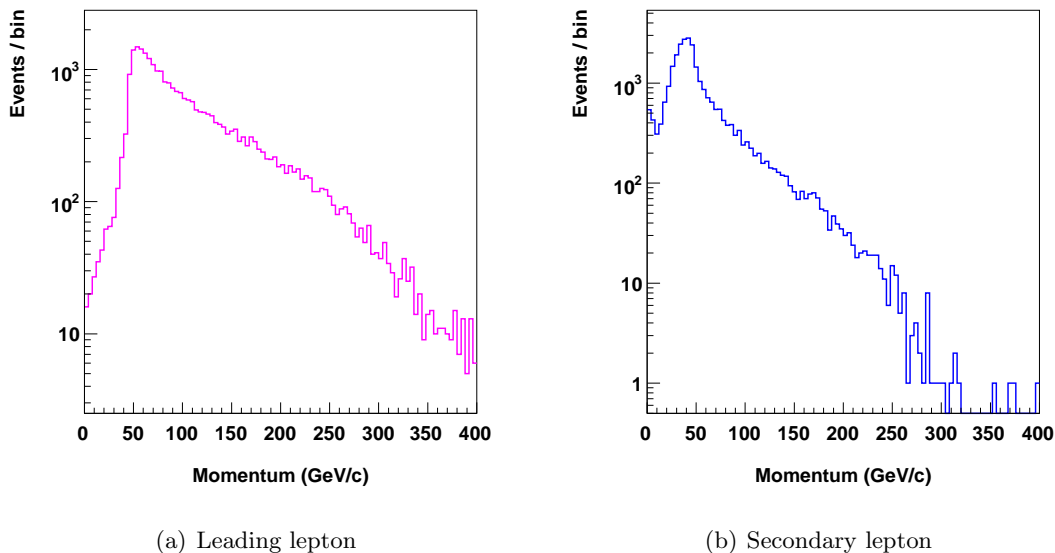


Figure 8.4: Distributions of the true momenta of the final state leptons from the $Z \rightarrow e^+e^-$ decay. The electron and positron are ordered according to their energy. The leading lepton is more energetic than the secondary lepton.

The reconstructed q/p residuals are shown in figure 8.5 and the corresponding effective 1σ and 2σ resolution values are provided in table 8.2. The momentum resolution is worse on the leptons from the Z decay than the J/ψ decay, since the leptons are significantly more energetic.

The invariant mass of the e^+e^- pair is shown in figure 8.6. The peak of the GSF invariant mass distribution is very close to the accepted value of the Z mass. The normalised 1σ and 2σ resolution quantities are provided in table 8.2. There is no significant difference in resolution between the GSF and the KF(BH). The KF(BB) performs worst at both 1σ and 2σ .

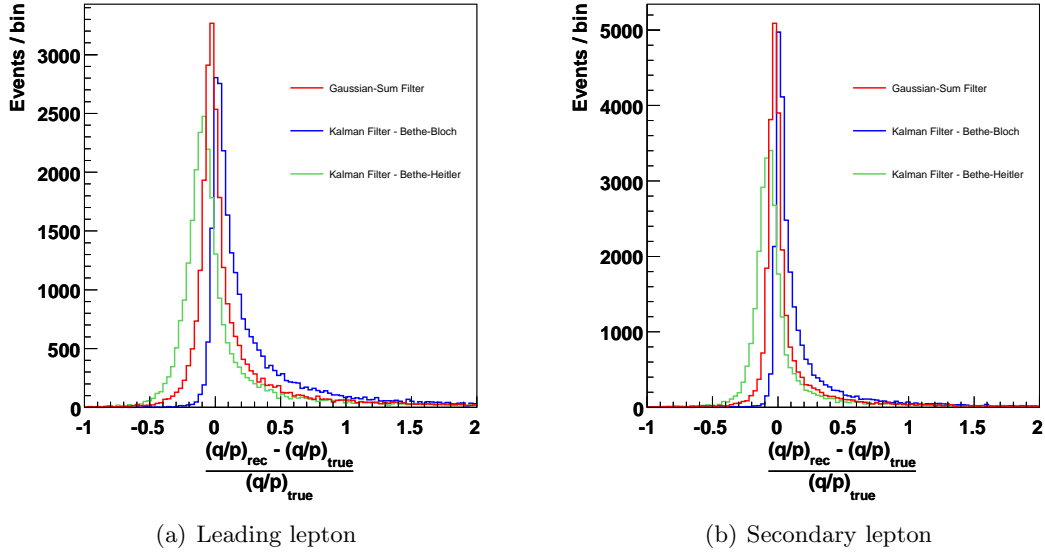


Figure 8.5: Normalised q/p residuals of the two leptons originating from the Z decay. Tracks reconstructed with the GSF (red) are compared with the KF with Bethe-Heitler (green) and Bethe-Bloch (blue) energy loss corrections.

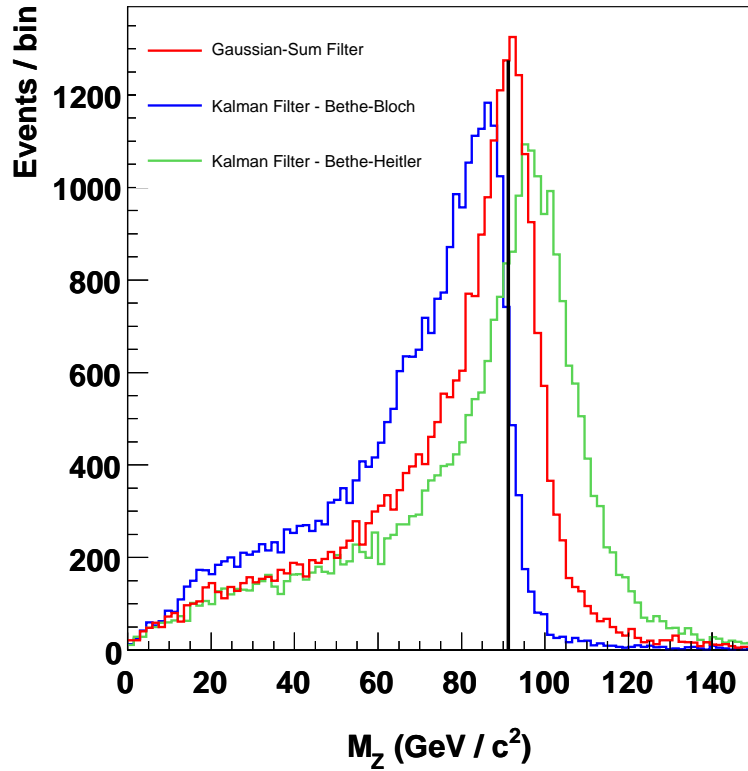


Figure 8.6: The reconstructed invariant mass of the Z boson. Events reconstructed with the GSF (red) are compared with the KF with Bethe-Heitler (green) and Bethe-Bloch (blue) energy loss corrections. The accepted value of the Z mass ($91.2 \text{ GeV}/c^2$) is indicated by the black line.

Fitter		Leading lepton	Secondary lepton	Mass
GSF	1σ	0.185 ± 0.002	0.099 ± 0.001	0.243 ± 0.003
	2σ	2.85 ± 0.04	1.42 ± 0.02	0.750 ± 0.009
KF (BH)	1σ	0.225 ± 0.003	0.153 ± 0.002	0.241 ± 0.003
	2σ	2.53 ± 0.04	1.27 ± 0.02	0.741 ± 0.009
KF (BB)	1σ	0.356 ± 0.005	0.169 ± 0.002	0.335 ± 0.005
	2σ	4.39 ± 0.05	2.14 ± 0.03	0.771 ± 0.009

Table 8.2: Effective 1σ and 2σ resolution quantities for: the reconstructed leptons from the Z decay; and the invariant mass of the e^+e^- pair. Values have been obtained using the GSF and two versions of the KF; one using the Bethe-Heitler (BH) model for energy loss and the other using the Bethe-Bloch (BB) formula. The resolution on the invariant mass is normalised to the accepted value of the Z mass ($91.2 \text{ GeV}/c^2$).

8.3 $H \rightarrow ZZ^* \rightarrow 4e$

ATLAS will search for the Higgs boson across the full allowable mass range ($114.4 \leq m_H \lesssim 1000 \text{ GeV}/c^2$). If $m_H \geq 130 \text{ GeV}/c^2$, the Higgs will be identified through the decay $H \rightarrow ZZ^* \rightarrow 4l^\pm$ ($l = e, \mu$). The momenta of the final state leptons increases with m_H . At low m_H , momentum estimates from the tracker may improve the estimate of the invariant mass.

A sample of 30,000 $H \rightarrow ZZ^* \rightarrow 4e$ decays has been produced with $m_H = 130 \text{ GeV}/c^2$. Figure 8.7 shows the true momenta of the final state leptons. The electrons and positrons are ordered according to their energy. The leading lepton carries the most energy. The trailing lepton is the least energetic.

The leptons originating from the Higgs have been reconstructed with the GSF, KF(BH) and KF(BB). The residual q/p distributions of the four leptons are shown in figure 8.8. The corresponding 1σ and 2σ effective resolution values are given in table 8.3. The resolution deteriorates as the momentum increases. The GSF provides the best 1σ momentum resolution in all cases.

The invariant mass of the four leptons is shown in figure 8.9. The peak of the invariant mass distribution from the GSF is in good agreement with the generated Higgs mass. The normalised 1σ and 2σ resolution quantities are shown in table 8.4. The core from the GSF is narrower than either of the Kalman filters.

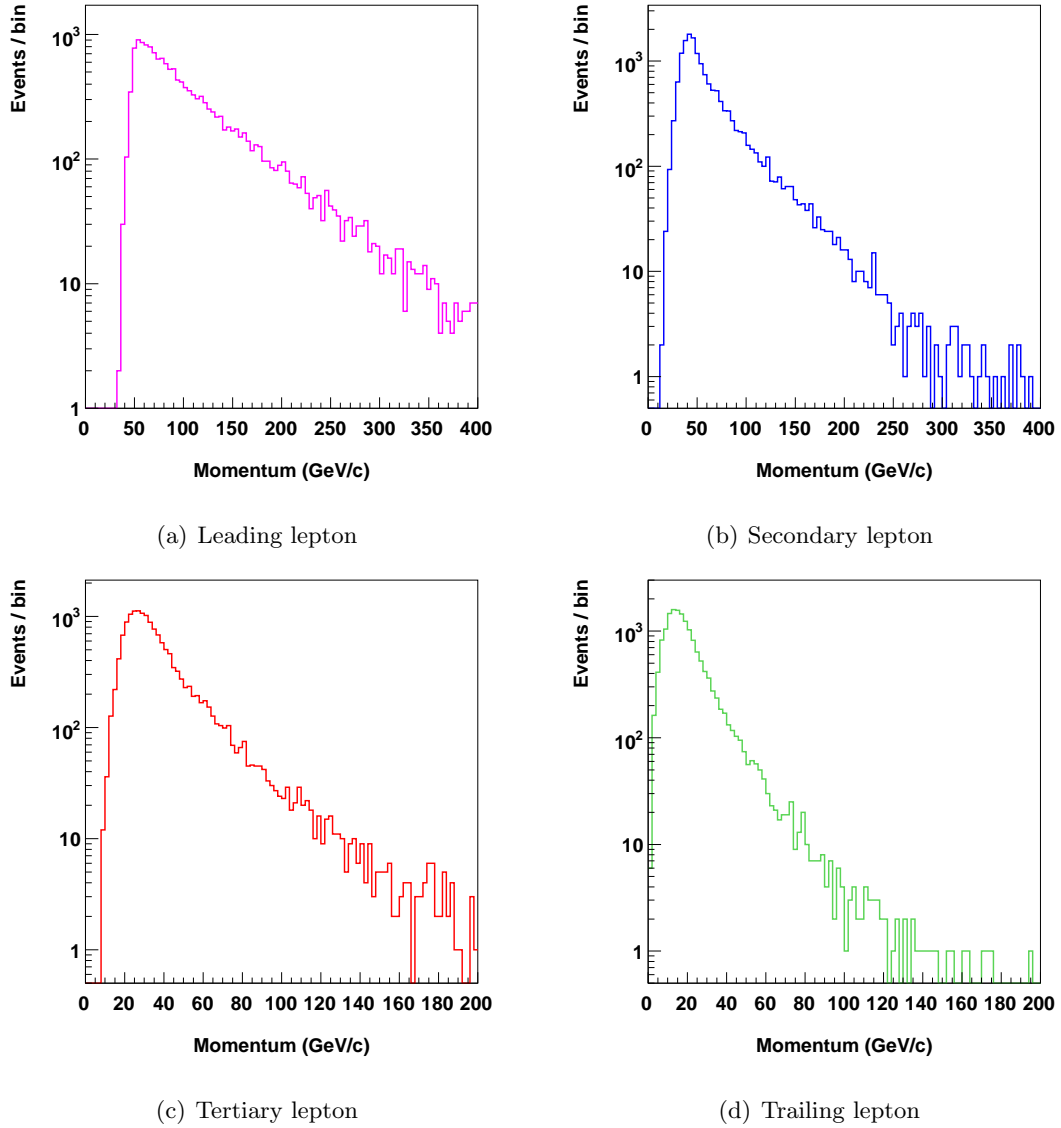


Figure 8.7: Distributions of the true momenta of the final state leptons from the $H \rightarrow 4e$ decay. The electrons and positrons are ordered according to their energy. The leading lepton carries the most energy. The trailing lepton is the least energetic.

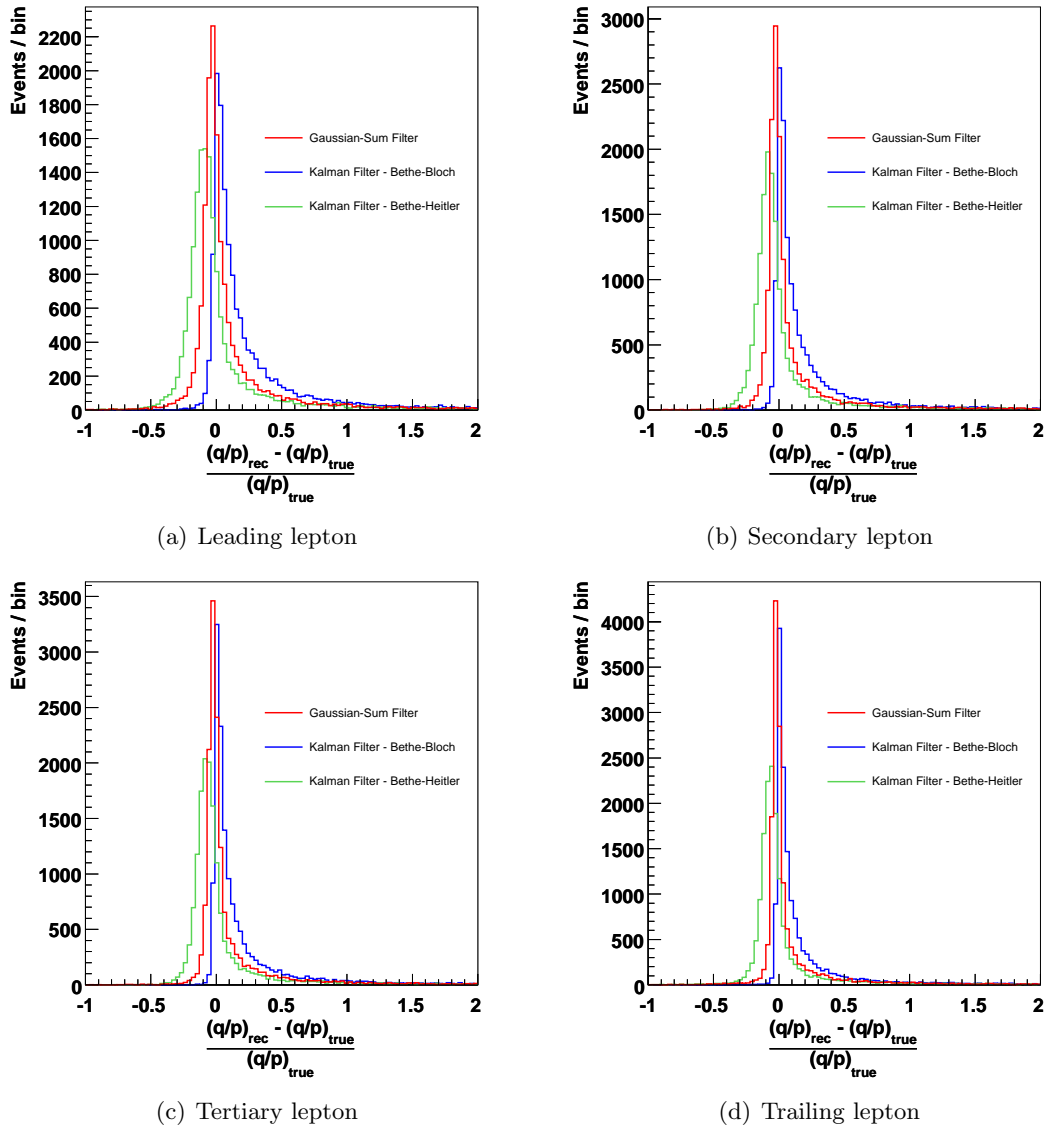


Figure 8.8: Normalised q/p residuals of the four leptons originating from the $H \rightarrow 4e$ decay. Tracks reconstructed with the GSF (red) are compared with the KF with Bethe-Heitler (green) and Bethe-Bloch (blue) energy loss corrections.

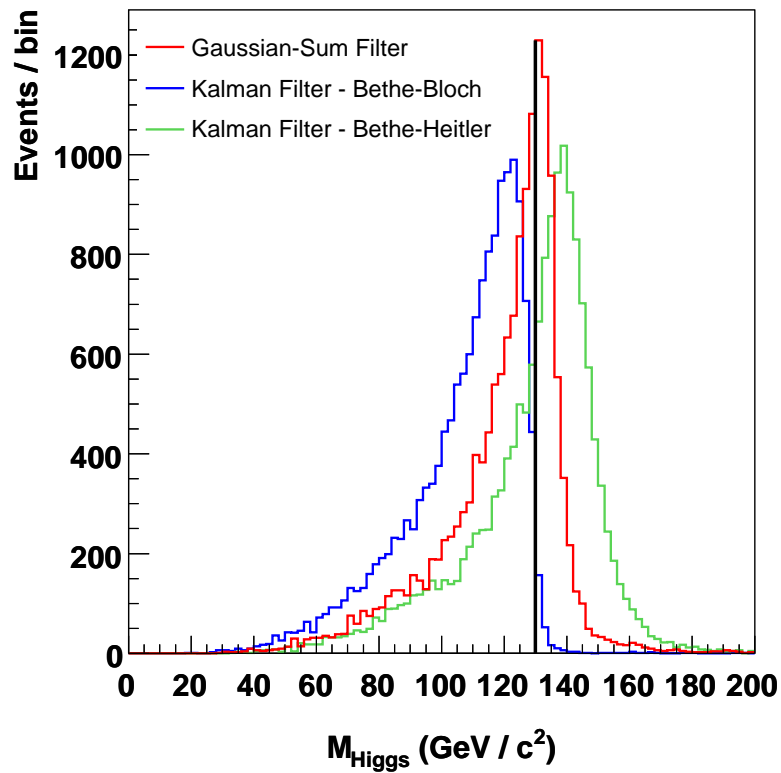


Figure 8.9: The reconstructed invariant mass of the Higgs boson. Events reconstructed with the GSF (red) are compared with the KF with Bethe-Heitler (green) and Bethe-Bloch (blue) energy loss corrections. Higgs bosons were generated with a mass of $m_H = 130 \text{ GeV}/c^2$, indicated by the black line.

Fitter		Leading lepton	Secondary lepton	Tertiary lepton	Trailing lepton
GSF	1σ	0.141 ± 0.003	0.103 ± 0.002	0.085 ± 0.002	0.068 ± 0.001
	2σ	2.14 ± 0.03	1.73 ± 0.03	1.52 ± 0.02	1.16 ± 0.02
KF (BH)	1σ	0.188 ± 0.003	0.155 ± 0.003	0.139 ± 0.002	0.123 ± 0.002
	2σ	1.90 ± 0.03	1.60 ± 0.03	1.35 ± 0.02	1.01 ± 0.02
KF (BB)	1σ	0.274 ± 0.005	0.207 ± 0.004	0.173 ± 0.003	0.134 ± 0.002
	2σ	3.25 ± 0.05	2.70 ± 0.04	2.14 ± 0.04	1.69 ± 0.03

Table 8.3: Effective 1σ and 2σ resolution quantities for the four reconstructed leptons from the $H \rightarrow 4e$ decay. Values have been obtained using the GSF and two versions of the KF; one using the Bethe-Heitler (BH) model for energy loss and the other using the Bethe-Bloch (BB) formula.

Fitter		Mass
GSF	1σ	0.118 ± 0.002
	2σ	0.400 ± 0.007
KF (BH)	1σ	0.131 ± 0.002
	2σ	0.361 ± 0.006
KF (BB)	1σ	0.211 ± 0.004
	2σ	0.475 ± 0.008

Table 8.4: Effective 1σ and 2σ resolution quantities for the invariant mass distributions in figure 8.9. Results are normalised to the generated value of the Higgs mass ($130 \text{ GeV}/c^2$). Values have been obtained using the GSF and two versions of the KF; one using the Bethe-Heitler (BH) model for energy loss and the other using the Bethe-Bloch (BB) formula.

8.4 Tracker / Calorimeter Performance

The complete reconstruction of an electron incorporates both the momentum estimate from the tracker and the energy estimate from the ECAL. The momentum resolution, obtained using the GSF, has been compared with the energy resolution from the calorimeter. While the resolution from the tracker deteriorates with increasing momentum, the energy resolution from the calorimeter improves. The error, σ , on the energy, E , measured in the calorimeter is given by the equation:

$$\frac{\sigma(E)}{E} = \frac{a}{\sqrt{E}} \oplus b. \quad (8.1)$$

For the barrel calorimeter $a \sim 10\%$ and $b \sim 0.2\%$ (section 2.5.1, page 19).

Samples of 6000 single electron events have been produced over the energy range 6 to 40 GeV . The response of the tracker and calorimeter have been determined using the full simulation. The mode of the q/p estimate from the GSF was used in this study. The energy in the ECAL is measured inside a ‘window’ around a hot cell. An ECAL window containing $\eta \times \varphi = 3 \times 7$ cells was used in this study. A comparatively large window size in φ ensures that the majority of the bremsstrahlung photons are collected.

Figure 8.10 shows the energy and momentum distributions for a number of samples. The effective 1σ resolution was determined for both the momentum and energy estimates. Figure 8.11 shows the tracker and calorimeter 1σ resolution as a function of energy. Below 15 GeV the tracker resolution is superior while at higher energies the calorimeter is better. When the KF is used to provide the momentum estimate, the tracker resolution is worse than the calorimeter above $\sim 10 GeV$.

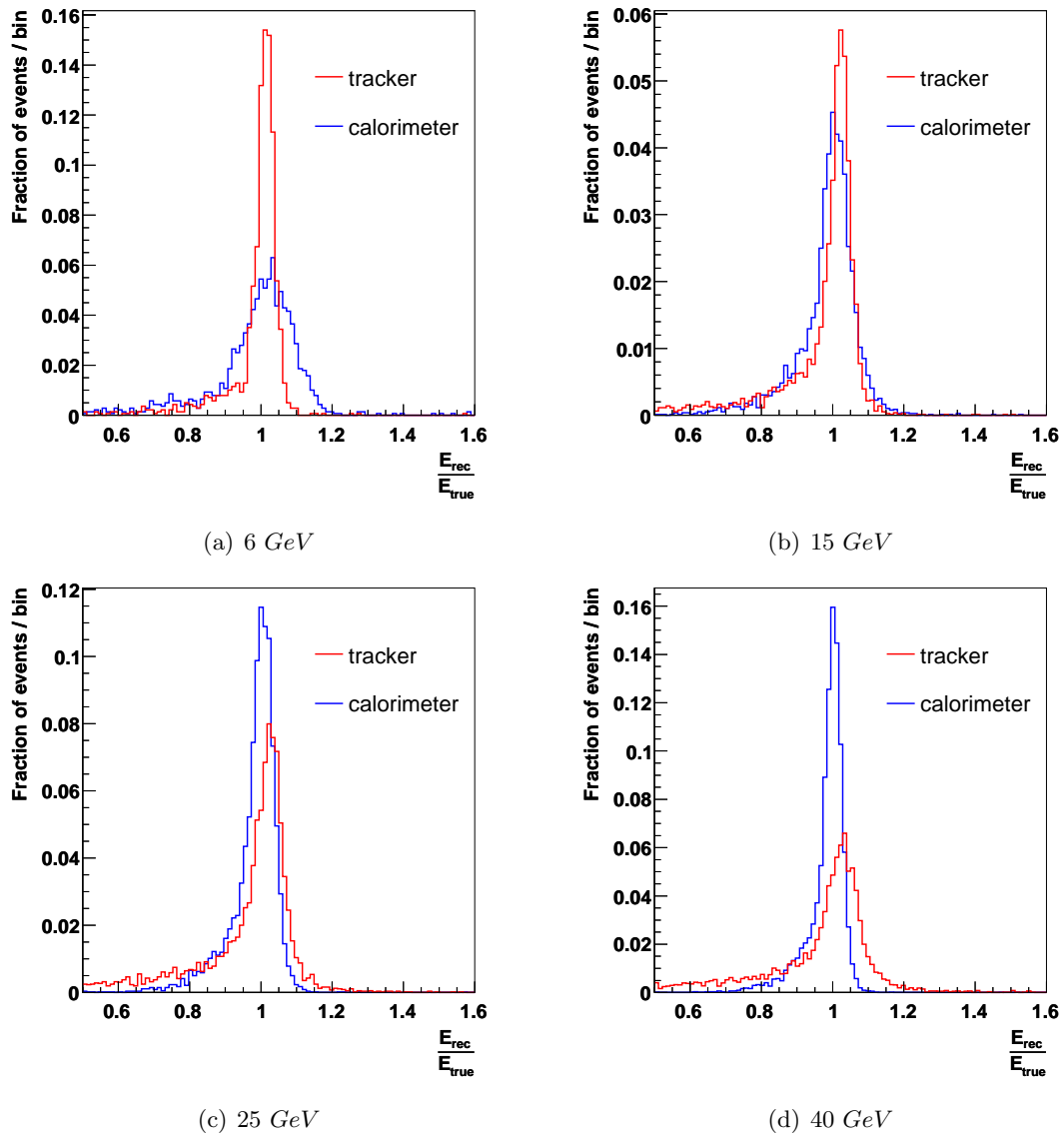


Figure 8.10: Examples of the momentum (tracker) and energy (ECAL) distributions for electron samples at a number of different energies.

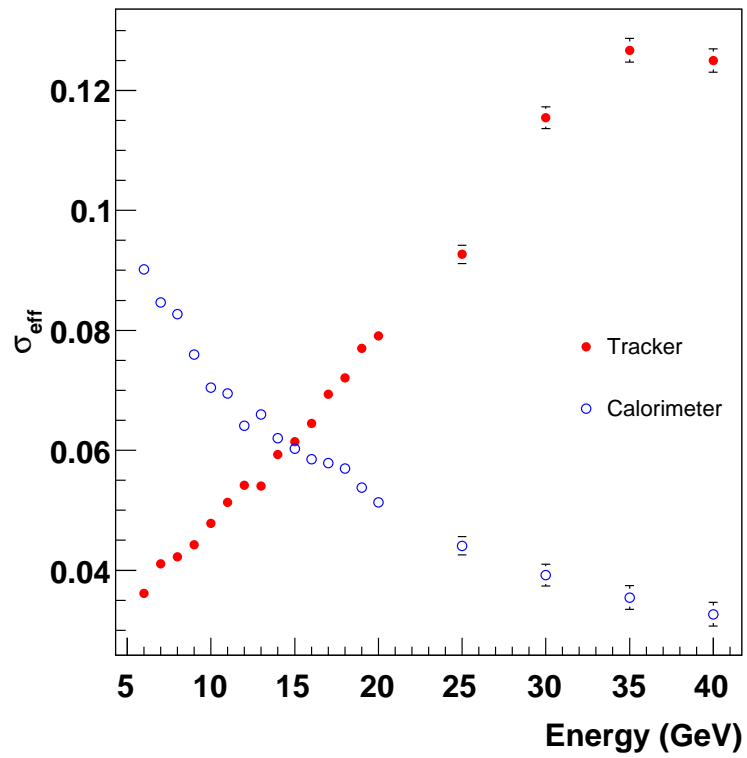


Figure 8.11: The effective 1σ momentum (tracker) and energy (ECAL) resolution as a function of energy.

Chapter 9

Conclusion

ATLAS will commence data-taking by the end of 2007. High p_T leptons facilitate tests of the electroweak sector and searches for the Higgs boson and physics beyond the SM. The importance of leptons is reflected in the design of the electromagnetic calorimeter and tracker, which together are used to identify and reconstruct electrons.

9.1 Summary

In this thesis, an examination of electron reconstruction performance using just the inner detector has been presented. There are two main aspects to this investigation: the study of the simulated response of the ATLAS tracker (chapters 6 and 8); and the analysis of data taken at the 2004 test-beam (chapter 7).

The baseline fitter for track reconstruction in ATLAS is a least-squares estimator. Both a global version of the LSE and a recursive version - the Kalman filter - are used by track reconstruction algorithms. The LSE performs optimally only when all measurement errors and material interactions can be described as gaussian probability density functions. Electrons lose energy in matter predominately by bremsstrahlung, which is modelled by the Bethe-Heitler distribution. The highly non-gaussian nature of the Bethe-Heitler pdf implies that non-linear track fitters may provide better estimates of the track parameters of electrons than the LSE.

The development, implementation and performance of a gaussian-sum filter, for the reconstruction of electrons, have been addressed in detail. The GSF uses a weighted gaussian sum to approximate the Bethe-Heitler distribution. Consequentially, the estimate of the track state is a multivariate pdf with an arbitrary number of gaussian components. Corrections

for radiative energy loss, incorporated during the fit, lead to an exponential increase in the number of components in the GSF track state. So that the size of the state remains computationally manageable, the number of components must be artificially regulated by a component reduction technique.

9.1.1 Monte-Carlo Studies

The GSF was validated initially using samples of single electrons in the tracker. Using a simplified version of the simulation (section 6.2, page 75), it was shown that the quality of the momentum estimate depends strongly on the size of the track state after component reduction. No statistically significant improvement in the resolution was obtained when more than 12 components were retained. Gaussian mixture approximations to the Bethe-Heitler pdf have been obtained by minimising either the Kullback-Leibler distance (KL-mixtures) or a cumulative distribution function (CDF-mixtures). Results obtained using CDF-mixtures, yielded consistently better resolution quantities than KL-mixtures.

The full simulation was used to compare the performance of the various track fitters. The momentum estimate from the GSF has been compared to versions of the LSE both with and without corrections for radiative energy loss. In order to make a comparison between the performance of the GSF and the KF, a single value of momentum must be extracted from the track state of the GSF, destroying a significant amount of the information in the mixture. The performance of the GSF has been determined using both the mean and most probable value of the momentum pdf.

Both the GSF and KF exhibit long tails in the momentum distribution due to irrecoverable bremsstrahlung occurring close to the beam-pipe. For samples of electrons distributed uniformly over the entire tracker (table 6.9, page 92), the mode of the GSF track state produces the optimal momentum resolution when considering only events close to the peak. The tail of the momentum distribution is best reconstructed using either the mean of the GSF track state or the version of the KF which incorporates corrections for radiative energy loss. The version of the LSE without corrections for bremsstrahlung is consistently the worst performing filter but provides competitive estimates of the momentum in the central tracker, where radiative energy losses are less significant (section 6.3, page 79).

The execution time of the GSF is greater than that of the KF by a factor of $\mathcal{O} 100$. The CPU-intensive nature of the GSF has important consequences for its use in the reconstruction of ATLAS events: it cannot be applied to every track, both because it takes far too long; and the energy-loss model used by the GSF is appropriate only for electrons. The GSF should be applied to a selection of electron candidates which have been identified by a preliminary particle identification algorithm.

Additionally, the performance of the GSF has been assessed using simulated LHC events. The decays $J/\psi \rightarrow e^+e^-$ and $Z \rightarrow e^+e^-$ have been examined as they are used extensively in calibration algorithms and physics analyses. The ‘golden decay mode’ of the Higgs boson, $H \rightarrow 4e$ ($m_H = 130 \text{ GeV}/c^2$), has also been investigated. The GSF provides the optimal, tracker based, estimate of the mass of the parent particle in all cases.

9.1.2 Test-beam Studies

The 2004 test-beam gave a realistic estimate of the detector response prior to commissioning. The reconstruction of test-beam data provided an excellent test for the GSF, allowing the sensitivity of the fitter to misalignment and uncertainties in the material distribution to be determined. The momentum resolution in real data was shown to be much worse than predicted by simulation because of the poor detector alignment and material in the beam-line upstream of the CTB.

The material upstream of the detector has a significant impact on the electron momentum distributions. Additionally, the amount of material must be known precisely for correct calibration of the ECAL. Some of the upstream material is contained within the beam-line quadrupoles. While the amount of material has been determined by direct measurement, the dynamics of bremsstrahlung in the quadrupole field can create a perturbation on the trajectory of an electron, preventing it from triggering the detector.

Tails in the electron momentum distributions, which arise due to catastrophic bremsstrahlung, were used to infer the effective amount of material in the beam-line. The results indicated that electrons which undergo considerable energy loss within the quadrupoles are perturbed sufficiently to exclude them from the experimental trigger. From the shape of the momentum tails in the data, the apparent amount of upstream material is consistent with the measured material between the quadrupoles and the detector. No evidence of energy loss inside the quadrupoles is observed.

Unlike the electrons which undergo catastrophic bremsstrahlung in the quadrupoles, those which experience only a small amount of energy loss are likely to be accepted by the trigger. The tracker based approach is insensitive to these electrons since they do not have a significant affect on the shape of the tail profile of the momentum distributions.

The calorimeter has also been used to determine the amount of upstream material. Unlike the tracker, it is sensitive to soft bremsstrahlung in the quadrupoles. The effect of energy loss in the quadrupoles is therefore evident in the energy distributions of the calorimeter while absent from the tracker based observations.

Appendix A

The SCT Outer End-cap Module

An brief summary of the SCT is provided in section 2.4.2 (page 17). In this appendix, a discussion of the geometry of a SCT outer end-cap module is presented (section A.1) followed by an explanation of the module assembly procedure implemented at the University of Melbourne (section A.2).

A.1 Design of the SCT Outer End-cap Module

An illustration of a SCT outer end-cap module [56] is shown in figure A.1.

The module is comprised of four silicon detectors [57], in two planes, placed back-to-back. Each detector has 768 microstrips. Aluminium wire bonds form the electrical connections between the microstrips on the two coplanar silicon detectors. The wafers are affixed to the module spine, which is made of TPG - because of its excellent thermal conductivity - and aluminium nitride, for mechanical stability.

The electronic readout is facilitated by 12 ABCD [58–60] chips, each with 128 channels. The chips are mounted on a wrap-around hybrid which is thermally decoupled from the detectors. Four fan-ins on the module electrically connect the chips to the microstrips.

On each module there are two mounting points: a circular hole and an elongated slot.

A.1.1 Wafer Positioning and Alignment

The silicon detectors must be positioned accurately, since alignment corrections at the level of individual wafers are not foreseen in the reconstruction software.

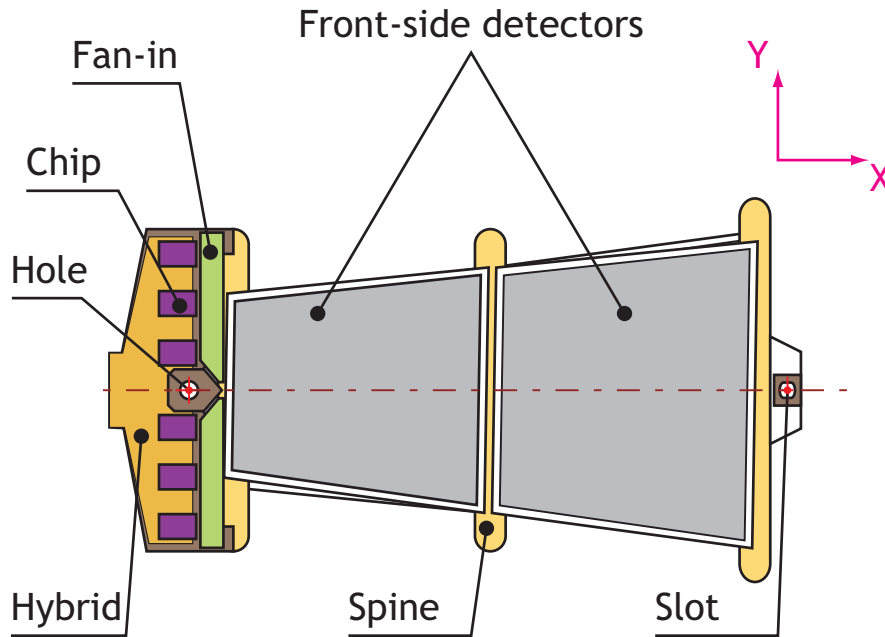


Figure A.1: Layout of a SCT outer end-cap module.

A set of 13 parameters [61] uniquely determines the geometry of the module in the silicon (XY) plane. An explanation of these parameters is given in figure A.2.

The thickness and flatness of the module are determined from a survey of 100 measurements of the height of the detectors above and below the mounting points.

The nominal values of the 13 XY design parameters and their tolerances are given in table A.1. The module thickness specifications are also provided.

A.2 Melbourne Assembly Procedure

A number of institutions / universities (CERN, Geneva, Valencia, Melbourne and a UK consortium) were involved in the construction of SCT outer end-cap modules. The Melbourne procedure for assembling a module has a number of steps:

- **Wafer-spine assembly:** The four silicon detectors are aligned and glued to the spine. This is the most challenging aspect of the assembly due to the precision placement of the wafers. An explanation of the technique used at Melbourne is given in section A.2.1.
- **Hybrid attachment:** The hybrid and fan-ins are glued to the spine.
- **Wire Bonding:** There are 4612 wire bonds required on every module: 768 per side to

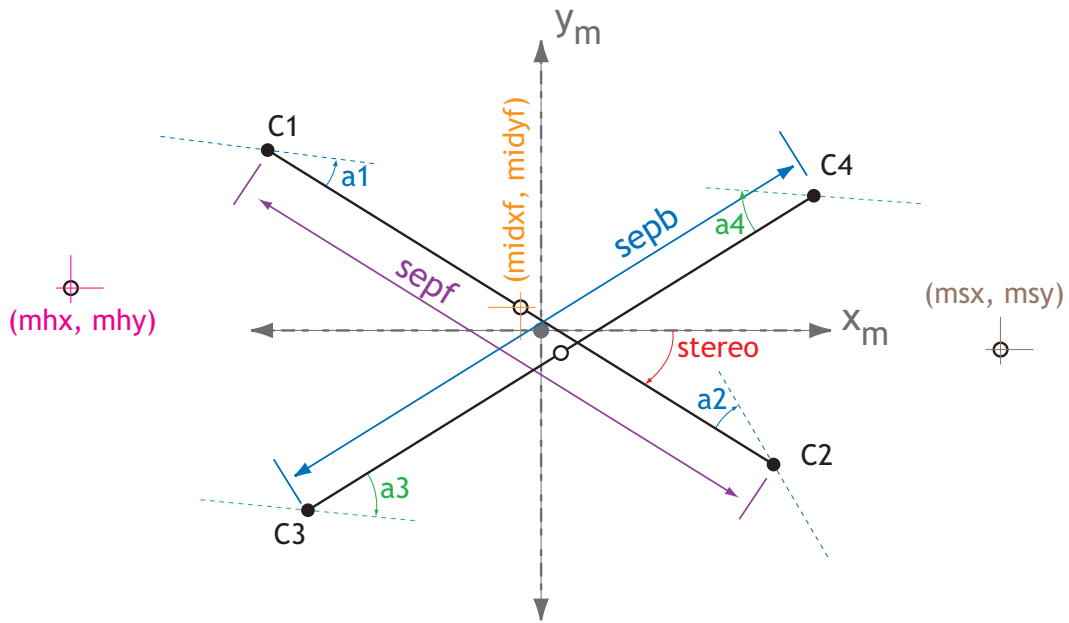


Figure A.2: Definition of the parameters which describe the XY geometry of a SCT module. A two dimensional, silicon-centred coordinate system (x_m, y_m) is established from the positions of the four detectors. The origin is the average of the centres of the wafers. Lines joining the centres of the two front-side detectors ($C1$ and $C2$) and two back-side detectors ($C3$ and $C4$) are constructed and the angle between them is determined. The x_m -axis bisects this angle. Positive x_m points towards the slot (away from the beam-line). The *stereo* angle is defined as the angle between the x_m -axis and the line constructed from the centres of the front-side silicon (the angle between the x_m -axis and the line from the back-side silicon is $-stereo$ by construction). Two coordinates describe the position of the hole (mhx, mhy) and slot (msx, msy) . The mid-point of the two front-side detectors is $(midxf, midyf)$. The separation of the two front (back) side wafers is $sepf$ ($sepb$). The relative orientation of the four detectors is given by a rotation about the wafer centre ($a1 - a4$).

XY Parameters		
Parameter	Nominal	Tolerance
mhx (μm)	-78139	20
mhy (μm)	0	20
msx (μm)	62241	100
msy (μm)	0	20
midxf (μm)	0	10
midyf (μm)	-40	5
sepf, sepb (μm)	61668	10
a1 - a4 ($mrad$)	0.00	0.13
stereo ($mrad$)	-20.00	0.13
Z Parameters		
front z (μm)	875	115
back z (μm)	-375	115

Table A.1: SCT outer end-cap module mechanical specifications. The tolerance on the Z survey parameters corresponds to the maximum allowable deviation from the nominal value for any of the 100 survey points on the module.

daisy-chain the microstrips on the two detectors; 768 per side to join the detector to the fan-ins; 768 per side to join the fan-ins to the chips and; two bias lines per side.

- **Electrical Characterisation:** The module is tested for electrical functionality.
- **Thermal Cycling:** Temperature fluctuations occur when the power or cooling to the module is switched on or off. The completed module's resilience to deformation under thermal fluctuation is assessed in a number of thermal cycles.

A.2.1 Wafer-Spine Assembly

The procedure used in Melbourne to align the detectors and attach them to the spine was unique: unlike other institutions, both the front and back side silicon detectors were glued to the spine at the same time. Figure A.3 shows the module assembly station.

Each silicon wafer is marked with fiducials in every corner so that the orientation of the detector in space can be resolved. Four cameras on the assembly station each monitor the positions of two fiducials in real time (figure A.4). The magnification of each camera and its position in space are determined using a two step calibration procedure [62].

Once the assembly station has been calibrated, the silicon wafers are transferred to four chucks. The chucks are mounted on motorised carriages which can move away from the central frame, allowing easy access. The chucks are adjusted manually until the detectors are correctly orientated. A glue pattern is applied to a module spine which is then inserted into the central frame. The carriages are driven up to the central frame and the wafers adhere to the spine.

After curing, the hybrid and fan-ins are attached to the silicon-spine subassembly. The placement accuracy of these components is considerably less stringent than for the wafers and can be achieved using mechanically machined tooling.

The module is then mounted on a specially designed metrology jig. A coordinate measuring machine (CMM) determines the positions of all the fiducials as well as the hole and slot. The CMM can only measure one side of the module at a time. Therefore the metrology jig is invertible and incorporates four glass (reference) fiducials which can be imaged from both sides. The reference fiducials are measured along with the silicon fiducials so that the positions of the measurements on the back-side of the module can be determined with respect to those on the front.

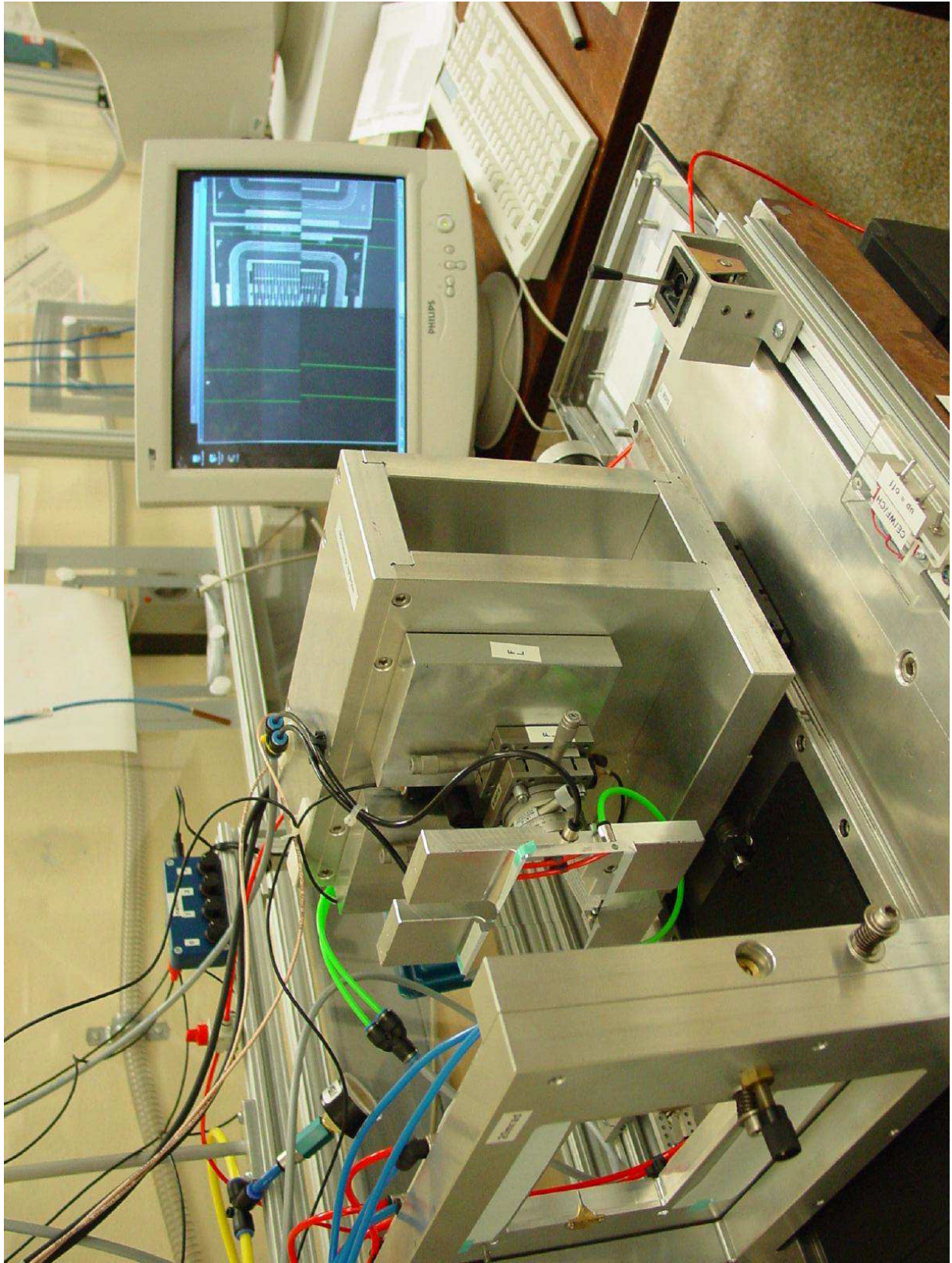


Figure A.3: The SCT outer end-cap module assembly station at the University of Melbourne.

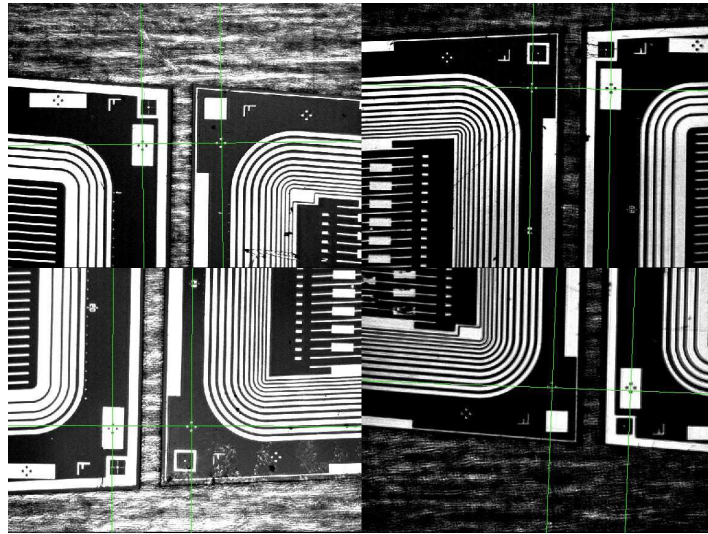


Figure A.4: Image of the four silicon wafers on the assembly station. The cameras on the assembly station monitor the positions of four fiducials.

A.3 Representations of the Module Geometry

The 13 parameters in table A.1 are one representation of the XY geometry of the module. The assembly station and CMM both use different representations, largely for convenience.

A.3.1 Assembly Station Representation

The assembly station reports the geometry of a module as a set of 16 parameters (table A.2). The explanation of the parameters is provided in figure A.5. The parameter set incorporates some redundancy, but it is preferred to the design representation since these parameters are more strongly correlated with the adjustment of individual chucks.

```

#Input data: Build
stereo_f      -19.9998
cor_f_x       76132.9
cor_f_y       0.0942275
iwd_f_t       700.54
iwd_f_b       700.54
fidy_f_t      -0.00969594
fidy_f_b      -0.00969594
iwa_f         0
stereo_b      19.9998
cor_b_x       76132.9
cor_b_y       -0.0942275
iwd_b_t       700.54
iwd_b_b       700.54
fidy_b_t      0.00969594
fidy_b_b      0.00969594
iwa_b         0

```

Table A.2: The assembly station representation of the XY geometry of a module.

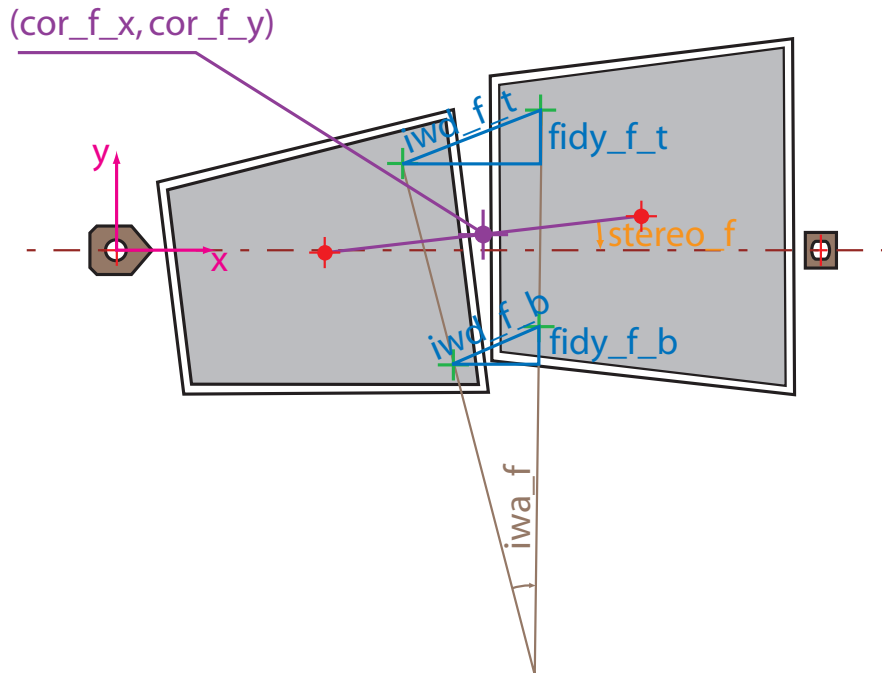


Figure A.5: The eight front side parameters, reported by the assembly station, describing the geometry of a module. Each one has a corresponding back-side parameter. The centre of rotation of the front-side silicon (cor_f_x , cor_f_y) and the stereo angle ($stereo_f$) are expressed with respect to the coordinate system defined by the hole and slot. The positions of the hole and slot are determined during the calibration of the assembly station since no camera directly images them.

```

#Input data: Metrology
# fn | x | y | dx | dy
1      14267.1      -26449.8      0.0102815      0.0130585
3      79151.7      -31836.2      0.0124667      0.0154572
5      80429.5       31691.5      0.117865       0.00817217
7      15380.8       28919.4      0.0120531      0.102634
11     79851        -31849.9     0.00266572     0.0108757
13     136724       -36574.8     0.00573994     0.0267708
15     138144        34111       0.00285441     0.00633077
17     81128.6       31677.7     0.0145785     0.00840406
41     -62961.4      -40166.6     0.949321       0.949321
42     156794       -39702.9     1.02109        1.02109
43     156675       40299.2     1.0312         1.0312
44     -63419.7     39862.6     1.06607        1.06607
49     0            0           0              0
50     140408        0           0.793807       0.0928383
51     15374.2      -28895.9     0.0247928     0.000948426
53     80421.8      -31687.3     0.10837        0.0433076
55     79163        31841.5     0.00436792     0.00409374
57     14276.8       26474.2     0.112562       0.0564274
61     81122.3      -31672.7     0.00182772     0.00503375
63     138138       -34120.4     0.0970959     0.0769044
65     136734       36566.5     0.112475       0.0927915
67     79860.1       31855.7     0.107516       0.0664362
91     -62961.5      -40166.2     1.03963        1.03963
92     156794       -39703.7     0.99354        0.99354
93     156676       40300       1.03677        1.03677
94     -63421.4     39862.2     1.04377        1.04377
# End data

```

Table A.3: Metrology representation of the XY geometry of a module. The positions of all silicon and glass fiducials as well as the hole and slot are expressed in the hole-slot coordinate system.

A.3.2 Metrology Coordinates

The CMM establishes a coordinate system with an origin at the centre of the hole. The x -axis connects the origin to the centre of the slot. The labelling convention for the module fiducials, hole, slot and glass fiducials on the metrology jig is illustrated in figure A.6. The positive y -axis points towards glass fiducial 41 (91). The CMM determines the positions of all the silicon and glass fiducials (table A.3) and performs the Z -survey (table A.4).

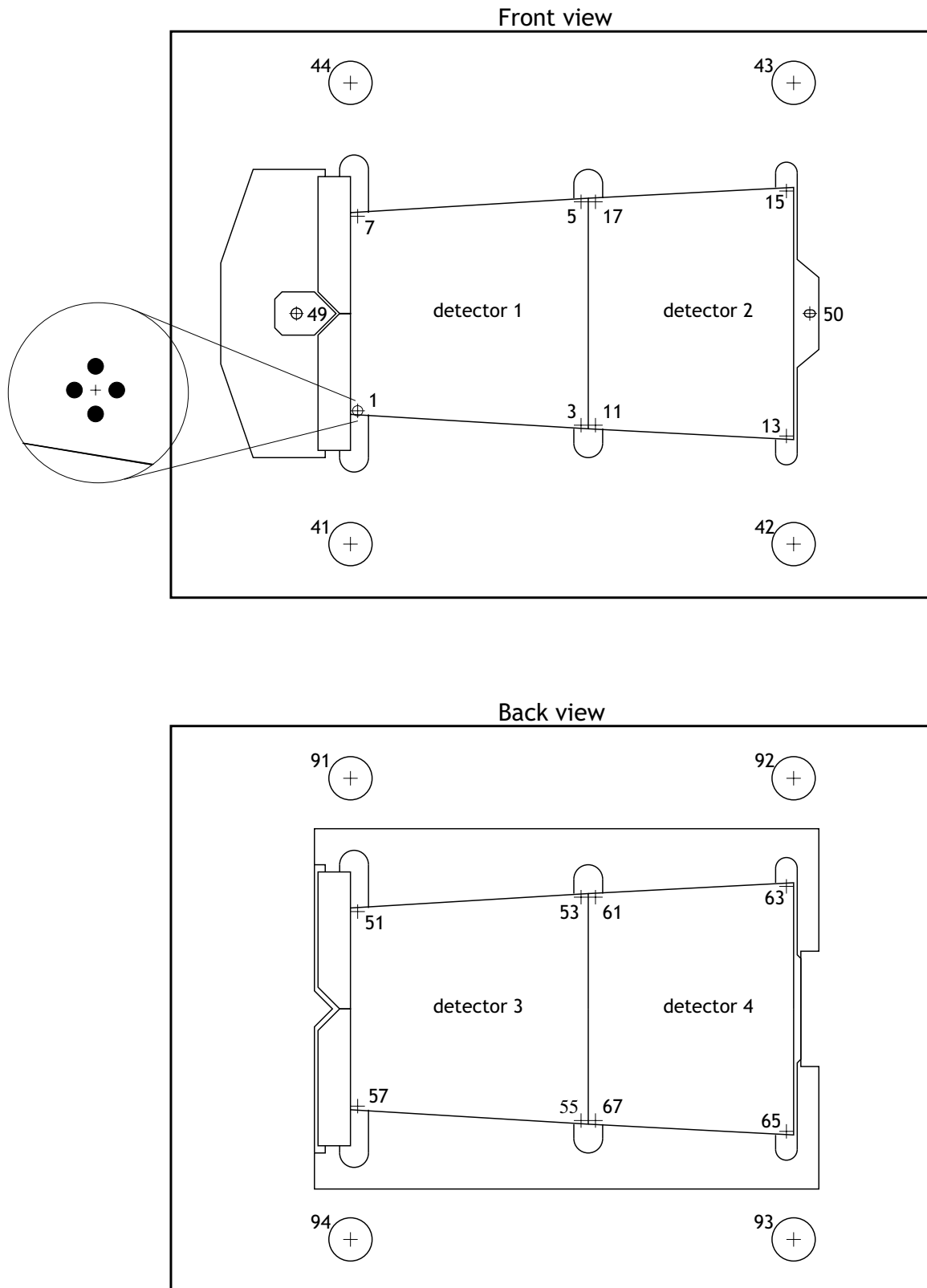


Figure A.6: Layout of a module on the metrology jig. The hole (slot) is labelled 49 (50). The measurements of the glass fiducials on the front (back) side are labelled 41 - 44 (91 - 94).

```
#Input Z data: Metrology
# no | x | y | z
0      14.2671      -26.4498      0.880865
1      14.5456      -12.6075      0.886829
2      14.824       1.23479      0.887621
...
99     147.759     -35.8139     0.391977
```

Table A.4: Metrology representation of the Z -profile of a module.

A.3.3 Module Measurement Software

There are three important representations of the XY geometry of a module: the design representation (table A.1), the assembly representation (table A.2) and the metrology representation (table A.3). The module measurement software provides the transformations between the three conventions. For one input representation, all the others are determined and stored. The software also analyses the Z -survey data, ensuring that all points are within design specifications.

The module measurement algorithm is called SAS (SCT analysis software) [63]. It has been implemented in the C programming language. As well as performing the transformations between the various representations of the geometry, the software also catalogues centrally all the data recorded from the assembly station and CMM. A unique identification number, the name of the module, location of the file and source of the data are all recorded. The layout of the catalogue is shown in figure A.7.

An example of how to run the module measurement software is provided in figure A.8. The software is available from [63]. Both interactive and batch modes are supported. The only necessary input in either case is the identification number of the data set to be processed. The module measurement software appends or recreates the file with the additional representations.

```
# File name: moduleDatabase.txt
# File created: April 2 2003
# File contents: Database information for module builds
# SAS ID | Module name | File created | Data location | Data origin
1000    AL24      20021212.1315  /home/tatkinson/atlas/assembly/      Assembly
1001    AL24      20030331.1501  /home/tatkinson/atlas/metrology/      Metrology
1002    ID         20030424.1435  /data/1/sctdata/sas/                  Unofficial
1003    ID         20030424.1502  /home/tatkinson/atlas/metrology/      Unofficial
1004    ID         20030424.1515  /home/tatkinson/atlas/metrology/      Unofficial
```

Figure A.7: The SCT module geometry catalogue.

```
tatkinso@onefish:~/sctprod/sas> sas -h

(S)CT (A)nalysis (S)oftware
Innovative computer solutions for the banana millenium
Version: 3.1.3
Last code modification: 10:46:44 Monday February 23, 2004
Usage:
(1) Manual Mode > sas
(2) Batch Mode > sas -b <sas identifier number> [back-front correction flag]
(3) SAS Version > sas -v, > sas --version

tatkinso@onefish:~/sctprod/sas> sas -b 2413
```

Figure A.8: Commands to run the module measurement software.

A.3.4 Control Software for the CMM

The CMM is a *Mitutoyo Quick Vision Pro V606* [64] (figure A.9). Table A.5 provides the key specifications of the machine. It is controlled by propriety *Visual Basic* libraries. An automated control algorithm has been implemented to measure the mechanical properties of a module. A graphic user interface (GUI) has also been developed, ensuring that the CMM is simple to use (figure A.10). The software is available from [65].

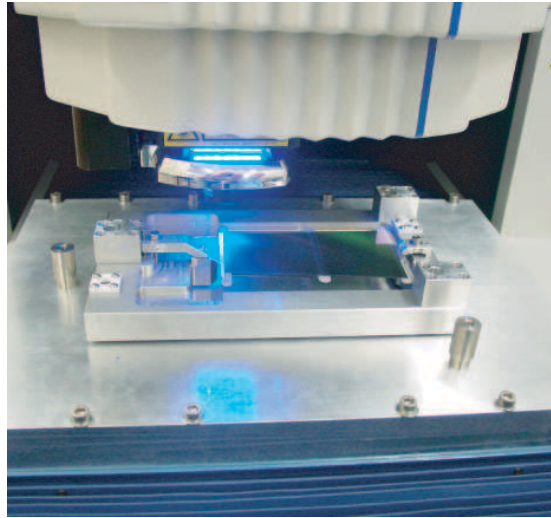


Figure A.9: The Melbourne CMM, shown here surveying a SCT module.

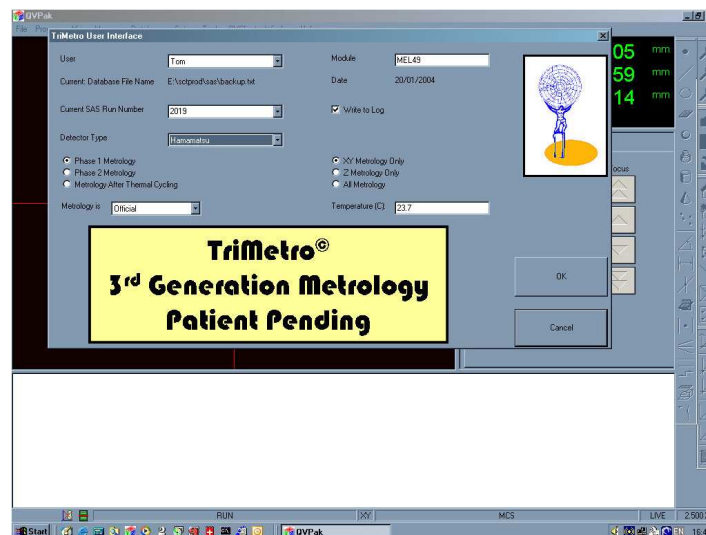


Figure A.10: The control GUI for surveying SCT modules with the Melbourne CMM.

Parameter	Specification
X resolution (μm)	0.8
Y resolution (μm)	0.8
Z resolution (μm)	3
Drive speed (mm/sec)	200
Measurement range ($X \times Y \times Z mm^3$)	$600 \times 650 \times 250$

Table A.5: Key specifications of the Quick-Vision Pro 606.

A.3.5 Results

The module measurement software and the CMM control algorithms were used extensively in the construction of SCT outer end-cap modules. The list of successfully completed modules, with their mechanical and electrical properties, is provided in [66].

Appendix B

GSF Implementation and EDM

The design of the ATLAS software framework (Athena [26]) reflects the challenges faced by LHC experiments: large volumes of data produced by the detectors; the longevity of the experiments; and a significant number of developers and users. A central feature of Athena is the delineation of algorithms and data structures, ensuring that the access and handling of data is independent of the specific procedure taken in event simulation or reconstruction.

The *event data model* (EDM) is the *C++* implementation of the data structures. A key feature of the tracking EDM [39] is a common track class which contains all the information necessary to characterise the trajectory of a charged particle in the inner detector or muon spectrometer. Tracking fitting tools, such as the GSF (chapter 5), use track data objects as input and output.

This appendix contains a brief introduction to the common track class (section B.1) as well as a description of the procedure required to configure the GSF (section B.2) and perform a track fit (section B.3).

Henceforth the names of *C++* classes are denoted in `courier face`.

B.1 The Common Track Class

The common track class (`Track` [67]) is sufficiently flexible that it can represent a track in a variety of ways. The most simple description is a single set of track parameters. A more complete representation incorporates the measurements from which the track parameters were derived, the quality of the fit, and the name of the algorithm used to create the track (the ‘author’).

The trajectory of a particle intersects many ‘surfaces’ in the detector. These correspond either to detector elements, inert material or can be entirely abstract constructions such as the perigee. It is useful to express the trajectory at these surfaces. Therefore the `Track` class contains a collection of `TrackStateOnSurface` [67] objects.

A `TrackStateOnSurface` can comprise pointers to the objects:

- `TrackParameters` [68]: The description of the trajectory at the surface.
- `MeasurementBase` [69]: An abstract base class representation of a measurement. The different detector subsystems produce different types of measurement. Each is a concrete implementation of the abstract base class. `TrackStateOnSurface` also incorporates a flag to denote a measurement as an outlier.
- `FitQualityOnSurface` [70]: The fit quality of the track with respect to the measurement.
- `ScatteringAngleOnSurface` [67]: A material interaction perturbing the trajectory of the track.

B.1.1 Extended representations of trajectory

The trajectory can, in most cases, be adequately described by a single `TrackParameters` object. This representation is used by track fitters to provide the optimal description of the trajectory in the case where all measurement errors and process noise are gaussian distributed. In the case of non-gaussian effects, a more general usage of `TrackParameters` objects must be employed. A technique commonly used by fitters such as the GSF, to approximate non-gaussian distributions, is to use a weighted gaussian sum. The `MultiComponentState` [71] class is used to describe such gaussian mixtures. It is a list of `TrackParameters` objects, each with a corresponding weight (figure B.1).

So that a gaussian-mixture description of the trajectory can be expressed at surfaces within the detector, an extended representation of `TrackStateOnSurface` is required. The class `MultiComponentStateOnSurface` [71] inherits from `TrackStateOnSurface`. In addition to the information held by the base class, it contains a pointer to a `MultiComponentState` object. This inheritance structure is transparently incorporated into the common track class (figure B.2).

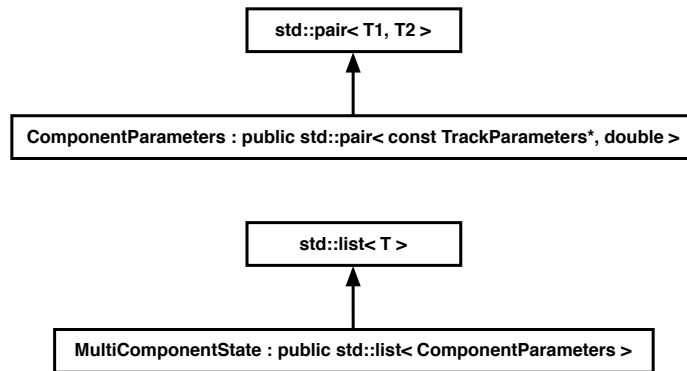


Figure B.1: Inheritance structures of the `ComponentParameters` and `MultiComponentState` classes. Each component has a pointer to a set of `TrackParameters` and a `double` representing the relative importance of the component in the mixture.

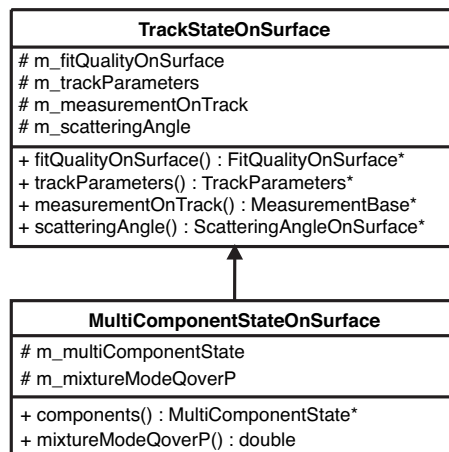


Figure B.2: The inheritance structure and most important data members and methods of the `TrackStateOnSurface` and `MultiComponentStateOnSurface` classes.

B.2 Configuring the GSF

The GSF has been implemented in the Athena framework [44]. It is configured using *Python* [32] classes:

B.2.1 Extrapolator

The most complex aspect of the GSF is the *extrapolator*. It is responsible for the geometric propagation of the track through the detector, incorporating corrections due to material interactions and the regulation of the size of the track state.

1. The extrapolator configuration classes are loaded:

```
include('TrkExTools/ExtrapolationConfiguration.py')
```

2. The magnetic field of the inner detector is defined:

```
InDetMagField = ConfiguredMagneticFieldTool( 'InDetMagField' )
InDetMagField.printInfo()
```

3. A propagator is configured to transport the trajectory parameters and the error matrix to different surfaces within the detector. The appropriate choice for an inhomogeneous magnetic field is a *Runge-Kutta* [38] propagator:

```
InDetPropagator = ConfiguredPropagator( 'Trk::RungeKuttaPropagator',
                                         'InDetPropagator' )
InDetPropagator.printInfo()
```

4. The tracking geometry [39] is built. This is a hierarchical collection of volumes enclosing different parts of the detector. A *TrackingVolume* [72] can contain an array of *Layer* [72] objects which hold information pertaining to the material distribution. The navigator ensures that the extrapolator steps correctly through the complex sequence of interconnected volumes.

```
include('TrkDetDescrSvc/AtlasTrackingGeometrySvc.py')
InDetNavigator = ConfiguredNavigator( 'Navigator',
                                     tgnname = AtlasTrackingGeometrySvc.trackingGeometryName() )
```

5. The multiple scattering and energy loss models are incorporated:

```
include( 'TrkGaussianSumFilter/ConfiguredMultiStateMaterialUpdater.py' )
GsfMaterialUpdater = ConfiguredMultiStateMaterialUpdater( 'GsfMaterialUpdater' )
GsfMaterialUpdater.printInfo()
```

6. The component reduction algorithm is configured:

```
include( 'TrkGaussianSumFilter/ConfiguredGsfComponentReduction.py' )
GsfComponentReduction = ConfiguredGsfComponentReduction( 'GsfComponentReduction',
                                                         12,
                                                         'CloseComponents',
                                                         'KullbackLeibler' )
GsfComponentReduction.printInfo()
```

In this case, the maximum size of the track state after component reduction is limited to 12. The method for component reduction is either: *‘CloseComponents’* or *‘LargestWeights’*. When the close-components technique is used, similar components are identified based on either the *‘KullbackLeibler’* or *‘Mahalanobis’* distance.

7. Finally, an instance of the extrapolator is created using the navigator, material interactions model, propagator and the component reduction algorithm:

```
include ('TrkGaussianSumFilter/ConfiguredGsfExtrapolator.py')
GsfExtrapolator = ConfiguredGsfExtrapolator( 'GsfExtrapolator',
                                             InDetNavigator,
                                             GsfMaterialUpdater,
                                             [ InDetPropagator ],
                                             GsfComponentReduction )

GsfExtrapolator.printInfo()
```

B.2.2 Measurement Updator

The measurement updator combines the predicted state from the extrapolator with the measurement at a specific surface. The GSF requires the use of the standard Kalman updator:

```
#Kalman updator
include ('TrkMeasurementUpdater_xk/ConfiguredTrkMeasuredUpdater_xk.py')
InDetUpdater = ConfiguredTrkMeasuredUpdater_xk( 'InDetUpdater' )
InDetUpdater.printInfo()

#GSF updator
include( 'TrkGaussianSumFilter/ConfiguredGsfMeasurementUpdater.py' )
GsfMeasurementUpdater = ConfiguredGsfMeasurementUpdater( 'GsfMeasurementUpdater',
                                                         InDetUpdater )

GsfMeasurementUpdater.printInfo()
```

B.2.3 The Fitter

In some cases, alignment or calibration corrections to detector measurements are applied during the fit. A `RIO_OnTrack` [73] object represents a cluster or drift-circle after these adjustments have been performed. A `RIO_OnTrackCreator` algorithm is responsible for the production of the `RIO_OnTrack` objects:

```
include ('TrkRIO_OnTrackCreator/ConfigurableRIO_OnTrackCreator.py')
```

```
InDetRotCreator = ConfiguredRIO_OnTrackCreator( 'InDetRotCreator', 'indet' )
InDetRotCreator.printInfo()
```

An instance of the track fitter is established from the extrapolator, measurement updator and the RIO_OnTrackCreator.

```
include ('TrkGaussianSumFilter/ConfiguredGsfFitter.py')
InDetTrackFitter = ConfiguredGsfFitter( 'InDetTrackFitter',
                                       GsfExtrapolator,
                                       InDetRotCreator,
                                       GsfMeasurementUpdator )

InDetTrackFitter.printInfo()
```

B.3 Fitting a Track

Complete examples of how to use the GSF are given in [74, 75]; only a brief description is provided here.

All track fitters inherit from the `ITrackFitter` abstract base class [76]. The common interface allows any fitter to be selected and loaded into transient storage (`StoreGate` [26]) during initialisation of an Athena algorithm. In this example, the instance of the GSF, defined in section B.2.3 under the name “`InDetTrackFitter`”, is selected:

```
// Initialise method:
StatusCode Trk::ExampleFitter::initialize()
{
// StatusCode describes the current state of the method
StatusCode sc;

// Define a pointer to the track fitter - in general this is a data member of the class
Trk::ITrackFitter* fitterTool(0);

// Create the pointer to the tool service
sc = service( "ToolSvc", toolService )

// Initialise the GSF
sc = toolService->retrieveTool( "Trk::GaussianSumFilter", "InDetTrackFitter", fitterTool );

return sc;
}
```

B.3.1 ITrackFitter Methods

The GSF provides concrete implementations of the abstract base class methods. The two most important methods for track fitting are described:

An existing track can be refitted:

```
virtual Track* fit ( const Track&,
                   const RunOutlierRemoval outlierRemoval,
                   const ParticleHypothesis particleHypothesis ) const;
```

This method takes three arguments: a reference to an existing track; a `true / false` switch which optionally strips the track of outliers; and a flag to indicate the likely particle type, so that the appropriate corrections for material interactions are applied. The particle hypothesis can take one of the following values:

```
particleHypothesis = { nonInteracting, electron, muon, pion, kaon, proton }
```

A track fit can be applied to a set of `MeasurementBase` objects:

```
virtual Track* fit ( const MeasurementSet&,
                   const TrackParameters&,
                   const RunOutlierRemoval outlierRemoval,
                   const ParticleHypothesis particleHypothesis ) const;
```

In addition to the `MeasurementSet` and the switches for outlier logic and particle hypothesis, a `TrackParameters` object is required to provide a crude initial estimate of the trajectory.

Appendix C

The CTB Tracking Geometry

In this appendix, a brief discussion of the implementation of the tracking geometry for the CTB is presented. The tracking geometry provides a simplified description of the material distribution within the detector. Track extrapolators use this information to incorporate corrections for material interactions.

The CTB tracking geometry was implemented using classes developed for the tracking geometry of the complete detector. A more thorough discussion of these classes is given in [77].

The CTB tracking geometry is an instance of the `TrackingGeometry` [72] class. It contains a pointer to a `TrackingVolume` object which encloses the entire fiducial volume of the CTB (the ‘world’ volume).

All `TrackingVolume` objects are capable of holding arrays of material layers or smaller tracking volumes. The CTB world volume should, in principle, hold three smaller volumes containing the inner detector, calorimeter and muon spectrometer. However, only the inner detector volume is currently filled.

`TrackingVolume` uses a triple inheritance scheme to incorporate geometric, field and material specific information. The inheritance structure is shown in figure C.1.

The inner detector comprises smaller tracking volumes for the three sub-systems. `Layer` objects (figure C.2) are used to combine the geometric description of the detector with a simplified representation of the material.

The `CTB_GeometryBuilder` [78, 79] constructs the tracking volumes and the arrays of layers which characterise the material distribution in the pixels, SCT and TRT.

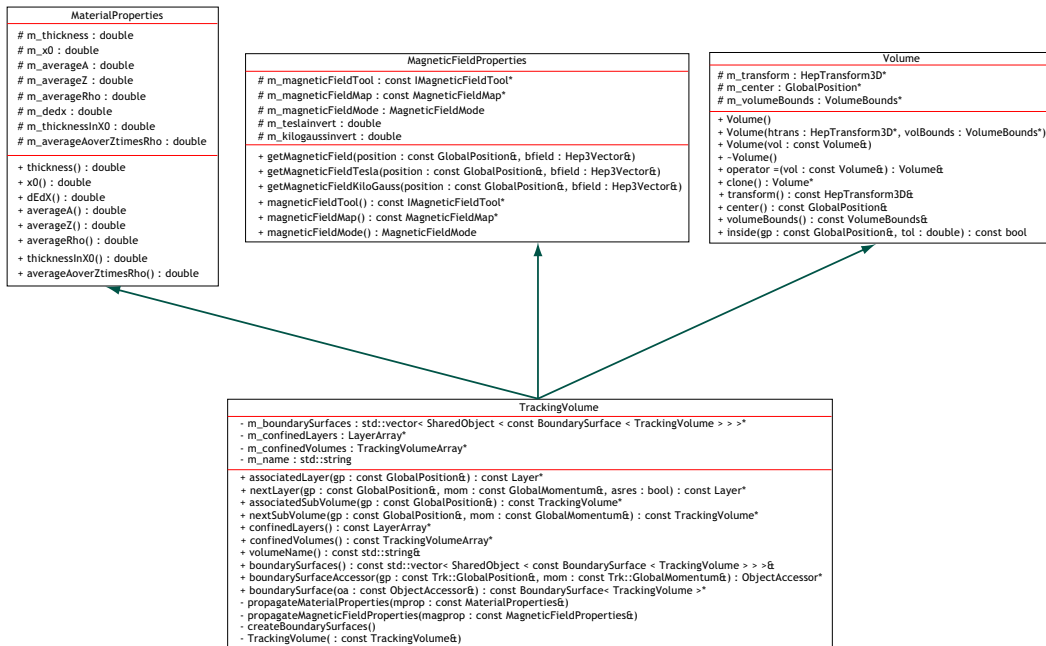


Figure C.1: Simplified UML diagram for the `TrackingVolume` class. A triple inheritance structure is used to provide geometric (`Volume`), field (`MagneticFieldProperties`) and material (`MaterialProperties`) specific information. Adapted from [77].

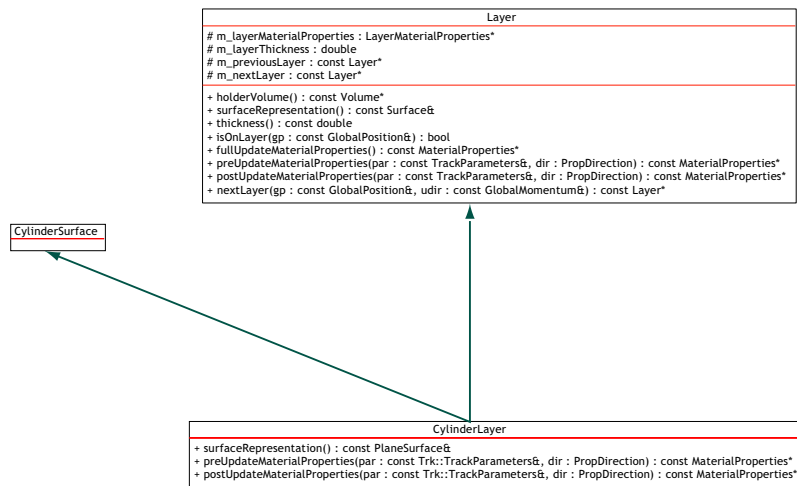


Figure C.2: Simplified UML diagram showing the inheritance structure for the `CylindricalLayer` class. The geometric information is held by the `CylinderSurface` [80] and the material description is held by the `Layer` base class. Adapted from [77].

Bibliography

- [1] I. J. R. Aitchison and A. J. G. Hey. *Gauge Theories in Particle Physics*. IOP Publishing, Bristol, 2nd edition, 1989.
- [2] M. Kaku. *Quantum Field Theory*. Oxford University Press, 1993.
- [3] M. Peskin and D. Schroeder. *An Introduction to Quantum Field Theory*. Addison-Wesley, 1995.
- [4] G. Kane. *Modern Elementary Particle Physics*. Perseus, 1993.
- [5] J. Kuti, L. Lin, and Y. Shen. Upper bound on the Higgs-boson mass in the Standard Model. *Phys. Rev. Lett.*, 61:678–681, 1988.
- [6] The LEP and SLD electroweak working groups. A combination of preliminary electroweak measurements and constraints on the Standard Model (hep-ex/0212036).
- [7] G. Abbiendi. Search for the Standard Model Higgs Boson at LEP. *Phys. Lett. B*, 565:61–75, 2003.
- [8] W-M Yao et al. Review of Particle Physics. *J. Phys. G*, 33, 2006.
- [9] D. Perkins. *Introduction to High Energy Physics*. Cambridge University Press, 4th edition, 2000.
- [10] S. Ferrara. *Supersymmetry*. World Scientific, 1987.
- [11] G. Kane. *Supersymmetry*. Perseus, 1997.
- [12] <http://lhc.web.cern.ch/lhc/>.
- [13] <http://cern.ch>.
- [14] The CMS Collaboration. The Compact Muon Solenoid Technical Proposal. Technical report, CERN, 1994.
- [15] The LHCb Collaboration. LHCb Technical Proposal. Technical report, CERN, 1998.

-
- [16] The ALICE Collaboration. ALICE Technical Proposal. Technical report, CERN, 1995.
- [17] Sterling, W. Workshop on Theory of LHC Processes, 1998. CERN.
- [18] The ATLAS Collaboration. ATLAS Technical Proposal. Technical report, CERN, 1994.
- [19] The ATLAS Collaboration. ATLAS Detector and Physics Performance Technical Design Report. Technical report, CERN, 1999.
- [20] D. Froidevaux and P. Spiccas. General-Purpose Detectors for the Large Hadron Collider. *Annu. Rev. Nucl. Part. Sci.*, 56:375–440, 2006.
- [21] The ATLAS Collaboration. ATLAS Inner Detector Technical Design Report. Technical report, CERN, 1997.
- [22] The ATLAS Collaboration. Calorimeter performance technical design report. Technical report, CERN, 1997.
- [23] The ATLAS Collaboration. Atlas muon spectrometer technical design report. Technical report, CERN, 1997.
- [24] The ATLAS Collaboration. ATLAS Level-1 Trigger Technical Design Report. Technical report, CERN, 1998.
- [25] The ATLAS Collaboration. ATLAS HLT, DAQ and DCS Technical Design Report. Technical report, CERN, 2002.
- [26] The ATLAS Collaboration. ATLAS Computing Technical Design Report. Technical report, CERN, 2005. CERN-LHCC-2005-022, <http://cdsweb.cern.ch/>.
- [27] B. Stroustrup. *The C++ Programming Language*. Addison-Wesley, 3rd edition, 2000.
- [28] Gaudi: Data Processing Applications Framework, 2001. Developer Guide.
- [29] Athena: The ATLAS Common Framework , 2004. Developer Guide.
- [30] The Geant 4 Collaboration. Introduction to Geant 4, 2006. <http://cern.ch/geant4>.
- [31] T. Sjöstrand, S. Mrenna, and P. Skands. Pythia 6.4 Physics and Manual. Technical report, Fermilab, 2006.
- [32] M. Lutz. *Programming Python*. O'Reilly Media, 3rd edition, 2006.
- [33] H. Bethe and W. Heitler. On the stopping of fast particles and on the creation of positive electrons. *Proceedings of the Royal Society of London. Series A.*, 146:83 – 112, 1934.
- [34] B. Rossi and K. Greisen. Cosmic-Ray Theory. *Rev. Mod. Phys.*, 13:240–309, 1941.

- [35] V. Highland. Some Practical Remarks on Multiple Scattering. *Nucl. Instrum. Meth.*, 129:497 – 499, 1975.
- [36] <https://uimon.cern.ch/twiki/bin/view/Atlas/NewIdOfflineTracking>.
- [37] J. Jackson. *Classical Electrodynamics*. John Wiley and Sons, 1998.
- [38] R. Frühwirth, M. Regler, R. Bock, H. Grote, and D. Notz. *Data Analysis Techniques for High-Energy Physics*. Cambridge University Press, 2nd edition, 2001.
- [39] F. Akesson, T. Atkinson, M. J. Costa, M. Elsing, S. Fleischmann, A. Gaponenko, W. Liebig, E. Moyses, A. Salzburger, and M. Siebel. ATLAS Tracking Event Data Model. Technical report, CERN, 2006. ATL-SOFT-PUB-2006-004, <http://cdsweb.cern.ch/>.
- [40] R. Frühwirth. Application of Kalman Filtering to Track and Vertex Fitting. *Nucl. Instrum. Meth.*, A262:444–450, 1987.
- [41] G. Kitagawa. Non-Gaussian Seasonal Adjustment. *Comp. and Math. Appl.*, 19:503–514, 1989.
- [42] R. Frühwirth. Track Fitting with non-Gaussian noise. *Comp. Phys. Comm*, 100:1–16, 1997.
- [43] R. Frühwirth, W. Adam, A. Strandlie, and T. Todorov. Reconstruction of electrons with the Gaussian-Sum Filter in the CMS Tracker at the LHC. CMS note 2005/001, 2005.
- [44] <http://atlas-sw.cern.ch/cgi-bin/viewcvs-atlas.cgi/offline/Tracking/TrkFitter/TrkGaussianSumFilter/>.
- [45] R. Frühwirth. A gaussian-mixture approximation of the Bethe-Heitler model of electron energy loss by bremsstrahlung. *Comp. Phys. Comm*, 154:131–142, 2003.
- [46] R. Clifft and A. Poppleton. IPatRec: Inner Detector Pattern-recognition and Track-fitting, 1994. ATL-SOFT-94-009, <http://cdsweb.cern.ch/>.
- [47] N. Benekos, R. Clifft, M. Elsing, and A. Poppleton. ATLAS Inner Detector Performance, 2004. ATL-INDET-2004-002, <http://cdsweb.cern.ch/>.
- [48] A. Salzburger. The new ATLAS fast track simulation engine (FATRAS). In *Computing in High Energy and Nuclear Physics*, 2006.
- [49] S. Grossman. *Calculus*. Saunders College Publishing, 5th edition, 1992.
- [50] W. Davey. Track fitting in the ATLAS inner detector. Technical report, The University of Melbourne, 2006.

- [51] I. Gavrilenko. Description of Global Pattern Recognition Program (XKalman), 1997. ATL-INDET-97-165, <http://cdsweb.cern.ch/>.
- [52] User's manual to the beam lines in the North area. <http://nahandbook.web.cern.ch>.
- [53] B. Di Girolamo, M. Gallas, and T. Koffas. ATLAS Barrel Combined Run in 2004. Technical report, CERN, 2005. ATC-TT-IN-0001, <http://edms.cern.ch>.
- [54] S. Pagnis. Electron Reconstruction with the EM-Barrel and EM-Endcap, 2006. ATLAS Calibration Workshop, Sant Feliu.
- [55] S. Wolfram. *The Mathematica Book*. Wolfram Media, 5th edition, 2003.
- [56] The ATLAS SCT end-cap detector modules final design review, 2002. ATL-IS-EN-0012, <http://edms.cern.ch>.
- [57] Silicon Detector PRR papers, 2000. ATL-IS-MR-0001, <http://edms.cern.ch>.
- [58] W. Dabrowski et al. Design and performance of the ABCD chip for the binary readout of silicon strip detectors in the ATLAS semiconductor tracker. *IEEE Trans. Nucl. Sci.*, 47:1843–1850, 2000.
- [59] W. Dabrowski et al. Progress in development of the readout chip for the ATLAS semiconductor tracker. In *Workshop on Electronics for LHC experiments (Cracow)*, 2000.
- [60] ABCD-T3 ASIC project specification. version 1.2.
- [61] S. Snow and J. Greenhalgh. How to survey an SCT module, 2003.
- [62] J. Hegeman. Development of new software for ATLAS forward SCT module assembly in Melbourne. Technical report, The University of Melbourne, 2002.
- [63] <http://epp.ph.unimelb.edu.au/epp/atlas/sctprod/sas/>.
- [64] Mitutoyo. *Quick Vision Series Measuring Machine*. CERN, 3rd edition, 2002.
- [65] <http://epp.ph.unimelb.edu.au/epp/sctprod/trimetro/>.
- [66] <http://epp.ph.unimelb.edu.au/epp/sctprod/sctprod.html>.
- [67] <http://sw.cern.ch/cgi-bin/viewcvs-atlas.cgi/offline/Tracking/TrkEvent/TrkTrack/>.
- [68] <http://atlas-sw.cern.ch/cgi-bin/viewcvs-atlas.cgi/offline/Tracking/TrkEvent/TrkParameters/>.

-
- [69] <http://atlas-sw.cern.ch/cgi-bin/viewcvs-atlas.cgi/offline/Tracking/TrkEvent/TrkMeasurementBase/>.
- [70] <http://atlas-sw.cern.ch/cgi-bin/viewcvs-atlas.cgi/offline/Tracking/TrkEvent/TrkEventPrimitives/>.
- [71] <http://atlas-sw.cern.ch/cgi-bin/viewcvs-atlas.cgi/offline/Tracking/TrkEvent/TrkMultiComponentStateOnSurface/>.
- [72] <http://atlas-sw.cern.ch/cgi-bin/viewcvs-atlas.cgi/offline/Tracking/TrkDetDescr/TrkGeometry/>.
- [73] http://atlas-sw.cern.ch/cgi-bin/viewcvs-atlas.cgi/offline/Tracking/TrkDetDescr/TrkRIO_OnTrack/.
- [74] <http://atlas-sw.cern.ch/cgi-bin/viewcvs-atlas.cgi/offline/InnerDetector/InDetRecAlgs/InDetBremFitAlg/>.
- [75] <http://atlas-sw.cern.ch/cgi-bin/viewcvs-atlas.cgi/offline/Tracking/TrkFitter/TrkRefitAlg/>.
- [76] <http://atlas-sw.cern.ch/cgi-bin/viewcvs-atlas.cgi/offline/Tracking/TrkFitter/TrkFitterUtils/>.
- [77] A. Salzburger. The tracking geometry in the new ATLAS offline reconstruction scheme. <http://atlas-sw.cern.ch/cgi-bin/viewcvs-atlas.cgi/offline/Tracking/TrkDoc/>.
- [78] <http://atlas-sw.cern.ch/cgi-bin/viewcvs-atlas.cgi/offline/Tracking/TrkDetDescr/TrkDetDescrTools/>.
- [79] <http://atlas-sw.cern.ch/cgi-bin/viewcvs-atlas.cgi/offline/InnerDetector/InDetDetDescr/InDetTrackingGeometry/>.
- [80] <http://atlas-sw.cern.ch/cgi-bin/viewcvs-atlas.cgi/offline/Tracking/TrkDetDescr/TrkSurfaces/>.